

Thermo-economic optimisation of large solar tower power plants

THÈSE N° 5648 (2013)

PRÉSENTÉE LE 24 JANVIER 2013

À LA FACULTÉ DES SCIENCES ET TECHNIQUES DE L'INGÉNIEUR
LABORATOIRE D'ÉNERGÉTIQUE INDUSTRIELLE
PROGRAMME DOCTORAL EN ENERGIE

ÉCOLE POLYTECHNIQUE FÉDÉRALE DE LAUSANNE

POUR L'OBTENTION DU GRADE DE DOCTEUR ÈS SCIENCES

PAR

Germain AUGSBURGER

acceptée sur proposition du jury:

Prof. C. Ballif, président du jury
Prof. D. Favrat, directeur de thèse
Dr V. Aga, rapporteur
Dr M. Romero, rapporteur
Prof. A. Steinfeld, rapporteur



ÉCOLE POLYTECHNIQUE
FÉDÉRALE DE LAUSANNE

Suisse
2013

Abstract

Given the growing number of solar tower power plants in operation, under construction and under planning, the assessment and the optimisation of their performance are required both at the energy level and the economic level. In other words, the same way as any other conventional power plant, large solar tower power plants have to convert the incoming solar radiation into as much electric power as possible, with as less money as possible on the long run.

First, the relevant local environmental conditions are identified : obviously the solar direct normal radiation and the sun's position over time, as well as the ambient temperature and the wind velocity and direction. Then the field of heliostat mirrors is created thanks to an algorithm that allows a compromise between the density of mirrors and the interferences occurring with each other. Using the Gemasolar set-up near Sevilla in Spain as a base case, the performance of the heliostat field is simulated over three specific days and interpolated over the entire year. As a result, the annual output of the central receiver is obtained and implemented as the input for a storage system and a conventional heat-to-electricity conversion cycle. A specific operating strategy provides the overall energy performance of the plant. In parallel, the incident flux distribution on the receiver is also simulated to identify peaks and transients, especially due to clouds. Two multi-aiming strategies are investigated and allow to decrease the peaks significantly without affecting too much the total power. Subsequently, the economic performance of a solar tower plant is assessed thanks to a detailed investment cost analysis and with an estimate of financial indicators such as the levelised electricity cost and the project net present value.

A thermo-economic optimisation allows then the description of optimal trade-off set-ups in comparison to the Gemasolar base case. The key decision variables are given by a sensitivity analysis that already shows a set of potential efficiency and cost improvements. The optimisation itself leads to even greater potential improvements of 24 points in field efficiency and 9 [¢/kWh_{el}] in levelised electricity cost. Furthermore, with variable ranges limited to the parameters of Gemasolar, the best equivalent plant set-up shows a 40% smaller land area. After that, multi-tower set-ups are proposed and also implemented in the optimisation, which highlights the optimal single- to multi-tower transition size. Finally, a combination of a parabolic trough collector field and a heliostat field in the same plant is studied and turns out to make a further cost decrease possible.

Keywords : solar tower thermal power plant, thermo-economic optimisation

Résumé

Étant donné le nombre croissant de centrales solaires à tour en service, en construction et en planification, l'évaluation et l'optimisation de leur performance sont requises au niveau énergétique et au niveau économique. En d'autres termes, comme n'importe quelle autre centrale conventionnelle, les grandes centrales solaires à tour doivent convertir la radiation solaire entrante en autant de puissance électrique que possible, avec le moins d'argent possible sur le long-terme.

Premièrement, les conditions environnementales locales pertinentes sont identifiées : la radiation solaire normale directe et la position du soleil dans le temps, la température ambiante, et la vitesse du vent et sa direction. Ensuite le champ de miroirs héliostats est créé avec un algorithme qui permet un compromis entre la densité des miroirs et leurs interférences. En utilisant la configuration de Gemasolar à Séville en Espagne comme cas de base, la performance du champ d'héliostats est simulée sur trois jours spécifiques et interpolée sur toute l'année. Ainsi, la production annuelle du receiver est obtenue et transmise à un système de stockage et un cycle conventionnel de conversion de puissance-chaleur en puissance électrique. Une stratégie opératoire spécifique fournit la performance énergétique globale de la centrale. En parallèle, la distribution du flux incident sur le receiver est simulée pour identifier des pics et les transitoires surtout dûs à des nuages. Deux stratégies de visée multiple sont étudiées et permettent de diminuer les pics significativement sans trop affecter la puissance totale. Par la suite, la performance économique d'une centrale solaire à tour est évaluée grâce à une étude détaillée des coûts d'investissement et avec une estimation d'indicateurs économiques comme le coût annualisé d'électricité et la valeur actuelle nette du projet.

Une optimisation thermo-économique permet alors la description de compromis optimaux de configurations en comparaison avec le cas de Gemasolar. Les variables-clés de décision sont données par une analyse de sensibilité qui montre déjà des améliorations potentielles d'efficacité et de coût. L'optimisation en soi même à d'encore plus grandes améliorations potentielles, de 24 points en efficacité de champ et de 9 [¢/kWh_{el}] en coût annualisé d'électricité. De plus, avec des intervalles de variation limités aux paramètres de Gemasolar, la meilleure centrale équivalente montre un terrain 40% plus petit. Après cela, des configurations multi-tour sont proposées et implémentées dans l'optimisation, ce qui met en lumière la taille de transition optimale de simple à multi-tour. Finalement, la combinaison de collecteurs cylindro-paraboliques et d'un champ d'héliostats dans la même centrale est étudiée et rend possible une diminution supplémentaire du coût.

Mots-clés : centrale solaire thermique à tour, optimisation thermo-économique

Remerciements

C'est tout d'abord au professeur Daniel Favrat, directeur du Laboratoire d'Energétique Industrielle (LENI) de l'Ecole Polytechnique Fédérale de Lausanne (EPFL), que je souhaite adresser mes remerciements. En tant qu'initiateur et directeur de cette thèse, il a apporté son indéniable compétence et expérience en génie mécanique, thermodynamique, énergétique, autant sur le plan académique qu'industriel. Son ouverture et sa vivacité d'esprit, produisant des critiques constructives et pertinentes, ont été précieuses tout au long de ce travail. Je le remercie pour les responsabilités qu'il m'a confiées en toute autonomie, et pour ces encouragements au-delà du doute.

Mes remerciements vont naturellement à Marco Simiano, Erik Boschek et Vipluv Aga qui ont successivement initié le financement de cette thèse par ALSTOM Switzerland AG, contribué à son intégration dans un projet industriel d'envergure, puis supervisé, relu, corrigé et commenté les résultats soumis.

Je tiens à remercier également les membres du jury, pour avoir accepté l'invitation, entrepris la lecture et la critique de ce travail, et apporté leur expertise dans ses détails.

Merci à tous mes collègues du LENI et de l'atelier de mécanique pour leurs nombreuses contributions dans le cadre professionnel autant qu'en-dehors.

Toute ma reconnaissance et ma satisfaction vont aussi envers les excellents étudiants que j'ai eu le privilège de superviser dans leur travail de diplôme, pour leur engagement, la tâche accomplie et leur apport à l'édifice de cette thèse.

Enfin, je remercie du fond du cœur mes amis et ma famille pour leurs encouragements et leur soutien.

Lausanne, le 10 janvier 2013

G. A.

Contents

| | |
|----------------------------------------------------------|--------------|
| Abstract | iii |
| Résumé | v |
| Remerciements | vii |
| Table of contents | xi |
| List of figures | xvi |
| List of tables | xviii |
| Nomenclature | xxv |
| 1 Introduction | 1 |
| 1.1 Concentrating Solar Power | 1 |
| 1.2 Solar Tower Power Plants | 3 |
| 1.3 Heliostat Fields | 6 |
| 1.4 Objectives & Methodology | 9 |
| 2 Environment and Plant Set-Up | 11 |
| 2.1 Direct Normal Irradiance | 11 |
| 2.2 Sun's Position | 14 |
| 2.3 Ambient Temperature | 16 |
| 2.4 Wind | 17 |
| 2.5 Heliostats | 18 |
| 2.6 Field Layout | 19 |
| 2.6.1 Algorithm for Staggered Circular Layouts | 20 |
| 2.7 Tower | 27 |
| 2.8 Receiver | 28 |
| 2.9 Power Conversion Unit | 31 |
| 2.10 Summary | 32 |
| 3 Energy Performance | 33 |
| 3.1 Heliostat Field | 33 |
| 3.2 Receiver | 40 |

Contents

| | | |
|----------|--------------------------------------------------------------|------------|
| 3.3 | Power Conversion Unit | 42 |
| 3.4 | Specific Days | 46 |
| 3.5 | Annual Interpolation | 48 |
| 3.6 | Summary | 53 |
| 4 | Receiver Incident Flux | 55 |
| 4.1 | Flux Distribution on the Receiver | 55 |
| 4.2 | Receiver Incident Flux Transients | 58 |
| 4.2.1 | Cloud Passage on the Heliostat Field | 59 |
| 4.2.2 | Transient Flux Distribution on the Receiver | 61 |
| 4.2.3 | Worst Case of Receiver Transient Flux | 64 |
| 4.2.4 | Strategy Proposal | 65 |
| 4.3 | Multi-Aiming on the Receiver | 67 |
| 4.4 | Summary | 71 |
| 5 | Economic Performance | 73 |
| 5.1 | Investment Costs | 73 |
| 5.1.1 | Heliostat Field | 73 |
| 5.1.2 | Tower & Receiver | 80 |
| 5.1.3 | Power Conversion Unit | 81 |
| 5.2 | Financial Performance | 83 |
| 5.3 | Summary | 85 |
| 6 | Thermo-Economic Optimisation | 87 |
| 6.1 | Plant Thermo-Economic Performance | 87 |
| 6.2 | Sensitivity Analysis | 89 |
| 6.3 | Thermo-Economic Optimisation | 95 |
| 6.4 | Summary | 102 |
| 7 | Multi-tower set-up | 103 |
| 7.1 | Multi-Tower Heliostat Field Layout | 103 |
| 7.2 | Aim Selection Criterion | 105 |
| 7.3 | Multi-Tower Conversion Cycle | 108 |
| 7.4 | Single- vs. Multi-Tower Comparison Case | 109 |
| 7.5 | Sensitivity Analysis | 111 |
| 7.6 | Thermo-Economic Optimisation of Multi-Tower Plants | 114 |
| 7.7 | Summary | 121 |
| 8 | Trough-Tower Combination | 123 |
| 8.1 | Parabolic Trough Plant | 123 |
| 8.2 | Trough/Tower Combination | 125 |
| 8.2.1 | Steam Cycle Integration | 126 |
| 8.2.2 | 100 [MW _e] Case Study | 128 |
| 8.3 | Summary | 132 |

| | |
|-----------------------------------------------------------------------------------------------------------------------|------------|
| 9 Conclusions and Outlook | 133 |
| 9.1 Thermo-Economic Simulation of Solar Tower Power Plants | 133 |
| 9.2 Optimal Thermo-Economic Trade-Off Set-Ups | 135 |
| 9.3 Future Work | 136 |
| A List of Heliostat Fields | 139 |
| B DNI comparison at Gemasolar | 157 |
| C Comparison with HFLCAL | 161 |
| C.1 Assumptions for Heliostat Field Simulations | 162 |
| C.2 Power Calculations with HFLCAL | 166 |
| C.3 Comparison | 168 |
| D Sensitivity Analysis on Gemasolar | 171 |
| E Heliostat Fields from the Single-Tower Thermo-Economic Optimisation | 177 |
| F Thermo-Economic Optimisation with Constrained Tower and Receiver Size | 183 |
| F.1 Pareto Front of Optimal Trade-Off Set-Ups with Constrained Tower and Receiver Size | 184 |
| F.2 Selected Points on the Pareto Front with $W_{Rec} = 8$ [m], $H_{Rec} = 10$ [m], $H_{Aim} = 120$ [m] | 185 |
| F.3 Selected Points on the Pareto Front with $W_{Rec} < 16$ [m], $H_{Rec} < 20$ [m], $H_{Aim} <$ 200 [m] | 189 |
| G Sensitivity Analysis on a Multi-Tower Set-Up | 193 |
| H Heliostat Fields from the Multi-Tower Thermo-Economic Optimisation | 195 |
| I Trough Field Model | 201 |
| I.1 Energy Performance | 201 |
| I.1.1 Trough Field | 201 |
| I.1.2 Power Conversion Unit | 207 |
| I.2 Economic Performance | 207 |
| I.2.1 Investment Costs | 207 |
| I.2.2 Financial Performance | 207 |
| I.3 Andasol-1 Case Study | 207 |
| J Life Cycle Analysis of CSP | 211 |
| Bibliography | 224 |
| Curriculum Vitae | 225 |

List of Figures

| | | |
|------|-------------------------------------------------------------|----|
| 1.1 | Concentrating solar collectors | 2 |
| 1.2 | Pressurized air-based plant diagram | 3 |
| 1.3 | Atmospheric air-based plant diagram | 4 |
| 1.4 | Molten salt-based plant diagram | 5 |
| 1.5 | Steam-based plant diagram | 6 |
| 1.6 | Annual DNI world map | 7 |
| 1.7 | World map of built heliostat fields | 7 |
| 2.1 | Time map of the Direct Normal Irradiation | 13 |
| 2.2 | Sun path vs. the Direct Normal Irradiation | 14 |
| 2.3 | Time map of the ambient temperature | 16 |
| 2.4 | Time map of the wind velocity | 17 |
| 2.5 | Staggered field layout | 21 |
| 2.6 | No-touching and no-blocking for azimuthal spacing | 22 |
| 2.7 | No-touching and no-blocking for radial spacing | 23 |
| 2.8 | Field layout circle boundary | 26 |
| 2.9 | Gemasolar-like field layout | 27 |
| 2.10 | Types of receiver discretization | 30 |
| 3.1 | Calculated shading coefficients | 34 |
| 3.2 | Calculated cosine loss coefficients | 35 |
| 3.3 | Calculated blocking loss coefficients | 36 |
| 3.4 | Calculated atmospheric attenuation coefficients | 37 |
| 3.5 | Calculated spillage coefficients | 38 |
| 3.6 | Receiver first-law efficiency | 42 |
| 3.7 | Storage operation strategy | 44 |
| 3.8 | Calculated heliostats efficiency | 47 |
| 3.9 | Calculated field efficiency vs. sun positions | 48 |
| 3.10 | Plant Sankey diagram of losses | 48 |
| 3.11 | Interpolated field efficiency vs. sun positions | 49 |
| 3.12 | Annual power profile | 50 |
| 3.13 | Time map of the electric output | 51 |
| 4.1 | Two picked heliostats | 57 |

List of Figures

| | | |
|------|----------------------------------------------------------------------------------------|-----|
| 4.2 | Gemasolar-like receiver incident flux | 57 |
| 4.3 | Cloud frequency in Tucson, Arizona | 60 |
| 4.4 | Receiver incident flux of the Gemasolar-like field covered by a cloud | 62 |
| 4.5 | Receiver incident flux of the Gemasolar-like field uncovered by a cloud | 63 |
| 4.6 | Receiver incident flux of the Gemasolar-like field in the worst case | 65 |
| 4.7 | Receiver incident flux of the Gemasolar-like field with progressive start-up | 66 |
| 4.8 | Distance-based multi-aiming | 68 |
| 4.9 | Deviation-based multi-aiming | 69 |
| 4.10 | Receiver incident flux without and with multi-aiming | 70 |
| 5.1 | Heliostat cost breakdown | 78 |
| 5.2 | Heliostat specific cost sensitivity. | 79 |
| 5.3 | Plant cost breakdown | 82 |
| 6.1 | Gemasolar sensitivity to aim point height | 90 |
| 6.2 | Gemasolar sensitivity to heliostat area | 91 |
| 6.3 | Gemasolar sensitivity to receiver area | 93 |
| 6.4 | Gemasolar potential improvements | 95 |
| 6.5 | Pareto front of single-tower set-ups | 98 |
| 6.6 | Heliostat field of the single-tower set-up at point A | 100 |
| 6.7 | Heliostat field of the single-tower set-up at point B | 100 |
| 6.8 | Heliostat field of the single-tower set-up at point C | 101 |
| 6.9 | Heliostat field of the single-tower set-up at point D | 101 |
| 7.1 | Multi-tower heliostat field layouts | 104 |
| 7.2 | Multi-tower aim selection | 106 |
| 7.3 | Multi-tower receiver incident flux | 107 |
| 7.4 | Multi-tower heliostats efficiency | 107 |
| 7.5 | Multi-tower conversion cycle | 109 |
| 7.6 | Multi-tower sensitivity to distance | 111 |
| 7.7 | Multi-tower sensitivity to number of towers | 113 |
| 7.8 | Multi-tower potential improvements | 114 |
| 7.9 | Pareto front of multi-tower set-ups | 117 |
| 7.10 | Transition Pareto front from single- to multi-tower set-ups | 118 |
| 7.11 | Heliostat field of one- to two-tower transition set-ups | 120 |
| 7.12 | Heliostat field of two- to three-tower transition set-ups | 121 |
| 8.1 | Trough/tower principle diagram | 125 |
| 8.2 | Steam cycle T-s diagram | 126 |
| 8.3 | Steam cycle pressures optimisation | 127 |
| 8.4 | Steam cycle T-s diagram | 127 |
| 8.5 | Steam cycle T-H diagram | 128 |
| 8.6 | Heliostat/trough field for 100 MW _{el} | 129 |

| | |
|--------------------------------------------------------------------------------------------------------|-----|
| 8.7 Trough/tower plant cost breakdown | 131 |
| A.1 Samar heliostat field | 151 |
| A.2 Hohai heliostat field | 151 |
| A.3 NSEC heliostat field | 151 |
| A.4 Odeillo heliostat field | 151 |
| A.5 UzAS heliostat field | 151 |
| A.6 WIS heliostat field | 151 |
| A.7 SSPS-CRS heliostat field | 151 |
| A.8 CRTF heliostat field | 152 |
| A.9 EURELIOS heliostat field | 152 |
| A.10 Themis heliostat field | 152 |
| A.11 CESA-1 heliostat field | 152 |
| A.12 Jülich heliostat field | 152 |
| A.13 SEDC heliostat field | 153 |
| A.14 eSolar heliostat field | 153 |
| A.15 SPP-5 heliostat field | 153 |
| A.16 Coalinga heliostat field | 153 |
| A.17 PS10 heliostat field | 154 |
| A.18 Solar One/Two heliostat field | 154 |
| A.19 PS20 heliostat field | 155 |
| A.20 Gemasolar heliostat field | 155 |
| A.21 Ivanpah heliostat field | 156 |
| B.1 Comparison of DNI databases for the Gemasolar site (1) | 158 |
| B.2 Comparison of DNI databases for the Gemasolar site (2) | 159 |
| C.1 4000 heliostats layout | 164 |
| C.2 Comparison of HFLCAL against [Monterreal, 1998] combined with [Collado et al., 1986] (1) | 168 |
| C.3 Comparison of HFLCAL against [Monterreal, 1998] combined with [Collado et al., 1986] (2) | 169 |
| D.1 Gemasolar sensitivity to field slope | 172 |
| D.2 Gemasolar sensitivity to field slope start | 173 |
| D.3 Gemasolar sensitivity to mirrors density | 174 |
| D.4 Gemasolar sensitivity to solar multiple | 175 |
| E.1 Heliostat field of the single-tower set-up at point A | 178 |
| E.2 Heliostat field of the single-tower set-up at point B | 179 |
| E.3 Heliostat field of the single-tower set-up at point C | 180 |
| E.4 Heliostat field of the single-tower set-up at point D | 181 |
| F.1 Pareto front of single-tower set-ups with constrained tower and receiver | 184 |

List of Figures

| | | |
|-----|---------------------------------------------------------------------------------|-----|
| E.2 | Heliostat field of the single-tower set-up at point I | 186 |
| E.3 | Heliostat field of the single-tower set-up at point J | 186 |
| E.4 | Heliostat field of the single-tower set-up at point K | 187 |
| E.5 | Heliostat field of the single-tower set-up at point L | 187 |
| E.6 | Heliostat field of the single-tower set-up at point I | 190 |
| E.7 | Heliostat field of the single-tower set-up at point J | 190 |
| E.8 | Heliostat field of the single-tower set-up at point K | 191 |
| E.9 | Heliostat field of the single-tower set-up at point L | 191 |
| G.1 | Multi-tower sensitivity to receiver area | 194 |
| H.1 | Heliostat field of one- to two-tower transition set-up (E) | 196 |
| H.2 | Heliostat field of one- to two-tower transition set-up (F) | 197 |
| H.3 | Heliostat field of one- to two-tower transition set-up (G) | 198 |
| H.4 | Heliostat field of one- to two-tower transition set-up (H) | 199 |
| I.1 | Trough calculated temperature profile with PTR70, LS-2 & Syltherm 800 | 205 |
| I.2 | Trough ΔT comparison with tests on PTR70, LS-2 & Syltherm 800 | 206 |
| I.3 | Trough efficiency comparison with tests on PTR70, LS-2 & Syltherm 800 | 206 |
| I.4 | Trough plant diagram of Andasol-1 | 208 |
| I.5 | Trough plant Sankey diagram of losses | 209 |
| I.6 | Trough cost breakdown | 209 |
| I.7 | Trough plant cost breakdown | 210 |
| J.1 | System limits for LCA | 212 |
| J.2 | Impact of CSP vs. fossil | 213 |
| J.3 | Impact of CSP vs. other renewable | 213 |

List of Tables

| | | |
|-----|---------------------------------------------------------------------------------------------------|-----|
| 1.1 | Concentrating solar collectors | 2 |
| 1.2 | List of medium and large commercial solar tower plants | 8 |
| 2.1 | Assumed properties of the heliostats used at the Gemasolar plant | 19 |
| 2.2 | Properties of the field layout applied at the Gemasolar plant | 26 |
| 3.1 | Properties of PCU at the Gemasolar plant | 46 |
| 3.2 | Annual energy performances of the Gemasolar plant | 53 |
| 5.1 | Heliostat direct cost parameters | 76 |
| 5.2 | Heliostat indirect cost parameters | 77 |
| 5.3 | Heliostat indirect costs | 78 |
| 5.4 | PCU cost parameters | 82 |
| 5.5 | PCU costs | 82 |
| 5.6 | Financial performance | 85 |
| 6.1 | Thermo-economic performance of the Gemasolar plant | 88 |
| 6.2 | decision variables, objectives and constraints | 97 |
| 6.3 | Design variables, energy and economic performances of four single-tower set-ups | 99 |
| 7.1 | Multi-tower comparison | 110 |
| 7.2 | Multi-tower decision variables, objectives and constraints | 115 |
| 7.3 | Design variables, energy and economic performances of transition multi-tower set-ups | 119 |
| 8.1 | Parameters of the trough/tower field for the 100 MW _{el} case study | 130 |
| 8.2 | Performance of the trough/tower field for the 100 MW _{el} case study | 131 |
| A.1 | List of heliostat fields (1a) | 140 |
| A.2 | List of heliostat fields (1b) | 141 |
| A.3 | List of heliostat fields (1c) | 142 |
| A.4 | List of heliostat fields (1d) | 143 |
| A.5 | List of heliostat fields (1e) | 144 |
| A.6 | List of heliostat fields (2a) | 146 |
| A.7 | List of heliostat fields (2b) | 147 |

Nomenclature

| | | |
|------|---------------------------------------------------------------------------------------------------------------------|-----|
| A.8 | List of heliostat fields (2c) | 148 |
| A.9 | List of heliostat fields (2d) | 149 |
| A.10 | List of heliostat fields (2e) | 150 |
| C.1 | DNI for the comparison with HFLCAL (1) | 163 |
| C.2 | DNI for the comparison with HFLCAL (2) | 164 |
| C.3 | Heliostat for the comparison with HFLCAL | 165 |
| C.4 | HFLCAL results (1) | 167 |
| C.5 | HFLCAL results (2) | 168 |
| F.1 | Design variables, energy and economic performances of four single-tower set-ups with fixed tower and receiver | 185 |
| F.2 | Design variables, energy and economic performances of four single-tower set-ups with constrained tower and receiver | 189 |
| I.1 | Trough direct cost parameters | 207 |
| I.2 | Parameters & performance of the trough field for Andasol-1 | 208 |

Nomenclature

Roman

| | | |
|-----------|-----------------------------------|----------------------|
| A | Area | $[m^2]$ |
| C | Coefficient, Ratio | $[-]$ |
| D | Diameter, Distance | $[m]$ |
| \dot{E} | Work power, Electric power | $[W]$, $[W_{el}]$ |
| E | Work energy, Electric energy | $[Wh]$, $[Wh_{el}]$ |
| G | Irradiance | $[W/m^2]$ |
| H | Height | $[m]$ |
| I | Investment | $[\$]$ |
| L | Length | $[m]$ |
| \dot{M} | Mass flow rate | $[kg/s]$ |
| N | Number | $[\#]$ |
| \dot{Q} | Heat power | $[W_{th}]$ |
| Q | Heat energy | $[Wh_{th}]$ |
| R | Radius | $[m]$ |
| S | Size | $[...]$ |
| T | Temperature | $[K]$ |
| U | Overall heat transfer coefficient | $[W/(m^2 \cdot K)]$ |
| V | Volume of production | $[u]$ |
| W | Width | $[m]$ |
| \dot{Y} | Transformation power rate | $[W]$ |
| Nu | Nusselt number | $[-]$ |
| Pr | Prandtl number | $[-]$ |
| Re | Reynolds number | $[-]$ |

Nomenclature

| | | |
|---------------|--------------------------------------|------------------|
| c | Specific cost | [\$/...] |
| d | Diameter | [m] |
| f | Friction factor | [-] |
| h | Hour Angle, Specific enthalpy | [°] , [J/kg] |
| i | Interest rate | [-] |
| k | Thermal conductivity | [W/(m·K)] |
| l | Latitude | [°] |
| n | Normal, Index | [-] , [#] |
| s | Scaling factor, Specific entropy | [-] , [J/(kg·K)] |
| t | Time | [h] , [s] |
| v | Velocity | [m/s] |
| x | X-Coordinate | [m] |
| y | Y-Coordinate | [m] |
| z | Z-Coordinate | [m] |
| az | Azimuth Angle | [°] |
| el | Elevation Angle | [°] |
| or | Overhead ratio | [-] |
| pi | Price index | [-] |
| pr | Progress ratio | [-] |
| Greek | | |
| Ψ | Angle to S-N axis | [°] |
| α | Absorptivity | [-] |
| β | Terrain Slope | [°] |
| δ | Solar Declination, Density | [°] , [-] |
| ε | First-law efficiency, Emissivity | [-] , [-] |
| η | Transformed y-coordinate | [m] |
| γ | Azimuthal Angle, Interception Factor | [°] , [-] |
| θ | Rotation angle | [rad] |
| ξ | Transformed x-coordinate | [m] |
| ρ | Reflectance | [-] |

| | | |
|----------|-----------------------------------------------|-----------------------------------------------|
| σ | Standard deviation, Stefan–Boltzmann constant | [rad] , [W/(m ² ·K ⁴)] |
| τ | Rotation angle, Transmissivity | [rad] , [-] |
| ω | Incidence angle | [°] |

Superscripts

| | | |
|----------|---------------------------|-----|
| * | Dimensionless | |
| ' | Transformed (rotated) | |
| " | Transformed and corrected | |
| 0 | Reference | |
| <i>i</i> | Index | [#] |

Subscripts

| | |
|---------------|-------------------------|
| <i>B</i> | Beam, Direct |
| <i>C</i> | Centre |
| <i>D</i> | Diffuse |
| <i>Z</i> | Zukauskas |
| <i>G</i> | Ground, Glass |
| <i>R</i> | Reflected |
| <i>Y</i> | Years |
| <i>Aim</i> | Receiver aim |
| <i>Atten</i> | Atmospheric attenuation |
| <i>Aux</i> | Auxiliary |
| <i>Avail</i> | Availability |
| <i>AzSpac</i> | Azimuthal Spacing |
| <i>Clean</i> | Cleanliness |
| <i>Cond</i> | Conduction |
| <i>Conv</i> | Convection |
| <i>Cov</i> | Covered |
| <i>Cy</i> | Cycle |
| <i>Dir</i> | Direct costs |
| <i>Field</i> | Heliostat field |
| <i>Gen</i> | Generator |

Nomenclature

| | |
|----------------|-------------------------------------------------|
| <i>Gi</i> | Glass envelope inner surface |
| <i>Glass</i> | Glass envelope |
| <i>Go</i> | Glass envelope outer surface |
| <i>Hel</i> | Heliostat |
| <i>Improv</i> | Land improvements |
| <i>Inc</i> | Incident |
| <i>Indir</i> | Indirect costs |
| <i>Land</i> | Land (including improvements) |
| <i>Mirr</i> | Mirror |
| <i>MultiA</i> | Multi-aiming |
| <i>Optic</i> | Optical improvement cost |
| <i>OverH</i> | Overhead costs |
| <i>Ped</i> | Pedestal |
| <i>Pip</i> | Piping |
| <i>Rad</i> | Radiation |
| <i>RadSpac</i> | Radial Spacing |
| <i>Rec</i> | Receiver |
| <i>Refl</i> | Reflection |
| <i>Ri</i> | Receiver tube inner surface |
| <i>Ro</i> | Receiver tube outer surface |
| <i>Row1</i> | First row |
| <i>S&M</i> | Sun and mirror |
| <i>Sep</i> | Separation |
| <i>ShiftA</i> | Shifted aim |
| <i>Sky</i> | Sky |
| <i>Slope</i> | Slope (curvature, waviness, alignment, gravity) |
| <i>Spill</i> | Spillage |
| <i>StoN</i> | South-to-north |
| <i>Stor</i> | Storage |
| <i>Terrain</i> | Terrain (without improvements) |

| | | |
|----------------|----------------|-----|
| <i>Tow</i> | Tower | |
| <i>Track</i> | Tracking | |
| <i>Wind</i> | Wind | |
| <i>a</i> | Atmosphere | |
| <i>h</i> | Horizontal | |
| <i>i</i> | Index | [#] |
| <i>j</i> | Index | [#] |
| <i>k</i> | Index | [#] |
| <i>m</i> | Index | [#] |
| <i>n</i> | Normal | |
| <i>t</i> | Tilted | |
| <i>an</i> | Annual | |
| <i>eff</i> | Effective | |
| <i>el</i> | Electric | |
| <i>in</i> | Input | |
| <i>max</i> | Maximum | |
| <i>min</i> | Minimum | |
| <i>noBlock</i> | No-Blocking | |
| <i>nom</i> | Nominal | |
| <i>noTouch</i> | No-Touching | |
| <i>out</i> | Output | |
| <i>sc</i> | Solar Constant | |
| <i>th</i> | Thermal | |

Acronyms

| | |
|----------|--------------------------------------------------------------------------------------------------|
| CESA-1 | Second Central Receiver Facility at the Plataforma Solar de Almería, Spain |
| CF | Capacity Factor |
| CRS | Central receiver system |
| CRTF-SNL | Central Receiver Test Facility of the Sandia National Laboratories, Albuquerque, New Mexico, USA |
| CSIRO | Commonwealth Scientific and Industrial Research Organisation, Australia |

Nomenclature

| | | |
|------------|------------------------------------------------------------------------------------------------------------------------|------------------------|
| CSP | Concentrating Solar Power | |
| DLR | Deutsches Zentrum für Luft- und Raumfahrt, Germany | |
| DNI | Direct Normal Irradiance | [W/m ²] |
| DSG | Direct Steam Generation | |
| EA | Evolutionary algorithm | |
| EOR | Enhanced oil recovery | |
| FiT | Feed-in tariff | [\$/Wh _{el}] |
| HFLCAL | Heliostat Field Layout Calculations | |
| HTF | Heat Transfer Fluid | |
| HTF | Heat Transfer Fluid | |
| IAM | Incidence Angle Modifier | [-] |
| IRR | Internal rate of return | [-] |
| ISCCS | Integrated Solar Combined Cycle System | |
| CSP | Linear Fresnel collector | |
| LCA | Life cycle analysis | |
| LEC | Levelised electricity cost | [\$/Wh _{el}] |
| LPT | Luz Power Tower, Negev, Israel | |
| MOO | Multi-objective optimiser | |
| MT | Mid-Sized Steam Turbine, Medium Temperature | |
| MTSA | Multi-tower solar array | |
| NAICS | North American Industry Classification System | |
| NPV | Net present value | [\$] |
| OM | Operating & Maintenance cost | [\$/Wh _{el}] |
| DoE | U.S. Department of Energy | |
| NSEC-CSIRO | National Solar Energy Centre of the Commonwealth Scientific and Industrial Research Organisation, Newcastle, Australia | |
| PCU | Power Conversion Unit | |
| PDC | Parabolic dish collector | |
| PPI | Production price index | |
| PROMES | Laboratoire de Procédés, Matériaux et Énergie Solaire, France | |

| | | |
|----------|----------------------------------------------------------------------------------------------------|------------------------|
| PS10 | Planta Solar 10, Sanlúcar la Mayor, Spain | |
| PS20 | Planta Solar 20, Sanlúcar la Mayor, Spain | |
| PSA | Plataforma Solar de Almería, Spain | |
| PTC | Parabolic trough collector | |
| PV | Photovoltaic | |
| S-N | South-North | |
| S2 | Solar Two, Barstow, California, USA | |
| SEDC | Solar Energy Development Center (BrightSource Energy), Rotem Industrial Park, Negev desert, Israel | |
| SM | Solar Multiple | [-] |
| SNL | Sandia National Laboratories, Albuquerque, New Mexico, USA | |
| SO | Solar One, Barstow, California, USA | |
| SSPS-CRS | First Central Receiver Facility at the Plataforma Solar de Almería, Spain | |
| ST | Solar Time | [h] |
| STE | Solar Thermal Electricity | |
| TMY | Typical Meteorological Year | |
| ToE | Tariff of electricity | [\$/Wh _{el}] |
| TRY | Test Reference Year | |
| UzAS | Uzbek Academy of Sciences | |
| W-E | West-East | |
| WIS | Weizmann Institute of Technology, Rehovot, Israel | |

1 Introduction

At the beginning of 2012, the solar thermal power plants in operation worldwide achieved a total capacity of 2'103 [MW_{el}], while new plants were under construction for 2'662 [MW_{el}] of additional capacity [Crespo et al., 2012]. Besides, more than 13'000 [MW_{el}] were under planning, which means with signed agreement or within short-term national programmes. Despite this high growth rate, the sector is still at an early stage of its learning curve in comparison with other renewable technologies such as photovoltaic (70 [GW_{el}]) and wind (250 [GW_{el}]). Therefore the continuous assessment and optimisation of both the energy and the economic performances of solar thermal power plants are required. In a simplified statement, solar thermal power plants have to convert solar radiation into as much electricity as possible, and at the same time cost as less money as possible, as any other conventional plant.

1.1 Concentrating Solar Power

The conversion of solar thermal electricity (STE) is mainly based on four concentrating solar power (CSP) technologies, given here in increasing order of deployment worldwide in 2011:

- parabolic dish collectors (PDC), ~1 [MW_{el}] in operation;
- linear Fresnel collectors (LFC), 10 [MW_{el}] in operation, 30 [MW_{el}] under construction;
- central tower systems (CRS), 55 [MW_{el}] in operation, 502 [MW_{el}] under construction;
- parabolic trough collectors (PTC), 1'630 [MW_{el}] in operation, 2'130 [MW_{el}] under construction.

On the one hand, Linear Fresnel and parabolic trough collectors are line-focussing concentrators and thus need a single-axis tracking system (see Figure 1.1). Their concentration ratio remains below 100 suns and allows medium temperature levels up to 550 [°C] (see Table 1.1). On the other hand, parabolic dish and central tower systems are point-focussing concentrators featuring a two-axis tracking system. They may reach concentration levels exceeding 1500 suns and high temperatures above 1500 [°C]. For this reason, parabolic dish and central tower systems are expected to reach higher efficiencies of energy conversion according to Carnot on the long run. Currently, the annual solar-to-electricity efficiency may achieve 13% for LFC plants, 11% to 16% for PTC, 12% to 25% for PDC, and 7% to 20% for CRS [IRENA, 2012].

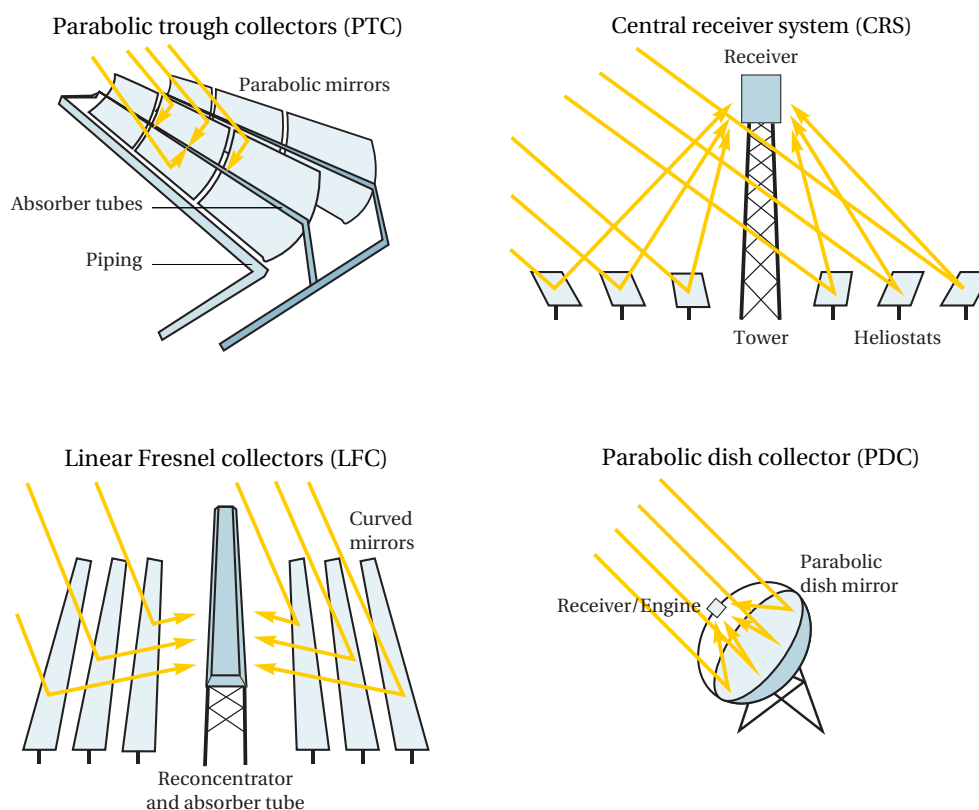


Figure 1.1 – Concentrating solar collectors (adapted from [SolarPACES, 2009]).

Regarding the cost of electricity, to this day only PTC and CRS plants have undergone enough deployment to provide an estimate of their range of variation: respectively 14 [¢/kWh_{el}] to 36 [¢/kWh_{el}], and 17 [¢/kWh_{el}] to 29 [¢/kWh_{el}]. In the medium term, a series of potential cost improvements have been identified, leading for instance to a projected cost of 8 [¢/kWh_{el}] for central tower plants by 2020 [Kolb et al., 2011]. Even more aggressive, the SunShot initiative launched by the U.S. Department of Energy (DoE) in 2011 aims at grid parity for CSP in general with 5-6 [¢/kWh_{el}] without subsidies [NREL, 2012], which requires disruptive rather than incremental technological advancements over the current decade.

Table 1.1 – Concentrating solar collectors (adapted from [Kalogirou, 2009, IRENA, 2012]).

| Collector | Focus | Tracking | Concentra- tion [-] | T [°C] | Sol. to el. eff. [%] | LEC [¢/kWh _{el}] |
|------------------|-------|-------------|------------------------|-----------|-------------------------|-------------------------------|
| Linear Fresnel | Line | Single-axis | 10-40 | 60-500 | 13 | - |
| Parabolic trough | Line | Single-axis | 10-85 | 60-550 | 11-16 | 14-36 |
| Parabolic dish | Point | Two-axis | 600-2000 | 100-1500 | 12-25 | - |
| Central tower | Point | Two-axis | 300-1500 | 150-2000 | 7-20 | 17-29 |

As central tower plants turn out to feature the highest potential improvement both at the energy level and the economic level, they are selected here for the discussion in this introduction. First a brief state of the art is presented, second the past and existing facilities are identified and located on the world map of solar potentials for CSP, third a description of the largest commercial central tower plants currently in operation is given, and finally the problem statement, the method and the plan of this work are proposed.

1.2 Solar Tower Power Plants

If the solar tower power plants in operation nowadays differ in the way the mirror field and the tower are set up (see discussion in §2.6), they also obviously differ in the way the concentrated heat is converted into electricity. There are mainly four known and experimented conversion cycles to this day, and among them only two that are implemented at an industrial and commercial scale:

- pressurized air cycles, experimental, up to 4.6 [MW_{el}] (e.g. Solugas [Solugas, 2012]);
- atmospheric air cycles, experimental, up to 1.5 [MW_{el}] (e.g. Jülich [DLR, 2008]);
- molten salt cycles, 17 [MW_{el}] in commercial operation (Gemassolar [Torresol, 2011]);
- direct steam cycles, 36 [MW_{el}] (PS10 [Abengoa, 2007], PS20 [Abengoa, 2009], Sierra SunTower [ESolar, 2009]) and 29 [MW_{th}] (Coalinga [BrightSource, 2011]) in commercial operation.

Basically, pressurized air cycles have an air primary loop where the compression (e.g. 6-5 [bar] in SOLGATE) is performed by the turbo-compressor of a gas turbine block as shown in Figure 1.2. Then the pressurized air is heated up to 800-900 [°C] in one or several closed receivers (see review by [Avila-Marín, 2011]) and sent to a combustion chamber where fuel is added before the intake of the turbine that drives both the compressor and the generator. Alternatively, the exhaust gases may be harnessed in a steam generator to run a steam cycle and thus increase

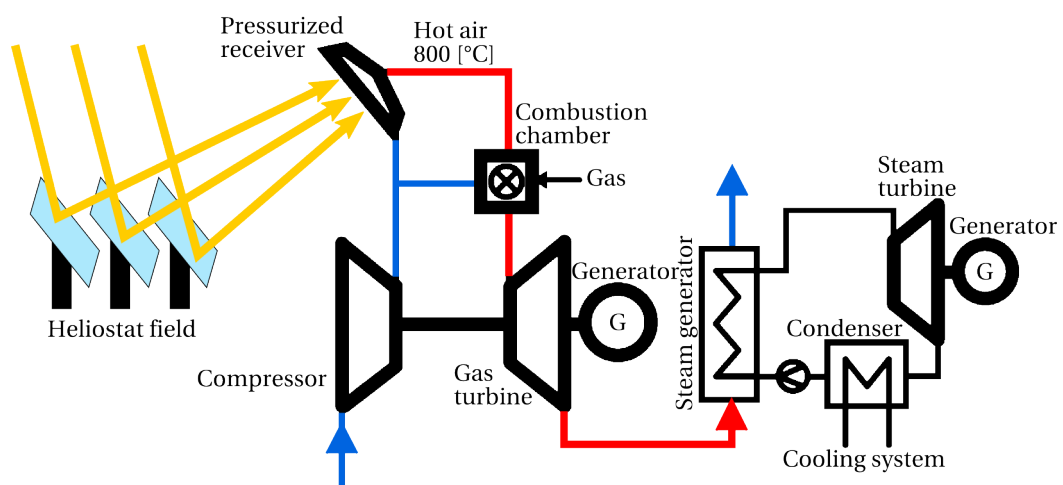


Figure 1.2 – Pressurized air-based plant diagram (SOLGATE, adapted from [Buck et al., 2002]).

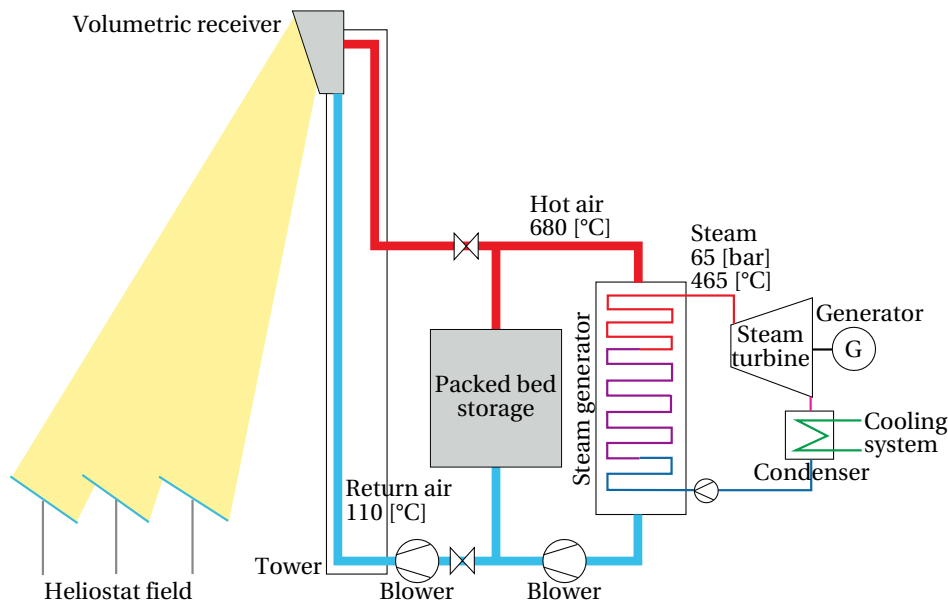


Figure 1.3 – Atmospheric air-based plant diagram (Jülich solar tower, adapted from [DLR, 2008]).

the overall cycle efficiency (combined cycle). Some more advanced pressurized air cycles are proposed and to be experimented now, such as the TopCycle concept with a tower-mounted topping gas turbine in addition to the main ground-based gas turbine [Strand et al., 2012].

Atmospheric air cycles are based on an open loop where the ambient air is drawn through a volumetric receiver made of wire mesh or porous ceramic foam [Hoffschmidt et al., 2003] (see Figure 1.3). There the air is heated up to 680-950 °C, and is directed further either through a packed bed storage unit typically made of rocks [Singh et al., 2010] (during charge), or through a steam generator driving a conventional steam cycle (during discharge). Subsequently the return air is blown back to the receiver inlet, and a share of it is drawn again into the loop (ARR: Air Return Ratio, e.g. 45%). Some innovative atmospheric air cycles have also been proposed, such as a pure solar combined cycle with an air-air heat-exchanger to replace the combustion chamber [Spelling et al., 2011].

Molten salt cycles feature a primary loop where cold molten salt at 290 °C is pumped from a tank up to an external tube receiver atop the central tower, heated up to 565 °C and stored in a second ground-based tank as pictured in Figure 1.4 [Pacheco, 2002, Burgaleta et al., 2011]. The hot salt is then circulated through a steam generator to run a conventional steam cycle, and goes back to the cold storage tank. Given the amount of available molten salt, the storage capacity may reach 15 hours and this way allow 24 hours of operation on a summer day. Even though without up-scaling the potential improvements are limited, some development perspectives are considered, for example new salts with a wider liquid temperature range, from below 100 °C up to 700 °C enabling the generation of supercritical steam [Ren et al., 2012, Raade et al., 2012].

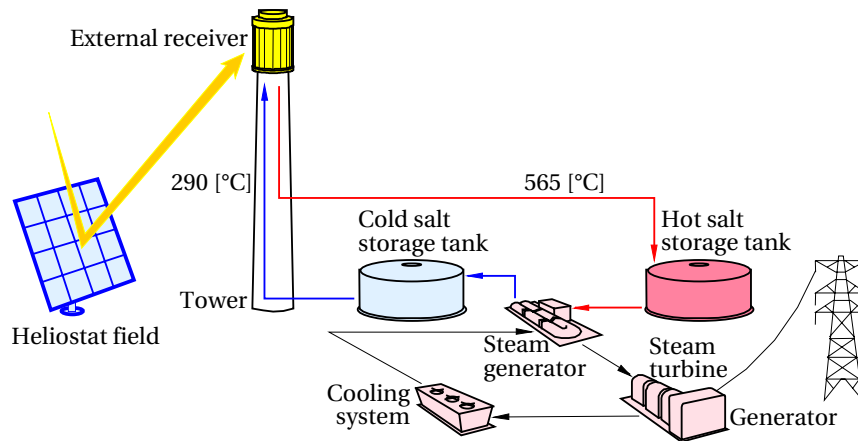


Figure 1.4 – Molten salt-based plant diagram (Solar Two, adapted from [Pacheco, 2002]).

Direct steam cycles use no intermediate loop between the receiver and the steam turbine: the feed water is directly pumped and evaporated in a cavity tube receiver (see Figure 1.5). The generated steam is kept at saturation (e.g. 40 [bar], 250 [°C] [Abengoa, 2007]) and is accumulated back to the ground in a short-time buffer tank (~45 minutes at half the nominal power). It drives then the turbine, is condensed at about 0.06 [bar], 50 [°C] and is pumped up in the tower again. The main development opportunity for direct steam cycles is the generation of superheated steam to allow the use of larger industrial turbines and exceed 40% of cycle nominal efficiency [Garmendia et al., 2012].

As a matter of fact, despite the noticeable progress in research, development and industrialisation over the last decade, the installed capacity of tower plants today in operation is still based on an outdated technology. Looking at the state of the art of steam turbines available on the market, the steam characteristics can achieve temperatures higher than 600 [°C], pressures above 250 [bar], and the output power can go beyond 1'000 [MW_{el}] [Alstom, 2012, Siemens, 2012, GE, 2005]. Furthermore, several steam cycle enhancements like multiple reheat allow to run with overall net efficiencies exceeding 45% in pulverised coal power plants for instance. Then looking at modern combined cycles, the discrepancy with current tower plant cycles is even greater, as the best demonstrated efficiencies reach 60%, with up to 700 [MW_{el}] units. Following these observations, the main challenge for solar tower plant cycles is the significant up-scaling of the unit capacity in order to open the road to state-of-the-art power blocks. A first milestone is the crossing of the 100 [MW_{el}] barrier, which is targeted by some projects in construction such as Ivanpah [BrightSource, 2012] (see Table 1.2).

At the same time, the power block has to play with relatively high condensation temperatures (40-50[°C]), due to the tough on-site conditions occurring in most regions appropriate for CSP. On the one hand, in some places the air temperature clearly exceeds 30 [°C] over long and repeated periods, and on the other hand water is not sufficiently available or simply not allowed for wet cooling (2-3 [m³/MWh_{el}] [IRENA, 2012]). Therefore dry cooling is implemented and decreases the Rankine cycle efficiency because of the higher condensation temperature and

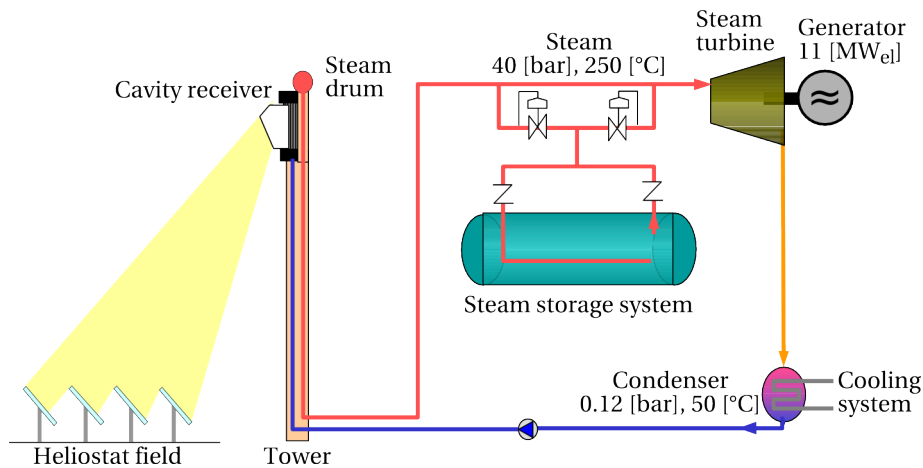


Figure 1.5 – Steam-based plant diagram (PS10, adapted from [Solàcar, 2005]).

the fans consumption. Reminding that the mirrors also need cleaning water if no dry cleaning is available ($\sim 0.25 \text{ [m}^3/\text{MWh}_{el}]$ [idem]), this makes water usage an additional challenge both for the efficiency and the environmental level.

1.3 Heliostat Fields

About 30 heliostat fields have been built worldwide so far (see definition in §2.5, list in Figure 1.7 and Appendix A), and not only for central tower systems. These heliostat fields divide into two main categories: *experimental* facilities and *commercial* facilities.

The construction of experimental heliostat fields goes back to the seventies and the early eighties, and was first linked to solar furnaces such as in Odeillo, France (1970) or at the Uzbek Academy of Sciences (UzAS, 1976), which are designed to reach temperatures above 3'000 [°C]. Second, some heliostat fields were built for research tower facilities featuring a platform to test multiple receiver types: the CRTF in Albuquerque, USA (1978), the SSPS-CRS in Almeria, Spain (1981), the Sunshine project in Nio, Japan (1981), the Thémis tower in Targassonne, France (1982), and the CESA-1 in Almeria, Spain (1983). Later on, the only heliostat field of that kind built in the nineties was at the WIS, Israel (1992), and some new facilities appeared from the mid 2000s, e.g. at the Hohai university, China (2005) and the NSEC, Australia (2005 and 2011). Third, in addition to these research heliostat fields, a couple of pilot plants were commissioned as well: Eurelios in Adrano, Italy (1981), Solar One and Two in Barstow, USA (1982 and 1996), SPP-5 in Ukraine (1986), and more recently the Jülich plant in Germany (2008) and the SEDC in the Negev desert, Israel (2008).

Regarding commercial heliostat fields, the first commercial tower plant started operation in 2007 in Sanlúcar la Mayor, Spain (PS10), after a rather cold period in the nineties and the early 2000s for the CSP sector in general. Following the trend and above all the appearance of financial incentives for solar thermal electricity (see §5.2), several commercial facilities

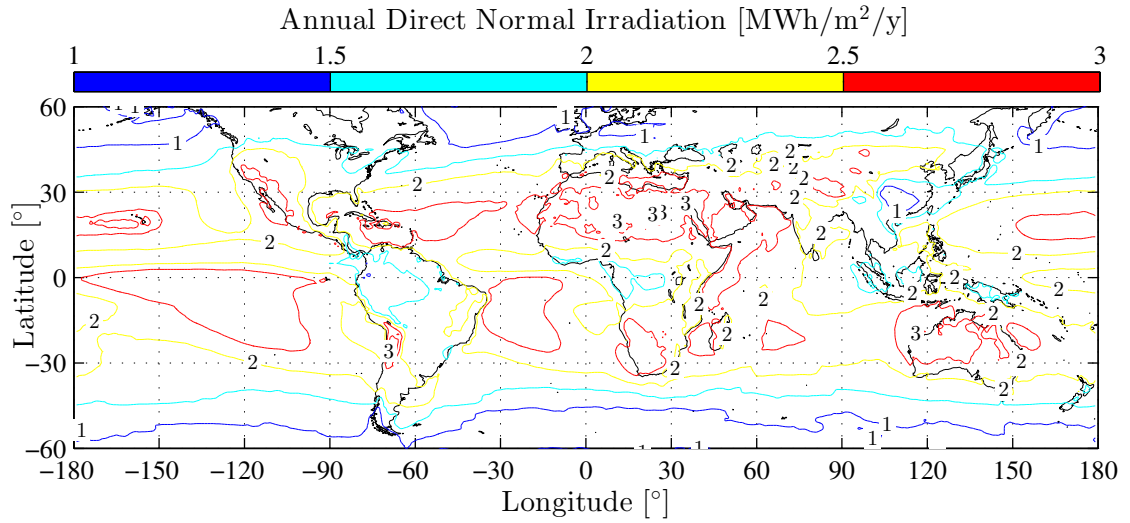


Figure 1.6 – World map of the annual direct normal irradiation, data from [Nasa, 2011], graphic from [Augsburger et al., 2012].

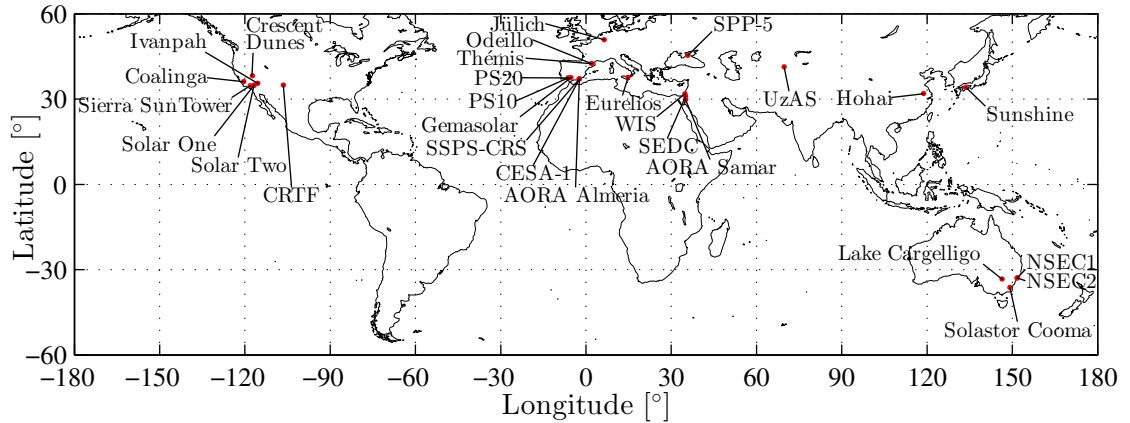







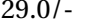



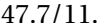
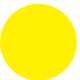


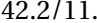








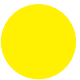





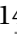



Figure 1.7 – World map of built heliostat fields to this day [Augsburger et al., 2012].

have been commissioned since and can be divided into three groups according to their total reflective area: small-scale ($<10'000 \text{ [m}^2\text{]}$), medium-scale ($10'000\text{-}100'000 \text{ [m}^2\text{]}$), and large-scale facilities ($>100'000 \text{ [m}^2\text{]}$). Small-scale facilities such as the AORA field in Samar, Israel (2009) or the Solastor field in Lake Cargelligo, Australia (2011) are designed to provide electricity and/or heat to relatively small communities. Medium-scale facilities such as the Sierra SunTower in Lancaster, USA (2009) and the enhanced oil recovery (EOR) plant in Coalinga, USA (2011) demonstrate the feasibility of modular solutions for local industrial needs (steam, heat in general, power generation below $10 \text{ [MW}_{\text{el}}]$). Large-scale facilities such as PS20 and Gemasolar in Spain (2009 and 2011), and Ivanpah in California (2013) are paving the way towards heliostat fields with more than $1'000'000 \text{ [m}^2\text{]}$ of total reflective area. This great area raises the question of how large is too large, and when do heliostat fields layout for multi-tower set-ups become more interesting than layouts for single-tower set-ups.

Chapter 1. Introduction

Table 1.2 – List of medium and large commercial solar tower thermal power plants built to this day (2012) with Solar Two as historical reference, see Tables A.1-A.10.

| <i>Description</i> | <i>Annual DNI</i> [kWh/m ² /y] | <i>Refl. area</i> [m ²] | <i>Tower height</i> [m] | <i>Rec. / Gen. pow.</i> [MW _{th}] / [MW _{el}] |
|--------------------|----------------------------------------------------------------------------------------------|--------------------------------------------------------------------------------------------------|--------------------------------------------------------------------------------------------|------------------------------------------------------------------------------------------------------|
| Sierra SunTower | 2'646  | 27'264  | 55  | -/5.0  |
| Coalinga | 2'281  | 59'653  | 100  | 29.0/-  |
| PS10 | 2'162  | 74'880  | 115  | 47.7/11.0  |
| Solar Two | 2'829  | 81'400  | 76  | 42.2/11.1  |
| PS20 | 2'162  | 150'600  | 165  | -/20.0  |
| Gemasolar | 2'097  | 318'000  | 140  | 120.0/17.0  |
| Crescent Dunes | 2'685  | 1'081'250  | 200  | 565.0/110.0  |
| Ivanpah | 2'646  | 1'408'000  | 140  | -/126.0  |

Looking now at the world map of heliostat fields built to this day (Fig. 1.7), most of them are located in developed countries and thus in only some of the regions with a high potential of direct solar radiation (>2500 [kWh/m²/y], Fig. 1.6). Southern Spain, western USA, the Middle-East and eastern Australia are well known and feature existing facilities, whereas northern and southern Africa, Chile, northern Brazil, western Australia and Mongolia have been unexploited so far. Obviously the high solar potential is not the only criterion: many areas are excluded from

a technical and economic point of view (topology, hydrography, land cover, power network available, etc.), but also tacitly from a social and political point of view [DLR, 2005].

1.4 Objectives & Methodology

The problem statement here is the following: what are the set-ups of a large solar tower thermal power plant that satisfy both energy and economic objectives, at a given location, with a given conversion cycle, and under given material safety constraints.

Thus the **objectives** of this thesis are:

- to develop a **method for the thermo-economic design of large solar tower plants**;
- to propose **optimal and innovative configurations**.

The methodology used is the thermo-economic modelling, simulation and optimisation of an energy system under constraints.

First, the environmental conditions at the given location and the plant set-up characteristics are identified. On the one hand, the environmental conditions include the solar radiation, the sun's position, the ambient temperature and the wind, and are taken as model inputs for annual simulations. On the other hand, the plant set-up is described by the design parameters of the heliostat mirrors, the field layout (where a special emphasis is put on), the tower and its receiver, as well as the power conversion unit with some simplifications.

Second, the energy performance of the solar tower plant is calculated through a simulation of the successive energy conversions from solar energy to electricity. The heliostat field losses are detailed, the receiver efficiency is estimated by experimental correlations, a strategy of operation is proposed for the power conversion unit, and the behaviour of the whole system is simulated over specific days and interpolated throughout the year.

Third, the heat flux distribution on the central receiver is calculated in order to be implemented later on as a safety constraint in the optimisation. In particular, the passage of clouds over the field is simulated and a strategy is proposed to avoid receiver failures. Another strategy is also presented to decrease the peak heat flux through multi-aiming of the heliostat mirrors onto the receiver.

Fourthly, the assessment of the plant economic performance is performed through a detailed cost analysis of the equipment, and the financial performance is estimated thanks to tools such as the levelised electricity cost or the project net present value.

Fifthly, the thermo-economic optimisation of the plant set-up is presented: a sensitivity of some key parameters is carried out to identify potential improvements of a base case (Gemasolar), and an evolutionary algorithm is used to find the set of set-ups that achieve the best trade-off between efficiency and cost.

Chapter 1. Introduction

Sixthly, a way of creating multi-tower layouts is proposed, as well as a selection criterion of the receiver that each single heliostat is aiming at instantaneously. A thermo-economic optimisation is also performed on large multi-tower set-ups to investigate the optimum transition size from single- to multi-tower plants.

Finally, the opportunity of coupling heliostat fields with parabolic trough collectors is studied, since trough collectors may provide heat to the low temperature level of the conversion cycle (e.g. better match the evaporation), and also drive the plant specific costs down.

2 Environment and Plant Set-Up

In this chapter, the relevant environmental characteristics for the assessment of a solar tower power plant are identified, then the plant set-up elements and parameters are presented. The environmental characteristics include the solar radiation, the sun's position, the ambient temperature, and the wind. The plant set-up elements divide into the heliostats, the field layout, the tower, the receiver and the power conversion unit. The emphasis is put on the first four elements, which constitute the solar collector field.

2.1 Direct Normal Irradiance

As the solar radiation reaches the earth's atmosphere, its intensity is given by the *solar constant*, G_{sc} . The solar constant is an amount of *irradiance*, which is the rate of incident radiant energy, in $[\text{W}/\text{m}^2]$. The value of the solar constant has been measured by different satellites over the last decades, reporting a 0.37% minimum-to-maximum range between 1363 and 1368 $[\text{W}/\text{m}^2]$ [ASTM, 2006]. The current standard solar constant is thus set at 1366.1 $[\text{W}/\text{m}^2]$. This amount of irradiance splits then into three parts,

- one part *reflected* by the atmosphere,
- another part *absorbed* by the atmosphere,
- and a last part *transmitted* down to the ground.

The exact instantaneous breakdown between reflection, absorption and transmission depends on the atmosphere composition, the meteorological conditions, and the beam angle of the incident radiation. For example, for moderate cloudy conditions, reflection and absorption each may exceed 20% of the solar constant, which limits the ground *global irradiance* G to 60% of the solar constant [Kiehl and Trenberth, 1997], typically 800 $[\text{W}/\text{m}^2]$.

The global irradiance observed from the ground breaks down into three main components:

- the *direct* or *beam* irradiance G_B ,
- the *diffuse* irradiance G_D ,
- and the *reflected* irradiance G_R .

The direct irradiance comes directly through the atmosphere and is observed at the sun's position in the sky. The diffuse irradiance results from scattered rays in the atmosphere and comes from the entire sky hemisphere. The reflected irradiance is the consequence of a more or less reflecting environment (sand, water, snow, buildings, etc.) and is generally described by a portion of the direct and diffuse components together: $G_R = \rho_G(G_B + G_D)$, where ρ_G is the ground albedo factor. Given the atmospheric conditions, the sky cover and the beam incident angle, the portion of diffuse radiation may vary between a few percent for clear-sky days and up to 100% for cloudy days. In practice, all components can be observed either

- from a *horizontal* plane (G_{Bh}, G_{Dh}, G_{Rh}),
- a *tilted* plane (G_{Bt}, G_{Dt}, G_{Rt}),
- or a plane *normal* to the beam radiation (G_{Bn}, G_{Dn}, G_{Rn}).

Since concentrating solar systems only harness the direct normal component G_{Bn} , the diffuse and reflected radiation components are left aside here.

The direct normal component G_{Bn} is also called the *Direct Normal Irradiance* (DNI). There are three ways to assess the DNI over time for a given location:

- measure directly from the ground thanks to a radiometer;
- derive estimates from satellite data;
- combine both ground and satellite data.

Direct ground measurements are available from various local meteorological facilities [Météo-suisse, 2012], but they are often given as a cumulated irradiation in [Wh/m^2] (or [J/m^2]) over daily, monthly, or yearly periods. They spread unevenly over the earth and are mostly located in populated areas [WMO, 2012], while the most appropriate sites for large CSP plants correspond to desert areas [Czisch and Trieb, 2002]. Therefore as a first assessment, combined ground and satellite data are used to estimate the DNI potential of a given location. Several databases provide this information by applying different calculation methods [Šúri et al., 2009]. They also differ on the geographical extent, the spatial resolution, the satellite used, the time period considered, and the time resolution. For example, the Satel-Light database [Satel-Light, 2005] features a 5.3 [km] grid size and a 30 minute time resolution from 1996 to 2000, whereas the PVGIS database [PVGIS, 2007] features a 1 [km] grid size and monthly averages with simulated daily profiles from 1981 to 1990. The comparison of five different databases shows that the DNI uncertainty expressed by the relative standard deviation may reach 17% [Šúri et al., 2009]. Consequently, once a site is selected, a second assessment must take place to avoid overestimates by making accurate ground measurements with a radiometer.

In the scope of this work, a freely available database with at least hourly data is selected [SoDa, 2004], in this case the year 2005. In practice, the representative database of annual weather data is known as the *test reference year* (TRY) or *typical meteorological year* (TMY). It consists of months that are statistically selected from individual years over a long period (e.g. 20 years), and concatenated to obtain an entire year whose average is consistent with the long-term averages for the given location. This way, the TMY does not smooth the DNI profile and preserves real hourly DNI variations as in a real-life year (see TMY comparison in Annex B), which allows the simulation of unstable DNI conditions to design a storage system.

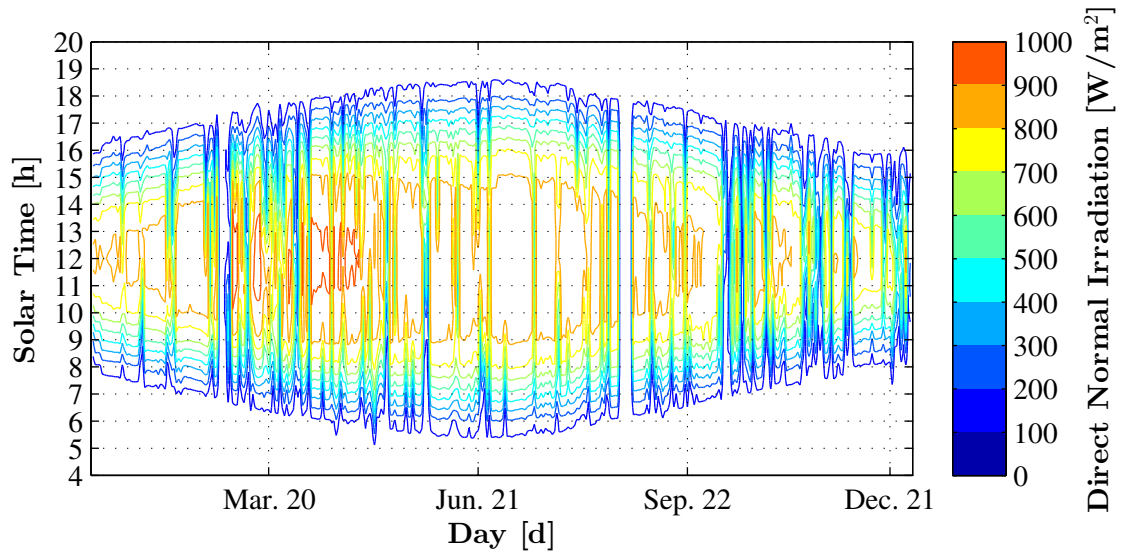


Figure 2.1 – Time map of the Direct Normal Irradiation in Fuentes de Andalucía, Spain, 2005, data from [SoDa, 2004], graphic from [Augsburger et al., 2012].

The hourly DNI over an entire year may be depicted by two types of graphical representation: a *time map* and a *sun path*. The time map features the 365 days (or 366) along the horizontal axis, the solar time along the vertical axis, and the DNI intensity according to the color axis (alternatively the height axis). The sun path representation features the sun's *azimuth* angle along the horizontal axis, the sun's *elevation* angle along the vertical axis, and the DNI intensity according to the color axis as well, but depicted as solar discs. -90° , 0° , and 90° azimuth angles are the East, South and North respectively. 0° and 90° are the horizon and the zenith. On the one hand, the time map shows how the day duration evolves over the year, and allows to identify seasons, stable or unstable DNI periods, and DNI peaks. On the other hand, the sun path representation allows to identify the connections between the DNI intensity and the sun's position.

For example, the estimated DNI time map at the *Gemasolar* tower power plant in South Spain [Burgaleta et al., 2011] is represented in Figure 2.1. The winter is located on the left- and right-hand sides of the graph, and the summer in the middle. The day duration evolves from 8 daylight hours in the winter up to 13 daylight hours in the summer. DNI instabilities turn out to be higher during the spring and the fall, while some large periods of stable and high DNI appear in the summer with about 6 hours above $800 \text{ [W/m}^2\text{]}$. A DNI peak of $931.5 \text{ [W/m}^2\text{]}$ is reached at 12 on the 4th of March.

In Figure 2.2 the DNI at Gemasolar is represented along the sun's path. The winter and summer solstices are depicted by the bottom and top lines respectively. The spring and fall equinoxes are merged along the same line in the middle. The fact that the maximal DNI intensities do not occur at the highest sun elevation is remarkable. They happen between the summer equinox line and the solstice line, at about 60° elevation angle. Besides, the value of $800 \text{ [W/m}^2\text{]}$

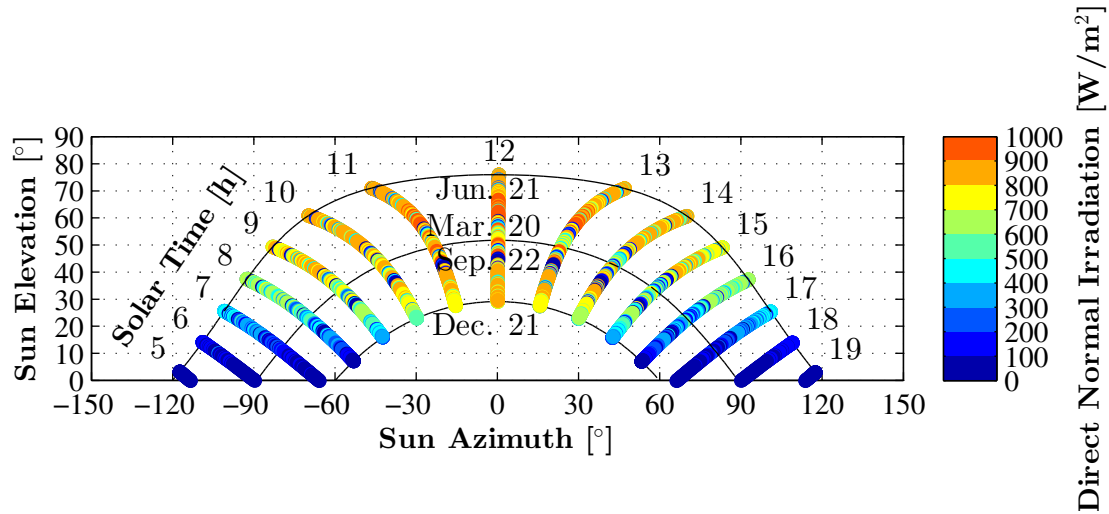


Figure 2.2 – Sun path vs. the Direct Normal Irradiation in Fuentes de Andalucía, Spain 2005, data from [SoDa, 2004], graphic from [Augsburger et al., 2012].

turns out to be exceeded only above a 30° elevation angle. Thus for this site, a qualitatively appropriate window appears between 30° and 80° elevation angle, and -90° and 90° azimuth angle.

The integration of the DNI over the entire year for a given location provides an aggregated value of the solar potential for a concentrating solar system in $[\text{kWh}/\text{m}^2/\text{y}]$. By plotting this value for different locations over the earth, a world map of the annual DNI potential can be obtained, as it is done by many of the databases cited here above. In the case of Gemasolar, the sum of the annual DNI represented in Figure 2.1 reaches $2085 [\text{kWh}/\text{m}^2/\text{y}]$, which is a typical value for South Spain. Some locations like the South African or the Atacama deserts may exceed a DNI potential of $2500 [\text{kWh}/\text{m}^2/\text{y}]$ [Meteonorm, 2012], while the North African area near the coast reaches $2200 [\text{kWh}/\text{m}^2/\text{y}]$.

2.2 Sun's Position

High concentration solar systems - trough, Fresnel, dish and heliostat field collectors - all feature a sun tracking system, *one-axis* for the trough and Fresnel collectors, and *two-axis* for the dish and heliostat field collectors. The tracking system may be *closed-loop* or *open-loop* (active or passive respectively). A closed-loop tracking system uses photo-sensors to detect the sun's position and accordingly assign the collector's position [Bolle et al., 1985]. An open-loop system computes the sun's position given the year, the day and the time thanks to an algorithm [Grena, 2008]. In practice a closed-loop system must be able to overcome cloudy periods, which either is done iteratively with the photo-sensors, or despite everything by combining an algorithm. On the opposite, in an open-loop system the sun's position may be computed in advance for several years or even decades [Grena, 2012] depending on the

numerical storage capacity of the tracking system.

Solar position algorithms have three main characteristics:

- the computational speed and complexity,
- the precision,
- and the range of validity over periods of time.

In the literature many algorithms are available, either for fast calculation in solar engineering applications, or for high-precision astronomical applications. The precision of fast algorithms ranges from 0.01° to 0.25° , and work correctly for limited periods of times, e.g. 1950-2050 or 1995-2015 [Grena, 2008]. The high-precision algorithms may reach a precision below 0.0003° over long periods of time (2000 b.C.-6000 a.C.), but require a large amount of calculation.

For the purpose of modelling and simulating the behaviour of concentrating solar systems over one year, a relatively small series of solar positions has to be computed (from 2000 to 2500 daylight hours if considered on a hourly basis). Besides, a precision level below 0.25° is widely sufficient in modelling. Experiments obviously require more accuracy, down to 0.01° . Therefore the conventional approach to calculate the sun's position is preferred here [ASHRAE, 2011]. The solar elevation angle el and azimuth angle az are expressed by

$$\sin(el) = \sin(l) \sin(\delta) + \cos(l) \cos(\delta) \cos(h) \quad (2.1)$$

$$\sin(az) = \frac{\cos(\delta) \sin(h)}{\cos(el)} \quad (2.2)$$

where l is the site latitude, δ is the solar declination and h the hour angle as follows:

$$\delta = 23.45 \sin \left[\frac{360}{365} (284 + N) \right] \quad (2.3)$$

$$h = (ST - 12)15 \quad (2.4)$$

ST is the solar time and N the day number. If the sun is behind the W-E line ($\cos(h) < \tan(\delta) / \tan(l)$), the azimuth angle is $-180^\circ + |az|$ in the morning and $180^\circ - az$ in the afternoon. The solar angles provide the direction of the sun's incident rays as a normal vector:

$$\vec{n}_{Sun} = \begin{bmatrix} \sin(az) \cos(el) \\ \cos(az) \cos(el) \\ -\sin(el) \end{bmatrix} \quad (2.5)$$

where the x-axis matches the W-E line with East positive, the y-axis matches the S-N line with North positive, and the z-axis matches the zenith line. The solar normal vector is used later on to calculate the angle of incidence on the mirrors and accordingly their orientation.

2.3 Ambient Temperature

The local ambient temperature has a significant influence on the first-law efficiency of a concentrating solar system. First, it affects the receiver first-law efficiency mainly because of the air convection losses that occur either by the wind (forced convection) or by gravity (free convection). The air convection losses may reach 25% of the total receiver thermal losses which comprise the reflection losses, the radiation losses, the convection losses and the conduction losses [Winter, 1991]. Second, the thermal storage losses are also influenced by the ambient temperature, even though nowadays the storage tanks are extremely well insulated and exceed a first-law efficiency of 99% [Pacheco, 2002]. Third, the temperature affects the first-law efficiency of the cycle that converts the thermal power from the receiver (or the storage) into mechanical power: the cycle exploits the temperature difference between the hot source from the receiver (storage) and the cold source from the environment. If no liquid water is available, which is the case in most desert areas, the cold source is at the atmospheric temperature. The higher the local ambient temperature, the worse the cycle first-law efficiency.

The same way as for DNI, several temperature databases are available [Meteonorm, 2012, Nasa, 2011, SoDa, 2004]. For the sake of convenience and consistency, the same database as that for DNI is used here. In Figure 2.3, the local ambient temperature on the Gemasolar site over the entire year 1990 is represented on a time map. Unlike the DNI time map, a shift towards 14:00 of the daily maximum temperature is observed. Besides, a period of about five months between May and September records maximum temperatures above 25 [°C] and minimum temperatures above 15 [°C]. The annual temperature maximum reaches 40.2 [°C] and occurs on the 20th of July, while the minimum goes down to -2.2 [°C] on the 1st of December.

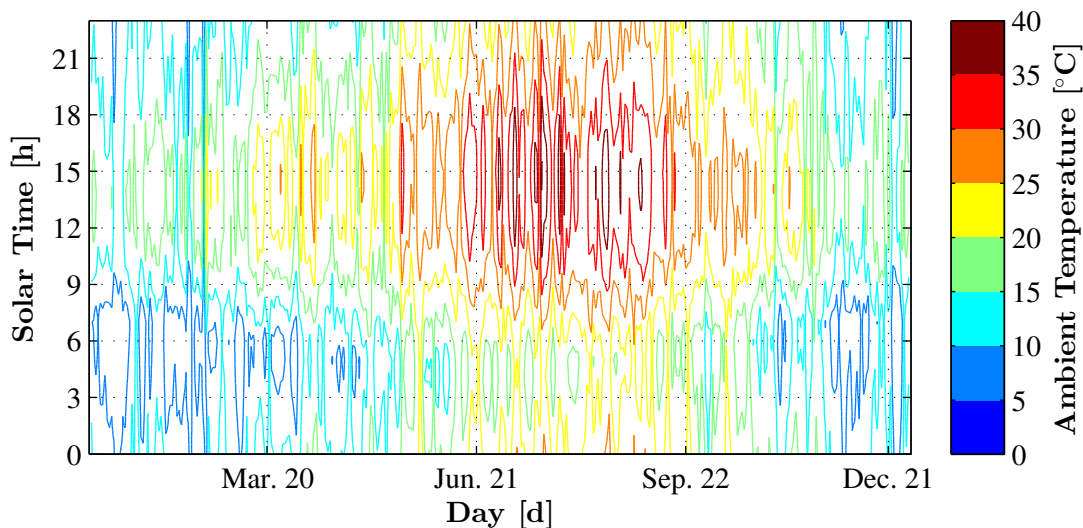


Figure 2.3 – Time map of the ambient temperature in Fuentes de Andalucía, Spain, 1990, data from [SoDa, 2004], graphic from [Augsburger et al., 2012].

2.4 Wind

The wind plays a role mainly in three aspects of a concentrating solar system: the mirrors tracking, the receiver first-law efficiency, and the receiver transient behaviour. The mirrors tracking accuracy is affected when the wind causes structure bending and oscillations [Peterka et al., 1987]. Furthermore, the mirror drive mechanism is able to work only until a given wind velocity, such as 36 [km/h] (10 [m/s]) for the heliostats used at the PS10 plant near Sevilla [Abengoa, 2011]. The manufacturers also specify a critical wind velocity that might lead to destruction, such as 140 [km/h] (39 [m/s]) in the same example. Then the receiver first-law efficiency is also affected, when the wind increases the heat transfer coefficient through convection to the atmosphere. For example the first-law efficiency of a central cylindrical receiver may drop by 10% with a wind velocity increase from 0 [km/h] to 30 [km/h] (8.3 [m/s]) [Pacheco, 2002]. The third aspect, the receiver transient behaviour, is indirectly affected by the wind: the velocity and the direction of the clouds passing over the mirror field influence the heat flux on the central receiver. Fast changes may cause thermal fatigue or even a failure of the receiver [Sobin et al., 1976]. The wind thus indirectly affects the receiver cyclic operation and therefore its life time.

Wind data contain two indications: the wind velocity and its direction. They are usually available at local airports [Aviador, 2011] and weather stations. However, not all databases cited previously feature this information: some provide a monthly mean [Meteonorm, 2012], others a series of 3-hourly intervals [Nasa, 2011], but still averaged monthly. Figure 2.4 shows the time map of the wind velocity monthly average of these 3-hourly intervals, at the location of Gemasolar. The wind tends to become stronger in the afternoon, reaches its maximum

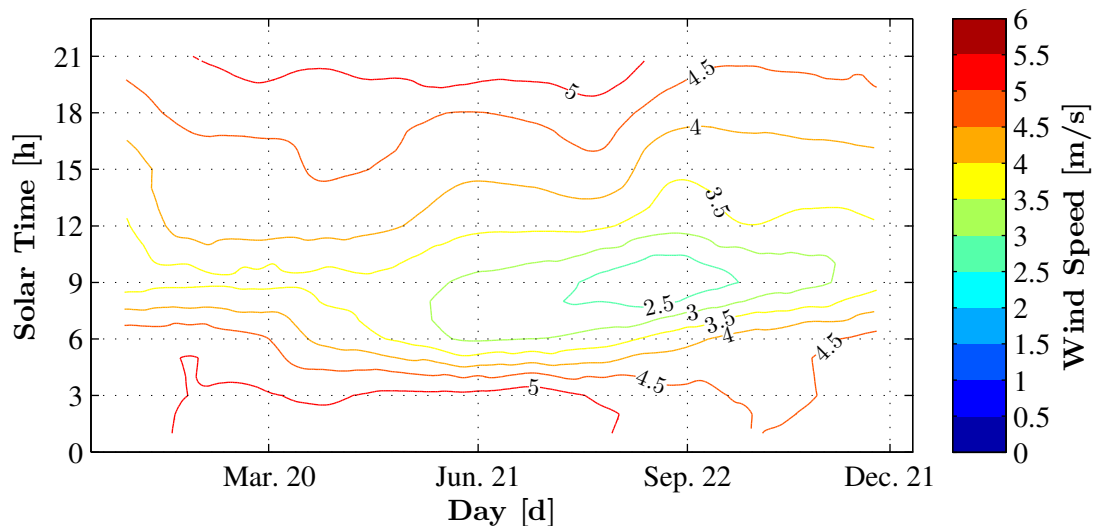


Figure 2.4 – Time map of the wind velocity monthly average of 3-hourly intervals in Fuentes de Andalucía, Spain, data from [Nasa, 2011], graphic from [Augsburger et al., 2012].

overnight, and gets weaker in the morning. Moreover, a seasonal trend appears, where the wind decreases at the end of the summer.

Nevertheless this representation does not provide maximal winds, which have to be taken from other indications in the same database. The indication of wind speed frequency is used to know how often strong and extreme winds occur. In the same example, winds ranging from 7 [m/s] to 10 [m/s] may occur with a 14% frequency, whereas winds between 11 [m/s] and 14 [m/s] may occur with a 1% frequency.

2.5 Heliostats

A heliostat is a mirror that tracks the sun in order to constantly reflect the rays of sunlight onto a fixed target. In the case of a solar tower power plant, a field of heliostats concentrates the sunlight onto a central receiver atop a tower. This application requires a high mirror reflectivity, accuracy of the tracking system, resistance to wind, and low specific costs. Current heliostats are either a single mirror facet or an assembly of several facets, mounted on a frame supported by an horizontal axis and a vertical axis [Mancini, 2000]. The mirror facets are plane rectangular mirror with a slight convex curvature. Alternative concepts have also been proposed, such as stretched membranes over steel rings, but were abandoned because of damaged membranes after a few years only [Kolb et al., 2007].

A heliostat is an *off-axis* sun tracker, which means that the target is fixed and the heliostat's normal vector must always bisect the angle between the sun's vector and the target's vector. As a consequence of the off-axis tracking, the size and the shape of the sun's image on the receiver strongly depends on the angle of incidence on the heliostat. Hence, there are two categories of heliostats: with either a fixed or a time-dependent *canting* of the mirror facets. The canting is the individual orientation of the mirror facets in order to minimize the size of the reflected sun's image and thus increase the concentration ratio of the heliostat. A fixed canting consists in the individual orientation of the mirror facets when assembling the heliostat, according to a spherical or a parabolic shape whose focus length is the distance to the target. A time-dependent canting needs individual controllers for the mirror facets to continuously change the geometry of the heliostat. For incident angles above 25° , the time-dependent canting has proven ability to divide the reflected area by three compared to a spherical shape [Chen et al., 2006]. Nevertheless fixed canting is preferred for the moment in commercial solutions, obviously more simple and less costly.

Here a list of parameters is defined to characterise the properties of a heliostat. This list divides into two categories: geometrical properties and optical properties. The geometrical properties regard the heliostat's dimensions, considering a rectangular shape: the *width* W_{Hel} and the *height* H_{Hel} of the assembly, the ratio C_{Ref} of the *reflective area* to the total area, and the base H_{Ped} of the heliostat's *pedestal*. The optical properties are given by the mirrors' *reflectivity* and cleanliness, the *slope error* of the overall shape, and the *tracking error*. The reflectivity ρ_{Mirr} is the mirrors' reflectivity when they are clean, while the cleanliness ε_{Clean}

Table 2.1 – Assumed properties of the heliostats used at the Gemasolar plant [Burgaleta et al., 2011, Osuna et al., 2007, Collado, 2008, Sargent & Lundy, 2003].

| <i>Property</i> | <i>Value</i> | <i>Unit</i> |
|-----------------------------|--------------|-------------|
| <i>Geometry</i> | | |
| Width | 10.9589 | [m] |
| Height | 10.95 | [m] |
| Ratio of reflective surface | 0.9583 | [-] |
| Pedestal | 5.675 | [m] |
| <i>Optics</i> | | |
| Reflectivity | 0.95 | [-] |
| Cleanliness | 0.95 | [-] |
| Slope error | 2.6 | [mrad] |
| Tracking error | 2.1 | [mrad] |
| <i>Operation</i> | | |
| Availability | 0.99 | [-] |

is the share of reflected sunlight that is not absorbed or scattered by dirt deposits on the mirror's surface. The heliostat's slope error includes the errors of facet curvature, mirror waviness, facet alignment (canting) and gravity effects. It is defined as the standard deviation σ_{Slope} of a gaussian distribution, in rad around the axis of reflection. The tracking error includes computational errors such as the sun position calculation and encoder bias, as well as hardware errors such as the elevation to azimuth axis non-orthogonality and the azimuth axis tilt of the drives. It is also defined by a standard deviation σ_{Track} in rad.

Table 2.1 shows the values of the heliostat parameters in the case of the Gemasolar plant. In addition to the properties listed previously, the availability ϵ_{Avail} is defined as the probability that the heliostat is working.

2.6 Field Layout

North vs. Surrounding

In a solar tower power plant, the heliostats are arranged according to a given field layout. First, the various field layouts divide into two categories: the *north* fields (or south in the Southern hemisphere) and the *surrounding* fields. The north fields have heliostats on one side of the tower only, whereas the surrounding fields feature heliostats all around the tower. The choice between a north field and a surrounding field mainly depends on the site latitude, as well as on the central receiver acceptance angle.

Most research facilities are north fields, such as the heliostat fields at the PSA, Spain, at the

CRTF-SNL, Albuquerque, USA, at the Weizmann Institute, Israel, or even at the NSEC-CSIRO, Australia (south field). Some commercial facilities are also north fields, such as the PS10 and PS20 in Spain, or the LPT in Israel. On the other hand, a couple of facilities are surrounding fields, like Solar Two and the Sierra SunTower in California, or Gemasolar in Spain.

Grid vs. Circular

Second, the field layouts divide into two additional groups: *grid* or *circular* layouts. The grid layouts feature heliostats according to a simple grid of W-E and S-N rows, whereas circular layouts have heliostats along concentric circles whose center is the tower's base. Both for grid and circular layouts, the spacing between rows may increase with the distance to the tower's base to avoid large disturbances between neighbouring heliostats. Moreover, especially for circular layouts, the rings of heliostats are staggered radially to allow enough distance between the heliostats that are on the same radial row.

For example, the CESA-1 at PSA, the CRTF at SNL in Albuquerque, and the commercial Sierra SunTower in California are all grid layouts, while the field of the Weizmann Institute, the Thémis field in France or the PS10/PS20 are circular layouts.

The field layout might also be elliptic as proposed by [Pelet et al., 2006], however the circular layout is chosen as the standard set-up in this study.

2.6.1 Algorithm for Staggered Circular Layouts

The generation of radially staggered circular layouts requires the use of a specific algorithm. The main task of this algorithm is to arrange the heliostats along rings according to a given *azimuthal spacing*, and determine the *radial spacing* between concentric rings (see Figure 2.5). The rings that have a heliostat on the S-N axis are called *essential rings* and the others *staggered rings*.

For radially staggered circular layouts, several algorithms have been implemented in various codes since the late seventies [Garcia et al., 2008]. Here the algorithm presented in the mathematical formulation proposed by [Siala and Elayeb, 2001] is used and adapted.

Heliostat characteristic diameter & first row

First of all, the *characteristic diameter* D_{Hel} of a heliostat is calculated as the rectangle's diagonal

$$D_{Hel} = \sqrt{W_{Hel}^2 + H_{Hel}^2} + C_{Sep} H_{Hel}, \quad C_{Sep} > 0 \quad (2.6)$$

where C_{Sep} is the coefficient of safety distance of separation between two neighbouring heliostats, related to the heliostat's height.

Secondly, the radius of the very first row of heliostats is expressed as a function of the aim height H_{Aim} :

$$R_0 = C_{Row1} H_{Aim}, \quad C_{Row1} > 0 \quad (2.7)$$

where C_{Row1} is specified as the ratio of the first radius to the aim height.

No-touching & no-blocking conditions

Then both for the azimuthal and the radial spacing, two conditions are defined: the *no-touching* and the *no-blocking* condition. The no-touching condition is the minimal spacing required to avoid collisions between heliostats, whereas the no-blocking condition is the minimal spacing required to avoid blocking of reflected rays from further rows. The no-touching condition is considered as the lower condition of spacing, and the no-blocking as the higher condition. Thus two spacing coefficients are applied to the interval between these two boundary conditions: the azimuthal spacing coefficient C_{AzSpac} and the radial spacing coefficient $C_{RadSpac}$.

Azimuthal spacing

In the definition of the azimuthal spacing, the no-touching condition is expressed as the characteristic diameter being equal to its primary definition 2.6, and the no-blocking is expressed

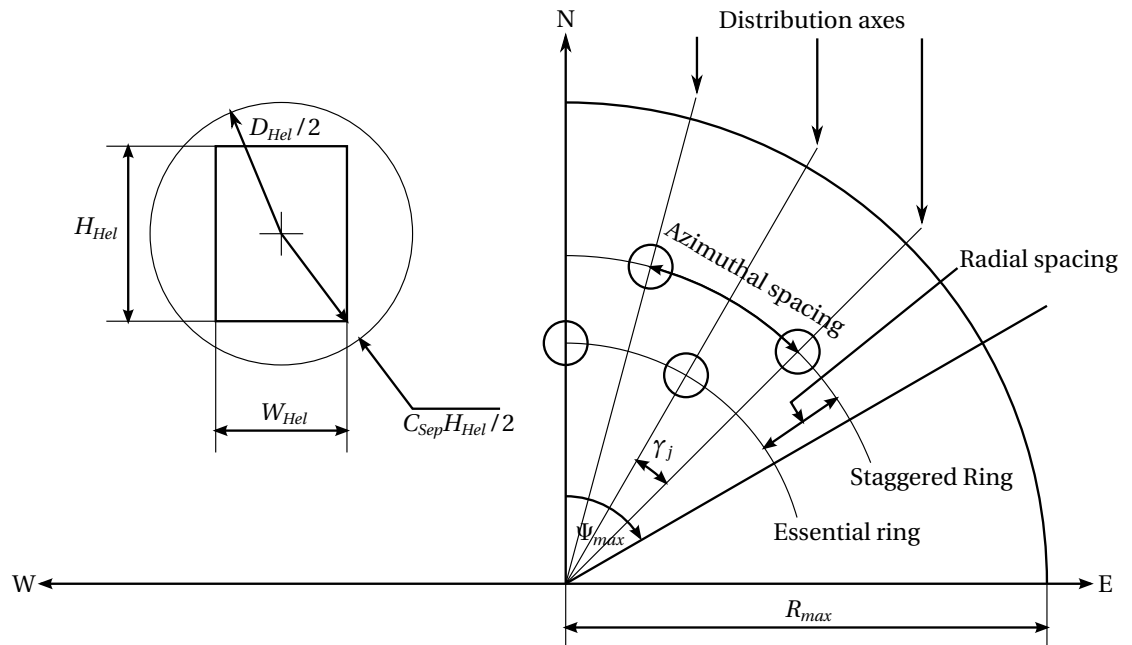


Figure 2.5 – Definition of a radially staggered circular layout, adapted from [Siala and Elayeb, 2001].

as the maximum between it and twice the heliostat width (see Figure 2.6):

$$D_{Hel,noTouch} = \sqrt{W_{Hel}^2 + H_{Hel}^2} + C_{Sep}H_{Hel} \quad (2.8)$$

$$D_{Hel,noBlock} = \max\left(\sqrt{W_{Hel}^2 + H_{Hel}^2} + C_{Sep}H_{Hel}, 2W_{Hel}\right) \quad (2.9)$$

Hence the azimuthal spacing coefficient C_{AzSpac} applies to the characteristic diameter in the following way:

$$D_{Hel} = D_{Hel,noTouch} + C_{AzSpac}(D_{Hel,noBlock} - D_{Hel,noTouch}), \quad C_{AzSpac} \in [0, 1] \quad (2.10)$$

The azimuthal angle γ between distribution axes is computed as the inverse tangent of the half characteristic diameter divided by the first row radius:

$$\gamma = \arctan\left(\frac{D_{Hel}/2}{R_0}\right) \quad (2.11)$$

Radial spacing

In the definition of the radial spacing, the no-touching condition is expressed as the next radius R_{i+1} being equal to the current radius R_i plus a minimum increment (see Figure 2.7):

$$R_{i+1} = R_i \cos \gamma + \sqrt{(D_{Hel} \cos \beta)^2 - (R_i \sin \gamma)^2} \quad (2.12)$$

$$R_{i+1,noTouch} = R_{i+1} + D_{Hel} \cos 30^\circ \cos \beta, \quad \beta \in [0^\circ, 90^\circ[\quad (2.13)$$

where β is the terrain slope rising away from the tower base. The calculation of the no-blocking condition $R_{i+1,noBlock}$ is more complex and is referred to the article cited previously.

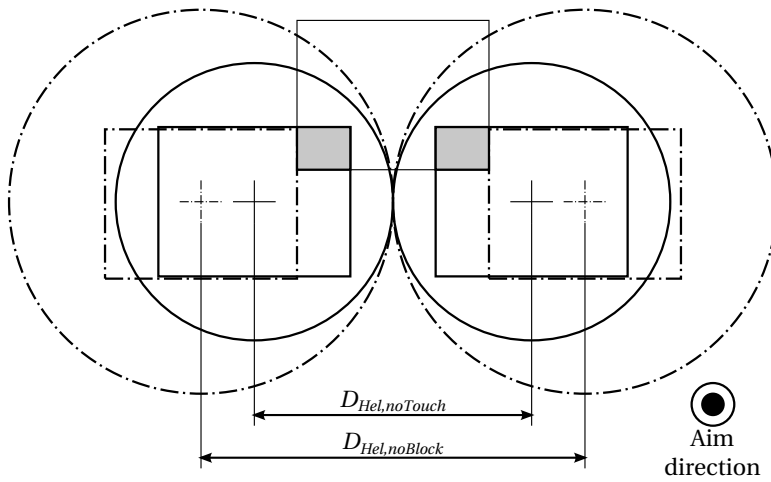


Figure 2.6 – The no-touching and no-blocking conditions for azimuthal spacing.

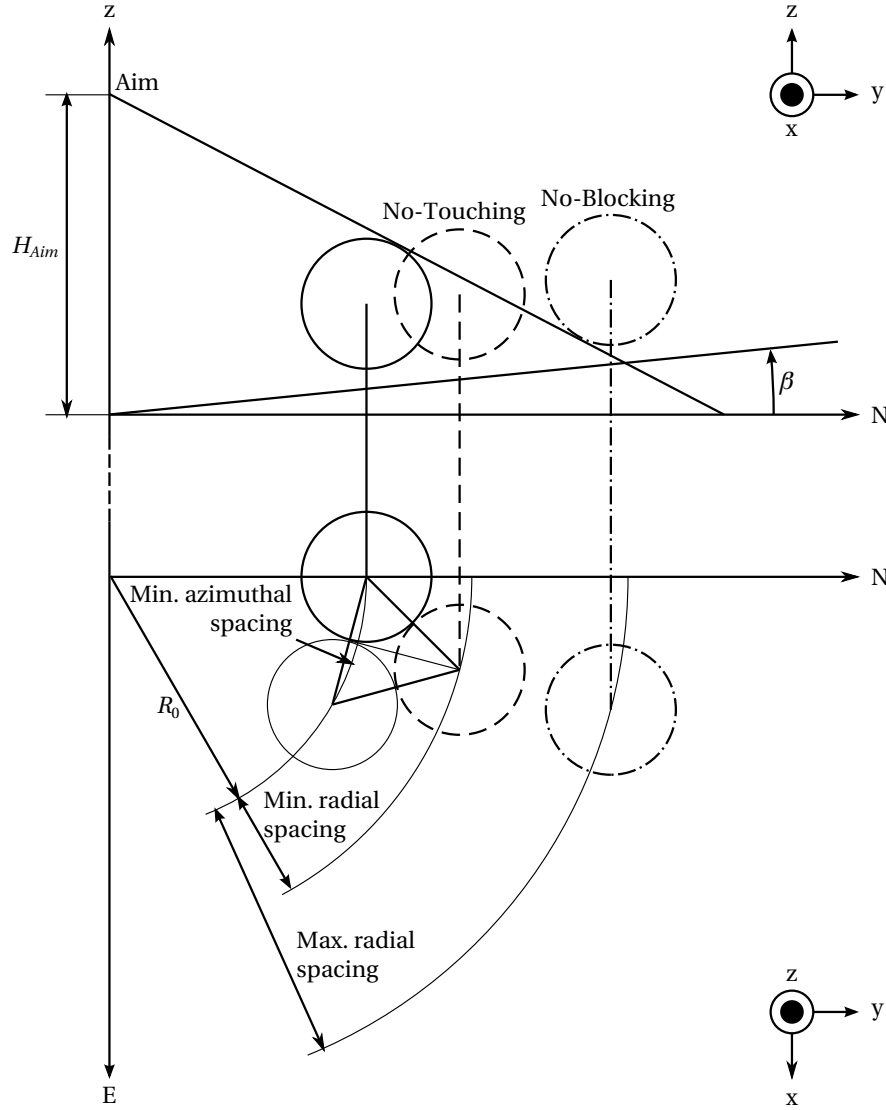


Figure 2.7 – The no-touching and no-blocking conditions for radial spacing.

In the end, similarly to the azimuthal spacing, the radial spacing coefficient $C_{RadSpac}$ is applied to the successive radii as a selected trade-off between no-touching and no-blocking:

$$R_{i+1} = R_{i+1,noTouch} + C_{RadSpac}(R_{i+1,noBlock} - R_{i+1,noTouch}), \quad C_{RadSpac} \in [0, 1] \quad (2.14)$$

Heliostat position

This way the heliostats are placed successively along the ring according to their own angle Ψ_m to the S-N axis, until the desired maximum Ψ_{max} is reached:

$$\Psi_m = \pm n\gamma \begin{cases} + & \text{if east half} \\ - & \text{if west half} \\ n = 0, 2, 4, \dots & \text{if essential ring} \\ n = 1, 3, 5, \dots & \text{if staggered ring} \end{cases}, \quad |\Psi_m| \leq \Psi_{max} \in]0^\circ, 180^\circ] \quad (2.15)$$

Based on the current row radius R_i , the azimuthal angle Ψ_m and the terrain slope β , the Cartesian coordinates of each heliostat m is given by

$$x_m = R_i \sin \Psi_m \quad (2.16)$$

$$y_m = R_i \cos \Psi_m \quad (2.17)$$

$$z_m = H_{ped} + R_i \tan \beta \quad (2.18)$$

Groups of same separation angle

During the iteration process on index i , the number of rows increases stepwise. As a result, the radius grows progressively as well as the azimuthal spacing, although the azimuthal angle between distribution axes is kept the same. At a given iteration step to determine, the azimuthal spacing is even large enough to define a new azimuthal angle and insert additional heliostats in between the others. Therefore a criterion is required to start a new group $j + 1$ of rows with a new azimuthal angle γ_{j+1} , where j is equal to zero for the very first group of rows of radii $R_i = R_{i,0}$ and angle $\gamma = \gamma_0$. This criterion is called the *mirror density criterion*, and states that the land area covered by heliostats should be maximal. The mirror density $\delta_{Mirr,i,j}$ of a ring is measured by the ratio of the net reflective area to the covered land area A_{Cov} :

$$\delta_{Mirr,i,j} = \frac{N_{Hel,i,j} A_{Ref}}{A_{Cov}}, \quad N_{Hel,i,j} = \begin{cases} 2 \text{ integer} \left(\frac{\Psi_{max}}{2\gamma_j} \right) + 1 & \text{if essential ring} \\ 2 \text{ integer} \left(\frac{\Psi_{max} - \gamma_j}{2\gamma_j} \right) + 2 & \text{if staggered ring} \end{cases} \quad (2.19)$$

where $A_{Ref} = C_{Ref} W_{Hel} H_{Hel}$ is the reflective area of a single heliostat. For each new radius generation, the mirror density is calculated for two options that have to be compared: a new row of radius $R_i + 1$, j that keeps the current azimuthal angle γ_j , and another possible new row of radius $R_{0,j+1}$ that creates a new azimuthal angle γ_{j+1} in a new group $j + 1$. Thus the covered land area A_{Cov} is given by the difference of area between the next disc of radius $R + D_{Hel}/2$

and the current disc of radius $R_{i,j} + D_{Hel}/2$:

$$A_{Cov} = \Psi_{max} \left[\left(R + \frac{D_{Hel}}{2} \right)^2 - \left(R_{i,j} + \frac{D_{Hel}}{2} \right)^2 \right] , \quad R = \begin{cases} R_{i+1,j} & \text{if same group } \gamma_j \\ R_{0,j+1} & \text{if new group } \gamma_{j+1} \end{cases} \quad (2.20)$$

The mirror density criterion is applied to the choice of the next ring by comparing the density of the ring of radius $R_{i+1,j}$ with that of radius $R_{0,j+1}$.

$$R = \begin{cases} R_{i+1,j} & \text{if } \delta_{Mirr,i+1,j} \geq \delta_{Mirr,0,j+1} \\ R_{0,j+1} & \text{if } \delta_{Mirr,i+1,j} < \delta_{Mirr,0,j+1} \end{cases} , \quad R \leq R_{max} \quad (2.21)$$

The whole process is then iterated until R reaches the desired maximum distance R_{max} from the tower base.

Layout boundary & number of heliostats

The layout boundary is defined by a circle shifted to the north (or south) along the S-N axis as shown in Figure 2.8. This circle is constrained by two parameters: the maximum ring radius R_{max} and the *south-to-north* coefficient C_{StoN} . The south-to-north coefficient is the ratio of the south furthest row to the north furthest row. It is equal to 0 for a north field and 1 for a tower-centred field. Hence, the centre of the boundary circle is simply given by

$$\begin{aligned} x_C &= 0 \\ y_C &= \frac{R_{max}}{2} (1 + C_{StoN}) \end{aligned} \quad (2.22)$$

and its radius by $R_{max}/2 \cdot (1 + C_{StoN})$.

Subsequently, the number of heliostats N_{Hel} is specified: only the first N_{Hel} closest heliostats to the centre of the boundary circle are kept.

Example

The algorithm for staggered circular layouts is applied here to the case of Gemasolar as an example. The Gemasolar layout features 2650 heliostats inside a circle boundary of radius 1500m, and the terrain is flat [Torresol, 2011]. The aim on the receiver atop the tower is at a 120 [m] height. The other parameters such as the radial spacing coefficient are estimated iteratively until the correct number of heliostats is reached within the given boundary circle (see Table 2.2). The radial spacing coefficient turns out to be in the middle of the interval between no-touching and no-blocking, while the south-to-north ratio is nearly two thirds of the maximum radius.

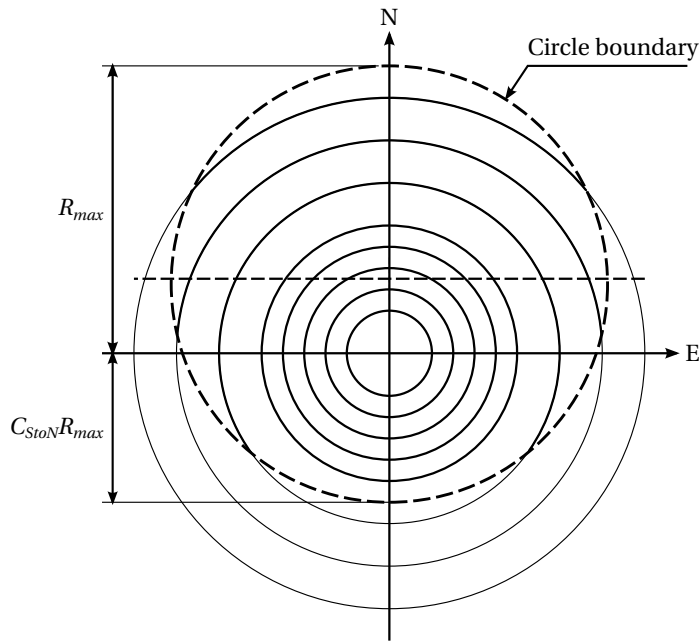


Figure 2.8 – Maximum row radius, circle boundary and south-to-north coefficient.

The output layout given by the algorithm is shown in Figure 2.9. The succession of different groups of same separation angle is visible especially where two neighbouring rows are more distant from each other, as a result of the mirror density criterion. Besides, since the row perimeter is not necessarily a multiple of the row azimuthal spacing, the rows do not close perfectly on the south field half. In practice, this small gap line formed by unoccupied terrain is needed to keep a road access to the plant at the tower's foot.

At this stage, the field layout may not be definitive: during the assessment of the field's performance, some bad heliostats may be eliminated to increase the overall efficiency.

Table 2.2 – Known and estimated properties of the field layout applied at the Gemasolar plant [Torresol, 2011].

| <i>Property</i> | <i>Value</i> | <i>Unit</i> |
|-------------------------------|--------------|-------------|
| Number of heliostats | 2650 | [#] |
| First row to aim ratio | 0.4167 | [-] |
| Safety separation ratio | 0 | [-] |
| Azimuthal spacing coefficient | 1 | [-] |
| Radial spacing coefficient | 0.4856 | [-] |
| Maximum radius | 912.7 | [m] |
| Maximum angle | 180 | [°] |
| South to north ratio | 0.6435 | [-] |
| Field slope | 0 | [°] |

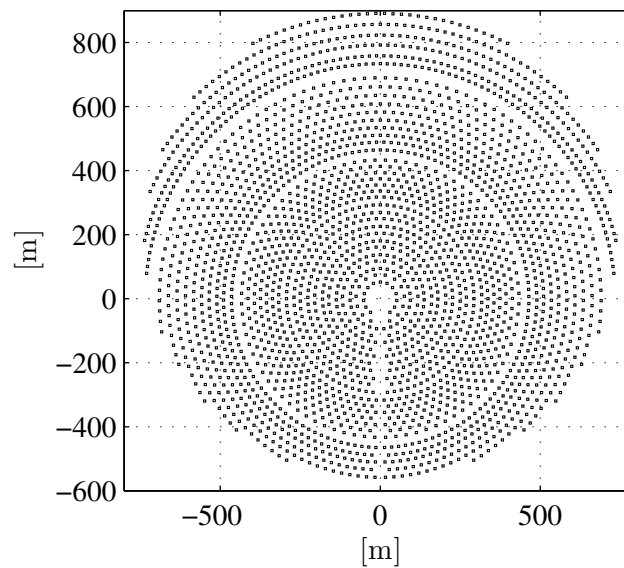


Figure 2.9 – Gemasolar-like field layout as given by the algorithm and the graphics from [Augsburger et al., 2012].

2.7 Tower

The main role of the central tower is obviously to contain the receiver at its top, and if necessary have enough room for a small buffer storage tank for the heat transfer fluid. Nevertheless, the tower also completes a couple of auxiliary but essential tasks and meets specific requirements. First, an additional target has to be defined in order to calibrate the heliostats one after the other, for instance as a white painted frame below the receiver location. Second, the heat transfer fluid, be it water, molten salt, or air, is conducted up and down the tower. Therefore on the one hand the tower must ensure the appropriate piping insulation to avoid heat losses by convection to the atmosphere and by conduction through the structure. And on the other hand, the tower has to feature enough room for pipes: these may be relatively large to minimise the pressure drop and thus the pump consumption (or fan for atmospheric air, compressor for pressurised air). Third, the tower should be designed by keeping in mind the following indirect influences: the sensitivity to wind and its impact on the focus accuracy of the heliostats, the shadow projected onto the field, and the impact on the landscape in the distance.

Steel Lattice vs. Concrete

The tower structure is made either of a steel lattice or reinforced concrete. At first sight, qualitatively, a steel lattice causes slightly less shadow on the heliostat field, whereas reinforced steel offers a better pipe insulation and wind resistance.

In theory the steel lattice towers for this application remain below 120 [m] high [Kistler, 1986], and this statement is verified in practice nowadays. For example, the steel lattice tower at Solar

One/Two is 90 [m] high, that at the former Eurelios research facility in Sicily is 50 [m] high, and the BrightSource towers at LPT, Israel and in Coalinga, California are 60 [m] and 100 [m] high respectively.

However, apart from the latter examples, most facilities are built with reinforced concrete, and even small towers below 120 [m] high. Especially in research facilities, the tower is used as a building with rooms dedicated to various experiments. Large facilities such as PS20 and Gemasolar in Spain feature towers above 120 [m] high. Regarding the shape, the concrete tower may be a cylinder or a parallelepiped, some towers such as the PS10/PS20 series have a large diamond-shaped hole that allows sight in the S-N direction.

Dimensions

Here the central tower is simply characterised by its height and its width. Among small-scale commercial facilities, the Aora tower in Samar, Israel, is only 30 [m] high. Then the research facilities range from 26 [m] for NSEC-CSIRO, Australia, up to 80 [m] for CESA-1, Spain, while the large commercial facilities range from 50 [m] for the Sierra SunTower in Lancaster, California, up to 165 [m] at PS20, Spain. For the sake of simplicity, the tower height here is calculated as the aim height plus half the receiver height: $H_{Tow} = H_{Aim} + H_{Rec}/2$.

The width varies from less than 10m for the Sierra SunTower up to 20 [m] at PS20, and does not necessarily matches the receiver width: it is smaller than the receiver for the Sierra SunTower and larger for PS20.

2.8 Receiver

The description of the central receiver in this paragraph regards its overall shape and aperture solely, independently from the equipment used (silicon carbide pipes, ceramic foam honeycomb modules, wire mesh, secondary concentrator, or quartz window) and from the heat transfer fluid (water, molten salt, atmospheric air, or pressurised air).

Cavity vs. External

The receiver concepts divide into two groups: *cavity* and *external* receivers. A cavity receiver is protected from the atmosphere in all directions except that of the heliostat field, and appears as a circular or rectangular window atop the tower. This way, convection and radiation heat losses to the atmosphere are reduced. Nevertheless, the acceptance angle remains lower than 180° : even though some concepts feature a series of four cavity receivers to catch 360° [Battleson, 1981], most cavity receivers are mounted alone and associated with a north field only, such as the PS10 and PS20 plants.

An external receiver has no protection and thus is prone to wind cooling and radiation losses

to the sky. But obviously the acceptance angle is not limited and surrounding fields are in practice combined with surrounding heliostat fields, such as Solar One/Two and Gemasolar. Some north fields are also associated with external receivers, for instance the BrightSource LPT and Coalinga fields.

Flat vs. Cylindrical

The receiver elements are then arranged according to a given overall pattern, in most cases either *flat* or *cylindrical*. The flat pattern may be tilted towards the heliostat field to improve the capture of reflected rays, as it is done for instance at CESA-1 and other research facilities. The cylindrical pattern may be external or internal in the form of a half-cylinder cavity receiver, such as the PS10 receiver.

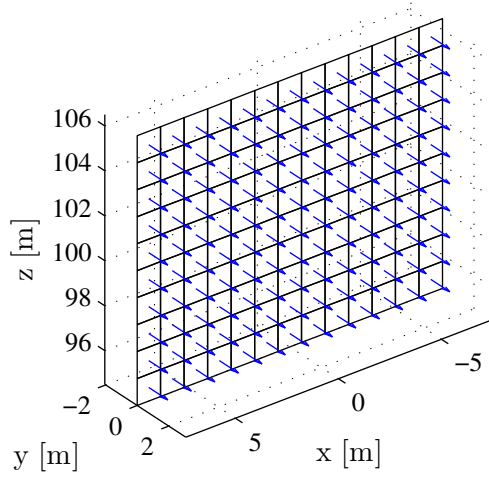
The corresponding receiver discretization for each pattern is presented in Figure 2.10. The discretization is defined by two numbers: the number of cells horizontally, and that vertically. Each cell has a normal vector. In the case of a flat pattern, the normal vector is the same for all cells, whereas for the cylindrical pattern it varies along the circumference.

The obtained discretized pattern is used to map the heat flux incident onto the receiver, but does not necessarily matches the real final shape of the receiver assembly. This way, the calculated heat flux may be geometrically projected further onto the final discretized receiver shape. For example, a half-cylindrical cavity receiver may be first considered as a flat pattern matching its aperture. Subsequently the heat flux incident on the flat pattern is projected further onto the half-cylindrical pattern (see Figures 2.10a and 2.10d).

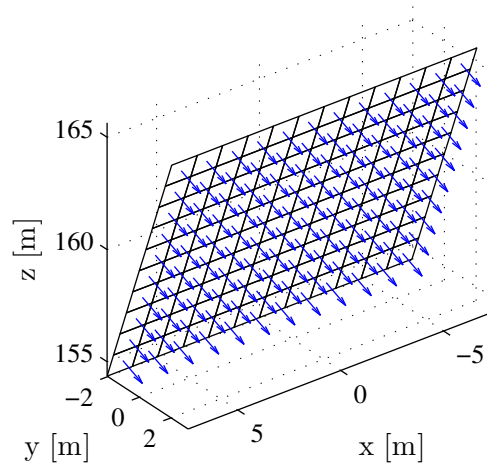
Dimensions

The overall dimensions of the receiver are given by its width W_{Rec} (or diameter) and height H_{Rec} . Current receiver dimensions range from less than 1 [m] for research facilities up to more than 10 [m] for large-scale commercial facilities. For example the PS10 receiver features 4 panels arranged according to a cavity half-cylindrical pattern of 14.83 [m] diameter and 12 [m] height [Fernandez, 2006].

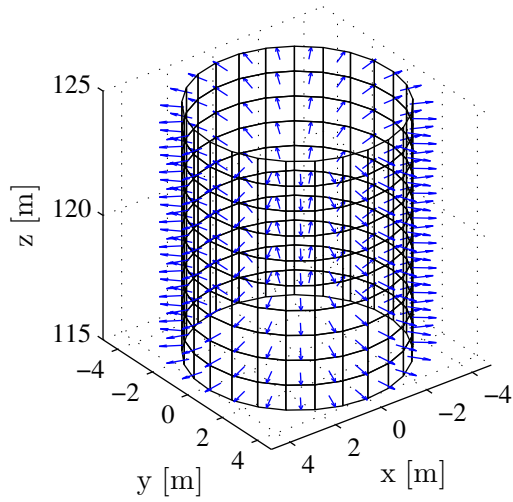
The receiver dimensions have a strong influence on the final optical efficiency, since a significant share of reflected light may miss the target (spillage loss). In practice in the case of Solar One/Two, the original receiver at Solar One was 7 [m] wide and 13.7 [m] high, and for Solar Two it was replaced by a 5.1 [m] by 6.2 [m] receiver, which was one of the reasons for large spillage losses, close to 10% of incident rays [Pacheco, 2002]. This may happen especially when the receiver is smaller than the heliostats, which increases the need for heliostat canting. On the other hand, when the receiver is at least as large as the heliostats, there is still always a need for focusing heliostats with curved mirrors and canting, but to a lesser extent such as in the example of the Sierra SunTower in Lancaster.



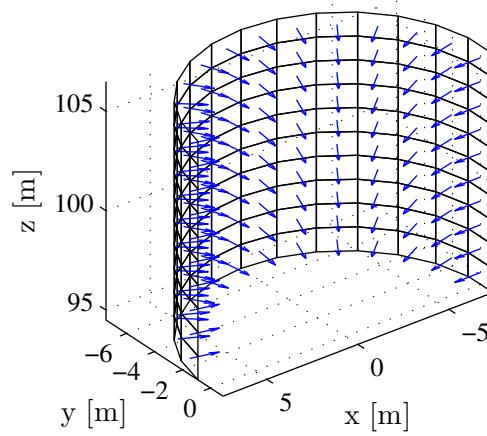
(a) Flat.



(b) Flat tilted.



(c) Cylindrical.



(d) Cylindrical cavity.

Figure 2.10 – Types of receiver discretization and normal vectors.

2.9 Power Conversion Unit

The Power Conversion Unit or PCU describes the whole energy conversion chain from the receiver output $\dot{Q}_{Rec,out}$ to the electric generator output $\dot{E}_{Gen,out}$. The same way as for the receiver, it is presented here independently from the applied technology. The PCU is assumed to feature a heat storage system in between the receiver and the heat-to-power conversion cycle, be it a Rankine, a Brayton or a combined cycle.

The heat storage system is characterised by a *storage capacity* Q_{Stor} in thermal energy units (Wh_{th}). Dividing it by the nominal thermal power input at the cycle provides the limit operation time when using the storage only. Nowadays the storage operation time ranges from a few minutes to more than 10 hours: PS10 features a 25 minutes saturated steam storage at full-load, while Gemasolar features a 15 hours molten salt storage.

The heat-to-power conversion cycle is described by its heat rate input $\dot{Q}_{Cy,nom}$ and its nominal first-law efficiency $\varepsilon_{Cy,nom}$. The cycle heat rate input is provided by the storage output and its level is chosen as a proportion of the maximal receiver output. Hence mathematically the maximal receiver output is a multiple of the cycle nominal input, which is called *solar multiple*:

$$SM = \frac{\max(\dot{Q}_{Rec,out})}{\dot{Q}_{Cy,nom}}, \quad SM > 1 \quad (2.23)$$

The solar multiple in practice varies from 1 up to nearly 3. For instance, Solar One was designed with $SM = 1$ and obviously would operate only when the receiver maximal output was reached, while today Gemasolar has a solar multiple of 2.8 which allows the large operation time under storage cited previously.

Then the cycle nominal first-law efficiency is defined by the ratio of the electric generator output to the cycle heat rate input under nominal design conditions:

$$\varepsilon_{Cy,nom} = \frac{\dot{E}_{Gen,nom}}{\dot{Q}_{Cy,nom}} \quad (2.24)$$

The cycle first-law efficiency mainly depends on the temperature difference between the storage output and the cooling source, according to the Carnot efficiency, and this difference is a function of the applied technology. Keeping the same previous examples, on the one hand the PS10 cycle uses direct saturated steam at 250 [°C] and condensates it at 50 [°C], leading to a 30.7% cycle efficiency [Fernandez, 2006]. On the other hand, the Gemasolar cycle generates steam at 538 [°C] thanks to a molten salt heat exchanger, increasing the cycle efficiency up to 39.5% [SENER, 2010].

In addition to the storage system and the conversion cycle, some extra elements are to be taken into consideration during the assessment of the plant performance, such as the pipes with their overall heat losses as well as the auxiliary devices with their own electricity consumption

(e.g. pumps, fans, electric heaters, etc.). These are characterised in the next chapter by a simple efficiency factor.

2.10 Summary

Four environmental characteristics are identified and implemented: the direct normal irradiance, the sun's position, the ambient temperature and the wind. The hourly direct normal irradiance is taken from a freely available database over an entire real year [SoDa, 2004]. The sun's position and its normal vector are calculated thanks to the conventional approach from the literature [ASHRAE, 2011]. The local ambient temperature is obtained from the same source as the DNI, while the wind velocity and its direction are extracted from a 3-hourly database [Nasa, 2011].

Then the elements of a solar tower plant are identified along the conversion from solar radiation to electric power: the heliostat field, the central tower and its receiver, and the power conversion unit. Key design parameters are described for each of them and their values are given as an example in the case of the Gemasolar plant [Burgaleta et al., 2011]. Regarding the field layout, an algorithm is presented by combining approaches from the literature [Siala and Elayeb, 2001] and specific geometrical parameters such as the azimuthal and radial spacing coefficients. Subsequently, the central receiver is defined as a discrete grid whose shape may be flat, flat tilted, cylindrical or half-cylindrical (cavity). Finally the power conversion is characterised independently from the conversion technology by a solar multiple and a cycle nominal efficiency.

Having identified the environmental conditions and the plant set-up, the energy performance of a solar tower plant is assessed in the following chapter.

3 Energy Performance

In this chapter, the behaviour of a solar tower power plant is modelled and simulated in order to assess its energy performance. First, the behaviour and the model of the three main elements performing the energy conversion is described: the heliostat field, the central receiver, and the power conversion unit. Their instantaneous power inputs and outputs, and first-law efficiency are presented as the successive steps in the solar-to-electric conversion chain. Second, the plant performance is simulated over three specific days, respectively two extreme and one intermediate set of conditions, according to the sun position throughout the year. Third, based on the three specific days, the annual performance is interpolated at each time step, and the main annual performance indicators of the plant are defined and presented in a case similar to the Gemasolar plant.

3.1 Heliostat Field

The energy performance of the heliostat field depends on a series of distinct optical losses between the direct normal irradiance incident on the heliostats and the concentrated beam on the receiver. These optical losses include shading, cosine, reflectivity, cleanliness, blocking, atmospheric and spillage losses. In order to simulate them, several codes have been developed since the mid-seventies [Garcia et al., 2008] in FORTRAN, Basic, C++, Matlab, and Delphi5. They divide into two main groups according to their calculation method: *convolution*-based and *ray-tracing*.

- The convolution-based codes assume a given statistical distribution of the sun disc intensity (simple pill-box, normal distribution, or measured sun shape [Biggs and Vittitoe, 1979]). This sun shape is then convoluted with the successive distributions of the heliostat slope and tracking errors. At the same time, it is multiplied by each loss factor listed previously, except spillage which is inherent in the resulting distribution intercepted by the receiver.
- The ray-tracing codes generate a large amount of rays from one or more specified virtual light sources. These rays are then blocked or reflected by the virtual two-/three-dimensional objects placed within the environment. Hence the amount of rays incident on

one of these objects can be measured, in the present case the central receiver. Qualitatively in practice, on the one hand the convolution-based codes require less computer resources, but on the other hand ray-tracing is more flexible and allows all kinds of geometry configurations. The code used and adapted here is convolution-based [Monterreal, 1998] and written in Matlab, which allows a straight connection with Matlab tools - especially optimisation and graphic tools - as well as with its free software equivalent Octave. A comparison of the results obtained with this own-adapted code and with the commercial HFLCAL code [Schwarzbözl et al., 2009] is presented in Appendix C.

Shading

The *shading* losses occur before the solar radiation hits a heliostat: one or more other neighbouring heliostats may cast their shadow on the considered heliostat. The shading losses are calculated by projecting the polygons of the neighbouring heliostats on that of the considered heliostat along the sun's direction. The shading ratio is given by the projected overlapping area divided by the projected total polygon area. The complementary value of the shading ratio results in the shading efficiency $\varepsilon_{Shad}^i(t)$ of a heliostat i at time t . Shading happens especially when the sun is low in the sky, at the beginning and the end of the day. Otherwise, depending on the field layout, it may occur throughout the day if the mirror density is maximal and the heliostats are stuck to each other.

The calculated value of the shading coefficient for each heliostat of the Gemasolar plant at 07:00 ST on March 20th is shown in Figure 3.1. The red arrow indicates the sun vector in the x-y plane. The shading coefficient does not exceed 0.6 for some areas, and in the case of

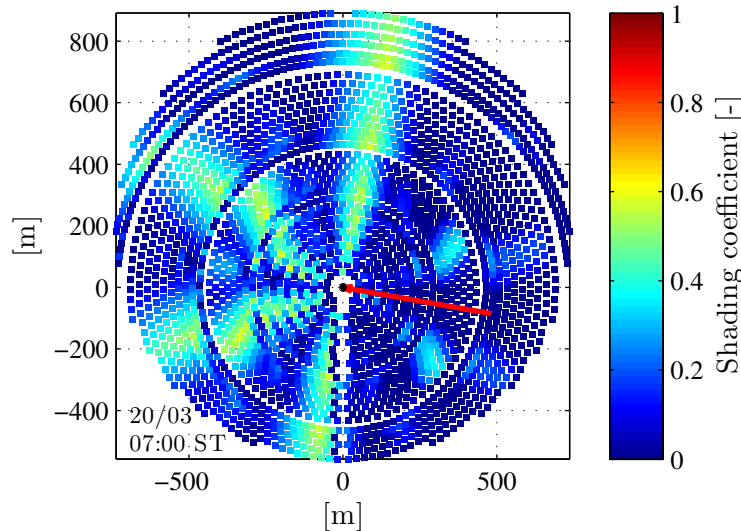


Figure 3.1 – Calculated shading coefficients for Gemasolar-like heliostats at ST 7:00 (rather extreme case, only to observe significant values).

Gemasolar, this early hour and its symmetric late hour (19:00 ST) turn out to be the only time periods with significant shading. Otherwise throughout the day and especially at noon the shading losses are much lower, however not negligible, up to 3%.

Cosine

The *cosine* losses happen when the heliostat plane is not perpendicular to the sun vector and this way reflects less than its own area towards the receiver. Since the heliostat continuously reflects rays in a fixed direction, the incidence angle between the sun vector and the heliostat normal is never equal to zero (except if the sun is aligned with the receiver, but then obviously the sun is hidden). Thus the cosine losses cannot be avoided and the cosine efficiency is given by the heliostat projection area along the sun vector divided by the heliostat total area, easily expressed by the cosine of the incidence angle $\cos \omega_{Hel}^i(t)$. The distance from the heliostat to the receiver indirectly increases the cosine losses, as the heliostat is less and less aligned with the receiver and the sun. Throughout the day, the cosine efficiency evolves such that roughly west-side heliostats undergo minimal losses in the morning and maximal losses in the afternoon, and vice-versa for east-side heliostats.

The cosine loss coefficients are pictured in Figure 3.2, in the same conditions as shading previously. The distribution shows an axis of symmetry matching the x-y projection of the sun vector, which then rotates around the tower throughout the day. The cosine loss is clearly higher when the heliostats are at a given moment located between the tower and the sun, up to more than 80%. On the opposite field side, the heliostats undergo almost no cosine loss. Since the situation evolves continuously, the cumulated losses at the end of the day for each single heliostat will be more interesting later on.

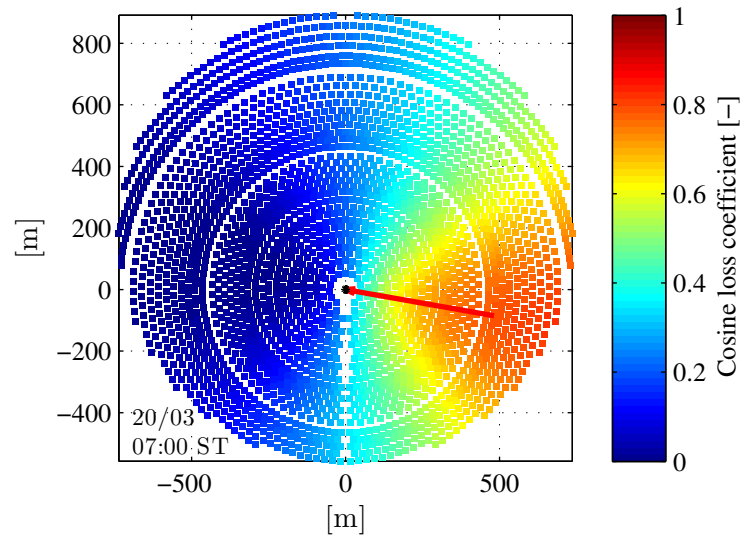


Figure 3.2 – Calculated cosine loss coefficients for Gemasolar-like heliostats at ST 7:00.

Reflectivity & Cleanliness

The *reflectivity* losses are given by the amount of light that is not reflected by the clean mirror, whereas the *cleanliness* losses are caused by absorption and diffusion through dirt on the mirror. The reflectivity depends on the manufacturing quality of the mirror as well as on its resistance to corrosion, while the cleanliness strongly depends on dust deposit and the frequency of cleaning or raining. These two losses are described by a loss coefficient which is equal for each heliostat and assumed constant over time at a given annual mean value.

For instance in the case of Gemasolar, both coefficients are assumed to be equal to 5% [Sargent & Lundy, 2003], which results in the estimate of the combined reflectivity/cleanliness efficiency of 90.3%.

Blocking

The *blocking* losses occur after the solar radiation has been reflected by a given heliostat: one or more neighbouring heliostats may intercept and thus block the reflected beam partially. They are calculated the same way as shading, through polygon projections and subtractions. But unlike shading, the axis of projection remains continually the same over time, the straight line between the heliostat centre and the receiver aim. Therefore blocking can be limited by the selection of appropriate field layouts, through the choice of the azimuthal and radial spacing between heliostats presented in §2.6.1. However blocking may be tolerated in order to satisfy a trade-off with the mirror density.

The blocking loss coefficient of each heliostat is shown in Figure 3.3, once again under the same conditions at Gemasolar. Blocking turns out to occur mainly among heliostats belonging

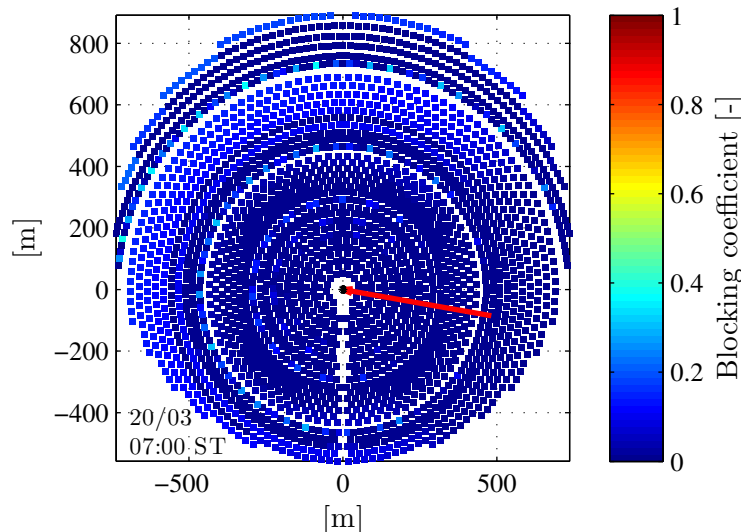


Figure 3.3 – Calculated blocking loss coefficients for Gemasolar-like heliostats at ST 7:00.

to the first row of a group with a new azimuthal angle (see §2.6.1). Since these rows do not stagger with the last row of the previous group (mirror density criterion), a few heliostats are partially blocked, with a blocking coefficient exceeding 35% for some of them. For the rest of the day, unlike shading, the distribution of the blocking losses remains nearly the same, with even lower blocking coefficients at noon.

Atmospheric Attenuation

The *atmospheric attenuation* affects the reflected beam by absorption and diffusion through the ambient air quality between the heliostat and the receiver. The attenuation coefficient is calculated thanks to polynomial correlations [Ballestrín and Marzo, 2012] expressed as a function of the distance $D_{Hel-Aim}$ from the heliostat centre to the receiver aim. The factors of these correlations may vary according to the daily visibility, but since the air quality is not a standard data available at any place any time in current databases, only one correlation is taken as the most frequent one and kept for all time steps:

$$C_{Atten} = C_{Atten1} + C_{Atten2}D_{Hel-Aim} + C_{Atten3}(D_{Hel-Aim})^2 + C_{Atten4}(D_{Hel-Aim})^3 \quad (3.1)$$

where

$$C_{Atten1} = 0.679$$

$$C_{Atten2} = 11.76$$

$$C_{Atten3} = -1.97$$

$$C_{Atten4} = 0$$

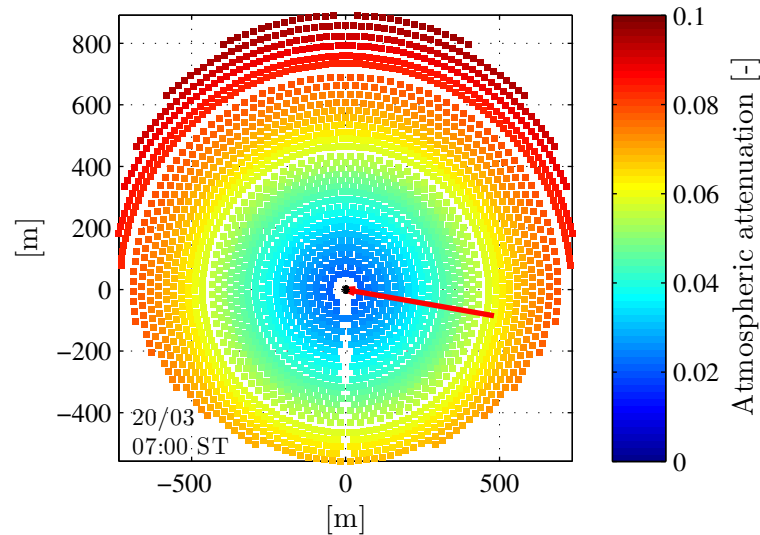


Figure 3.4 – Calculated atmospheric attenuation coefficients for Gemasolar-like heliostats.

The distribution heliostat by heliostat of the atmospheric attenuation coefficient is presented in Figure 3.4 with a color scale divided by 10 in order to increase the contrast. As explained previously, this distribution is kept the same at any moment, and shows a clear increase in attenuation from the tower foot to the furthest heliostats. The attenuation coefficient ranges here from 2% for a distance of 125 [m] up to 10% at 900 [m]. Unlike blocking, no layout selection can avoid attenuation, except by keeping heliostat reasonably close to the receiver aim (10% may be a criterion).

Spillage

The *spillage* losses occur as the rays reflected by the heliostats hit the receiver: a share of these rays may miss the receiver area and thus be lost to the atmosphere. They are given by the area that is not intercepted between the projection of the reflected flux distribution and the projection of the receiver along the heliostat-aim axis. Without going into details (see later on in Chapter 4), several calculation methods for the reflected flux distribution may be found in the literature: the analytical function presented by [Collado et al., 1986] is used and adapted here. For the calculation of spillage losses solely, the knowledge of the flux distribution itself on the receiver is not needed, hence the function is not applied as such here, but analytically integrated over the receiver projection. This analytical integration is performed in two dimensions, along the receiver width and height, and leads to the following

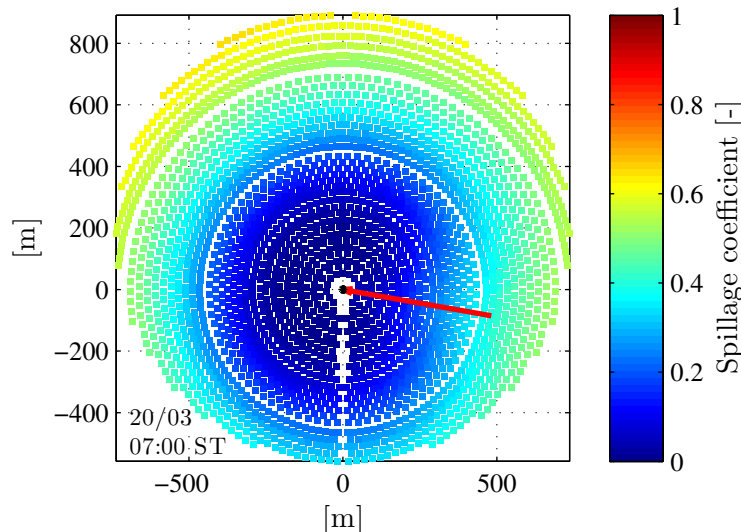


Figure 3.5 – Calculated spillage coefficients for Gemasolar-like heliostats at ST 7:00.

spillage coefficient for a single heliostat:

$$\begin{aligned}
 C_{Spill} = 1 - \frac{1}{4W''_{Hel}H''_{Hel}} & \left\{ (W''_{Rec} + W''_{Hel}) \operatorname{erf}(W''_{Rec} + W''_{Hel}) + \frac{1}{\sqrt{\pi}} e^{-(W''_{Rec} + W''_{Hel})^2} \dots \right. \\
 & \dots - (W''_{Rec} - W''_{Hel}) \operatorname{erf}(W''_{Rec} - W''_{Hel}) + \frac{1}{\sqrt{\pi}} e^{-(W''_{Rec} - W''_{Hel})^2} \left. \dots \right\} \dots \\
 & \dots \cdot \left\{ (H''_{Rec} + H''_{Hel}) \operatorname{erf}(H''_{Rec} + H''_{Hel}) + \frac{1}{\sqrt{\pi}} e^{-(H''_{Rec} + H''_{Hel})^2} \dots \right. \\
 & \dots - (H''_{Rec} - H''_{Hel}) \operatorname{erf}(H''_{Rec} - H''_{Hel}) + \frac{1}{\sqrt{\pi}} e^{-(H''_{Rec} - H''_{Hel})^2} \left. \dots \right\} \quad (3.2)
 \end{aligned}$$

where W''_{Hel} and H''_{Hel} are the transformed heliostat dimensions, and W''_{Rec} and H''_{Rec} the transformed receiver dimensions, both corrected by the standard deviation σ_{Rec} of the reflected rays in the receiver image plane:

$$\sigma_{Hel} = D_{Hel-Aim} \sqrt{\sigma_{Sun}^2 + 2(1 + \cos^2 \omega_{Hel}) \sigma_{Slope}^2 + \sigma_{Track}^2} \quad (3.3)$$

$$\sigma_{Rec} = \frac{\sigma_e}{\sqrt{\cos \omega_{Rec}}} \quad (3.4)$$

See §2.5 for the definition of σ_{Sun} , σ_{Slope} and σ_{Track} . Besides, the same way as the incidence angle ω_{Hel} on the heliostat, ω_{Rec} is the incidence angle on the receiver. Thus the transformed heliostat and receiver dimensions are given by the following :

$$\begin{aligned}
 W'_{Hel} &= \sqrt{\frac{\text{Jacobian}}{\cos \omega_{Rec}}} W_{Hel} & H'_{Hel} &= \sqrt{\frac{\text{Jacobian}}{\cos \omega_{Rec}}} H_{Hel} \\
 W''_{Hel} &= \frac{W'_{Hel}}{2\sqrt{2}\sigma_{Rec}} & H''_{Hel} &= \frac{H'_{Hel}}{2\sqrt{2}\sigma_{Rec}} \\
 W''_{Rec} &= \frac{W_{Rec}}{2\sqrt{2}\sigma_{Rec}} & H''_{Rec} &= \frac{H_{Rec}}{2\sqrt{2}\sigma_{Rec}} \quad (3.5)
 \end{aligned}$$

The calculation of the Jacobian is referred to the article cited previously. Figure 3.5 shows the distribution of the spillage loss coefficient at a given time. As expected, spillage grows with the distance to the receiver aim up to 65% for the furthest heliostats. Moreover, it turns out to be slightly higher for the heliostats lying between the sun and the tower, that means those where the incidence angle is greater than on the opposite side of the field. Therefore the distribution varies a bit throughout the day following the sun vector as a symmetry axis. There are basically two means to keep spillage low: locate the heliostats closer to the receiver aim, and improve their optical accuracy expressed by the slope and tracking standard deviation σ_{Slope} and σ_{Track} .

First-Law Efficiency

The total radiation input of the heliostat field is easily defined as the radiation input that would hit the entire reflective area of a heliostat multiplied by the number of heliostats in the field:

$$\dot{Q}_{Field,Inc}(t) = N_{Hel} \cdot DNI(t) \cdot C_{RefI} \cdot W_{Hel} \cdot H_{Hel} \quad (3.6)$$

Once all the individual losses are known from previous paragraphs, the radiation power output of the heliostat field is estimated by adding each single heliostat output taking its own efficiency into account. The sum results in the radiation power incident on the receiver:

$$\begin{aligned} \dot{Q}_{Rec,Inc}(t) = \sum_{i=1}^{N_{Hel}} & \epsilon_{Avail}^i(t) \cdot \epsilon_{Shad}^i(t) \cdot \epsilon_{Cos}^i(t) \cdot \epsilon_{RefI}^i(t) \cdot \epsilon_{Clean}^i(t) \dots \\ & \dots \cdot \epsilon_{Block}^i(t) \cdot \epsilon_{Atten}^i(t) \cdot \epsilon_{Spill}^i(t) \cdot DNI(t) \cdot C_{RefI} \cdot W_{Hel} \cdot H_{Hel} \end{aligned} \quad (3.7)$$

As a result, the first-law efficiency of the heliostat field is expressed as the ratio of the total radiation power incident on the receiver to the total radiation input of the heliostat field:

$$\epsilon_{Field}(t) = \frac{\dot{Q}_{Rec,Inc}(t)}{\dot{Q}_{Field,Inc}(t)} \quad (3.8)$$

3.2 Receiver

The energy performance of the central receiver is given by its ability to convert the incident concentrated radiation into heat power carried by the heat transfer fluid. This conversion is affected by four heat loss types: *reflection*, *radiation*, *convection* and *conduction* (negligible here). They are presented and illustrated here succinctly, and modelled altogether within a correlation of the receiver first-law efficiency, in order to remain independent of the receiver technology.

Reflection

The reflection losses rely on the reflectivity factor (and its complementary absorption factor) of the receiver materials. Silicon carbide as used in steam or molten salt receivers may exceed a 10% total reflectivity above 500 [°C] [Bergman et al., 2011] without selective coating, and drop down to 5% with coating [Pacheco, 2002]. Reflection may reach 30% [Winter, 1991] of the total receiver losses depending on the receiver technology.

Radiation

Then the radiation losses depend on the materials emissivity according to the Stefan-Boltzmann law applied to a real surface. Taking the same example, the total normal emissivity of silicon

carbide gets close to 90% of a blackbody for a temperature between 500 [°C] and 1000 [°C]. Therefore the role of a selective coating is crucial here: to absorb radiation in the domain of visible wavelengths (between 0.4 [μm] and 0.7 [μm], where most of the terrestrial solar radiation occurs) and at the same time to radiate as little as possible in the domain of wavelengths that correspond to the material temperature according to Planck's law (typically infrared, e.g. between 2 [μm] and 4 [μm] at 700 [°C]). Radiation losses may exceed 50% [Winter, 1991] of the total receiver losses depending on the receiver temperature and emissivity.

Convection

The convection losses are dependent on the ambient atmospheric temperature and the wind velocity, as well as on the receiver shape as presented in §2.8. The average heat transfer coefficient of convection may reach 20 [W/(m²K)] [Winter, 1991] for a cavity receiver with tube bundles. The knowledge of the convection coefficient for a given receiver is frequently expressed by a correlation based either on measurements or calculations, only valid for a specific concept [Stoddard, 1986]. In practice, the convection losses are often close to a quarter of the total receiver losses as well.

First-Law efficiency

The physical expression of each thermal loss here above strongly depends on the receiver technology, its materials, and temperature level. Hence a simplified expression of the total receiver first-law efficiency is presented here, whose coefficients might be adapted according to measurements or calculations of specific receiver concepts. This correlation is based on the results obtained at Solar Two with an external cylindrical molten salt receiver made of tube bundles [Pacheco, 2002]. It is a function f of the dimensionless incident power $\dot{Q}_{Rec,Inc}^*$ on the receiver surface and of the wind velocity v_{Wind} , and provides the receiver first-law efficiency ε_{Rec} as the ratio of the output heat power $\dot{Q}_{Rec,Out}$ carried by the heat transfer fluid to the incident power $\dot{Q}_{Rec,Inc}$:

$$\varepsilon_{Rec}(t) = \frac{\dot{Q}_{Rec,Out}(t)}{\dot{Q}_{Rec,Inc}(t)}$$

$$\varepsilon_{Rec}(t) = f(\dot{Q}_{Rec,Inc}^*(t), v_{Wind}(t)), \quad \dot{Q}_{Rec,Inc}^*(t) = \frac{\dot{Q}_{Rec,Inc}(t)}{\max(\dot{Q}_{Rec,Inc}(t))} \quad (3.9)$$

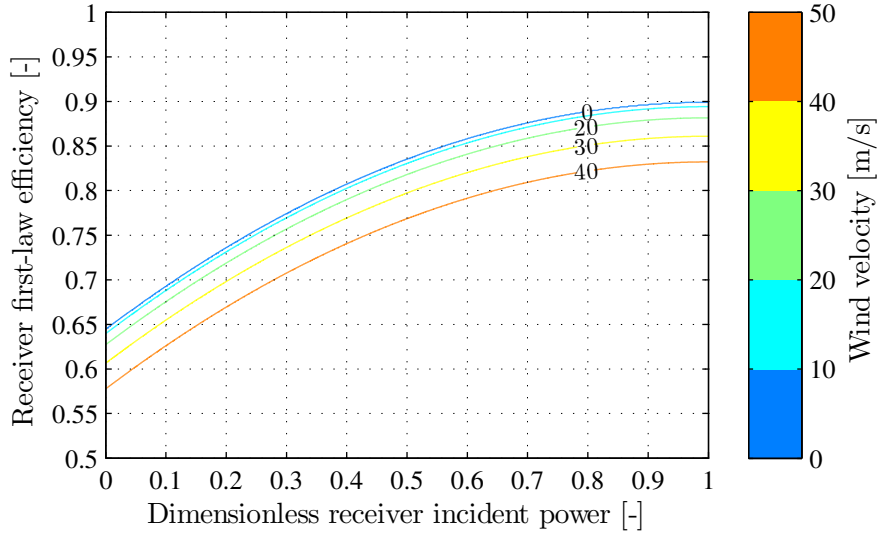


Figure 3.6 – Receiver first-law efficiency vs. dimensionless receiver incident power and wind velocity generalised from [Pacheco, 2002].

where

$$f : (x, y) \mapsto C_{Rec1} + C_{Rec2} \left(x - \frac{x^2}{2} \right) + C_{Rec3}y + C_{Rec4}y^2$$

$$C_{Rec1} = 0.6441$$

$$C_{Rec2} = 0.5089$$

$$C_{Rec3} = -3.892 \cdot 10^{-5}$$

$$C_{Rec4} = -4.053 \cdot 10^{-5}$$

Figure 3.6 shows the receiver first-law efficiency on the y-axis against the dimensionless receiver incident power on the x-axis and the wind velocity on the color axis. Since the receiver is designed to achieve a given maximal incident power, its efficiency increases with the dimensionless power up to a maximum at $\dot{Q}_{Rec,Inc}^* = 1$. In parallel, the efficiency goes down with the wind velocity, with an accelerating decrease towards high winds. In the case presented, the efficiency reaches a maximum of 0.9 without wind, falls to 0.88 with 20 [m/s], and down to 0.83 with 40 [m/s]. However, as presented in §2.4, wind velocities higher than 10 [m/s] are rare for the given location, and lead to the shutdown of the heliostats. Therefore for the most frequent winds below 10 [m/s], the receiver efficiency remains close to the no-wind curve and can be approximated as a function of the receiver incident power solely.

3.3 Power Conversion Unit

The performance of the power conversion unit is assessed by how well the heat power from the receiver is converted into electric power at the generator. The conversion undergoes a

series of losses that are divided into four categories here: *piping*, *storage*, *cycle*, and *auxiliary*. Each loss is described and modelled without going into details that would be specific to a given technology.

Piping

As mentioned in §2.7, the piping losses occur when the heat transfer fluid is conducted to and from the receiver, up and down the tower, as well as at the ground level between the tower base and the storage system (this might change according to the concept, especially if the PCU is partially or entirely located atop the tower). Hence piping losses include convection losses with the ambient air around the pipes, conduction losses through the supporting structure, and possibly radiation losses if the pipes are not shielded against it. In practice they are kept nowadays far below 1% of the receiver power output [Pacheco, 2002], and here they are taken into account with a simplified efficiency factor ε_{pip} .

Storage

The storage losses consist in heat losses to the ground and to the atmosphere. The storage tank, be it direct storage of transfer fluid or indirect through intermediate carrier, is built at the ground level or even buried. This way the storage system is subjected to convection losses to the atmosphere and conduction losses to the ground, as well as radiation losses if the structure is not shielded. In concrete terms, the storage losses nowadays can remain below 0.5% of the storage input power [Pacheco, 2002], and similarly to piping an efficiency factor ε_{stor} is introduced into the PCU performance.

In addition to thermal losses, the storage system defines the profile of the plant power output over time. This profile is the consequence of a specific storage *strategy*, which has to determine the operation mode among the following three:

- only store the receiver power output,
- directly transfer the receiver power output to the conversion cycle and store the excess,
- or only discharge the storage tank.

There are at least two possible criteria to decide between them: the level of the receiver power output or that of the storage filling. On the one hand, the receiver criterion specifies at what receiver output level the conversion cycle should be started, e.g. as soon as it is equal to the cycle nominal input (given by the solar multiple in §2.9). On the other hand, the storage criterion specifies at what filling level the cycle should be started, e.g. when the storage is able to ensure at least two operating hours without the sun. When comparing both criteria, it turns out that the receiver criterion alone may start the cycle with a storage filling ensuring not more than a few minutes of operation. This inevitably leads to an increasing number of startups and shutdowns throughout the day. Therefore the storage filling criterion allows to minimise the number of operating periods and maximise their length. The strategy presented and expressed here below is a combination of the two criteria:

if $\varepsilon_{Pip} \dot{Q}_{Rec,out}(t) < \dot{Q}_{Cy,nom}$

$$\dot{Q}_{Stor,in}(t) = \dot{Q}_{Rec,out}(t) \quad , \quad \dot{Q}_{Stor,out}(t) = \begin{cases} 0 & \text{if } Q_{Stor}(t) < Q_{Stor,min} \\ \dot{Q}_{Cy,nom} & \text{if } Q_{Stor}(t) \geq Q_{Stor,min} \end{cases}$$

if $\varepsilon_{Pip} \dot{Q}_{Rec,out}(t) \geq \dot{Q}_{Cy,nom}$

$$\dot{Q}_{Stor,in}(t) = \dot{Q}_{Rec,out}(t) - \dot{Q}_{Cy,nom} \quad , \quad \dot{Q}_{Stor,out}(t) = \dot{Q}_{Cy,nom} \quad (3.10)$$

where

$$Q_{Stor,min} = \begin{cases} \dot{Q}_{Cy,nom} \Delta t_{Stor,min} & \text{if } \dot{Q}_{Stor,out}(t - \Delta t) = 0 \quad (\text{cycle still off}) \\ \dot{Q}_{Cy,nom} \Delta t & \text{if } \dot{Q}_{Stor,out}(t - \Delta t) > 0 \quad (\text{cycle already on}) \end{cases}$$

In Figure 3.7, the case of Gemasolar on a perfect spring equinox is presented with a combination of the receiver criterion and a storage filling criterion of 2.3 hours to avoid early startup (corresponding to 1 startup and 1 shutdown per day in average over the entire year, see §3.5). As the sun rises at 6:00 ST in the morning, the receiver starts filling the storage tank, without starting the cycle, as long as the receiver output is lower than the cycle nominal input needed and the storage filling status is below 2.3 hours. Then as soon as the receiver output exceeds the cycle requirement, the cycle is started, and the receiver feeds both the cycle and the storage with the power surplus until the receiver output becomes insufficient again. Thus around 17:00 ST the storage system starts discharging, progressively replaces the receiver output, and feeds all by itself the cycle until full discharge at 3:00 ST on the following day. This way an operation period of 19 hours is ensured. In practice, the cycle is also operated at part-load.

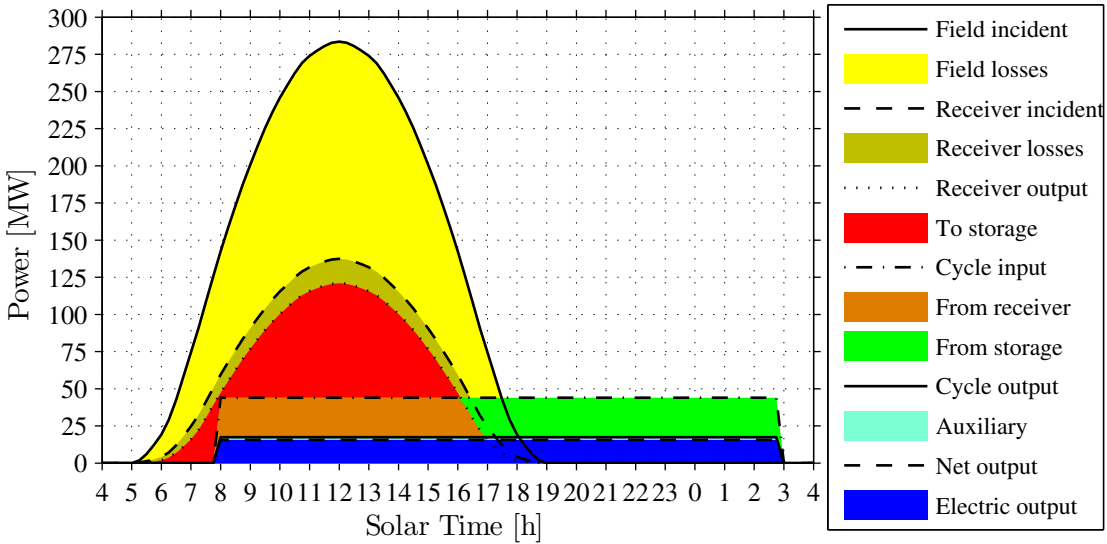


Figure 3.7 – Storage operation strategy in the Gemasolar-like case on a perfect spring equinox (March 20th).

Cycle

The cycle losses are the largest losses in the PCU and are inherent in the conversion of heat into mechanical power according to Carnot applied to the hot and the cold temperature levels. They occur after the heat-to-mechanical conversion, at the cooling system where about 60% to 70% of the cycle heat input is evacuated to the environment (air or water), depending on the cycle technology. The electric generator is also subjected to losses, but to a much lesser extent, nowadays less than 1% of the mechanical power. Hence as presented in §2.9, the gross cycle first-law efficiency of existing solar tower plants ranges roughly from 30% to 40% and higher for innovative concepts [Spelling et al., 2011].

Here the value of the gross cycle efficiency $\varepsilon_{Cy,nom}$ is either specified with known data from operational plants, or estimated as a function of the cycle nominal power input whose coefficients may be modified according to the technology. For instance in the case of a Rankine cycle, a correlation for the scaling effect on the efficiency improvements of facilities between 10 [MW_{el}] and 220 [MW_{el}] is presented, based on data from [Sargent & Lundy, 2003]:

$$\varepsilon_{Cy,nom} = \varepsilon_{Cy,nom}^0 \left(\frac{\dot{Q}_{Cy,nom}}{\dot{Q}_{Cy,nom}^0} \right)^{C_{Cy}}, \quad 25[\text{MW}_{th}] \leq \dot{Q}_{Cy,nom} \leq 480[\text{MW}_{th}] \quad (3.11)$$

where

$$\begin{aligned} \varepsilon_{Cy,nom}^0 &= 0.403 \\ \dot{Q}_{Cy,nom}^0 &= 33.995 \quad [\text{MW}_{th}] \\ C_{Cy} &= 0.04632 \end{aligned}$$

As a result, within the range of validity, the estimated gross cycle efficiency of the Rankine cycle varies from 40% at 10 [MW_{el}] up to 45% at 220 [MW_{el}]. The gross electric output from the conversion cycle is expressed as follows:

$$\dot{E}_{Cy,Out}(t) = \varepsilon_{Cy,nom} \dot{Q}_{Stor,out}(t) \quad (3.12)$$

Auxiliary

The auxiliary loss is the share of the electric power output at the generator that is used internally in the plant to feed various essential devices, mainly in three domains: in the loop of the heat transfer fluid, in the storage system, and in the conversion cycle. In the HTF loop, the fluid transport up and down the tower is performed by pumps in the case of molten salts or liquid water, and by fans or compressors in the case of pressurised or atmospheric air. The storage system may also feature pumps or fans, and especially for molten salts it features electric heaters to keep the temperature level constant. Then in the conversion cycle, if it is assumed a Rankine cycle, two main auxiliary consumptions occur: at the feedwater pump and the cooling system. The feedwater pump is required to circulate water from the condenser to the evaporator, while the cooling system requires pumps for wet cooling (water) or fans for dry

Table 3.1 – Known and estimated properties of the PCU at the Gemasolar plant.

| <i>Property</i> | <i>Value</i> | <i>Unit</i> |
|-------------------------|--------------|-------------|
| Piping efficiency | 0.99 | [-] |
| Storage efficiency | 0.995 | [-] |
| Solar multiple | 2.7907 | [-] |
| Cycle efficiency | 0.3953 | [-] |
| Auxiliary efficiency | 0.9 | [-] |
| Availability efficiency | 0.94 | [-] |

cooling (air). In addition to these three domains, power is needed as well for the heliostats drives and control, and other miscellaneous equipments whose consumption is negligible.

In practice, the auxiliary losses may exceed 20% of the generator electric output as this was the case at the former Solar Two plant [Pacheco, 2002]. Nevertheless, they are nowadays kept below 10%, and taken into consideration here with a simple efficiency factor ϵ_{Aux} .

Finally, the PCU also undergoes availability losses, which occur when the plant has to go through maintenance or possibly must be inadvertently shut down because of failures. The same way as for heliostats, this is taken into account with the availability efficiency $\epsilon_{PCU,Avail}$, and may be in practice typically be equal to 95% [Sargent & Lundy, 2003]. Table 3.1 shows a summary of the PCU efficiencies and properties known and estimated in the Gemasolar case. The *net* electric output from the PCU is expressed as a function of the storage output:

$$\begin{aligned}\dot{E}_{PCU,nom} &= \epsilon_{Aux}\epsilon_{PCU,Avail}\dot{E}_{Cy,nom} \\ \dot{E}_{PCU,Out}(t) &= \epsilon_{Aux}\epsilon_{PCU,Avail}\dot{E}_{Cy,Out}(t)\end{aligned}\tag{3.13}$$

3.4 Specific Days

In order to assess the plant and especially the heliostat field, the energy performance is calculated over three specific days that are representative of both the extreme and middle annual conditions: on the spring equinox (equivalent to the autumn equinox), on the summer solstice, and on the winter solstice (respectively March 20th, June 21st and December 21st). Besides, the DNI is assumed to be perfect over time (clear-sky, no cloud) in order to obtain first a field efficiency that is independent of the solar input. The time step of the simulation is set to one hour, which leads to the calculation of 72 steps where only 41 steps have a positive DNI (13 on the spring equinox, 17 on the summer solstice and 11 on the winter solstice).

The cumulated performance of the heliostats when considering all the field losses described in §3.1 is shown in Figure 3.8. As expected the most efficient heliostats are located in the middle of the field, north of the tower. The circular limit corresponding to a 50% efficiency appears at a distance of 300 [m] from the tower base, while the minimum efficiency goes down to 20%

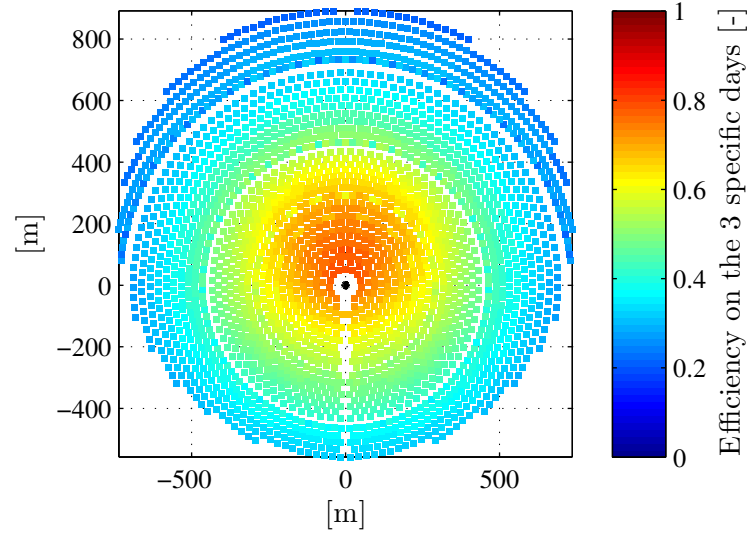


Figure 3.8 – Calculated efficiency for Gemasolar-like heliostats over the three specific days.

for the furthest heliostats and the maximum up to 80% for the closest ones. Nevertheless, as introduced previously, these values are not necessarily representative of the annual average conditions, but of two extrema and one middle in order to interpolate the performance over the entire year (see §3.5).

This way the efficiency of the heliostat field $\varepsilon_{Field}(t)$ is calculated (eq. 3.8) for the positions of the sun that correspond to the intersections between the equinox and solstice lines and the hourly lines (see 2.2). Its graphical representation against the solar azimuth and elevation angles is given in Figure 3.9. The field efficiency ranges from a minimum of 21.5% in the morning/evening of the spring equinox, up to a maximum of 50.3% at noon on the summer solstice. Besides, within a window spanning the azimuth -90° to 90° and the elevation 30° to 80° , where most of the DNI cumulation occurs, the efficiency remains above 0.45. This level is low but acceptable in comparison for instance with the overall thermal efficiency of conventional parabolic trough collectors [Kalogirou, 2009].

Subsequently, the solar input, the losses and the electric output are cumulated on the three specific days to obtain a first estimate of the overall energy performance of the entire solar tower plant. Figure 3.10 shows the Sankey diagram of losses for the Gemasolar-like plant, as a cascade of losses pictured by arrows going out of the system. The ingoing arrow represents the cumulated DNI incident on the heliostat field, while the final total electric output appears at the end of the cascade. The dotted line separates the two successive phases of the energy conversion: first the conversion of solar radiation into heat performed by the heliostat field and the central receiver, second the conversion of heat into electricity performed by the PCU. During the first phase, the cosine and the spillage are the highest losses, both greater than 10% of the solar input, respectively 23% and 16.5%. On the one hand the cosine losses are inherent and inevitable as explained in §3.1, and on the other hand the spillage losses might

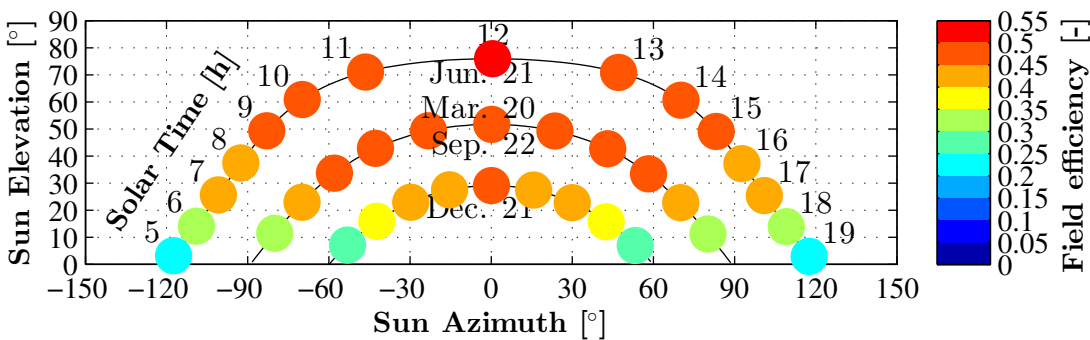


Figure 3.9 – Calculated field efficiency for the Gemasolar-like layout over the three specific days.

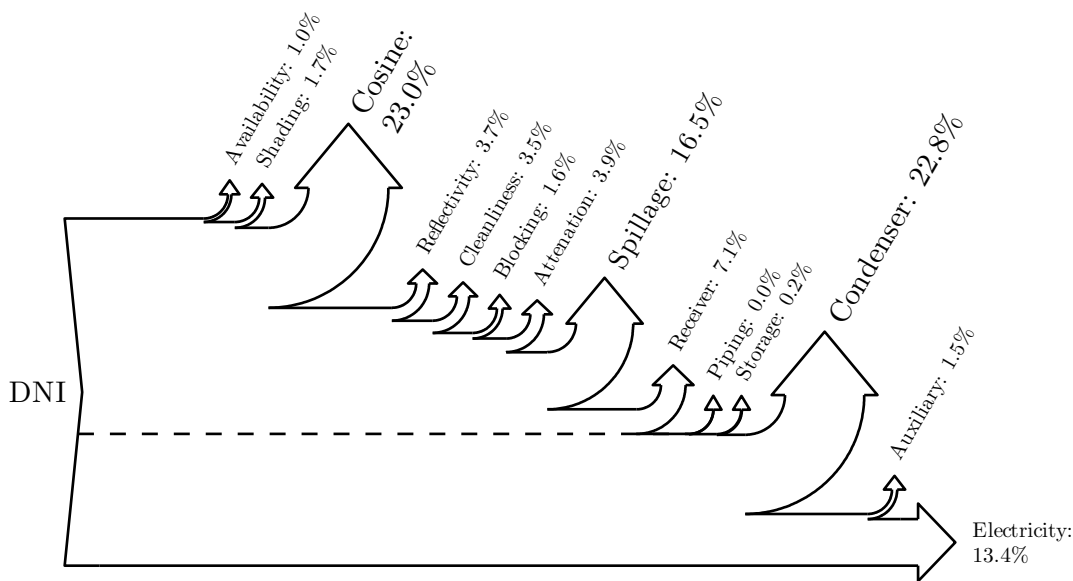


Figure 3.10 – Plant Sankey diagram of losses for the Gemasolar-like layout over the three specific days (graphic tool from [Spelling et al., 2011]).

be kept lower with a bigger receiver and more accurate heliostats. Then the receiver losses reach an important share of 7.1%, while the other losses remain below 5%. During the second phase, the cycle clearly features the highest losses with a share of 22.8%, because of the heat being released to the environment through the cooling system of the conversion cycle. In the end, the cumulated electric output of the plant reaches 13.4% of the cumulated incident solar radiation, which is defined as the solar-to-electric efficiency.

3.5 Annual Interpolation

In order to assess the plant on the entire year, the efficiency of the heliostat field is interpolated based on the calculations performed previously over the three specific days. First of all, the

field efficiency is considered as being a two-dimensional function of the azimuth and the elevation of the sun, if all other parameters are fixed. The output value of this function is known for the hourly positions on the three specific days, which form the boundaries and the centerline of a curved two-dimensional grid. Then for each hourly time step of the year, the field efficiency is interpolated between the N known points according to an embedded numerical method [MathWorks, 2011], for the current sun position (az, el) :

$$\varepsilon_{Field}(t) = f(az(t), el(t)) \quad (3.14)$$

where

$$f : (az, el) \mapsto \text{interpolation} \left(\begin{bmatrix} az_1 \\ az_2 \\ \vdots \\ az_N \end{bmatrix}, \begin{bmatrix} el_1 \\ el_2 \\ \vdots \\ el_N \end{bmatrix}, \begin{bmatrix} \varepsilon_{Field1} \\ \varepsilon_{Field2} \\ \vdots \\ \varepsilon_{FieldN} \end{bmatrix}, az, el \right)$$

As a result, the interpolation divides the calculation time by 80, and its overall relative error compared to the direct calculation remains below 1%. The interpolated field efficiency against the sun position is shown in Figure 3.11 by the smaller markers, along the hourly lines between the values obtained on the three specific days (larger markers). The maximum efficiency is still reached by the known calculated value at noon on the summer solstice, nevertheless this might not be the case depending on the field layout: in order to better spread the high efficiencies over time, the best value could also appear around the equinox for other layouts, such as Solar One. Moreover, the interpolated efficiencies reveal more clearly the efficiency window above 0.45 described in §3.4, from azimuth -90° to 90° , and elevation 30° to 80° .

Subsequently, the estimate of the heliostat field efficiency over the entire year allows the prediction of the annual power profile according to the storage strategy presented in §3.3. The power profile of the Gemasolar-like plant is shown in Figure 3.12 against the 8760 hours of the year along the x-axis. The level of the receiver incident power follows the seasonal trends, about 10% higher in the summer than in the winter. In parallel, the conversion cycle

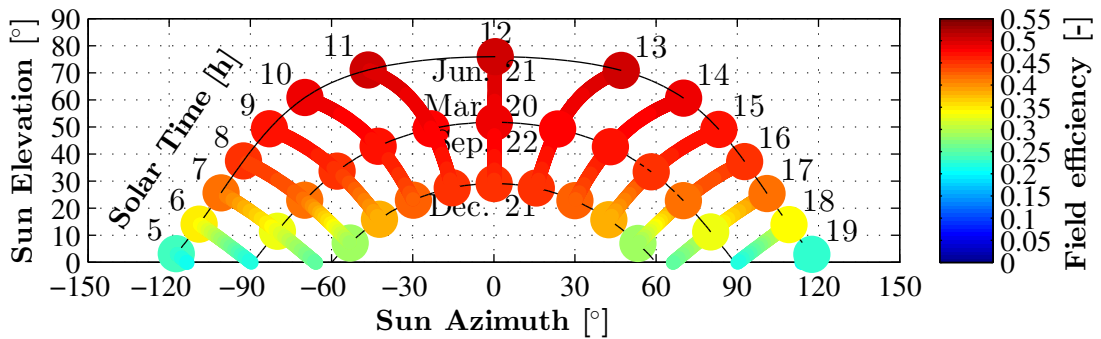


Figure 3.11 – Interpolated field efficiency for the Gemasolar-like layout over the entire year.

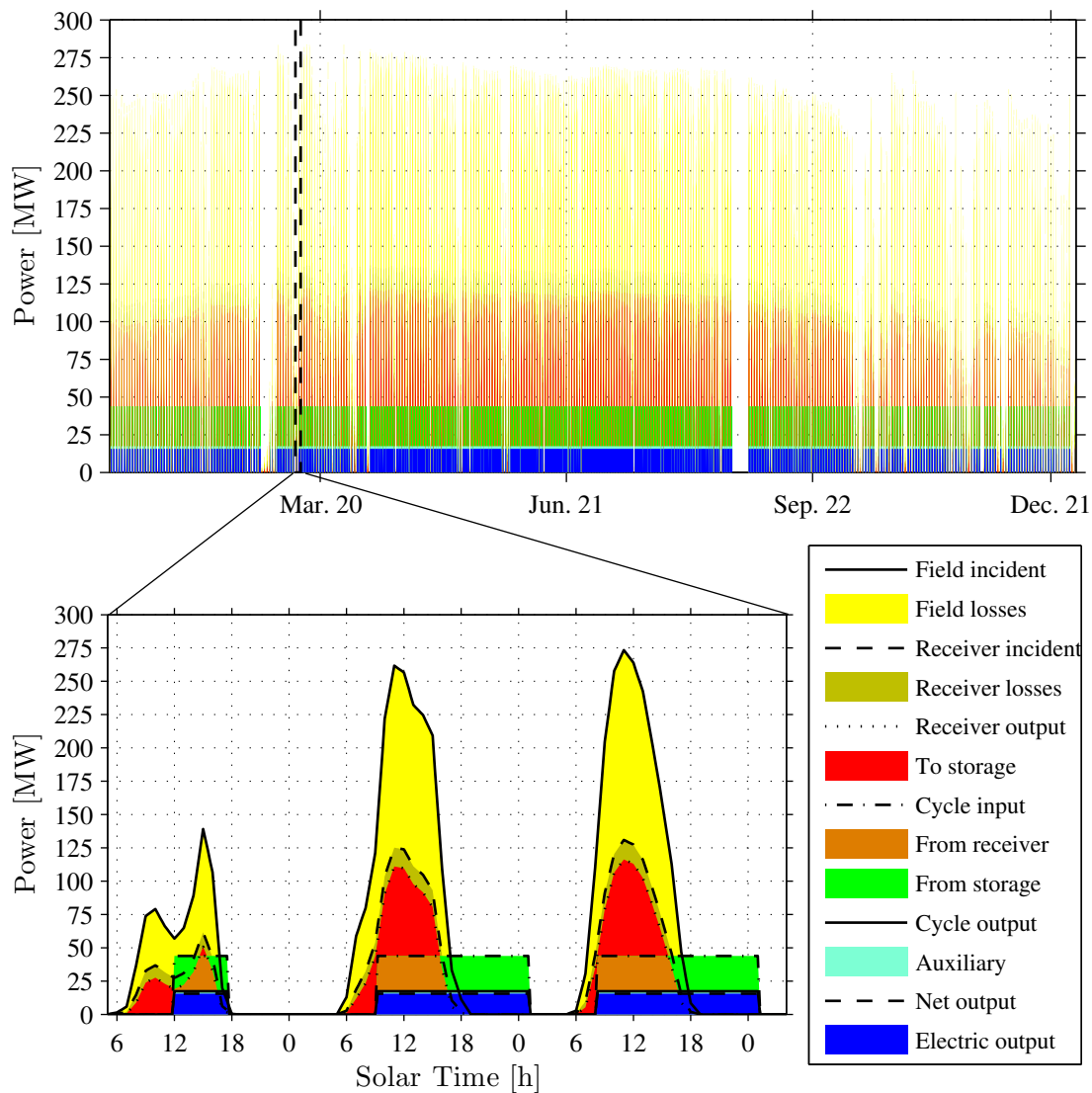


Figure 3.12 – Annual power profile for the Gemasolar-like plant, and an example of three different days close to March 20th.

obviously remains at its nominal level when turned on, but more frequently in the summer than in the winter, as indicated by the spacing between blue bars. Three different days are then picked close to the spring equinox as an example of the plant behaviour over time. The first day pictures a bad day where the receiver output never exceeds the cycle input requirement (except at a very short moment). Hence the criterion used to start the cycle is the storage capacity criterion, which only operates as the specified storage length is reached. This way the plant has an electric output over 6 hours although the solar radiation is not perfect, whereas the receiver criterion would never start the cycle under these bad conditions. The second day shows a much better DNI input, but still not perfect, especially in the morning where the receiver output reaches the startup level slightly after 9:00 ST only. Later on, the radiation

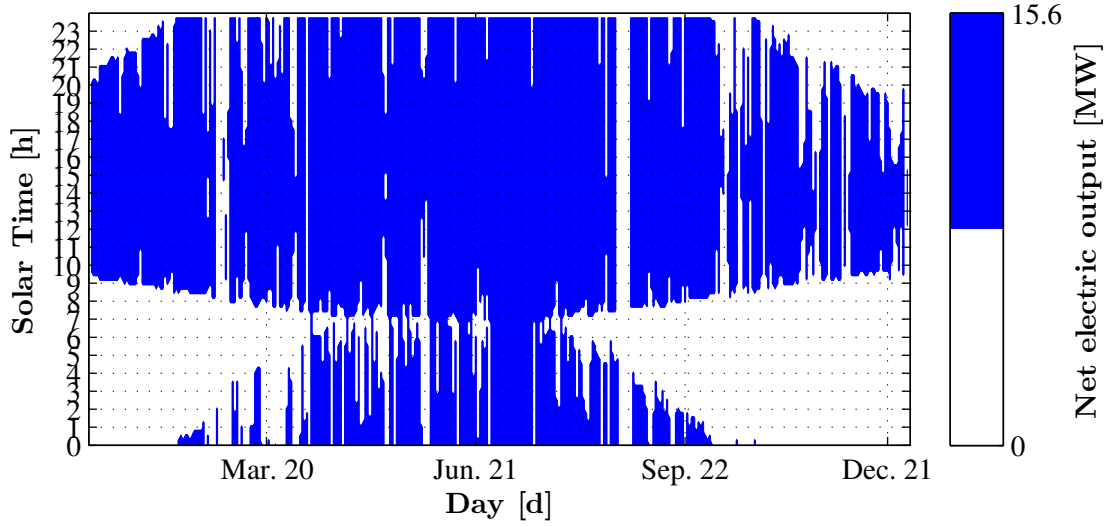


Figure 3.13 – Time map of the electric output for the Gemasolar-like plant, graphic from.

drop around 13:00 ST decreases the amount of thermal energy stored, and the operation period is limited to 14 hours, with a shutdown at 1:00 overnight. The third day has a nearly perfect DNI input, which allows a cycle startup at 8:00 ST and a longer operation period of 15 hours. Nevertheless, none of these three days performs 24 hours of operation, due to spring conditions.

Based on the knowledge of the calculated power profile of the plant, the annual time map of the electric output is presented in Figure 3.13 as blue areas against the days along the x-axis and the solar time along the y-axis (the same way as DNI in Figure 2.1). The lower and upper limits of these areas give in general the cycle startups and shutdowns respectively. From February, the storage allows the cycle to operate until the next day early in the morning, and then progressively later and later towards the summer. During spring, some days appear where the plant is able to operate 24 hours without interruption, but only for two or three days in a row. After the summer solstice, a longer uninterrupted period appears, during about three weeks in July, and the operating periods start decreasing again towards autumn. In comparison with the DNI potential which is vertically symmetric of axis 12:00 ST, the overall electric output is obviously shifted towards the evening, with a pseudo-axis of symmetry at 15:00 ST. Besides, the ratio of the total blue area to the total area of the time map provides the plant annual *capacity factor* CF, which corresponds to the time share of operation over the entire year. In the Gemasolar-like example, the annual capacity factor reaches 64%, that is about 5600 full-load hours (pure solar, without natural gas hybridisation).

$$CF = \frac{\sum_{t=0}^{8760} \dot{E}_{PCU,Out}(t) \Delta t}{\dot{E}_{PCU,nom}} \quad (3.15)$$

Chapter 3. Energy Performance

Finally, the overall annual energy performance of the plant is given by the cumulation over the entire year of the instantaneous power rates multiplied by the time steps (see Table 3.2). First, the annual incident solar energy is provided by the sum of the DNI multiplied by the total field reflective area, and the annual field output is given by the sum of the receiver incident heat rate multiplied by the time step. The field annual efficiency is obtained with the ratio of these two values, 0.4534 in the Gemasolar-like case:

$$\varepsilon_{Field,an} = \frac{\sum_{t=0}^{8760} \dot{Q}_{Rec,Inc}(t)\Delta t}{\sum_{t=0}^{8760} DNI(t)N_{Hel}A_{Ref}\Delta t} \quad (3.16)$$

Second, the receiver annual output is calculated in the same way and provides the annual receiver efficiency as well, reaching 0.8428. At the same time, the maximum receiver output rate is extracted: 123.2 [MW_{th}], which is confirmed by the Gemasolar specifications (120 [MW_{th}] [Burgaleta et al., 2011]).

$$\varepsilon_{Rec,an} = \frac{\sum_{t=0}^{8760} \dot{Q}_{Rec,Out}(t)\Delta t}{\sum_{t=0}^{8760} \dot{Q}_{Rec,Inc}(t)\Delta t} \quad (3.17)$$

Third, the sum of the electric power rate profile according to Figures 3.12 and 3.13 gives an annual electric output of the plant of 87.46 [GWh_{el}] (88 [GWh_{el}] in the specifications). Thus the *solar-to-electric* efficiency $\varepsilon_{Plant,an}$ is obtained by dividing it by the annual solar energy calculated previously, which leads to 0.1376 for the Gemasolar-like plant.

$$\varepsilon_{PCU,an} = \frac{\sum_{t=0}^{8760} \dot{E}_{PCU,Out}(t)\Delta t}{\sum_{t=0}^{8760} \dot{Q}_{Rec,Out}(t)\Delta t} \quad (3.18)$$

$$\varepsilon_{Plant,an} = \frac{\sum_{t=0}^{8760} \dot{E}_{PCU,Out}(t)\Delta t}{\sum_{t=0}^{8760} DNI(t)N_{Hel}A_{Ref}\Delta t} \quad (3.19)$$

Moreover, the number of operation periods is kept below an annual average of one per day, with 306 startups and shutdowns.

Table 3.2 – Calculated annual energy performances of the Gemasolar-like plant.

| <i>Annual energy performance</i> | <i>Value</i> | <i>Unit</i> |
|----------------------------------|-----------------|------------------------------------------------|
| Solar incident | 635.56 (283.76) | [GWh _{th}] ([MW _{th,max}]) |
| Field efficiency | 0.4534 | [-] |
| Receiver incident | 288.15 (138.15) | [GWh _{th}] ([MW _{th,max}]) |
| Receiver efficiency | 0.8428 | [-] |
| Receiver output | 245.82 (123.2) | [GWh _{th}] ([MW _{th,max}]) |
| PCU efficiency | 0.3558 | [-] |
| Net electric output | 87.46 (15.61) | [GWh _{el}] ([MW _{el,nom}]) |
| Plant efficiency | 0.1376 | [-] |
| Plant capacity factor | 0.6395 | [-] |
| Plant full-load hours | 5602 | [h] |
| Plant startups/shutdowns | 306 | [#] |

3.6 Summary

The energy performance of a solar tower power plant is assessed by modelling the main elements that perform the conversion from solar radiation to electric power: the heliostat field, the central receiver and the power conversion unit. First, the efficiency of the heliostat field is calculated from the successive losses occurring for each heliostat: shading, cosine, reflectivity and cleanliness, blocking, atmospheric attenuation and spillage. Second, the efficiency of the central receiver is estimated thanks to measurements [Pacheco, 2002] in the case of molten salt as heat transfer fluid. Third, the performance of the power conversion unit is obtained by applying heat loss factors for the piping, storage and auxiliary systems, by implementing a specific strategy for the plant operation over time, and assuming a nominal cycle efficiency as a function of the nominal thermal cycle input.

Subsequently, the plant operation is simulated over three perfect specific days: the spring equinox, and the summer and winter solstices. This allows the hourly interpolation of the heliostat field efficiency on the entire year, and the calculation of the annual receiver and PCU outputs. In the case of Gemasolar, a field efficiency of 45.3% is obtained and a solar-to-electricity efficiency of 13.8% with 5'602 full-load hours. Furthermore, multiple startups and shutdowns on the same day are avoided thanks to the applied strategy.

Once the overall plant performance is assessed, the heat flux distribution on the central receiver is investigated more in detail in the next chapter to identify critical conditions.

4 Receiver Incident Flux

In this chapter, the heat flux distribution on the receiver surface is simulated in order to identify the flux peak, the flux gradient and the flux transients. First, the calculation method is presented and an example is given for the flux distribution of a single heliostat. Second, the study of the flux transients caused by cloud passing over the field is proposed, as well as a strategy to avoid the worst transients. Third, two strategies of multi-aiming on the receiver are presented and implemented, that allow the flux peaks and gradients to be decreased significantly without increasing the spillage losses more than a few percent.

4.1 Flux Distribution on the Receiver

The flux distribution on the central receiver of a solar tower power plant is defined by the incident energy rate in $[\text{W}/\text{m}^2]$ on the receiver surface from all directions. The solar beam radiation is concentrated by the heliostat field with a ratio that may exceed 1000 suns and may lead for instance to a flux peak beyond $1 [\text{MW}/\text{m}^2]$ with a DNI of $1000 [\text{W}/\text{m}^2]$. Besides this potentially high flux peak, the incident flux is not evenly distributed on the receiver surface and discrepancies between flux maxima and minima lead to thermal stresses. In the case of a cylindrical external receiver surrounded by a heliostat field extended to the north (in the northern hemisphere), at noon the maximum fluxes are located on the north side of the receiver and the minimum fluxes on the south side. In practice for steam cycle receivers the high-flux areas are allocated to boiling or superheating of the steam while the low-flux receiver areas are allocated to preheating.

In order to calculate the instantaneous flux distribution incident on the receiver, the entire optical loss cascade between the solar beam incident on the heliostat field and the concentrated beam on the receiver surface is taken into account (see Chapter 3). The two main calculation methods are described in §3.1, and in this thesis the convolution-based method is used. It takes a series of three successive distributions into consideration: the sun shape σ_{Sun} , the heliostat slope error σ_{Slope} , and the heliostat tracking error σ_{Track} (see §2.5). The sun shape distribution incident on the field is assumed to be a circular gaussian shape with the given

Chapter 4. Receiver Incident Flux

standard deviation σ_{Sun} of 2.51 [mrad]. The Kuiper sun shape [Biggs and Vittitoe, 1979] usually better matches the measured distribution, but is left aside here for the sake of simplicity.

Now the successive convolutions of these three circular gaussian distributions lead to the analytic function described by [Collado et al., 1986], which also takes into account the successive geometrical rotations and projections of the heliostat plane and the receiver plane. By combining it with the optical loss cascade and considering a single heliostat i at time t , it results in the instantaneous flux distribution $F^i(x, y)$ incident onto the receiver plane with coordinates x and y :

$$\begin{aligned}
 F^i(x, y) = & \frac{\cos \omega_{Hel}^i \cos \omega_{Rec}^i}{(1 - \cos \omega_{Hel}^i)^2} \cdot \text{DNI}(t) \cdot \dots \\
 & \dots \cdot \varepsilon_{Avail}^i(t) \cdot \varepsilon_{Shad}^i(t) \cdot \varepsilon_{Cos}^i(t) \cdot \varepsilon_{RefI}^i(t) \cdot \varepsilon_{Clean}^i(t) \cdot \varepsilon_{Block}^i(t) \cdot \varepsilon_{Atten}^i(t) \cdot \dots \\
 & \dots \cdot \frac{1}{2} \left\{ \text{erf}(\xi + W_{Hel}'') - \text{erf}(\xi - W_{Hel}'') \right\} \cdot \dots \\
 & \dots \cdot \frac{1}{2} \left\{ \text{erf}(\eta + H_{Hel}'') - \text{erf}(\eta - H_{Hel}'') \right\}
 \end{aligned} \tag{4.1}$$

where ω_{Hel} and the ω_{Rec} are the angles of incidence respectively on the heliostat and on the receiver as described in §2.5, and erf is the error function known as:

$$\text{erf}(x) = \frac{2}{\sqrt{\pi}} \int_0^x e^{-t^2} dt \tag{4.2}$$

ξ and η are the heliostat coordinates transformed and corrected by the standard deviation σ_{Rec} (eq. 3.3) of the reflected rays in the receiver image plane:

$$\begin{aligned}
 \xi &= \frac{x'}{\sqrt{2}\sigma_{Rec}} & x' &= x \cos(\theta - \tau) + y \sin(\theta - \tau) \\
 \eta &= \frac{y'}{\sqrt{2}\sigma_{Rec}} & y' &= -x \sin(\theta - \tau) + y \cos(\theta - \tau)
 \end{aligned} \tag{4.3}$$

W_{Hel}'' and H_{Hel}'' are the heliostat dimensions also transformed in the receiver image plane and corrected by the standard deviation σ_{Rec} (see eq. 3.5). x and y are the coordinates in the receiver plane, θ and τ are the rotation angles, whose demonstration and expression is referred here to [Collado et al., 1986].

Hence for the entire heliostat field, the total receiver incident flux distribution is the result of the sum of all the individual heliostat distributions:

$$F(x, y) = \sum_{i=1}^{N_{Hel}} F^i(x, y) \tag{4.4}$$

As an example, the calculation of the flux distribution on the receiver surface is applied to

4.1. Flux Distribution on the Receiver

the case of the Gemasolar-like heliostat field with a cylindrical receiver: first, two separate heliostats are picked from the field, second the entire heliostat field is considered, and in both situations at 9:00, 12:00 and 15:00, on the spring equinox near Seville.

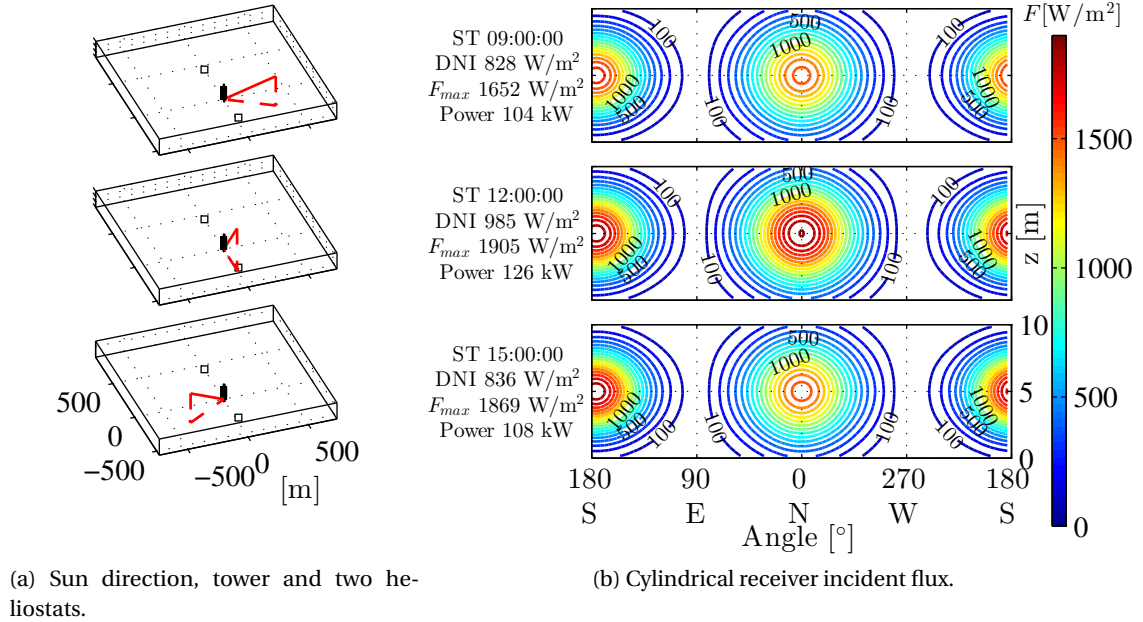


Figure 4.1 – Receiver incident flux of two heliostats picked from the Gemasolar-like field layout, on the spring equinox (March 20th) at ST 9:00, 12:00 and 15:00.

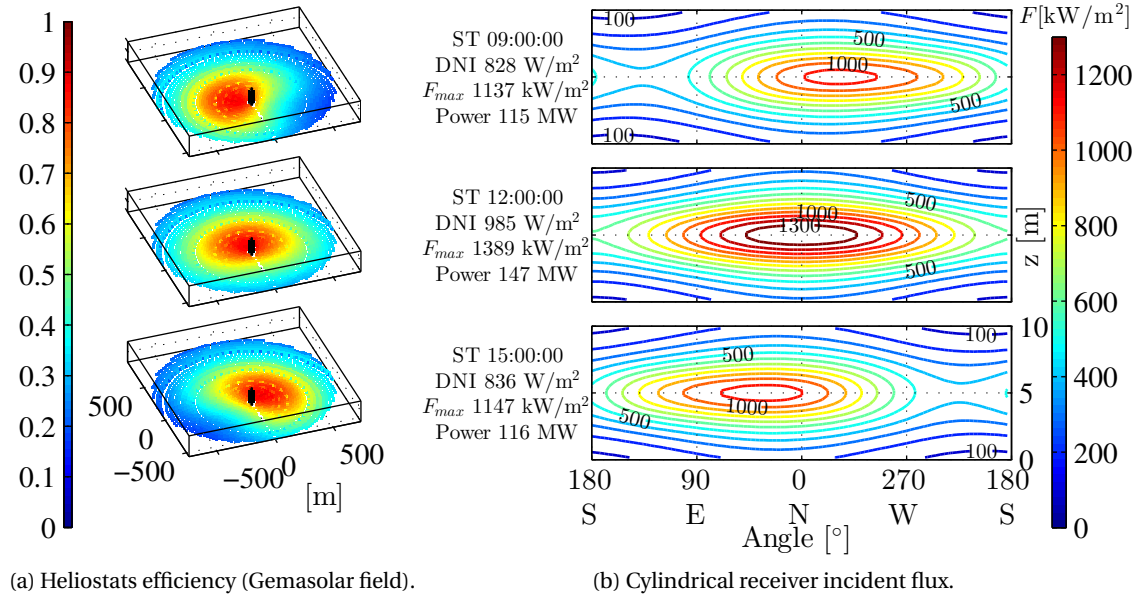


Figure 4.2 – Receiver incident flux of the Gemasolar-like field layout, on the spring equinox (March 20th) at ST 9:00, 12:00 and 15:00.

In the case of the two heliostat shown in Figure 4.1, the flux distribution is concentrated on the receiver on a smaller area than the area of the heliostat itself. As expected the shape matches an elliptic gaussian function, which is vertically slightly stretched since the first heliostat is located in a straight line from the tower towards north. The flux peak is $1.91 \text{ [kW/m}^2\text{]}$, which means a concentration ratio of 1.93:1 with respect to DNI. The flux gradient peak is $555 \text{ [W/m}^2\text{/m]}$ and the maximal incident power is 126.5 [kW] . On the other hand, the second heliostat on the south side of the field shows lower spillage losses according to the $100 \text{ [W/m}^2\text{]}$ contour line, obviously due to its smaller distance to the aim.

Considering now the entire heliostat field in Figure 4.2, the flux distribution spreads all around the receiver, with obviously less intensity on its south side than on its north side. From the morning to the afternoon, the flux peak is slightly shifted from the west side to the east side of the receiver surface, reaching $1385 \text{ [kW/m}^2\text{]}$ at noon, which corresponds to a concentration of 1410 suns. The flux gradient peak is $335 \text{ [kW/m}^2\text{/m]}$ and occurs vertically at noon, and the maximum incident power is 147 [MW] .

As the day considered in this illustration is an ideally bright day, it does not take any cloud passage into account, which is done in the following (see also [Augsburger and Favrat, 2013]).

4.2 Receiver Incident Flux Transients

During operation, the receiver materials undergo transient irradiation intensity that cause strong thermal stresses and may lead to fatigue and failure before the expected number of thermal cycles. The most common reason for incident flux transients is the intermittent passage of clouds on the heliostat field, and the available literature divides the analysis into five aspects: the modelling of clouds and their passage on the heliostat field, the control strategy of heliostats, the control strategy of the receiver and its testing, the overall plant dynamic modelling and operation strategy, and the regenerative short-term storage of heat in the primary receiver loop.

Among examples of cloud models study, a shadow model was proposed by [Aerospace, 1978] in the late seventies: a cloud was defined by its type, area, shape and velocity, and was combined with a cloud-to-cloud spacing, a probability of occurrence, and a worst case situation. Later on [Karg et al., 1982] confirmed that these characteristics largely determine the receiver incident power, and stated that increasing the mirror field can make the power station much less sensitive to changes in clouds. More recently, a methodology was proposed by [Kroyzer, 2011] to define images representative of cloud shadows in order to determine shading parameters and adjust plant operation.

Coming to the control strategy of heliostats, the detection of cloud passage by heliostats groups was presented by [Eugene Moeller et al., 1980]: after detection, heliostats were directed to standby points, and then returned to their original orientation after passage in a controlled manner. More than twenty years later, [López-Martínez et al., 2002] submitted the anticipation

of cloud presence: after computing a field cover factor, several heliostats are ordered to turn away so that the receiver temperature can decrease before the cloud covers the sun, and in that way prevent from potential rupture by thermal stress.

Moving on to the receiver control strategy and testing, the key factors for the receiver fatigue and creep characteristics were identified even earlier: for instance, [Sobin et al., 1976] investigated the design of the receiver thermal cyclic life, reaching several hundred thousand cycles. They addressed the receiver irregular shapes due to changes in expected flux by timely sensing and controlling the energy intensity. Subsequently, [McDonnell, 1978] and [Lowrie, 1979] performed tests on a pilot plant including intermittent cloud conditions to determine transient characteristics. Six years later, [Maffezzoni and Parigi, 1982] presented a dynamic analysis and control of the receiver under flux variations, and concluded that the successful operation could only be met by controlling the steam pressure instead of operating with floating steam pressure. Then in the early nineties, [Pritzkow, 1991] described the quick reaction of the receiver during simulated clouds by opening and closing an attenuator, and similarly almost twenty years later [Andrade da Costa and Lemos, 2009] established an adaptive temperature control law thanks to a shutter test.

Regarding the plant dynamic modelling and the definition of overall operation strategies taking clouds into account, some theoretical studies date back to the seventies: mathematical models and computer programs comprising time-dependent irradiation and dynamic simulation, such as affected by cloud passages, were presented by [Honeywell, 1977].

Finally, heat storage within the receiver primary loop turns out to be solving a series of problems during solar transients caused by clouds: as proposed by [Fricker, 2004] and as already demonstrated in some existing receiver facilities, a regenerative thermal storage unit can supply hot fluid until the solar irradiation returns or a controlled plant shut-down is performed.

Keeping in mind these previous studies, the present study focusses on the modelling of the incident transient flux distribution on the receiver under cloud passage. First the cloud and the characteristics of typical cloud passages are defined based upon available meteorological data. Second the receiver transient distribution is described through two cases representing the most likely occurrences for the given location. Third, a worst case situation is defined and investigated in order to provide warnings about upper limits of operation. Then a strategy for the progressive start-up or shut-down of the heliostats is proposed.

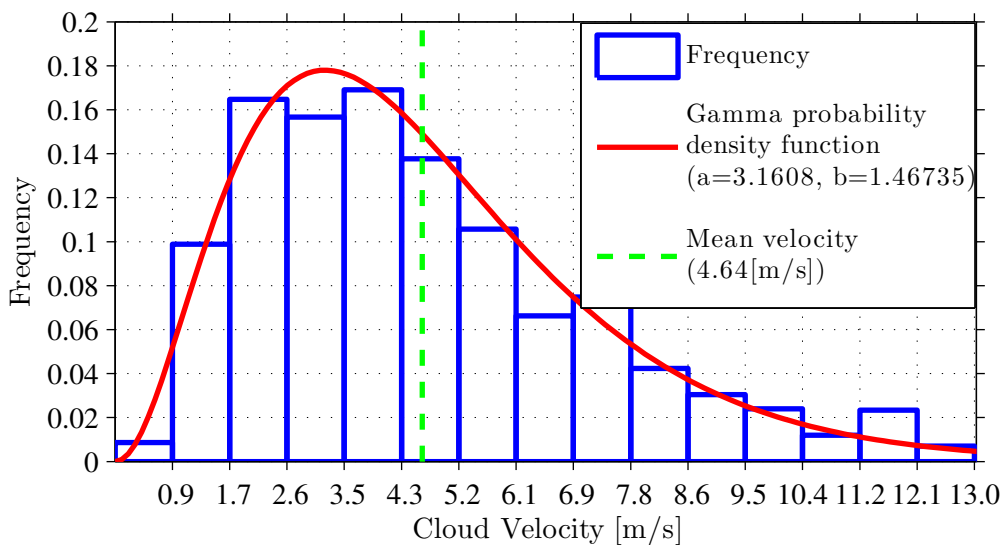
4.2.1 Cloud Passage on the Heliostat Field

Cloud passages on a heliostat field are given by the local meteorological conditions. The characterisation of the clouds is accounted for by four key parameters: cloud direction, velocity, frequency and type.

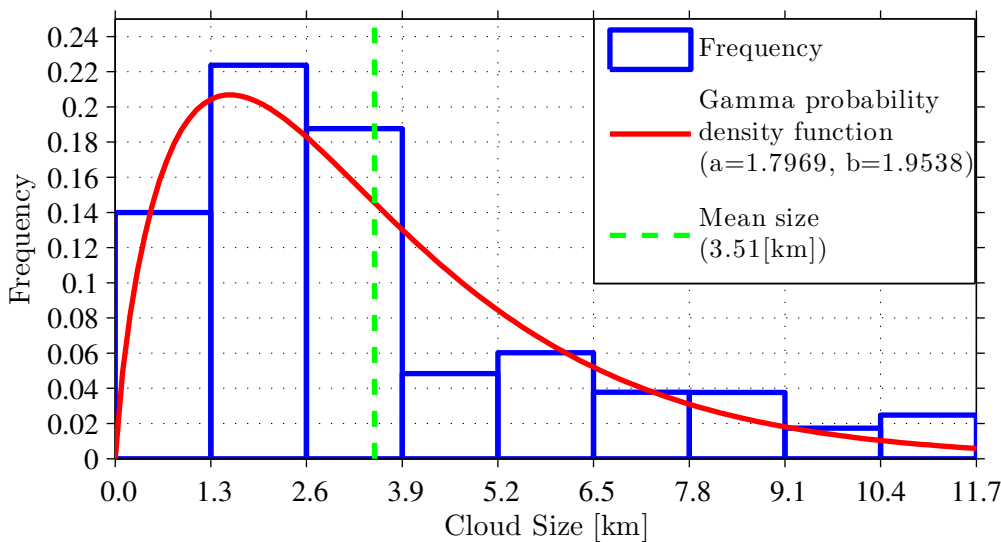
Cloud direction affects the way the heliostat field is covered (or uncovered): a cloud moving

for instance from the North first affects the northern receiver panels, and subsequently affects the southern panels, whereas another one moving from the South acts the other way around. This effect is even more so significant when the heliostat field is extended towards North (or South), as northern receiver panels undergo higher transients as southern panels.

Cloud velocity directly affects the level of transient on the receiver: for example, a slowly moving cloud at 1 [m/s] leads to relatively low transients of 1 [kW/m²/s], whereas a cloud speed of 15 [m/s] may easily lead to thermal shocks on the receiver panels if not properly



(a) Cloud velocity.



(b) Cloud size.

Figure 4.3 – Cloud frequency in Tucson, Arizona, data adapted from [Aerospace, 1978].

managed. The cloud velocity is the key factor that determines the operators ability or inability to anticipate and limit transients, either by controlling the mass flow in the receiver or by progressively switching off/on some selected heliostats in advance.

Cloud frequency affects the receiver thermal cycling on the one hand, and the overall plant operation on the other hand. High cloud frequency multiplies thermal cycles of the receiver panels and thus accelerates the process of metal fatigue, but may also lead to plant shut-down when the storage capacity does not allow overcoming repeated cloud passages.

Cloud type includes transmissivity, size, and edge shape and sharpness. The cloud transmission coefficient gives the ratio of direct radiation that still passes through the cloud: a cirrus cloud transmits more than 80% of direct radiation, while a cumulus cloud transmits less than 40% [Martínez-Chico et al., 2011]. The cloud size determines whether the heliostat field is entirely covered or not by the cloud, whereas the edge shape affects the geometrical progression of transients on the receiver panels, which is directly linked to the location of heliostats being covered first. The cloud edge sharpness may slightly affect the speed of transients: progressive edges tend to smooth transients, while sharp edges increase their speed.

The case of Tucson, Arizona, is taken here as an example of cloud characterisation by on-site observations on an eight-month period [Aerospace, 1978]. The frequency distributions of cloud velocity and cloud size are represented in Figure 4.3. The frequency of cloud velocity shows a mean value of 4.64 [m/s] and a maximum of 15 [m/s], which in practice is beyond the limit of plant operation fixed at 13 [m/s] in the case of Solar One. On the other extreme, only a few clouds (less than 1%) remain below 1 [m/s]. The frequency of cloud size gives a mean value of 3.51 [km], which is by far larger than existing heliostat fields, and a limited share of 14% of the clouds have a size below 1 [km].

Based on these observations, the focus is set on a cloud class considered as leading to the worst case of receiver flux transients: cumulus clouds with no transmittance, larger than the heliostat field, and with a straight sharp edge for the sake of convenience. A cloud shadow is thus modelled as a straight line on the ground, beyond which all heliostats are deactivated in the calculation. This front line is given a velocity and a direction matching that of the cloud, and goes across the heliostat field until all heliostats are deactivated (or activated, in case of uncovering). Figure 4.4a shows the case of a Gemasolar-like heliostat field being covered from a south-west direction at 10.3 [m/s].

The impact over short time periods of these covered heliostats on the receiver flux distribution is described in the following section.

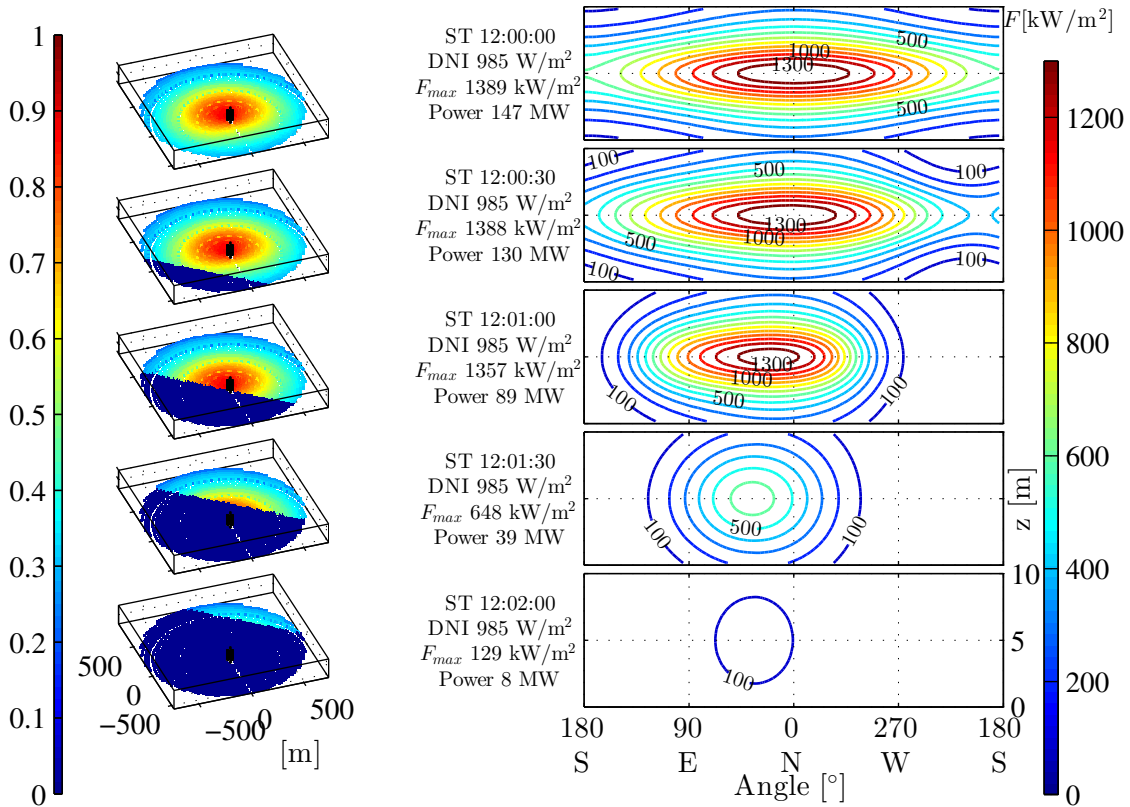
4.2.2 Transient Flux Distribution on the Receiver

A transient flux distribution on the central receiver is defined as a local intensity variation over time, here arbitrarily chosen of at least 1 [kW/m²/s], and limited to the case of cloud passage, leaving aside transients caused by sunrise and sunset. The proposed methodology to identify

some likely receiver flux transients goes through the following steps:

1. cloud direction and velocity are set at values taken from the on-site most frequent wind direction and velocity;
2. cloud type is cumulus and transmittance is set to zero;
3. cloud size is assumed to be larger than the heliostat field size;
4. cloud edges are assumed to be sharp straight lines;
5. time is fixed at noon on the spring equinox and DNI is taken from available database;
6. both covering cloud and uncovering cloud are simulated;
7. five time steps are calculated for both cases, from full activity to full cover and vice-versa in uncovering.

In the following example, the plant parameters are kept the same as Gemasolar in Table 2.2. The most frequent wind direction is taken from the Seville airport [Aviador, 2011] and is assumed to be equal to the cloud direction: more than 80% of the wind occurrences are blowing from south-west between 190° and 250° (0° is North, 90° is East), wind direction is thus set at 220° .



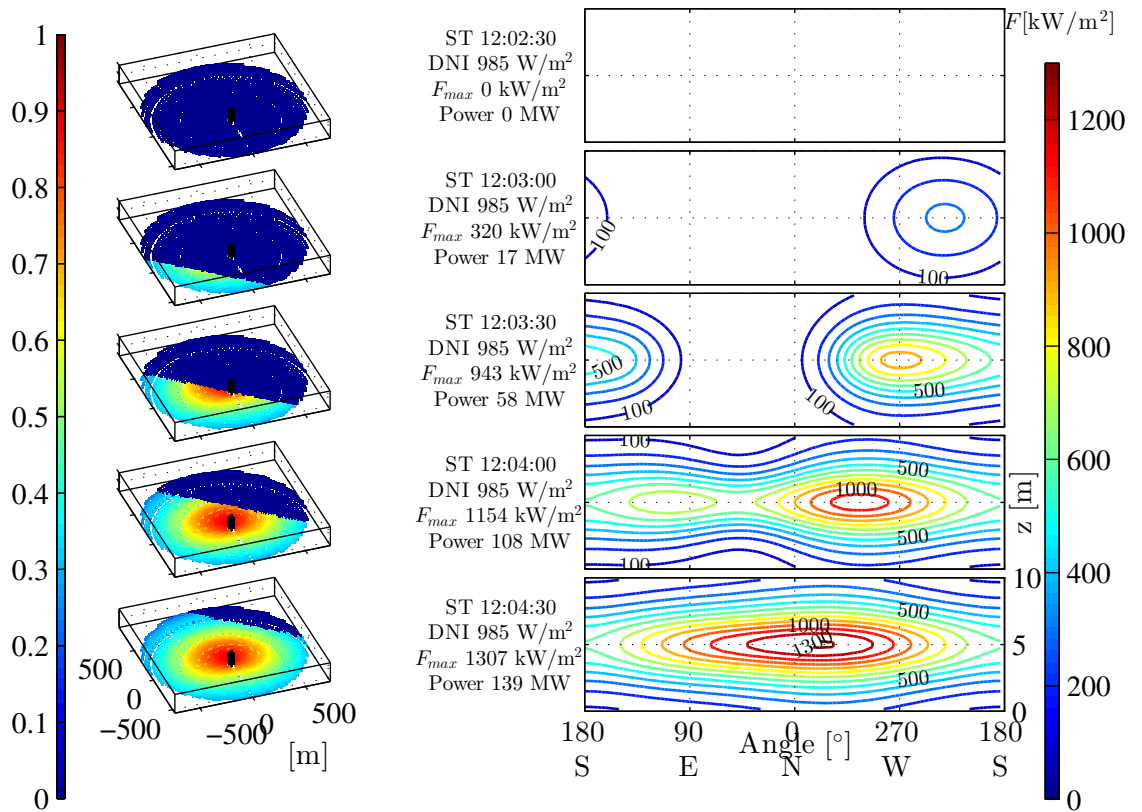
(a) Heliostats efficiency (Gemasolar field).

(b) Cylindrical receiver incident flux.

Figure 4.4 – Receiver incident flux of the Gemasolar-like field layout, on the spring equinox (March 20th), covered by a cloud from 220° at 10.3 m/s .

The most frequent wind velocity averaged on this direction range is 6.6 [m/s], and is assumed to be measured at 50 [m] height on the top of the airport control tower. Since the clouds are moving at higher altitudes in the atmosphere (cumulus clouds usually are below 2000 [m]), their velocity is approximated by applying $v(1000\text{m}) = v(50\text{m}) \cdot (1000\text{m}/50\text{m})^{0.15} \approx 10.3$ [m/s] [Pacheco, 2002]. Regarding the solar irradiation, the DNI at noon on the spring equinox (20th March) is set at 985 [W/m²], based on available data [SoDa, 2004] for the given location. Since the Gemasolar-like heliostat field is circular and 1500 [m] wide [Burgaleta et al., 2011], it is covered in less than 3 minutes. The time span is divided here into 5 steps from 0 [s] up to 120 [s] for the sake of convenience. The calculation time for one single step reaches 1.7 [s] (processor: Core i7-2620M (2.70GHz); OS: Linux Ubuntu 11.10 32-bit; Matlab: 7.13.0.564 (R2011b)), which makes the prediction possible during plant operation.

First the covering of the field is considered (Figure 4.4), then the uncovering (Figure 4.5). In covering after 30 [s], the south-west receiver panels are the first ones affected by a flux decrease, whereas the overall flux peak remains unchanged on the north panels. Then at 90 [s] the irradiation on the south-west panels fades away, and that on the north panels starts



(a) Heliostats efficiency (Gemasolar field).

(b) Cylindrical receiver incident flux.

Figure 4.5 – Receiver incident flux of the Gemasolar-like field layout, on the spring equinox (March 20th), uncovered by a cloud from 220° at 10.3 [m/s].

decreasing as well. A maximum flux transient of $29 \text{ [kW/m}^2\text{/s]}$ is achieved when the cloud shadow reaches the second field half, and is located on the north-west panels. At the same time, the flux differences rise between adjacent receiver areas: a maximum horizontal gradient of $223 \text{ [kW/m}^2\text{/m]}$ is observed between the north and west areas at 60 [s]. Concerning the total incident power, its maximum transient of 1.7 [MW/s] is achieved at half field coverage between 60 [s] and 90 [s].

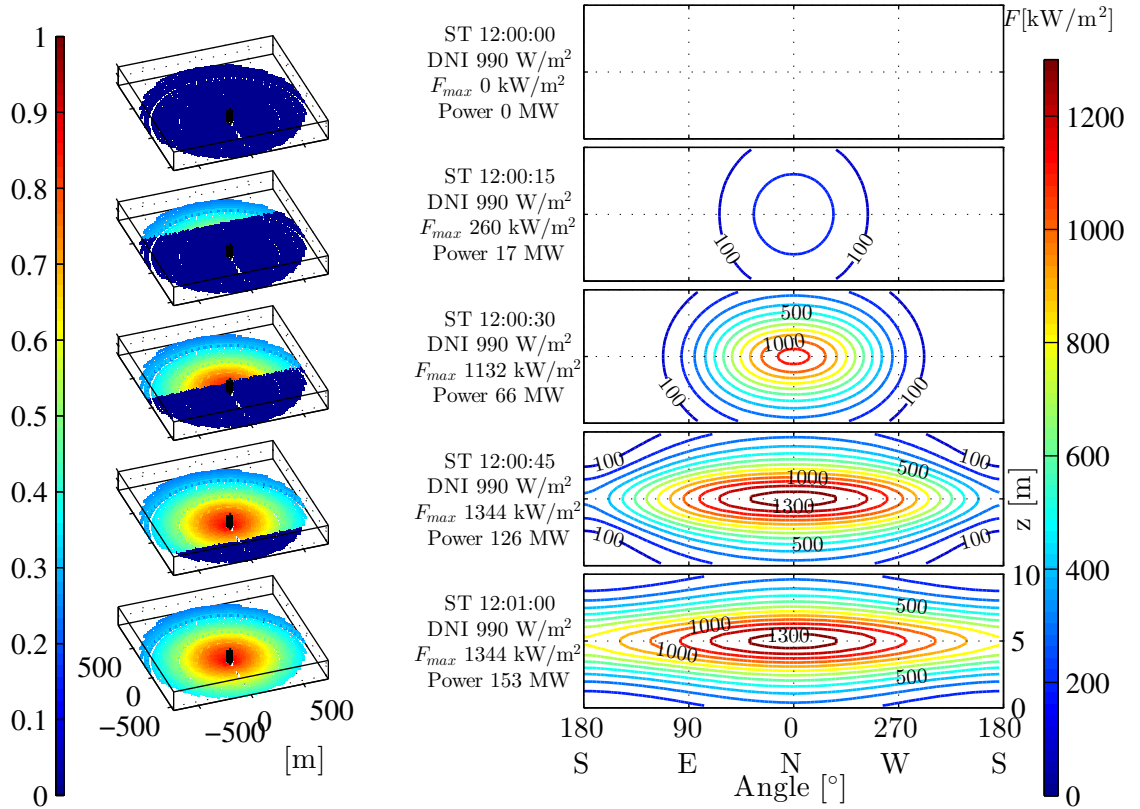
In uncovering, the evolution of the flux distribution is significantly different. After 30 [s] a first spot of $320 \text{ [kW/m}^2\text{]}$ appears on the south-west panels. The irradiation then spreads towards the north areas, with an emphasis on the west receiver side since the cloud shadow comes from south-west. Two time steps later, at 90 [s], a second spot starts appearing on the south-east panels, which leads to a maximum flux transient of $28 \text{ [kW/m}^2\text{/s]}$ between 60 [s] and 90 [s]. In the meantime, a maximum flux horizontal gradient of $235 \text{ [kW/m}^2\text{/m]}$ is reached on the north-west panels at 60 [s], while the total incident power undergoes a maximum transient of 1.6 [MW/s] after the cloud shadow uncovered one half of the field.

As these two examples only attempt to identify situations that are most likely to occur for the given plant location, they do not address cases that may lead to even shorter transients and riskier thermal stresses. Therefore a worst case definition is proposed in the following section.

4.2.3 Worst Case of Receiver Transient Flux

Ideally the transient flux worst case is defined as the situation where the flux variation in $\text{[kW/m}^2\text{/s]}$ reaches its annual maximum. Since the conditions leading to the real annual worst case are not known and randomly occurring, assumptions are made on them concerning time, DNI, cloud direction and velocity, and covering or uncovering. Time is set on the summer solstice (June 21st) at noon, in other words when the theoretical DNI is expected to reach its maximum in the northern hemisphere. Thus the highest value of DNI is picked from the available database used previously: $990 \text{ [W/m}^2\text{]}$, again at the given location in Fuentes de Andalucía. The cloud is assumed moving from the north and uncovering the heliostat field, which implies a sudden irradiation incident on the receiver - in the case where the heliostats are not shut-down previously to be then progressively reactivated (e.g. if the cloud is not much larger than the field). The cloud velocity is taken from the maximum operation wind velocity of the plant at 10 m: typical value is 12.5 [m/s] [Aerospace, 1978], which gives an approximated cloud velocity of 25 [m/s] . With this velocity the heliostat field is uncovered in 60 [s] only, therefore time steps are cut by half and range from 0 [s] to 60 [s] every 15 [s].

As the cloud shadow starts uncovering the first heliostats, a central spot immediately appears with a flux peak of $260 \text{ [kW/m}^2\text{]}$ on the north receiver face. After 60 [s], the incident irradiation spreads on both east and west sides, and as southern heliostats are progressively uncovered, the south receiver face is irradiated as well, but the irradiation remains below the northern flux peak. The maximum flux transient reaches $58 \text{ [kW/m}^2\text{/s]}$ and occurs before the cloud shadow achieves the field half distance, after which the highest power transient of 4 [MW/s] occurs



(a) Heliostats efficiency (Gemasolar field).

(b) Cylindrical receiver incident flux.

Figure 4.6 – Receiver incident flux of the Gemasolar-like field layout, on the summer solstice (June 21st), uncovered by a cloud from north at 25 [m/s].

between 30 [s] and 45 [s]. Then after 45 [s] the flux gradient hits a maximum of 327 [kW/m²/m] on the north panels, as the incident flux reaches and stabilises at a maximum of 1344 [kW/m²].

Those predictions and descriptions of extreme receiver flux transients allow anticipating and defining operation strategies: first to avoid material failures, second to avoid unnecessary shut-down and continuously operate as much as possible. On the one hand, operation strategies concern the progressive start-up or shut-down of heliostats. On the other hand, they apply to the control of devices that feed the receiver with heat transfer fluid, be it water, molten salt or air.

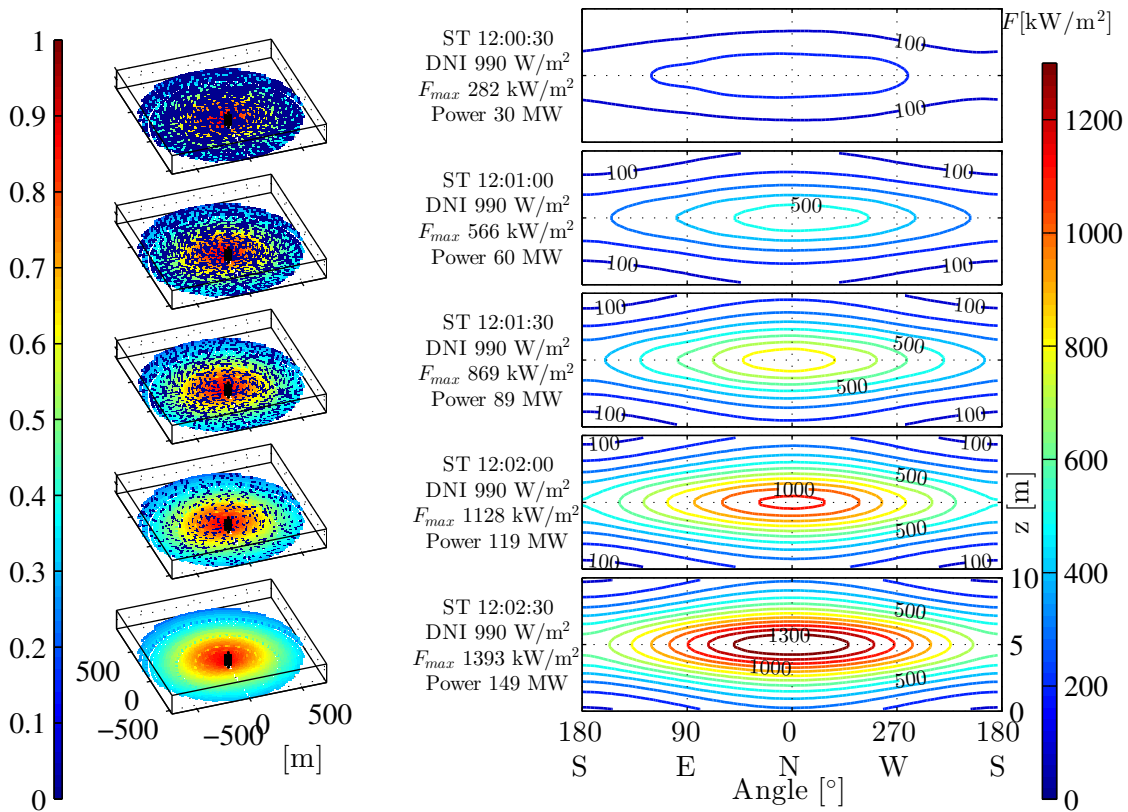
4.2.4 Strategy Proposal

A strategy is proposed for the progressive start-up/shut-down of heliostats, and its impact on the receiver transient flux distribution is described by simulation. Prior to applying the strategy, a maximum flux transient must be specified by the operator: the example here takes 10 [kW/m²/s]. This means that the progressive start-up or shut-down should occur within at

least 150 [s], which is approximately given by the ratio of the maximum flux $1389 \text{ [kW/m}^2]$ to the specified limit of $10 \text{ [kW/m}^2/\text{s}]$. Subsequently, the procedure differs between covering and uncovering clouds:

- Covering cloud:
 1. Detect the cloud at least 150 [s] before it reaches the field, which under the worst conditions corresponds to a distance of about 4 [km] ($25 \text{ [m/s]} \times 150 \text{ [s]}$) ;
 2. Shut-down the heliostats progressively at the rate of 18 per second evenly spread all over the field ($2650 / 150 \text{ [s]}$), and in parallel decrease the receiver mass flow rate.
- Uncovering cloud:
 3. Wait for the field to be uncovered entirely ;
 4. Start-up the heliostats progressively with at most the same rate of 18 per second, and in parallel increase the receiver mass flow rate.

The results of the strategy implementation are shown in Figure 4.7 for a progressive start-up after an uncovering cloud. The flux transient remains below a maximum of $10.1 \text{ [kW/m}^2/\text{s}]$,



(a) Heliostats efficiency (Gemasolar field).

(b) Cylindrical receiver incident flux.

Figure 4.7 – Receiver incident flux of the Gemasolar-like field layout, on the summer solstice (June 21st), progressive start-up at 18 heliostats per second evenly spread all over the field.

slightly higher than the fixed limit, reached between the steps 12:01:00 and 12:01:30. For all the other steps, the transient is lower than $10 \text{ [kW/m}^2/\text{s]}$. Moreover, the total incident power shows a more regular pace of 1 [MW/s] throughout the 150 [s] time span.

Regarding the progressive shut-down of the field by anticipation of a covering cloud, the opposite actuation of the start-up is applied and leads to the same results, with a reversed order of the time steps. Besides, in both cases the delay for the rotation of the heliostats has to be anticipated as well. In both cases the receiver mass flow has to be varied accordingly, in order to keep the temperature variations as low as possible.

On the one hand, the results presented can be used to anticipate cloud passage and consequences on the receiver thermal cyclic life during operation, and on the other hand, in the design phase, they are now to be implemented in larger multi-objective optimisation of solar tower power plants to eliminate configurations that would inherently lead to unmanageable transients according to the current know-how.

4.3 Multi-Aiming on the Receiver

As observed so far in general, the level of the incident heat flux over the surface of the central receiver in operation is high, far above $1 \text{ [MW/m}^2]$ at its peak. Moreover, the flux on the north panels turns out to be twice as high as that on the south panels, and the maximal vertical gradient exceeds $300 \text{ [kW/m}^2/\text{m]}$. Therefore the operator may define an aiming strategy for the heliostats, in order to decrease the flux level, better spread the distribution over the receiver height, and keep the flux gradient lower. And in parallel, the aiming strategy has to keep the spillage losses at a comparable level, so that the total incident power is affected by a few percent only. In this perspective, two different aiming strategies are proposed here, implemented, and their impact on the receiver incident flux is analysed in the case of Gemasolar.

In the conventional case, when no multi-aiming strategy is applied, all the heliostats are aiming at the same target point located on the z-axis at the middle of the receiver height. Now if a multi-aiming strategy is applied, each heliostat aims at a distinct target point along the vertical axis. The individual target points range from a lower boundary to an upper boundary located within the receiver height, and the height of this interval is defined by a ratio C_{MultiA} of the receiver height (see Figure 4.8). Then the centre of the target interval may be shifted up or down according to the original aim point, with a shift ratio C_{ShiftA} (see eq. 4.5).

The first method proposed is a distance-based multi-aiming: the z-coordinate of the target point is a linear function of the heliostat distance to the tower base. As shown in Figure 4.8, the heliostats with the minimum distance hit the lower boundary, those with the maximum distance hit the upper boundary, while all the other heliostats in between hit a target point

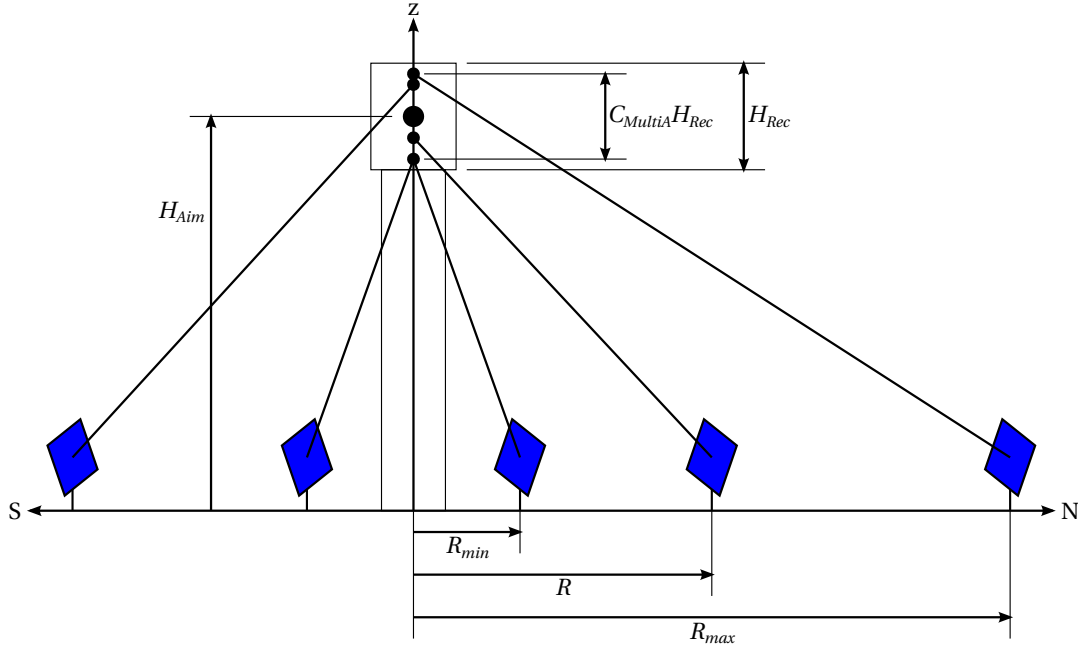


Figure 4.8 – Distance-based multi-aiming.

whose z -coordinate increases linearly with the distance:

$$z_{Aim}^i = z_{Aim} + C_{MultiA} H_{Rec} \left(\frac{1}{2} + C_{ShiftA} - \frac{R_{max} - R_i}{R_{max} - R_{min}} \right) \quad (4.5)$$

where

$$C_{MultiA} \in]0, 1[\quad , \quad C_{ShiftA} \in \left[-\frac{1}{2}, \frac{1}{2} \right] \quad (4.6)$$

The distance-based multi-aiming strategy is then implemented and applied to the Gemasolar-like heliostat field, on the spring equinox (March 20th) at ST 12:00, with DNI 985 [W/m²] (same case as in Figure 4.2). The receiver height ratio C_{MultiA} is set to 0.8 and the centre of the interval is slightly shifted with a ratio C_{ShiftA} of 0.05. The results are presented in Figure 4.10b and show a 22.4% decrease of the heat flux peak with regard to the 1389 [kW/m²], down to 1078 [kW/m²]. At the same time, the total incident power drops by 4.1% from 147 [MW] to 141 [MW], and the vertical gradient is lower on the upper receiver half, but increases from 335 [kW/m²/m] to 340 [kW/m²/m] on the lower half, which obviously is the drawback of this first method.

The second method proposed here is a deviation-based multi-aiming: the z -coordinate of the target point is a function of the standard deviation σ_{Rec}^i of the flux distribution reflected by the heliostat i , in the receiver plane. The principle of this approach is the attribution of the best concentrating heliostats to the lower and upper boundaries, while the worse concentrating heliostats aim at the centre of the interval (see Figure 4.9). In order to achieve this attribution,

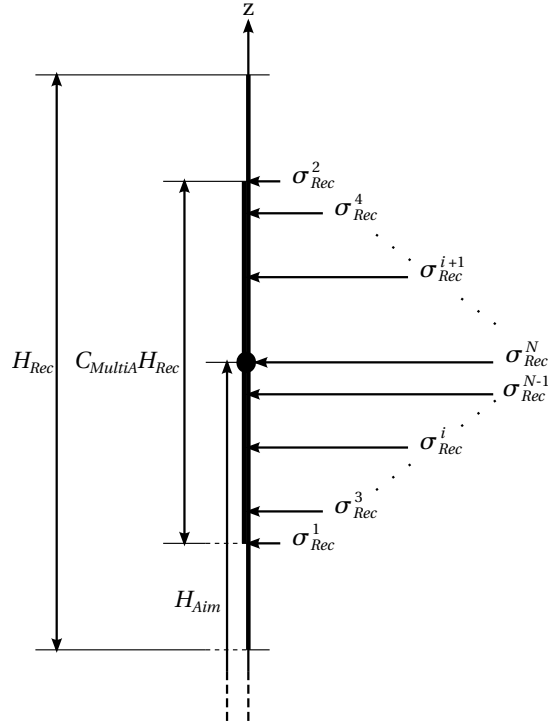


Figure 4.9 – Deviation-based multi-aiming.

the heliostats deviations are sorted out in the ascending order, which provides the variable i to the function of output z_{Aim}^i :

$$z_{Aim}^i = z_{Aim} \pm \frac{1}{2} C_{MultiA} H_{Rec} \frac{N_{Hel} - i}{N_{Hel}} \begin{cases} + & \text{if } i = 2, 4, 6, \dots \\ - & \text{if } i = 1, 3, 5, \dots \end{cases} \quad (4.7)$$

where

$$\sigma_{Rec}^1 < \sigma_{Rec}^2 < \dots < \sigma_{Rec}^i < \dots < \sigma_{Rec}^{N_{Hel}} \quad (4.8)$$

Hence the deviation-based multi-aiming strategy is also implemented in the same conditions as for the first method, and the results are shown in Figure 4.10c. The receiver height ratio is set to 0.4 and the centre of the interval is not shifted. The decrease of the heat flux peak is slightly better than that of the previous method, with a 25.8% drop to 1031 [kW/m²]. Moreover, the total incident power is only 2.1% lower than without multi-aiming, reaching 144 [MW], while the maximum vertical gradient falls by 27% to 245 [kW/m²/m].

When comparing the two multi-aiming strategies in terms of efficacy, on the one hand the distance-based strategy achieves the primary objective of decreasing the heat flux peak but misses that of lowering the maximum gradient. On the other hand, the deviation-based strategy achieves both objectives, and by affecting less the total incident power. Now in terms of feasibility, the distance-based strategy is simple to implement and the heliostats

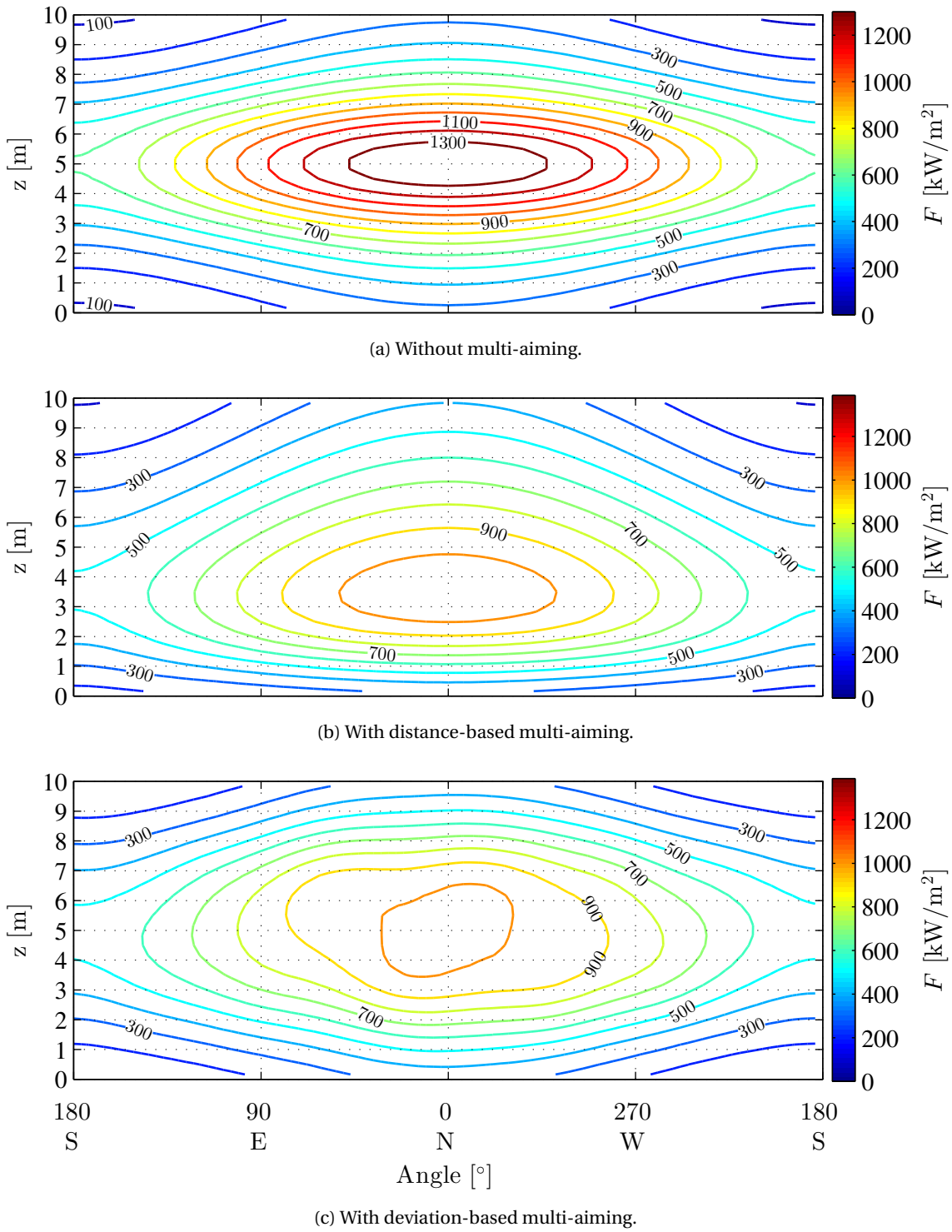


Figure 4.10 – Receiver incident flux for the Gemasolar-like field, without and with multi-aiming, on the spring equinox (March 20th) at ST 12:00.

individual targets remain the same over time, whereas the deviation-based strategy implies the continuous recalculation and sorting of the individual deviations, causing the targets to move over time.

4.4 Summary

The incident heat flux on the central receiver is calculated in order to identify critical conditions and propose operating strategies that avoid them. The receiver incident flux distribution is estimated thanks to a method allowing short computation times and programming interactivity [Collado et al., 1986]. In the example of Gemasolar, the flux peak achieves 1385 [kW/m²] with a DNI of 985 [W/m²]. Then the passage of clouds and its impact on the receiver flux transients are investigated: the most frequent case and the worst case are simulated with clouds either covering or uncovering the heliostat field. The maximum transient reaches 58 [kW/m²/s] with a power change rate of 4 [MW/s]. In order to avoid potentially damaging peaks, a transient limit is set (10 [kW/m²/s] in the example) and a strategy is proposed that prevents from exceeding this limit by progressive shutdowns (or startups) of the heliostats at the rate of 18 per second.

Besides, two distinct multi-aiming strategies are presented: distance-based and deviation-based. In the distance-based strategy, the heliostats are oriented onto different positions along the y-axis of the receiver surface based on their distance to the tower foot. Applied to Gemasolar, the distance-based strategy shows a 22.4% decrease in flux peak with a 4.1% lower total incident power. In the deviation-based strategy, the heliostats are oriented according to their calculated optical deviation from the target. In the same example, it performs better with a 25.8% drop in flux peak and only 2.1% less total power.

As the energy performance and the constraints of the receiver flux distribution are modelled, the following chapter presents now the economic performance of a solar tower plant.

5 Economic Performance

In this chapter, the costs involved by the planning, the construction and the operation of a solar tower thermal plant are investigated in order to estimate its economic performance. First, the investment costs are broken down into distinct categories of equipment, with an emphasis on the level of detail for the heliostat field, and an expression of the corresponding expenses is presented. Based on the reference cases from the literature, the cost breakdown and the investment costs of the Gemasolar plant are estimated as an example. Second, specific financial indicators are proposed to set up the project funding, and assess its financial viability and the cumulated incomes over the entire plant lifetime.

5.1 Investment Costs

The estimate of the plant investment costs is required to identify the main cost drivers and thus the potential improvements to bring them down. By breaking down the plant equipment into distinct cost categories, a detailed cost analysis is presented especially for the heliostat field, whose share is expected to be the highest. Then a set of cost functions is proposed for the receiver and the tower on the one hand, and the power conversion unit on the other hand.

5.1.1 Heliostat Field

The investment costs of the heliostat field include the land costs on the one hand, and the heliostat costs on the other hand.

Land

The land costs are divided into the investment cost $I_{Terrain}$ of purchasing the terrain, and the cost of land improvements I_{Improv} such as levelling, roads, civil works in general. As in general the appropriate lands for a solar plant are situated far away from populated areas and widely available, their specific cost $c_{Terrain}$ is expected to remain low, or even non-existent

under certain conditions given by the local authorities. In the literature, the cost per square meter may range from 0.5 [\$/m²] up to 2.18 [\$/m²] for instance [Sargent & Lundy, 2003, Kistler, 1986, Pitz-Paal et al., 2005]. Then the cost of the land improvements is assumed to be a function of the land area with a scaling factor $s_{Improv} = 0.3687$ according to a reference case of area $A_{Terrain}^0 = 2.8$ [km²] and cost $I_{Improv}^0 = 1.1$ [M\$] [Sargent & Lundy, 2003]. Hence the overall land costs are expressed as the following:

$$I_{Land} = I_{Terrain} + I_{Improv} \quad (5.1)$$

where

$$I_{Terrain} = c_{Terrain} A_{Terrain}$$

$$I_{Improv} = I_{Improv}^0 \left(\frac{A_{Terrain}}{A_{Terrain}^0} \right)^{s_{Improv}}$$

with

$$c_{Terrain} = 0.5 \text{ [$/m}^2\text{]} \quad I_{Improv}^0 = 1.1 \text{ [M$]}$$

$$A_{Terrain}^0 = 2.8 \text{ [km}^2\text{]} \quad s_{Improv} = 0.3687 \text{ [-]}$$

By implementing the land area $A_{Terrain} = 1.7$ [km²] of Gemasolar, it results in the terrain cost $I_{Terrain} = 1$ [M\$] and the land improvement cost $I_{Improvement} = 3.3$ [M\$].

Heliostats

Subsequently, the heliostat costs break down into direct costs, optical improvement costs, overhead costs and indirect costs:

$$I_{Hel} = I_{Hel,Dir} + I_{Hel,Optic} + I_{Hel,OverH} + I_{Hel,Indir} \quad (5.2)$$

First of all, the direct heliostat costs include the parts and materials such as the support structure, the drives and the mirrors, and take the labour costs into account, such as the shop fabrication and the installation (see Table 5.1). Each one of these direct costs is estimated from a reference specific cost in [\$/u] for one heliostat, multiplied by three cost effects: a scaling effect, a volume effect and a price index (see eq. 5.3).

The scaling effect is a measure of the economy of scale when increasing the heliostat area: it is given by the ratio of the current size A_{Hel} to the reference size A_{Hel}^0 , with the scaling factor s as exponent. This scaling factor is estimated by interpolating the costs provided in the literature for different sizes [Kolb et al., 2007] and presented in Table 5.1 for each sub-cost.

The volume effect is a measure of the economy occurring with a large volume of production: it

follows here the approach of the progress ratio pr , with in exponent the binary logarithm of the current volume V_{Hel} divided by the reference $V_{Hel}^0 = 1625$ [u] [Kolb et al., 2007]. This approach is an estimate of the cost improvement that occurs for each doubling of the production volume. The progress ratio for each heliostat sub-cost is directly taken from the literature [Sargent & Lundy, 2003] and presented in the same table.

The price index is a measure of the price changes from the reference year until today (here 2011): several sources nowadays provide a detailed production price index (PPI) for a large set of materials, parts and services [CHE, 2011, BLS, 2011]. Hence the price indices are estimated by looking for the matching PPI category of each heliostat sub-cost, e.g. in the North American Industry Classification System (NAICS).

As a result, the heliostat direct cost $I_{Hel,Dir}$ is expressed as the sum of the estimated specific sub-costs multiplied by the number N_{Hel} of heliostats in the field:

$$I_{Hel,Dir} = N_{Hel} \sum_i \{c_{Dir}\}_i \quad (5.3)$$

where

$$\begin{aligned} c_{Dir} &= \text{reference} \times \text{scaling effect} \times \text{volume effect} \times \text{price index} \\ &= c_{Dir}^0 \times \left(\frac{A_{Hel}}{A_{Hel}^0} \right)^s \times pr^{\log_2 \frac{V_{Hel}}{V_{Hel}^0}} \times pi \end{aligned} \quad (5.4)$$

with

$$\begin{aligned} A_{Hel}^0 &= 148 \text{ [m}^2\text{]} \\ V_{Hel}^0 &= 1625 \text{ [u]} \end{aligned}$$

An estimate of the direct specific costs in the case of the Gemasolar case is shown in Table 5.3, with a production volume being equal to the number of heliostats in the field $N_{Hel} = 2650$ [u].

Second, the heliostat optical cost may also be considered as a direct cost, but is taken apart here in order to identify the economic value of the heliostat optical variables, or in other words of the standard deviation σ_{Slope} . Thus based on nine cases presented in the literature with different areas and deviations leading to distinct costs [Kolb et al., 2007], the optical specific cost is proposed in the following as a function the current slope deviation and a reference deviation $\sigma_{Slope}^0 = 4.14$ [mrad] [Pacheco, 2002], where the cost increases if the current deviation decreases:

$$I_{Hel,Optic} = N_{Hel} c_{Optic} \quad (5.5)$$

where

$$c_{Optic} = 0.01 \cdot 10^{-3} \left(\frac{1}{(\sigma_{Slope})^2} - \frac{1}{(\sigma_{Slope}^0)^2} \right) A_{Hel} \quad (5.6)$$

with

$$\sigma_{Slope}^0 = 4.14 \cdot 10^{-3} \text{ [rad]}$$

In the Gemasolar example, the heliostat deviation is taken as $\sigma_{Slope} = 2.6$ [mrad] and leads to a rather insignificant 108 \$/u optical cost, but for instance would result in a non-negligible 4'730 \$/u cost with a 0.5 [mrad] deviation.

Third, the heliostat overhead costs comprise the corporate overhead as well as the profit and the contingency costs, including both the management and the engineering oversight for the procurement of parts and the heliostat construction. In practice, the overhead costs are expressed as a ratio *or* of the direct costs, ranging from 15% to 25% in the literature. Moreover, in order to take the volume effect into account, a progress ratio pr_{OverH} is implemented with the same exponent as seen previously for the heliostats:

$$I_{Hel,OverH} = I_{Hel,Dir} \cdot or \cdot (pr_{OverH})^{\log_2 \frac{V_{Hel}}{V_{Hel}^0}} \quad (5.7)$$

If an overhead ratio of 20% and a progress ratio of 0.96 is applied to the case of Gemasolar, the heliostat overhead cost reaches 3'714 \$/u].

Fourth, the heliostat indirect costs include the engineering design, the manufacturing facilities and tooling (building lease, mirror module tooling, etc.), and the equipment lease (cranes, fork lifts, etc.). The reference indirect costs are taken from [Kolb et al., 2007], where the engineering reaches 250'000 \$], the facilities 800'000 \$], and the equipment 200'000 \$], for

Table 5.1 – Estimated direct cost parameters of a heliostat [Kolb et al., 2007, Sargent & Lundy, 2003, BLS, 2011].

| <i>Heliostat direct cost i</i> | c^0 \$/u] | s [-] | pr [-] | pi [-] |
|--------------------------------|-------------|---------|----------|----------|
| Foundation | 200 | 0.2274 | 0.9806 | 1.0816 |
| Pedestal & structure | 3'777 | 1.4700 | 0.9900 | 1.8070 |
| Drives | 6'000 | 0.6000 | 0.9400 | 1.3702 |
| Mirrors | 4'996 | 1.0420 | 0.9700 | 1.0861 |
| Control & communications | 875 | 0.2311 | 0.9600 | 1.2841 |
| Wiring | 877 | 0.4479 | 1.0000 | 1.0302 |
| Shop fabrication | 480 | 0.4264 | 0.9800 | 1.0000 |
| Installation & checkout | 450 | 0.2610 | 1.0000 | 1.0000 |
| Total reference direct costs | 17'655 | | | |

1'625 heliostats of 148 [m²]. Then the same way as for the direct costs, the three cost effects are applied separately to each one of these sub-costs. The estimate of the respective scaling factors, progress ratios and price indices is presented in Table 5.2. As a result, the total heliostat indirect cost is given by the sum of the three sub-costs:

$$I_{Hel,Indir} = \sum_j \{ I_{Indir} \}_j \quad (5.8)$$

where similarly to eq. 5.4

$$I_{Indir} = I_{Indir}^0 \cdot \left(\frac{A_{Hel}}{A_{Hel}^0} \right)^s \cdot pr^{\log_2 \frac{V_{Hel}}{V_{Hel}^0}} \cdot pi \quad (5.9)$$

In the case of Gemasolar, the estimated heliostat indirect costs are lower than the reference since the heliostat area is smaller and the volume of production is higher (see Table 5.3).

Finally, the breakdown of the estimated heliostat costs is pictured in Figure 5.1 for Gemasolar-like heliostats ($A_{Hel} = 120$ [m²], $V_{Hel} = 2650$ [u], $\sigma_{Slope} = 2.6$ [mrad]). The drives feature by far the highest costs with about 30%, while the structure and the mirrors achieve nearly 20% each. As a result, the direct costs reach 80% of the total heliostat costs. Then the cost share of the optical improvement has almost no impact with the assumed heliostat deviation, but might increase rapidly above 15% with a higher optical accuracy as shown previously. Based on the direct costs and the assumed ratio of 20%, the overhead cost slightly exceeds 15%, which is non-negligible especially if the overhead level is considered as a higher uncertainty than the other sub-costs. Besides, the share of the indirect costs remains below 4%, as the number of heliostats helps better amortising the investment of the facilities and equipment.

With the estimate of the Gemasolar case as reference, the sensitivity of heliostat cost breakdown is now estimated against the heliostat area on the one hand and the volume of production on the other hand, as presented in Figure 5.2.

The first graph shows the variation of the heliostat specific costs in [\$/m²] as a function of the heliostat area, while the volume of production is fixed at 2'650 [u]. The black vertical line highlights the breakdown for a 120 [m²] heliostat. Below 50 [m²], the total specific cost grows exponentially when the area gets smaller, especially due to the specific cost of the drives whose

Table 5.2 – Estimated indirect cost parameters of a heliostat [Kolb et al., 2007, Sargent & Lundy, 2003, BLS, 2011].

| <i>Heliostat indirect cost j</i> | c^0 [\$] | s [-] | pr [-] | pi [-] |
|------------------------------------|------------|---------|----------|----------|
| Engineering | 250'000 | 0.9551 | 0.96 | 1.2623 |
| Manufacturing facilities & tooling | 800'000 | 0.9551 | 0.86 | 1.1460 |
| Equipment lease | 200'000 | 0.9551 | 0.86 | 1.1460 |
| Total reference indirect costs | 1'250'000 | | | |

Chapter 5. Economic Performance

Table 5.3 – Estimated specific costs of a heliostat at the Gemasolar plant ($A_{Hel} = 120 \text{ [m}^2\text{]}$, $V_{Hel} = 2650 \text{ [u]}$, $\sigma_{Slope} = 2.6 \text{ [mrad]}$).

| <i>Helioestat direct costs</i> | | |
|------------------------------------|-----------|--------|
| Foundation | 203 | [\$/u] |
| Pedestal & structure | 4'979 | [\$/u] |
| Drives | 6'939 | [\$/u] |
| Mirrors | 4'268 | [\$/u] |
| Control & communications | 1'040 | [\$/u] |
| Wiring | 823 | [\$/u] |
| Shop fabrication | 433 | [\$/u] |
| Installation & checkout | 426 | [\$/u] |
| Optical improvement | 108 | [\$/u] |
| <i>Total direct cost</i> | 19'219 | [\$/u] |
| Overhead | 3'714 | [\$/u] |
| <i>Helioestat indirect costs</i> | | |
| Engineering | 250'967 | [\$] |
| Manufacturing facilities & tooling | 674'635 | [\$] |
| Equipment lease | 168'659 | [\$] |
| <i>Total indirect cost</i> | 1'094'260 | [\$] |
| <i>Total heliostat cost</i> | 23'606 | [\$/u] |

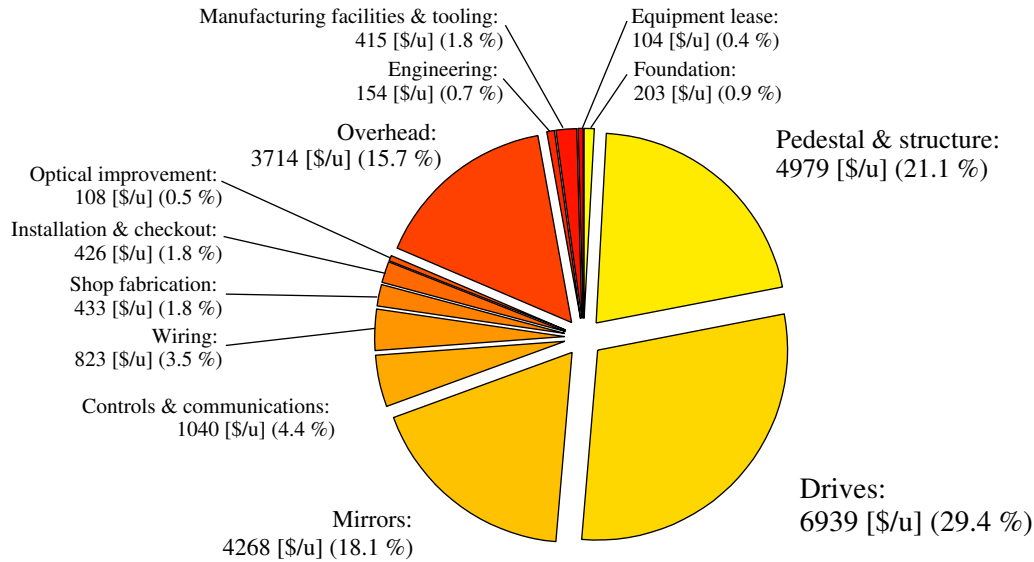


Figure 5.1 – Estimate of the heliostat cost breakdown in the Gemasolar-like case.

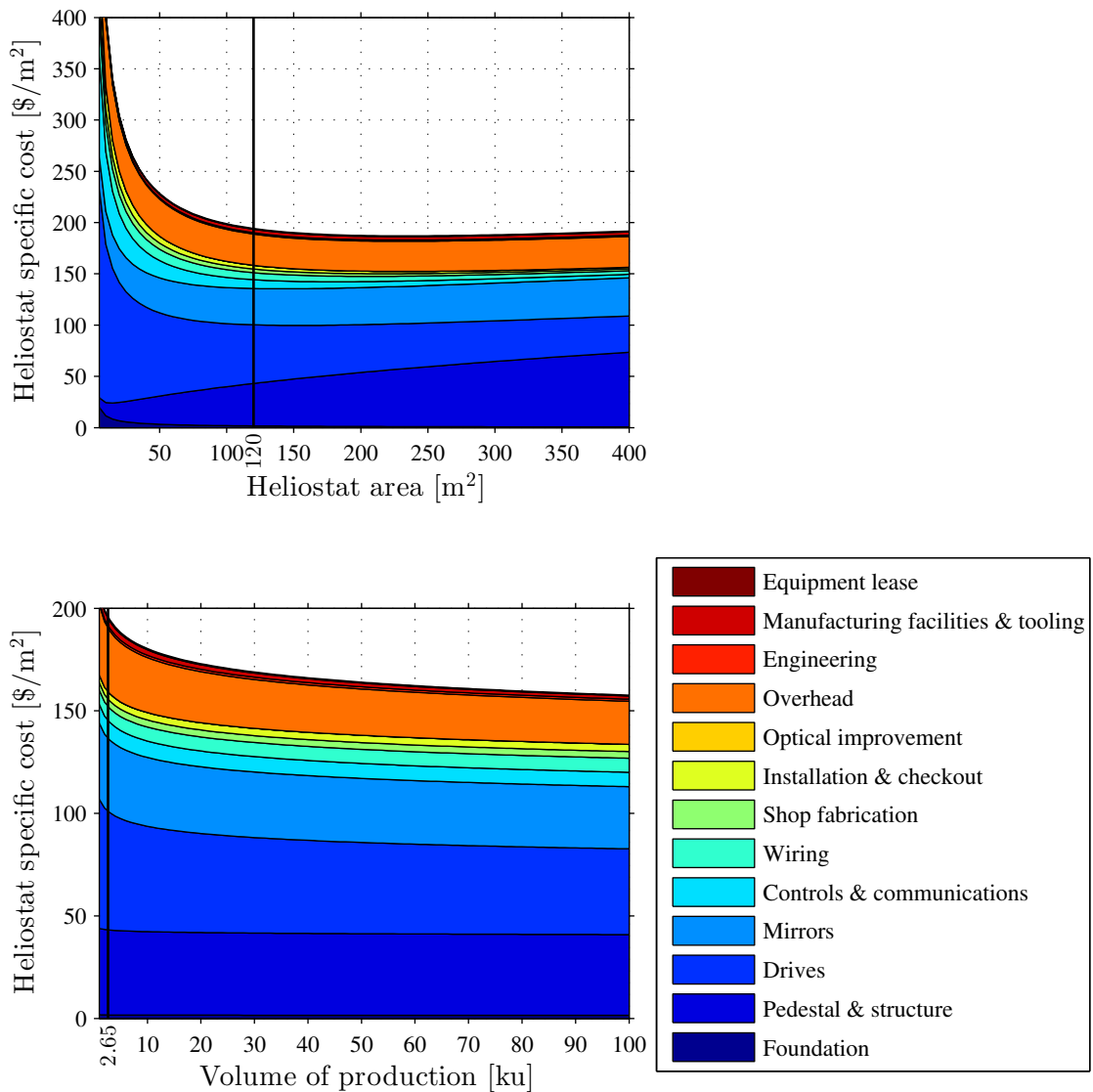


Figure 5.2 – Heliostat specific cost sensitivity against the heliostat area at a fixed production volume of 2650 [u], and against the volume of production at a fixed heliostat area of 120 [m²].

share may go beyond 50%. Above 50 [m²], the share of the foundation for instance becomes negligible, whereas that of the structure starts growing and that of the drives starts shrinking. In parallel, the mirror specific cost obviously remains unchanged, as well as the overhead. Then between 200 [m²] and 250 [m²], the total specific cost reaches a minimum slightly above 185 [\$/m²], and grows up again slowly for larger areas. At the same time, the shares of the respective sub-costs stabilise progressively, with an increase of the structure cost along with a decrease of the drives cost.

The second graph pictures the variation of the same heliostat specific costs now against the volume of production, while the heliostat area is fixed at 120 [m²]. Thus the black line on the

left-hand side shows the breakdown for a 2'650 [u] production volume. From that volume up to 100'000 [u] and above, the total specific cost turns out to decrease exponentially down to the limit of 150 [\$/m²], while no remarkable change of the different sub-cost shares is observed. In the end, the increase of the production volume appears to be the most efficient way to bring the heliostat cost down, more than the scaling of the area.

5.1.2 Tower & Receiver

In practice, the investment cost of the tower obviously depends on its height, but also on the type of structure it features, be it steel lattice or concrete. Hence in the literature, some propositions of cost functions are split into two distinct correlations, e.g. a first one for steel up to 120 [m] height, then a second one for concrete beyond 120 [m] [Kistler, 1986], and both undergoing an exponential increase with the height. For the sake of consistency, the tower cost function presented here follows the same approach as previously for the costs of the heliostat field. Based on a reference case of 75 [m] made of concrete with 1.6 [M\$] and a set of cost studies up to 250 [m] [Sargent & Lundy, 2003], the scaling factor s_{Tow} is estimated at 1.8. Subsequently, the estimate of the cost reduction through the deployment of several distinct plants over the territory allows to approximate a progress ratio $pr_{Tow} = 0.9526$ for the volume effect. The studied deployment ranges from 1.2 [GW_{el}] to 8.7 [GW_{el}], or in other words from 12 to 87 plants of 100 [MW_{el}] for instance. Regarding the price index from the reference year until now, the tower is assumed to belong to the NAICS category that includes the construction of concrete chimneys, which provides $pi_{Tow} = 1.08$ [BLS, 2011]. Thus the combination of the three cost effects results in the following expression, similarly to the heliostat costs:

$$I_{Tow} = I_{Tow}^0 \cdot \left(\frac{H_{Tow}}{H_{Tow}^0} \right)^{s_{Tow}} \cdot (pr_{Tow})^{\log_2 \frac{V_{Tow}}{V_{Tow}^0}} \cdot pi_{Tow} \quad (5.10)$$

where

$$\begin{aligned} I_{Tow}^0 &= 1.6 \text{ [M\$]} & H_{Tow}^0 &= 75 \text{ [m]} \\ s_{Tow} &= 1.797 \text{ [-]} & pr_{Tow} &= 0.9526 \text{ [-]} \\ V_{Tow}^0 &= 1 \text{ [u]} & pi_{Tow} &= 1.0816 \text{ [-]} \end{aligned}$$

With the parameters of Gemasolar (aim point at 120 [m], receiver height of 10 [m]), the function leads to a tower investment cost of 4.3 [M\$].

Now concerning the receiver, the investment cost directly depends on its area as well as on the selected technology as described in §2.8 (i.e. materials and heat transfer fluid). For example, the specific cost of a saturated steam receiver may be expected to reach 107 [\$/kW_{th}], with atmospheric air 112 [\$/kW_{th}], molten salt 127 [\$/kW_{th}], and pressurised air 148 [\$/kW_{th}] [Pitz-Paál et al., 2005]. In general the receiver cost function is similar to that of a conventional heat exchanger, which includes a scaling factor based on a reference case of exchange area A_{Rec}^0 and investment I_{Rec}^0 , here the Solar Two plant with 100 [m²] and 9.1 [M\$]. In addition to the

scaling effect, the volume effect is obtained the same way as for the tower, with a progress ratio pr_{Rec} , and the price index is taken from the NAICS category for the manufacturing of heat exchangers, $pi_{Rec} = 1.44$:

$$I_{Rec} = I_{Rec}^0 \cdot \left(\frac{A_{Rec}}{A_{Rec}^0} \right)^{s_{Rec}} \cdot (pr_{Rec})^{\log_2 \frac{V_{Rec}}{V_{Rec}^0}} \cdot pi_{Rec} \quad (5.11)$$

where

$$\begin{aligned} I_{Rec}^0 &= 9.1 \cdot 10^6 \text{ [\$]} & A_{Rec}^0 &= 100 \text{ [m}^2\text{]} \\ s_{Rec} &= 0.5283 \text{ [-]} & pr_{Rec} &= 0.9526 \text{ [-]} \\ V_{Rec}^0 &= 1 \text{ [u]} & pi_{Rec} &= 1.44 \text{ [-]} \end{aligned}$$

The implementation of the Gemasolar receiver dimensions ($W_{Rec} = 8 \text{ [m]}$, $H_{Rec} = 10 \text{ [m]}$) provides a cost estimate of 21.3 [M\$] and a specific cost of 173 [\$/kW_{th}], which is significantly higher than the reference from 2003 cited previously, mainly because of the influence of the price index.

5.1.3 Power Conversion Unit

According to the receiver type and technology, the investment cost of the PCU is also clearly influenced by the type of conversion cycle and equipments. From the same previous reference, the power block of a conversion cycle based on atmospheric air may have a specific cost of 585 [\$/kW_{el}], that of a saturated steam turbine 620 [\$/kW_{el}], for a hybrid gas turbine 693 [\$/kW_{el}], and with molten salt 758 [\$/kW_{el}] [Pitz-Paal et al., 2005]. Assuming now a molten-salt-based conversion cycle as in the Gemasolar plant, the PCU is divided here into five main equipments: the storage system, the steam generator, the steam turbine coupled with the electric generator, the cooling system, and the master control system. The respective investment cost of each equipment k is assumed to undergo the same cost effects as described in eq. 5.4: scaling, volume and price index, with regard to a reference case of size S^0 and investment I^0 to be specified:

$$I_{PCU} = \sum_k \{ I_{PCU} \}_k \quad (5.12)$$

where

$$I_{PCU} = I_{PCU}^0 \cdot \left(\frac{S}{S^0} \right)^s \cdot pr^{\log_2 \frac{V}{V^0}} \cdot pi \quad (5.13)$$

For the storage system, the reference size is given in [MWh_{th}], for the steam generator in nominal [MW_{th}], and for the power block and its cooling system in [MW_{el}] of the design plant output. Table 5.4 shows the reference values and the parameters of the three cost effects for each equipment estimated here. Some figures are worthy of notice, such as the storage

Chapter 5. Economic Performance

Table 5.4 – Estimated cost parameters of a Gemasolar-like PCU [Kolb et al., 2007, Sargent & Lundy, 2003, BLS, 2011].

| <i>PCU cost k</i> | S^0 [...] | I^0 [M\$] | s [-] | pr [-] | pi [-] |
|---------------------------|---------------------------|-------------|---------|----------|----------|
| Storage | 88.2 [MWh _{th}] | 3.7 | 0.6202 | 0.9526 | 2.2000 |
| Steam generator | 34.0 [MW _{th}] | 1.6 | 0.6734 | 0.9526 | 1.4400 |
| Steam turbine & generator | 13.5 [MW _{el}] | 8.8 | 0.6829 | 0.9526 | 1.2971 |
| Cooling system | 13.5 [MW _{el}] | 7.4 | 0.2514 | 0.9526 | 1.2254 |
| Master control | - | 1.6 | - | - | 1.1690 |
| Total reference PCU costs | | 23.1 | | | |

Table 5.5 – Estimated costs of a Gemasolar-like PCU.

| <i>PCU costs</i> | [M\$] |
|---------------------------|-------|
| Storage | 30.1 |
| Steam generator | 2.7 |
| Steam turbine & generator | 13.5 |
| Cooling system | 9.7 |
| Master control | 1.9 |
| <i>Total PCU costs</i> | 57.9 |

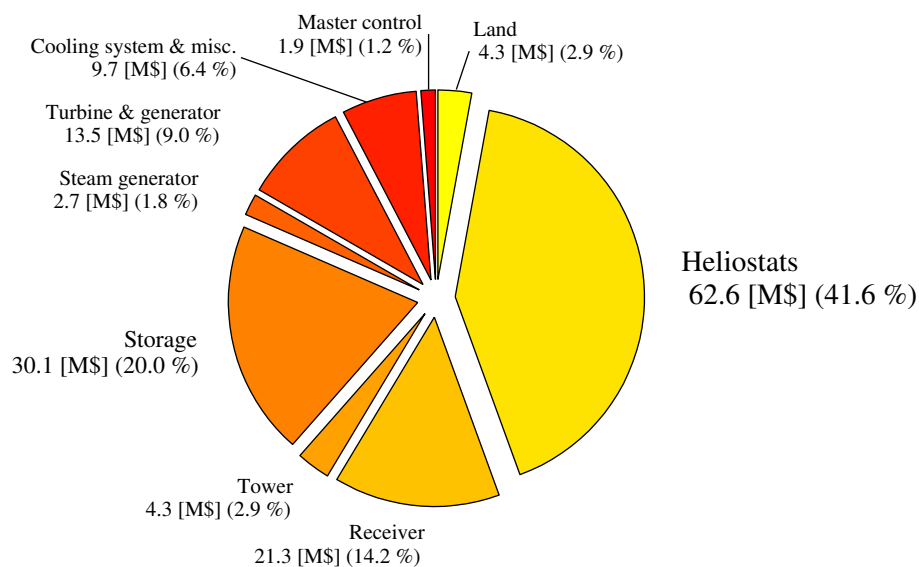


Figure 5.3 – Estimate of the plant cost breakdown in the Gemasolar-like case.

price index exceeding 2, which is due to a significant cost increase over time of potassium nitrate manufacturing according to the NAICS. Besides, whereas the storage system, the steam generator and the power block follow a conventional scaling factor between 0.6 and 0.7, the cooling system features a rather low factor of around 0.25 [Sargent & Lundy, 2003]. Then the master control system is assumed to undergo no other cost effect than the price index.

By applying the Gemasolar configuration, the total PCU cost estimate turns out to reach 57.9 [M\$] (see Table 5.5). Unlike the reference case in Table 5.4, the storage cost is more than twice higher than the power block cost, because of the large storage capacity selected at the Gemasolar plant.

In order to sum up the overall plant investment costs, the estimated cost of each equipment and its share of the total cost is given in Figure 5.3. As a result, the investment of the heliostat field accounts for the highest share, with 62.6 [M\$] and exceeding 40%. In comparison, the receiver cost remains below 15% and the tower below 3%. Subsequently, the total PCU cost reaches a cost share similar to that of the heliostat field, with in details and in descending order: 20% for the storage system, 9% for the power block, 6.4% for the cooling system, and 3% for the steam generator and the master control together. Considering now the final estimate of the plant investment, the sum of all sub-costs provides the total amount of 150.5 [M\$].

5.2 Financial Performance

Once the cost breakdown of the plant is identified and estimated, the funding of the project is to be set up by the contractors with the investors. Whatever the nature of financing might be (banks, private companies, subsidies, etc.), the financial assessment of the project requires the estimate of specific financial indicators, such as among others the levelised cost of electricity, the payback period and the net present value. These indicators help to select the most viable projects, but are to be taken with caution, as they strongly depend on the forecast of the future financial situation, such as the interest rate or the tariff of electricity.

Levelised Electricity Cost

In order to estimate the cost of 1 [kWh_{el}] provided by a solar tower power plant to the power network throughout its entire lifetime, a loan is assumed to be issued for the total plant investment. The payments of this loan are made yearly, hence the interest rate per period is equal to the yearly nominal interest rate and is set at $i = 9\%$. Moreover, the number of periods matches the number of years in the plant lifetime, with the assumption of $N_Y = 25$ [y]. This way, the periodic payment of the loan (or annuity) is calculated as the plant investment I_{Plant} multiplied by the annuity factor $[i(1+i)^{N_Y}] / [(1+i)^{N_Y} - 1]$, and then divided by the total annual electric output $E_{PCU,an}$ to obtain a cost in [¢/kWh_{el}]. In addition to the annuity payment, the cost of operating and maintenance is taken into consideration with $OM = 5.4$ [¢/kWh_{el}] [Ortega et al., 2008], whereas the plant is assumed to operate without fuel backup

and thus no fuel cost. For the sake of simplicity, the insurance cost is left aside and may be considered as being included within the yearly nominal interest rate. By summing up the costs, the estimate of the levelised electricity cost (LEC) in [¢/kWh_{el}] is expressed as follows:

$$LEC = \frac{\frac{i(1+i)^{N_Y}}{(1+i)^{N_Y} - 1} I_{Plant}}{E_{PCU,an}} + OM \quad (5.14)$$

with

$$E_{PCU,an} = \sum_{t=0}^{8760} \dot{E}_{PCU,Out}(t) \Delta t$$

and where

$$i = 0.09 \text{ [-]}$$

$$N_Y = 25 \text{ [y]}$$

$$OM = 5.4 \text{ [¢/kWh}_{el}]$$

By replacing with the plant investment and the annual electric output of Gemasolar calculated previously, the estimate of the levelised electricity cost reaches 24 [¢/kWh_{el}], which provides a measure of the minimum required sale price per unit of electricity such that the power plant is economically viable. In comparison, the LEC of a 50 [MW_{el}] molten salt solar tower plant may be expected to range from 21 [¢/kWh_{el}] to 25 [¢/kWh_{el}] in the literature [Ortega et al., 2008].

Payback Period

The payback period is the amount of years needed to start being profitable, based on a given sale price. In order to support the development of solar thermal plants, this sale price may be a feed-in tariff (FiT) defined by the authorities. It allows the operator to sell electricity at a higher price than the market price, where the difference is paid by the state for instance through taxes on conventional energy carriers (e.g. CO₂-emitting). For example, a Spanish royal decree insures a FiT of 34 [\$/Wh_{el}] guaranteed over 25 years for the solar thermal plants with at most 15% of natural gas backup [Boletín Oficial del Estado, 2007] (suspended as of 2013, but not retroactive [Boletín Oficial del Estado, 2012]). Now taking the tariff of electricity (ToE) as equal to the FiT, the payback period of the plant is obtained with the following expression, by balancing the expenses and incomes:

$$N_{Y,Payback} = \frac{\log\left(\frac{(ToE - OM) E_{PCU,an}}{(ToE - OM) E_{PCU,an} - I_{Plant} \cdot i}\right)}{\log(1 + i)} \quad (5.15)$$

$$\text{where } ToE = 34 \text{ [¢/kWh}_{el}]$$

As a result, the simulated Gemasolar plant is expected to achieve profitability after 10 years approximately.

Net Present Value

When several distinct projects are to be compared to each other, financial indicators such as the internal rate of return (IRR) or the net present value (NPV) are used. The IRR is the interest rate level that would make the balance of expenses and incomes equal to zero over the project lifetime, while the NPV is the sum of the actualised values of all expenses and incomes. Since the IRR can only be obtained if the ingoing and outgoing cash flows are fixed periodic flows, the NPV is preferred here to provide an estimate of the total actualised amount earned until the end of the defined plant lifetime. Hence the expression of the NPV is given by the discounted incomes minus the current value of the plant investment:

$$NPV = \frac{(1+i)^{N_y} - 1}{i(1+i)^{N_y}} (ToE - OM) E_{PCU,an} - I_{Plant} \quad (5.16)$$

With the Gemasolar assumptions, the NPV estimate reaches 80.3 [M\$], which in itself provides a positive indication: below zero, the project would obviously not be viable at all.

Table 5.6 – Estimate of the financial performance at the Gemasolar plant.

| <i>Financial parameters</i> | | |
|-------------------------------|------|------------------------|
| Interest rate | 0.09 | [-] |
| Plant lifetime | 25 | [y] |
| Operating & maintenance costs | 5.4 | [¢/kWh _{el}] |
| Tariff of electricity | 34 | [¢/kWh _{el}] |
| <i>Financial performance</i> | | |
| Levelised electricity cost | 24 | [¢/kWh _{el}] |
| Payback period | 10 | [y] |
| Net present value | 80.3 | [M\$] |

5.3 Summary

The economic performance of a solar tower plant is estimated by breaking down the equipment investment costs in detail, and by using common financial indicators. In general, each investment cost category is calculated based on a reference specific cost per size unit, modified by a scaling effect, a production volume effect and the price index from the reference year until now. In particular, the heliostat costs divide into nine categories of direct costs and three categories of indirect costs: the three main direct costs are caused by the structure (21.1%), the drives (29.4%) and the mirrors (18.1%) in the simulation case of Gemasolar. A sensitivity analysis on the volume of production shows the potential of achieving 150 [\$/m²] of heliostat

area. On the long run, further drops in cost are expected mainly thanks to innovations on the heliostat technology [Pitz-Paal et al., 2005]. Looking at the whole plant, the heliostats turn out to account for 41.6% of the total investment, the receiver for 14.2% and the storage for 20%.

Subsequently, the financial performance is measured mainly with three indicators: the levelised electricity cost, the payback period, and the net present value. The values in the Gemasolar example are estimated by assuming the interest rate, the plant lifetime, the operating and maintenance costs and a given feed-in tariff. For instance, the LEC reaches 24 [€/kWh_{el}] and the payback period 10 years, which matches the expected range in the literature [Ortega et al., 2008].

Now that both the energy performance and the economic performance of a solar tower plant are modelled, a thermo-economic optimisation of the plant set-up can be performed under the constraint of a receiver flux limit.

6 Thermo-Economic Optimisation

The energy and economic assessments of a solar tower plant are now combined in this chapter to investigate the best trade-off set-ups. First the thermo-economic performance of a plant is defined and a short literature review of previous works applying thermo-economic to CSP is presented. The estimated performance of Gemasolar is reminded and used as a the base case. Second, a sensitivity analysis is performed on some important design parameters of the plant: the aim height, the heliostat and receiver areas, the field slope and its starting distance, the density of mirrors, and the solar multiple. As a result, the key potential improvements of both the energy and economic performances are identified through the impacts on the field efficiency and the plant LEC. Third, the multi-objective optimisation of the design parameters is presented: a range of allowed variation is applied to each of them, and two objectives are chosen, where obviously the efficiency is to be maximised and the LEC is to be minimised. Finally some optimal trade-off set-ups are selected and presented in detail.

6.1 Plant Thermo-Economic Performance

In practice, the thermo-economic performance of a power plant is measured by a combination of both energy and economic indicators. These indicators may be any of the performances presented in Chapters 3 and 5 (see Tables 3.2 and 5.6), associated by pairs, such as the investment cost and the electricity output for instance. They divide into two main groups: the *primary* and the *derived* indicators. On the one hand, the primary indicators provide the knowledge of *quantities* like the raw energy and economic inputs or outputs of the plant, and are usually expressed in single units (e.g. investment in [M\$], electricity in [kWh_{el}]). Besides, they are better appropriate to get an idea of the plant size. On the other hand, the derived indicators assess the *quality* of both the energy and the capital conversion, such as the efficiency and the LEC, with combined units ([kWh_{el}/kWh_{th}], [¢/kWh_{el}]).

As a result for solar tower plants, the thermo-economic performance is the expression of the contradiction between energy and economic objectives, e.g. when the investment is to be minimised and the energy output maximised in parallel, or similarly the LEC versus the

Table 6.1 – Calculated thermo-economic performance of the Gemasolar-like plant.

| <i>Energy performance</i> | <i>Value</i> | <i>Unit</i> |
|-----------------------------|--------------|-------------------------------------|
| Annual field efficiency | 0.4534 | [-] |
| Max. receiver incident pow. | 138.15 | [MW _{th}] |
| Heat flux peak at max. pow. | 1296 | [kW _{th} /m ²] |
| Net annual electric output | 87.46 | [GWh _{el}] |
| <i>Economic performance</i> | <i>Value</i> | <i>Unit</i> |
| Total investment cost | 150.5 | [M\$] |
| Levelised electricity cost | 24 | [¢/kWh _{el}] |
| Payback period | 10 | [y] |
| Net present value | 80.3 | [M\$] |

efficiency. In the latter case, the contradiction expresses that low quality is cheap whereas high quality is expensive, in other words efficient tower plants may have a higher LEC than less efficient ones (for a given range of plant sizes), unlike many conventional fossil-based plants. In this way, a set of thermo-economic trade-offs between the two objectives has to be found, before deciding which one is to be selected, based on the desired plant size.

Among previous works, some thermo-economic modelling and optimisation methods have been applied to parabolic trough systems by [Allani et al., 1997] and later by [Kane et al., 2000] for an Integrated Solar Combined Cycle System (ISCCS) in a Tunisian project. In the absence of subsidies, a predicted solar power cost lower than 13 [¢/kWh_{el}] was quoted for a solar share close to 25%. [Kane and Favrat, 2002] then performed a multi-criteria optimisation of a small hybrid solar power system, including aspects such as the energy performance, the economic and financial analysis, and the environmental impacts.

Regarding solar tower thermal plants, [Pelet et al., 2006] introduced a multi-objective approach for designing their concentrator field, and [Zhang et al., 2007] extended this work with a simplification of the model in order to facilitate the identification of the heliostat fields with the lowest specific energy cost. Keeping the methodological concept of a multi-objective thermo-economic optimisation, the current chapter presents its application to the more complete model described in the previous chapters, which among others includes the receiver heat flux distribution, the coupling of a thermal conversion cycle to assess the overall plant performance, and the detailed investment cost breakdown.

For the sake of consistency, the following sensitivity analyses and the thermo-economic optimisation are based on the Gemasolar plant set-up, so that the potential improvements are clearly identified in that case (see [Augsburger and Favrat, 2010] for an application to Solar One). Assuming the same energy and economic plant parameters presented throughout the Chapters 3 and 5, the calculated thermo-economic performance of Gemasolar is reminded in Table 6.1 with a set of some selected results. Thus the main pairs of performance indicators

appear: the net annual electric output of 87.46 [GWh_{el}] with the total investment cost of 150.5 [M\$] as primary indicators on the one hand, and the annual field efficiency of 45.3% with the LEC of 24 [¢/kWh_{el}] as derived indicators on the other hand. Now the interest of the current study is obviously to investigate the existence of plant set-ups with the same electric output but a lower investment than Gemasolar, or the same efficiency but a lower LEC.

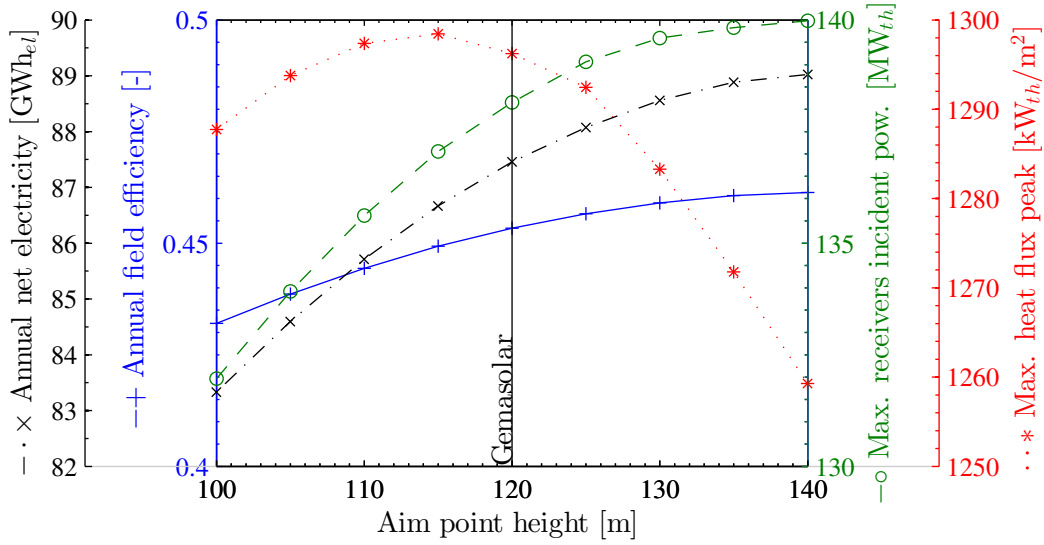
6.2 Sensitivity Analysis

All the parameters of Gemasolar being fixed, a series of key variables are varied one after the other in order to observe their respective impact on the performance of the plant. From these variations, some potential improvements of the plant design are identified, both at the energy and economic levels. The selected variables are the aim height, the heliostat and receiver areas, the field slope and its starting distance, the density of mirrors, and the solar multiple. For each of them the thermo-economic performance of the plant is given graphically against their variation in multi-axis representations.

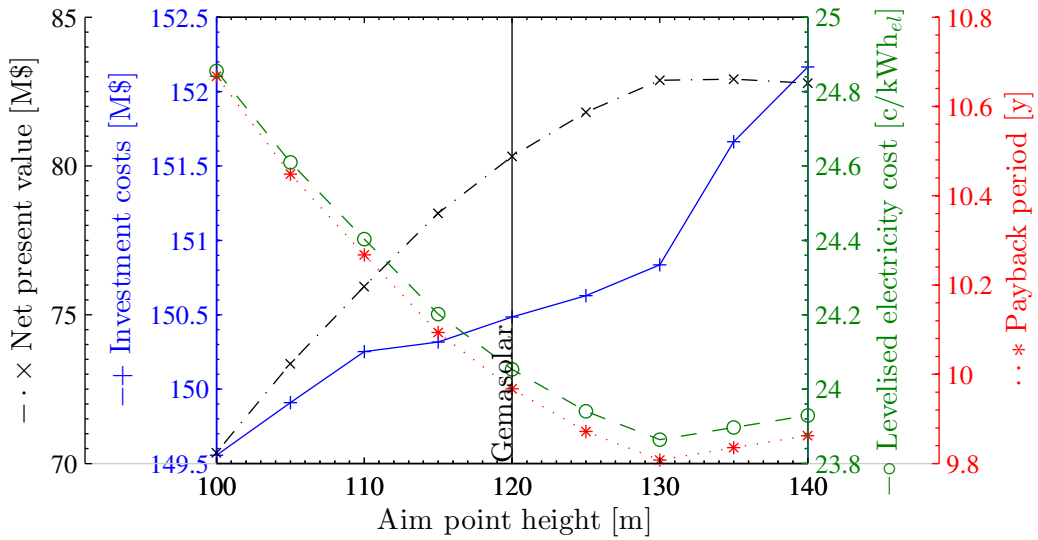
Aim Point Height

Hence, as the aim point height is varied around the Gemasolar reference from 100 [m] to 140 [m], the annual field efficiency rises slowly from 0.43 up to 0.46 where it seems to stabilise (see Figure 6.1a). Building a higher tower up to that height thus provides a very first potential improvement of 1 point in efficiency, which is slight but worth to notice. At the same time, the receiver incident power increases from 132 [MW_{th}] to 140 [MW_{th}], as well as the total electricity output from 83 [GWh_{el}] to 89 [GWh_{el}] over the entire year. Following another trend, the peak heat flux on the receiver reaches an upper limit of 1300 [kW_{th}/m²] at the aim height of 115 [m], and then starts decreasing with a rather low pace down to 1260 [kW_{th}/m²]. As a matter of fact, within this range the height turns out to have a small impact on the receiver heat flux.

On the other hand, Figure 6.1b shows the influence of the aim height variations on the plant economic performance. Since the share of the tower investment cost is relatively small compared with the major equipments (see Figure 5.3), the total investment cost only grows by 3 [M\$] over the entire range, remaining close to the 150 [M\$] estimate of Gemasolar. Nevertheless, the curve of the LEC shows a lower limit slightly below the reference at 130 [m] with 23.9 [¢/kWh_{el}]. In this regard, the height of Gemasolar appears to be well designed for the minimum LEC, while the payback period follows the exact same trend at about 10 years, and the NPV the reverse trend with a maximum at 83 [M\$] against 80.3 [M\$] for the reference.



(a) Sensitivity of the energy performance.

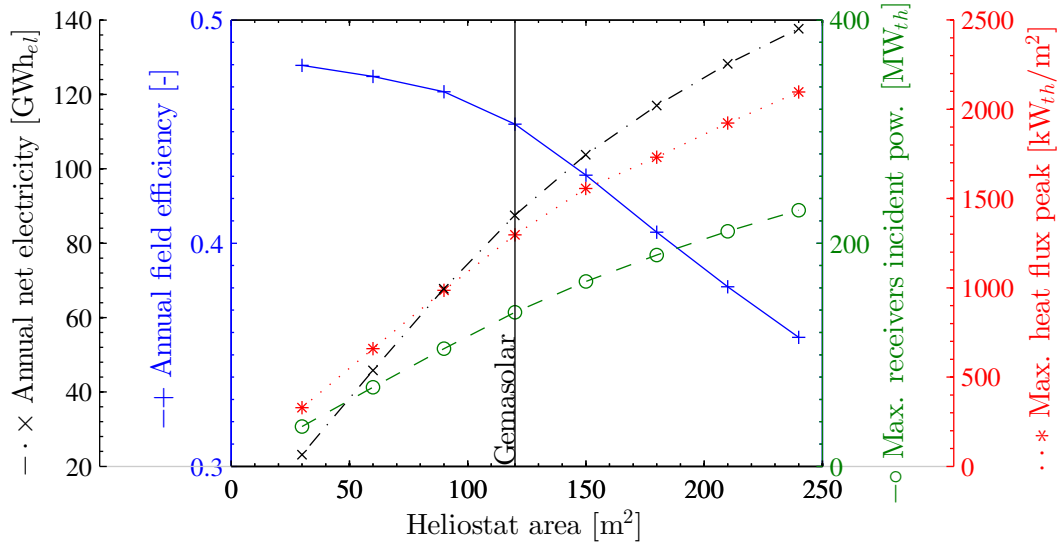


(b) Sensitivity of the economic performance.

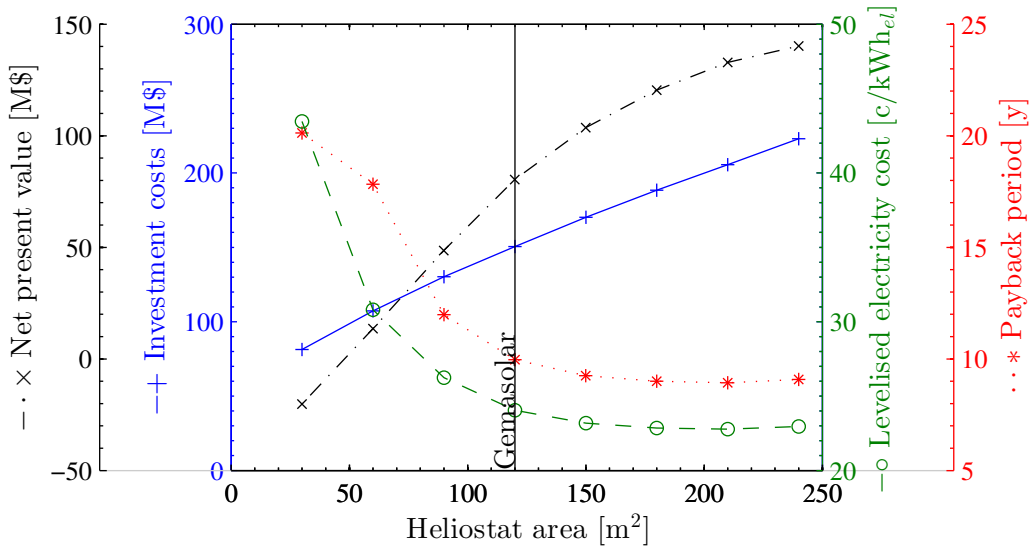
Figure 6.1 – Sensitivity of the energy and economic performance to the aim point height for the Gemasolar plant set-up.

Helioestat Area

The second key variable whose sensitivity has to be analysed is the heliostat area. Keeping the same width-to-length ratio (equal to 1), the effect of heliostat area variations is investigated here from one fourth to twice the Gemasolar heliostat (30 [m²] to 240 [m²]). As a result, a smaller surface leads to higher field efficiencies, up to 0.48 at 30 [m²] as seen in Figure 6.2a, clearly due to a decrease in shading and blocking between neighbouring heliostats. On the opposite direction, as the area gets larger the losses increase as well, which causes an efficiency



(a) Sensitivity of the energy performance.



(b) Sensitivity of the economic performance.

Figure 6.2 – Sensitivity of the energy and economic performance to the heliostat area for the Gemasolar plant set-up.

fall to 0.36 at 240 m^2 . But that does not prevent the rise in receiver power from 36 $[\text{MW}_{\text{th}}]$ up to 229 $[\text{MW}_{\text{th}}]$ over the entire range, obviously making the annual electricity going up significantly at the same time. However, the receiver peak heat flux quickly increases from the reference, even exceeding 2000 $[\text{kW}_{\text{th}}/\text{m}^2]$ at the highest point, which is by far beyond conventional values.

Looking at the economic performance, the total investment cost undergoes a quasi-linear growth (Figure 6.2b), since the scaling effect on the heliostat specific cost shrinks beyond 120

[m²] as estimated from Figure 5.2. In parallel, the LEC drops from 43.5 [¢/kWh_{el}] at 30 [m] down to a minimum of 22.8 [¢/kWh_{el}] with a 8.9 years payback period, below the reference of Gemasolar. Therefore the NPV grows at a linear pace in the first half of the variation, then starts stabilising towards larger heliostat areas. In combination with the energy performance, these results underline the first contradiction between the two objectives of efficiency and LEC: the highest field efficiency is reached as the LEC is prohibitive (even above the assumed FiT of 34 [¢/kWh_{el}]), whereas the lowest LEC is reached as the field efficiency falls below 0.4.

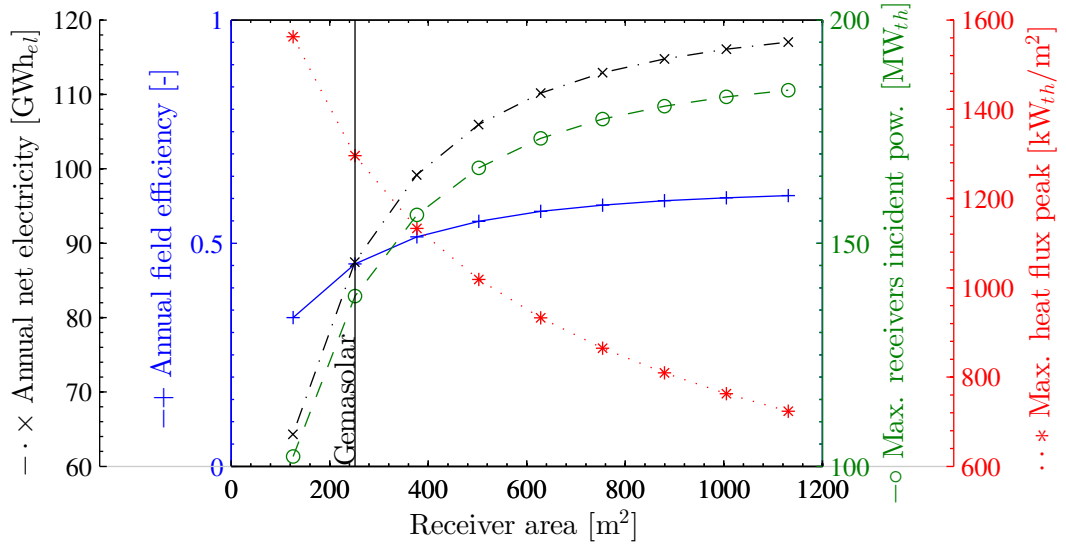
Receiver Area

The receiver area is also expected to have a large influence on the plant thermo-economic performance, as it determines the amount of radiation captured atop the tower, as well as a significant cost share among the other plant equipments. In the current sensitivity calculation, the receiver area ranges from one half to 4.5 times the Gemasolar receiver, while the diameter-to-height ratio is kept at 8 [m] by 10 [m]. Figure 6.3a shows how the field efficiency increases from the reference and then reaches a limit around 0.61 when the receiver area gets larger, even beyond 1000 [m²]. The maximum receiver incident power and the annual electric output follow the same trend, with a ceiling at 185 [MW_{th}] and 117 [GWh_{el}] respectively, which is 34% higher than Gemasolar. At the same time, the receiver heat flux decreases down to 724 [kW_{th}/m²] since the distribution over the surface better spreads per unit of area.

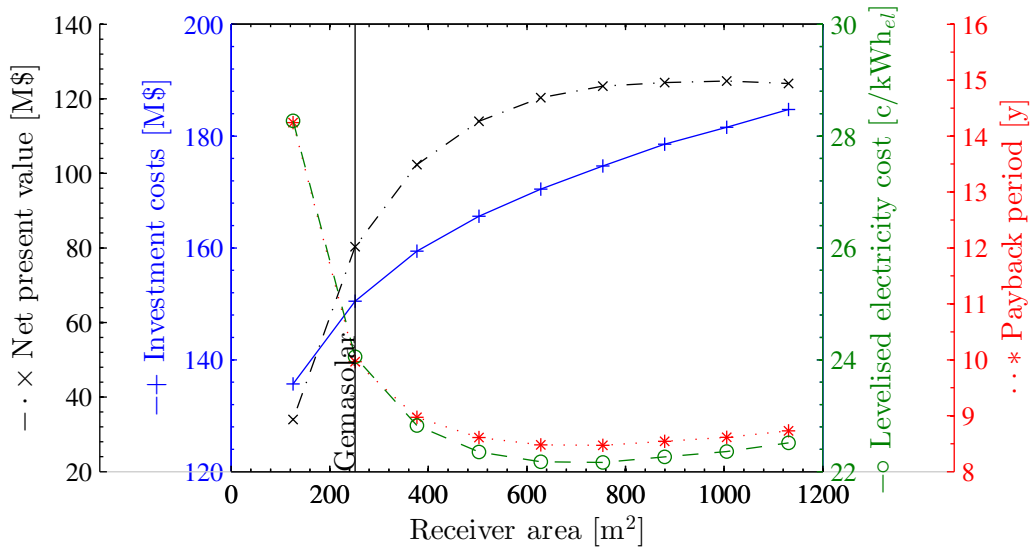
In Figure 6.3b, the growth of the total investment curve turns out to be affected by the scaling effect assumed in §5.1.2, which in the end limits the incidence of the receiver cost. Thus the LEC curve reveals a potential improvement down to a minimum of 22.2 [¢/kWh_{el}] in multiplying the Gemasolar area by three (payback period of 8.5 years). In the meantime, the NPV goes up steeply from the reference and then stagnates around a maximum of 124.8 [M\$] at about 1000 [m²] (four times Gemasolar). Hence unlike the heliostat area, the variation of the receiver area shows no contradiction between the LEC and the efficiency until the LEC achieves its lower limit. Nevertheless, beyond that point, the two objectives are contradictory again.

Field Slope

When the terrain features soft hills, the heliostat field layout may be envisaged with a slope rising towards north (northern hemisphere). As the Gemasolar layout is assumed to be on flat ground, the slope is first varied from 0° to 10° to identify a possible efficiency improvement. Indeed, as the field slope increases the field efficiency undergoes a slight increase as well, peaking at 0.459 with 9°, while the receiver incident power rises by 1.8 [MW_{th}] (see Figure D.1). Similarly, the LEC goes down slowly to a minimum of 23.5 [¢/kWh_{el}] at 8°, where all economic performances reach their respective optimum as well. These results make the presence of a terrain slope interesting, but in practice not enough to be necessarily looking for it when planning the plant construction.



(a) Sensitivity of the energy performance.



(b) Sensitivity of the economic performance.

Figure 6.3 – Sensitivity of the energy and economic performance to the receiver area for the Gemasolar plant set-up.

When both a plain and a hill are available, a combination between a flat and a sloping field sector separated by a west-east breaking line is also envisaged. This way the y-coordinate of the breaking line is taken here as an additional sensitivity variable, ranging from -100 [m] to 400 [m] while the field slope is kept at its best level from the previous analysis (8°). As a result, the variation of this so-called slope start brings a tiny gain in efficiency from 0.459 to 0.461 at an optimum corresponding to a breaking line located 100 [m] north from the tower foot (see Figure D.2). At the same value, the LEC also hits an optimum at 23.6 [¢/kWh_{el}], which shows

no improvement relative to the entirely sloped layout. In the end the slope start is not expected to have a significant influence on the plant performance, but should not be considered as a drawback either.

Mirrors Density

By moving the heliostat rows closer or away from the field centre, the mirrors density of the layout can be adjusted to meet efficiency requirements. Here the reference density is fixed at 1 for the Gemasolar field, and is investigated from one half up to twice its density, which is obtained by multiplying or dividing the heliostat distance to the tower by two respectively (see Figure D.3). Along this variation, the annual field efficiency shows a peak with a significant improvement of almost five points: 0.505 at 1.5 times the reference (two thirds of the original heliostat distance). This result is clearly due to the decrease in attenuation and spillage losses through the distance, not being compensated by the increase in shading and blocking losses. All the other energy performances follow the same trend, except the maximum receiver heat flux whose high value has to be taken cautiously, exceeding $1800 \text{ [kW}_{\text{th}}/\text{m}^2]$. Then the observation of the economic performance gives a LEC minimum of $22.2 \text{ [¢/kWh}_{\text{el}}]$ that matches the efficiency maximum at 1.5 times the Gemasolar density as well, since the impact of density on the total investment costs is relatively small. Therefore making the heliostat field denser appears as an effective means of enhancement both for the energy and economic performances in the current case.

Solar Multiple

Regarding the power conversion unit, the solar multiple is the main design parameter that determines the level of the cycle input and outputs as a ratio of the receiver peak power. Its value fixes the storage capacity of the plant: 1 implies no storage (the cycle thermal input follows the receiver power), 2 enables operation until midnight in the summer, 3 allows 24 hours in the summer, and 5 would be necessary in the winter (for southern Spain conditions [Winter, 1991]). As Gemasolar features a 2.8 solar multiple, it is worth searching for potential improvements around this value, here ranging from 2.5 up to 3 by steps of 0.1 (see Figure D.4). During this variation, the energy performance does not undergo any change, as the solar multiple turns out to have no effect on the overall energy balance of the plant. However, since the storage system remains a major cost position in the investment breakdown, the solar multiple starts seriously impacting the economic performance once the limit of a 24 hours operation is reached. As a matter of fact, beyond that point the storage systems is oversized even for the summer: a given share of the capacity is not used and therefore is not amortised, while the gain in operating hours during the winter is not able to compensate throughout the year. In the current case, the limit matches the Gemasolar solar multiple of 2.8, which confirms that the plant is well designed for overnight operation in the summer.

Finally, Figure 6.4 gives a summary of the potential improvements obtained by adjusting each

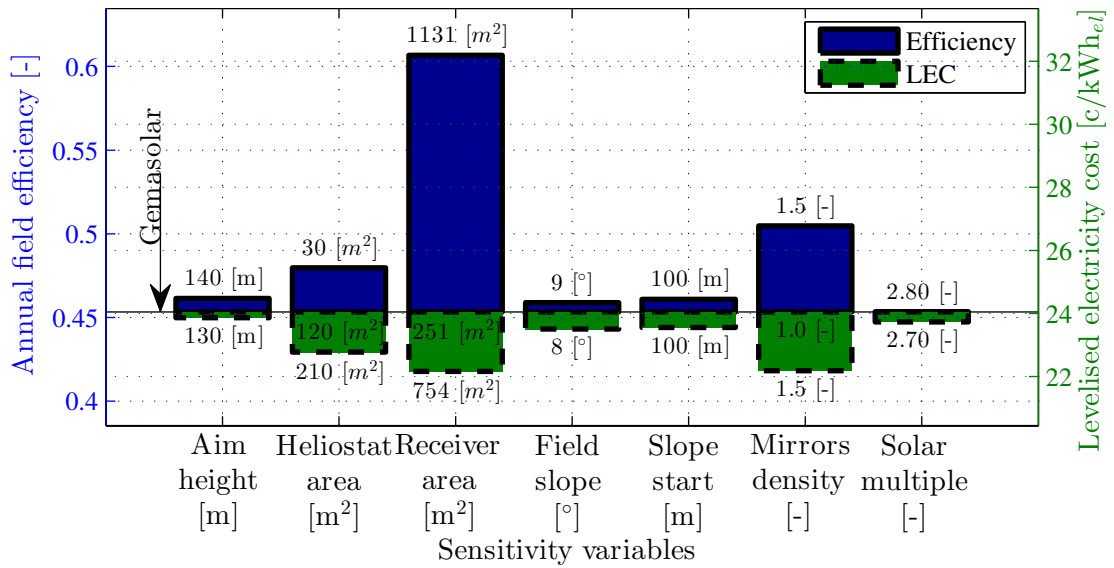


Figure 6.4 – Best potential improvements of the annual field efficiency and the LEC relative to Gemasolar brought by each sensitivity variable individually.

sensitivity variable individually at its best impact on the plant thermo-economic performance. The receiver area, the mirrors density and the heliostat area show the most significant improvements from the Gemasolar base case both of the annual field efficiency and the LEC. In comparison, all the other variables affect only slightly the performance and may be considered as having already achieved an optimum. Nonetheless, the improvements demonstrated here are neither definitive nor cumulative, since a combined variation of all the variables at the same time is expected to result in even better plant set-ups. With this aim in view, the following section proposes a multi-objective optimisation based on a given set of design variables similar to those from the sensitivity analysis.

6.3 Thermo-Economic Optimisation

Multi-Objective Optimiser

In order to find the plant configurations that achieve both the best energy and economic performances, the use of a multi-objective optimiser (MOO) based on an evolutionary algorithm (EA) is proposed [Molyneaux et al., 2010]. Hence the key parameters of a solar tower plant have to be defined as decision variables, with a lower and upper limit of variation. In this way, the optimiser is able to randomly pick a value for each variable within the specified boundaries, and calculate the two objectives (e.g. investment cost in [\$] and electricity output in [Wh_{el}]) for this very first set of values. The MOO then repeats this operation until it reaches a given initial population of plants (e.g. 100 individuals). Subsequently, only the best individuals are kept: every individual that is worse than another in both objectives is eliminated. In other words, a plant set-up is left aside if any other plant set-up has both a lower investment cost

and a higher electricity output. Based on this population of selected set-ups, some operations of crossover and mutation allow the creation of new individuals, and the operation of selection can be performed on the whole population once again. The entire process is repeated until the desired number of individual evaluations is reached (e.g. 5000 evaluations).

Decision Variables

The decision variables are selected among the key design parameters of the heliostats, the field layout, and the receiver (see Table 6.2). Unlike the previous sensitivity, the two heliostat dimensions are now independent from each other, and they are allowed to vary between 1 [m] and 30 [m]. Then the layout geometry is modified by applying different radial spacing coefficients and south-to-north ratios within 0 and 1, keeping the azimuthal spacing fixed at 1 to enable a higher radial mirrors density. Obviously the number of heliostats is also taken as a decision variable, with a very wide range of possibilities from 100 [u] up to 100'000 [u] to ensure the diversity of the evaluated set-ups. The aim point height and the receiver dimensions are imposed large intervals as well, which even may sound unreasonable, but are necessary to let the optimiser search for solutions in a large domain without being stuck by any variable. Therefore the results presented here are to be taken with caution, since the variables may exceed the range of validity of some correlations from the previous chapters, e.g. cost estimates such as the receiver investment. Hence in addition, an optimisation with constrained tower and receiver size is presented in Appendix F, with dimensions closer to known and feasible values nowadays.

Contradictory Performance Objectives

The objectives have to be contradictory, otherwise if they are correlated the population of plant set-ups degenerates into the single trivial solution of a mono-objective problem. As stated previously in the definition of the thermo-economic performance, the energy and economic performances are expected to be contradictory: a more efficient plant turns out to be more costly, and vice versa, a cheaper plant is less efficient. Therefore the two objectives have to be an indicator of the energy performance on the one hand, and of the economic performance on the other hand: here the main derived indicator of each performance is taken, the annual field efficiency and the LEC of the plant. Clearly the LEC is an objective to minimise, whereas the annual field efficiency is to be maximised (see Table 6.2). In parallel, further objectives would be some primitive indicators such as the plant investment cost and its annual electricity output.

Constraints

To narrow the domain of the objectives, or to avoid some damaging situations, one or more constraints may be added to the optimisation problem. By applying a strong penalty function

Table 6.2 – Decision variables, contradictory objectives and constraints in the thermo-economic optimisation of a solar tower plant.

| <i>Decision variables</i> | Range | Unit |
|---------------------------------|-------------|-------------------------------------|
| Heliostat width | 1-30 | [m] |
| Heliostat height | 1-30 | [m] |
| Radial spacing coefficient | 0-1 | [-] |
| South-to-north ratio | 0-1 | [-] |
| Number of heliostats | 100-100'000 | [u] |
| Tower height | 1-1'000 | [m] |
| Receiver diameter | 1-100 | [m] |
| Receiver height | 1-100 | [m] |
| <i>Contradictory objectives</i> | | |
| Levelised electricity cost | min. | [¢/kWh _{el}] |
| Annual field efficiency | max. | [-] |
| <i>Constraints</i> | | |
| Receiver heat flux peak | < 1500 | [kW _{th} /m ²] |

to the plant set-ups that do not satisfy the constraints, extremely bad performances are artificially associated with them, and the optimiser eliminates them from the population. In the current case, the upper limit of 1500 [kW_{th}/m²] is put on the incident receiver heat flux peak, so that situations potentially leading to a receiver failure are restricted (e.g. materials fatigue, strong transients). This is a rather high value compared to practice, and it should also undergo a sensitivity analysis in a future work. In any case, the large fields presented in the following never reach this level of flux peak (see Table 6.3).

Pareto Front of Optimal Trade-Off Set-Ups

Following the MOO process described previously, a cloud of plant set-ups appears with the creation of the initial population (see Figure 6.5). Then after a series of repeated selections, mutations and crossovers, a front of trade-off solutions starts shaping, narrowing and smoothing progressively. As the front converges towards what seems to be a limit, it stabilises and finding new set-ups that are equivalent or better than the others becomes more difficult. At this stage, the final Pareto front of optimal trade-off solutions is assumed to be achieved empirically, and there is no more need to perform additional evaluations. Since the optimiser here is seeking for minimum LEC and maximum efficiency, the domain below the trade-off curve is considered as naive: all the plant set-ups within this domain are worse than those on the curve. On the other hand, the domain above the trade-off curve is considered as infeasible: no set-up can achieve any of the performances in this domain.

The thermo-economic performance of the simulated Gemasolar plant is represented by the

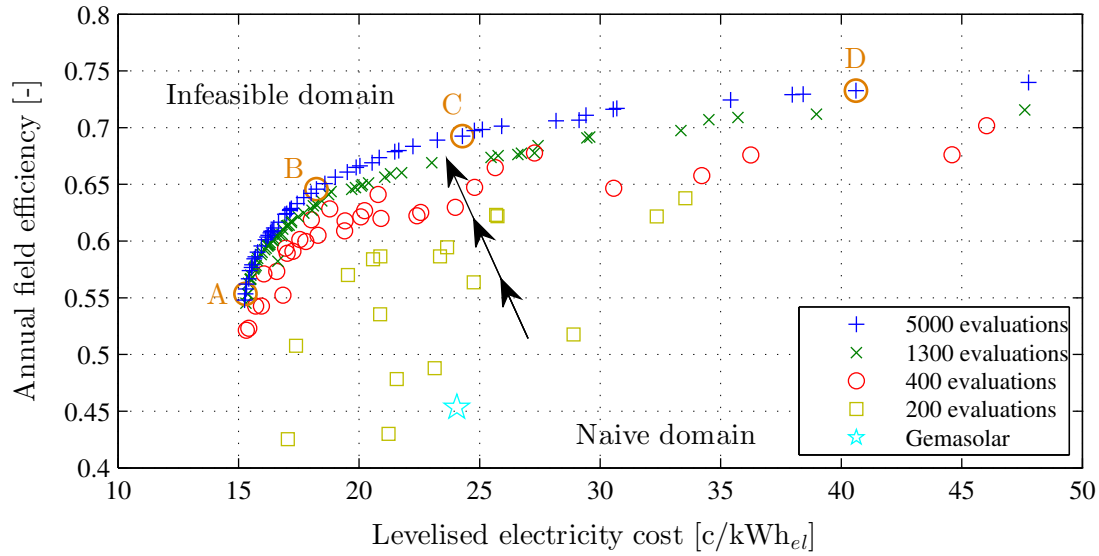


Figure 6.5 – Pareto front of single-tower set-ups as an optimal trade-off between the field efficiency and the LEC.

light-blue star at the bottom of the graph. In comparison with the Pareto front, on a vertical line at the LEC level of Gemasolar, it turns out that some optimal set-ups are feasible with the same LEC as Gemasolar but with a much better efficiency (around 24 points higher). This improvement is even above the level expected in Figure 6.4 from the sensitivity analysis, and seems to be the result of combinations between the various variables potential improvements such as the receiver area and the mirrors density (measured here by the radial spacing between heliostat rows). In the other direction, no optimal set-up appears on a horizontal line at the efficiency level of Gemasolar, but the last solution at the left end of the Pareto shows a much lower LEC at about 15 [c/kWh_{el}] and with an efficiency of 0.56. That latter point is expected to be the limit where the LEC starts increasing again with growing field sizes.

Selected Points on the Pareto Front

In order to understand what kind of plant set-ups corresponds to each region of the Pareto front, four points are picked along the curve in Figure 6.5: point A at the left end with low LEC and low efficiency, points B and C at intermediate levels (C having the same LEC as Gemasolar), and point D at the right end with high LEC and high efficiency. For the sake of comparison, Table 6.3 presents the design variables and the energy and economic performances of each plant set-up at the four selected points.

First of all, the width and the height of the heliostats remain in the same order of magnitude for all the points, ranging from 9 [m] up to 13 [m] except for point A which features a height close to 17 [m]. And looking at the height-to-width ratio, the heliostats have almost square surfaces, once again except for point A with a greater height than the width, which is a sign that

6.3. Thermo-Economic Optimisation

Table 6.3 – Design variables, energy and economic performances of four single-tower set-ups from the Pareto front.

| <i>Design variables</i> | A | B | C | D | <i>Unit</i> |
|------------------------------|--------|-------|-------|-------|-------------------------------------|
| Heliostat width | 11.31 | 11.80 | 11.06 | 9.51 | [m] |
| Heliostat height | 16.57 | 12.45 | 10.36 | 9.05 | [m] |
| Radial spacing coefficient | 0.59 | 0.69 | 0.59 | 0.47 | [-] |
| South-to-north ratio | 0.71 | 0.37 | 0.28 | 0.27 | [-] |
| Number of heliostats | 29'866 | 9'377 | 3'903 | 1'058 | [u] |
| Tower height | 697 | 552 | 429 | 246 | [m] |
| Receiver diameter | 71 | 53 | 41 | 21 | [m] |
| Receiver height | 65 | 51 | 40 | 25 | [m] |
| <i>Energy performance</i> | | | | | |
| Annual field efficiency | 0.55 | 0.65 | 0.69 | 0.73 | [-] |
| Max. receiver incident power | 3'051 | 870 | 304 | 66 | [MW _{th}] |
| Max. heat flux peak | 698 | 516 | 396 | 362 | [kW _{th} /m ²] |
| Annual field output | 6'191 | 1'779 | 619 | 133 | [GWh _{th}] |
| Nominal electric power | 345 | 98 | 34 | 7 | [MW _{el}] |
| Annual electric output | 1'876 | 539 | 188 | 40 | [GWh _{el}] |
| <i>Economic performance</i> | | | | | |
| Total investment costs | 1'710 | 638 | 327 | 131 | [M\$] |
| Levelised electricity cost | 15.29 | 18.23 | 24.29 | 40.61 | [¢/kWh _{el}] |
| Payback period | 4.23 | 5.86 | 10.17 | 28.14 | [y] |
| Net present value | 3'240 | 785 | 168 | -25 | [M\$] |

for achieving a lower LEC the optimiser needs to make the reflective area denser. Indeed, with greater heights it fills in the gaps between the heliostats of the next row from the receiver point of view, but obviously at the same time increases the unused reflective area through shading and blocking. Then among the geometrical parameters of the layout, the south-to-north ratio rises from 0.27 at point D to 0.71 at point A, showing a clear growth of the field region south of the tower when reaching large set-ups with low LEC. Regarding the number of heliostats, a wide range is observed from about 1'000 to 30'000 units: points D, C and B can be considered as belonging to the same category as Gemasolar, however point A features a reflective area more than 17 times greater, which is totally unknown for single-tower set-ups nowadays. The same way, while the tower height and the receiver dimensions remain reasonable at point D for a small field, they go by far beyond existing values at points C, B and A since this turns out to be the only way to keep the efficiency at an acceptable level (e.g. larger receivers allow lower spillage losses, higher tower allow lower cosine losses). Therefore, in practice with a conservative approach, the tower height and the receiver area can be fixed around the values of Gemasolar, which comes to the same result as obtained in the sensitivity analysis: a denser field (smaller radial spacing coefficient) leads to a 5 points improvement in efficiency and a 2 [¢/kWh_{el}] drop in LEC, and may be combined with either smaller heliostats to improve further

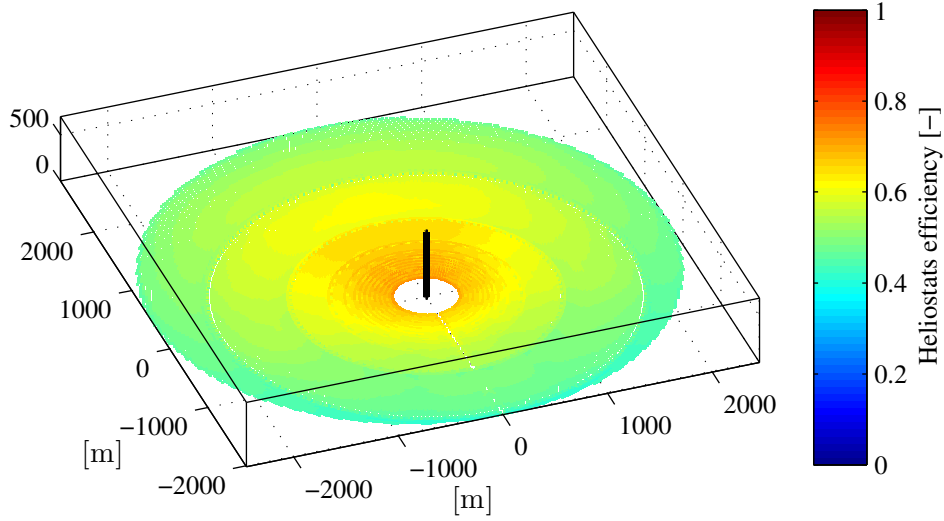


Figure 6.6 – Heliostat field layout and efficiency of the single-tower set-up at point A on the the trade-off Pareto fronts (see zoom in Figure E.1).

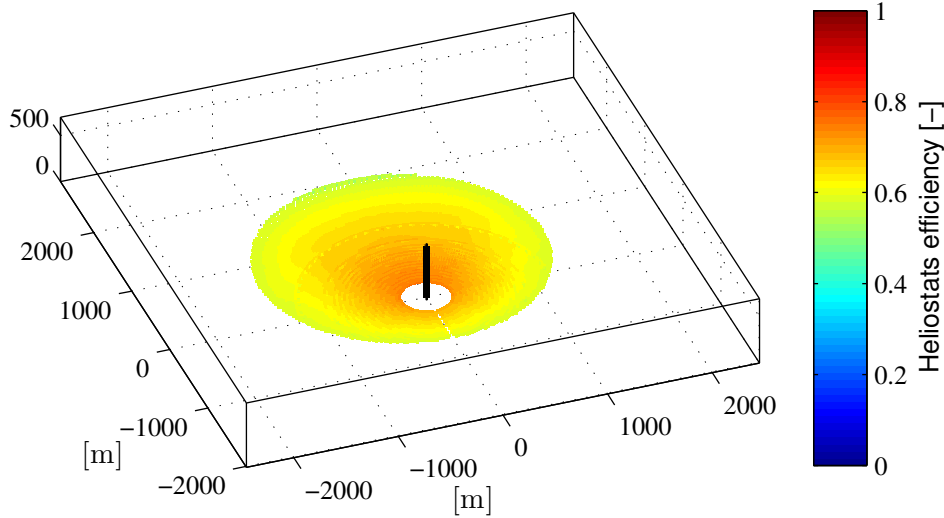


Figure 6.7 – Heliostat field layout and efficiency of the single-tower set-up at point B on the the trade-off Pareto fronts (see zoom in Figure E.2).

the efficiency or larger heliostats to decrease further the LEC.

Second, the energy performance shows wide variations as well along the Pareto curve: the annual field efficiency ranges from 0.55 at point A to 0.73 at point D, and is expected to get better for even smaller fields than point D. But clearly the maximum receiver incident power evolves the other way around, from 66 [MW_{th}] at point D up to 3 [GW_{th}] at point A, as a direct consequence of the growing field size given by the design variables. Similarly, the nominal

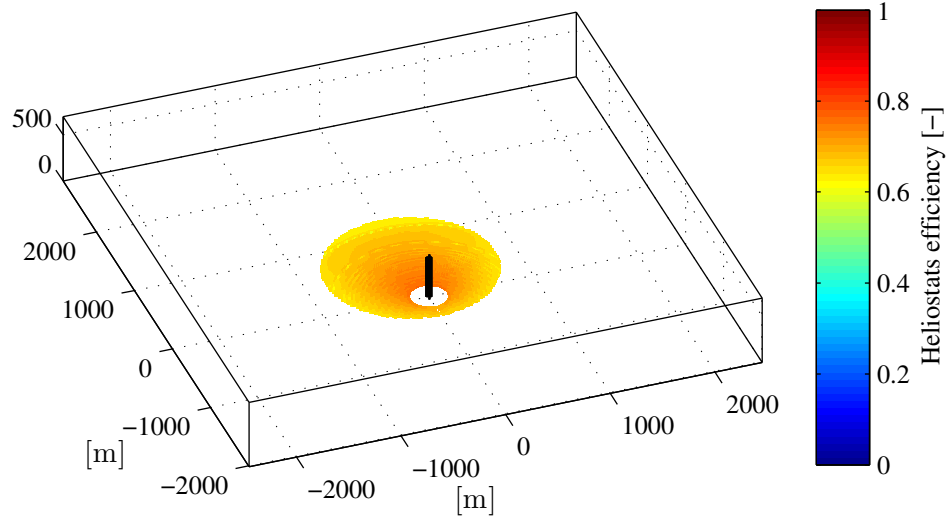


Figure 6.8 – Heliostat field layout and efficiency of the single-tower set-up at point C on the the trade-off Pareto fronts (see zoom in Figure E.3).

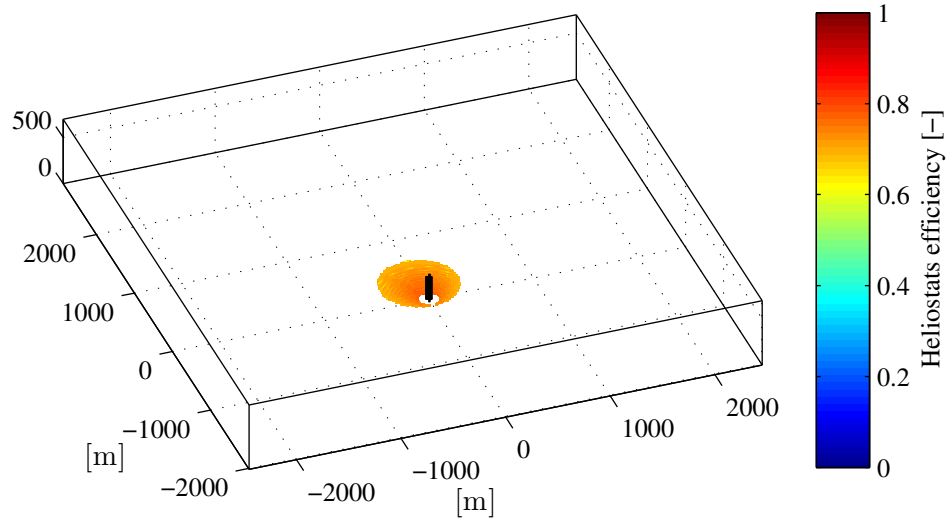


Figure 6.9 – Heliostat field layout and efficiency of the single-tower set-up at point D on the the trade-off Pareto fronts (see zoom in Figure E.4).

electric power varies from 7 [MW_{el}] to 345 [MW_{el}]. In the meantime, the constraint on the maximum heat flux peak of 1500 [kW_{th}/m²] is well respected, the point A featuring the highest level at about 700 [kW_{th}/m²].

Third, the estimate of the economic performance reveals various levels of profitability. As the total investment costs go up with the field size from point D towards point A, the LEC goes down from non-profitable values at 40 [¢/kWh_{el}] to viable values at 15 [¢/kWh_{el}] (thanks to

the FiT, see §5.2). From the payback period point of view, the trend appears even stronger, spanning the range of 28 down to 4 years. In the end, the net present value is the only tool able to highlight that point D has a net loss over the plant lifetime, while all the three other points turn out to remain viable.

In Figures 6.6 through 6.9, the four field layouts are all given with the same axis limits, as well as the heliostats efficiency with the same color scale. The layout A shows a large diameter, with a maximum distance between the heliostats and the tower exceeding 2 [km], which is only possible thanks to the large receiver and the high tower. As a matter of fact, the heliostats efficiency does not go below 0.4, even at the field edge on the south of the tower, whereas the best heliostats exceed 0.7 at the tower foot. Then at point B, the diameter decreases to 2'700 [m] and the minimum and maximum efficiencies increase to 0.5 and 0.75 respectively. Points C and D are even smaller, with a diameter of 1600 [m] and 700 [m] and again better minimum/maximum efficiencies of 0.6/0.77 and 0.6/0.78. A zoom of each heliostat field is available in Appendix E and provides a more precise view of their exact layout.

6.4 Summary

The thermo-economic performance of a solar tower plant is defined by combining energy and economic indicators, and the best trade-off set-ups are investigated by optimising the key design variables. First, a sensitivity analysis is performed around the Gemasolar reference case on several design variables in order to identify their influence on the performance indicators and select them or not for the optimisation. For instance, the receiver dimensions show a tremendous impact on the heliostat field efficiency, with a potential increase of about 15 points for 4.5 times the reference size. At the same time, the minimum levelised cost electricity is achieved with 3 times the reference size, which highlights the contradiction between energy and economic objectives.

Second, a thermo-economic optimisation is performed thanks to an evolutionary multi-objective optimiser [Molyneaux et al., 2010] by defining a set of eight decision variables (Table 6.2), a constraint limiting the receiver flux peak to $1500 \text{ [kW}_{\text{th}}/\text{m}^2]$, and the annual field efficiency and the LEC as contradictory objectives to maximise and minimise respectively. This results in a set of optimal trade-off set-ups on a Pareto front curve (Figure 6.5), where a potential efficiency increase of 24 points is detected with the same LEC as the simulated Gemasolar, whereas a potential LEC decrease of 9 [¢/kWh_{el}] is detected for larger plants. Four optimal set-ups are picked from both ends of the trade-off curve and two intermediate levels: the one with the maximum efficiency is not economically viable according to its negative net present value, whereas the three other ones show lower efficiencies but a much lower LEC with a positive NPV.

As the LEC turns out to hit a lower boundary at about 15 [¢/kWh_{el}] with the current conditions, further possible set-ups are investigated in the following chapter on multi-tower plants.

7 Multi-tower set-up

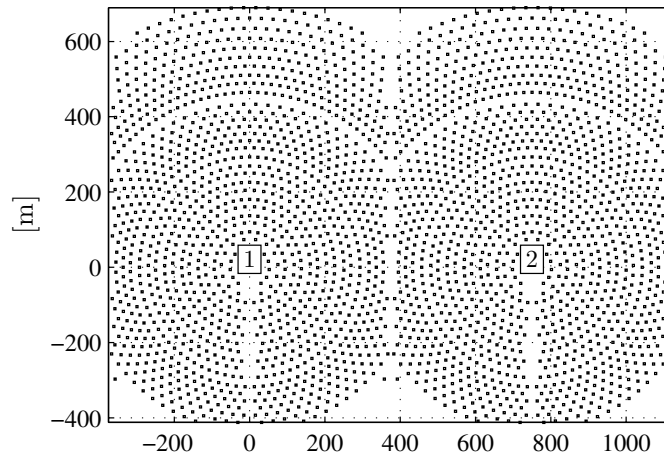
When considering very large single-tower heliostat fields, the attenuation and spillage losses are growing with the distance to the central receiver. Therefore multi-tower configurations are modelled and investigated to find the thermo-economic optimal size of transition from single- to multi-tower plants.

First a method of building a multi-tower layout is defined, second a criterion is set up to select which receiver an individual heliostat is instantaneously aiming at, and third the thermo-economic performance of a three-towers heliostat field is compared to that of an equivalent single-tower heliostat field. Subsequently, a sensitivity analysis and a thermo-economic optimisation are performed both on single- and multi-tower configurations to find the two energy/cost trade-off curves and their intersection, which gives the thermo-economic optimum transition size from single- to multi-tower plants (see [Augsburger and Favrat, 2012]).

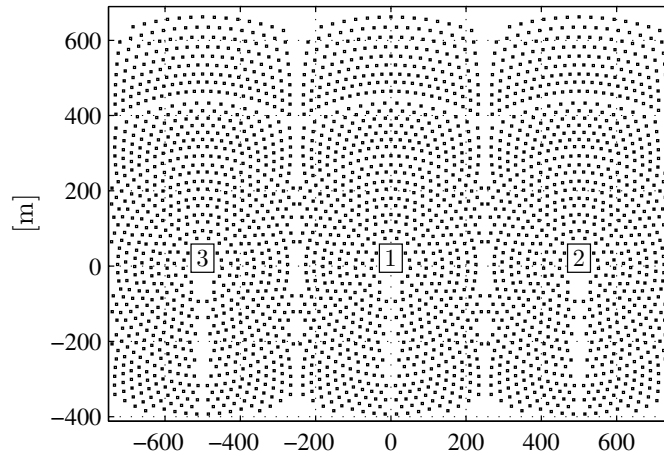
7.1 Multi-Tower Heliostat Field Layout

A multi-tower heliostat field features two towers or more with their respective receivers, whereat each heliostat can aim alternatively. Therefore the two main aspects of a multi-tower plant to investigate are the field layout and the heliostat aiming strategy. On the one hand, the field layout has to take into account the presence of one additional tower or more, without increasing the shading and blocking losses between neighbouring heliostats. On the other hand, the aiming strategy has to define a criterion to select the receiver whereat each heliostat is aiming instantaneously, e.g. by minimising the cosine, attenuation and spillage losses.

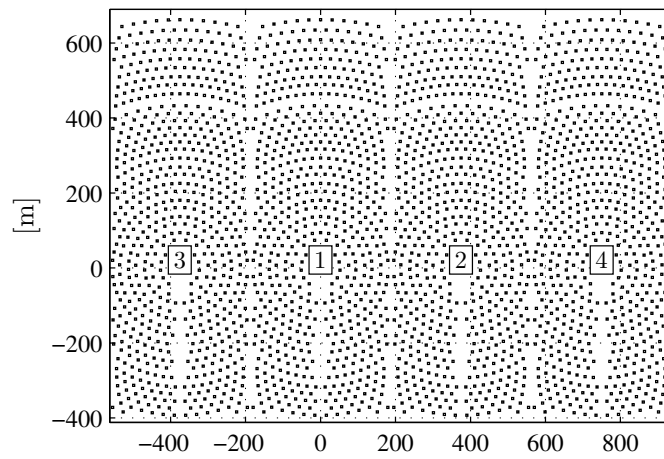
In this way, a multi-tower solar array (MTSA) was proposed by [Schramek, 2003], where several grid-based heliostat fields are overlapping, and two to four towers are arranged in squares or triangles. This leads to a dense layout with small heliostats and towers ($< 5 \text{ [m}^2\text{]}$, $< 10 \text{ [m]}$) suited for urban areas, where the radiation unused by a conventional set-up is exploited by the mirrors inserted in-between the original rows. Then, given their distance to each tower, the heliostats are enabled to aim at a fixed number of receivers only, one up to four, whereon they



(a) Two towers.



(b) Three towers.



(c) Four towers.

Figure 7.1 – Multi-tower heliostat field layouts with two, three and four towers, and the same amount of heliostats as Gemasolar (2650 [u]) on a land area of 1500 [m] by 1100 [m].

are alternately directed. As a result, the amount of incident beam radiation hitting the ground can be captured by the field with a share of more than 85% (annual ground area efficiency).

Similarly, a multi-receiver heliostat system architecture was patented by [Caldwell, 2009], with the objective of increasing the heliostat and land utilisation efficiency for large fields and distributed receivers. Furthermore, by dynamically assigning the heliostats to the receivers the same way as previously, the cosine losses are reduced.

Since the land coverage of large solar tower plants in uninhabited areas remains a secondary issue and a minor cost driver, the two main objectives of the multi-tower layout presented here are the increase of the optical efficiency and the decrease of the specific costs (especially influenced by additional receivers). The layout is obtained by duplicating a single-tower circular layout, whose east and west borders are set by straight north-south lines. The duplicated layouts are assembled side-by-side along an east-west line, so that the duplicated towers are aligned as well. In addition to the common parameters of a single-tower circular layout (radial and azimuthal spacing), the distance between two towers is introduced as a decision variable. For the sake of simplicity, each tower is assigned the same height, although this also may be taken as a variable.

Figure 7.1 shows the field layouts for two, three and four towers, each featuring the same number of heliostats as the Gemasolar plant (2650 [u]). In this example, the distance between the towers is arbitrarily set at 750 [m], 500 [m] and 375 [m] respectively. Increasing that distance up to the original west-east diameter would lead to a configuration that is equivalent to the layout of several separated smaller solar tower plants.

7.2 Aim Selection Criterion

Once the heliostats and the towers are laid out, the way the heliostats are aiming at the receivers has to be defined. First, the heliostats are not linked to one receiver permanently: each heliostat is assumed to be able to aim at any of the receivers at any time. Second, each single heliostat selects the receiver whereon its reflected radiation is the maximum at the given moment: the incident radiation that would hit the receiver surface is calculated for each of the three closest receivers separately, then the results are compared and sorted out, and finally the receiver with the highest amount of captured radiation is selected. Hence in other words, the receiver selection criterion is defined as the minimum optical loss occurring in the conversion of the incident radiation on the heliostat into the reflected beam captured by the receiver. This minimum loss criterion may include one, two or three of the following losses: the cosine loss, the atmospheric attenuation, and the spillage loss. Applying the cosine loss criterion ensures that the heliostat selects the receiver which involves an orientation with the minimum incidence angle on the mirror surface, and thus the maximum projected area in the aim direction. Subsequently, the atmospheric attenuation criterion allows to select the receiver direction where the reflected rays go through as less air mass as possible, to maximise the transmission. Then the spillage loss criterion leads to the selection of the receiver where

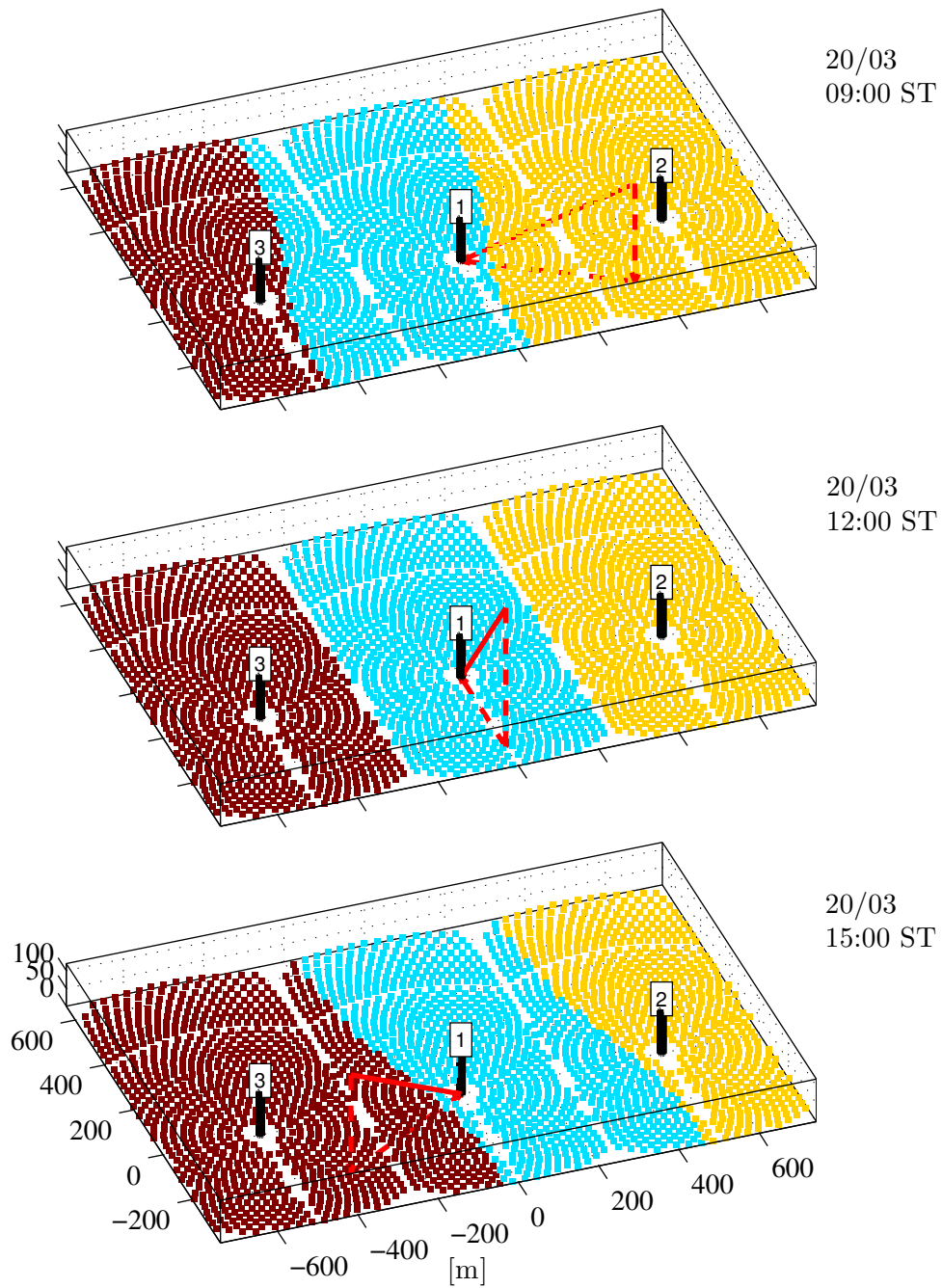


Figure 7.2 – Aim selection by each heliostat for the three-tower layout from Figure 7.1b on the spring equinox (March 20th) at ST 9:00, 12:00 and 15:00, based on the criterion of minimum cosine, attenuation and spillage losses (the direction of the sun is given by the red arrow).

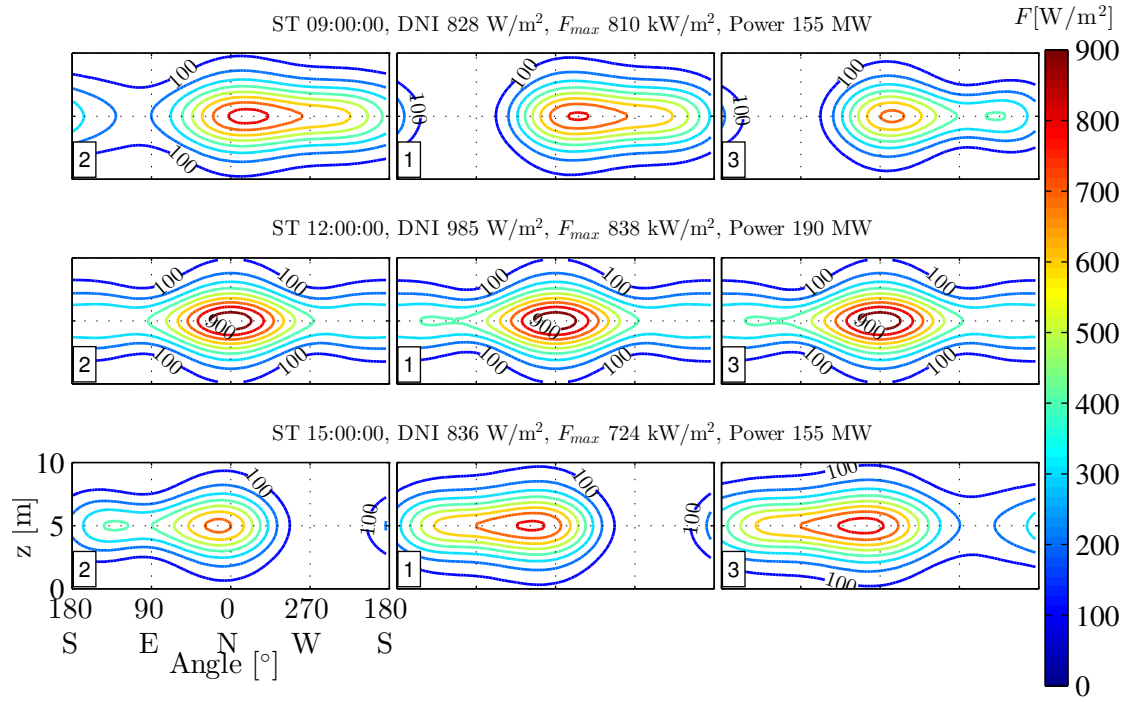


Figure 7.3 – Incident heat flux on the three cylindrical receivers of the three-tower layout from Figure 7.1b on the spring equinox (March 20th) at ST 9:00, 12:00 and 15:00.

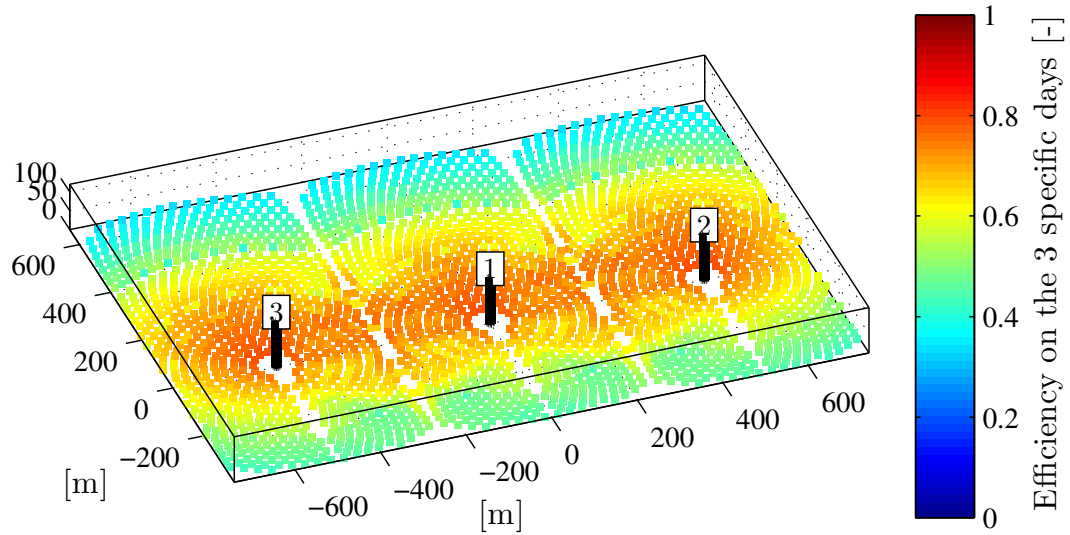


Figure 7.4 – Calculated efficiency for the heliostats of the three-tower layout from Figure 7.1b over the three specific days.

the captured beam is the most concentrated, to minimise the radiation that misses the receiver surface.

The interest of applying the three loss criteria together is demonstrated in Table 7.1 by comparing the use of one, two or three of them. While the cosine criterion alone improves the field efficiency by 7% with regard to the Gemasolar layout, the combination of the cosine and the attenuation criteria improves it by 17%, and then by 32% adding the spillage criterion.

Figure 7.2 shows the receiver selected by each heliostat on the spring equinox (March 20th) at ST 9:00, 12:00 and 15:00, for a three-tower layout with the same number of heliostats as Gemasolar (see Figure 7.1b). The red arrow indicates the direction of the solar direct normal radiation. In the morning, the heliostats tend to aim at a receiver located on their east side, as the sun is still east and low in the sky hemisphere. As a result, the eastern receiver is selected by more heliostats than the two others, and its incident heat flux is the highest of all three, with a peak of 810 [kW_{th}/m²] (see Figure 7.3). The total thermal power reaches 155 [MW_{th}]. At noon, each heliostat obviously aims at its corresponding receiver according to the sub-field layout, and all three receivers are hit by the same flux distribution, achieving 190 [MW_{th}] altogether. Then the situation in the afternoon is symmetric to that in the morning, with more heliostats for the western receiver.

The efficiency of each heliostat is given in Figure 7.4, cumulated on the three specific days (spring equinox, winter and summer solstice). The heliostats located roughly between the two lines of y-coordinate -200 [m] and 400 [m] exceed the 50% efficiency, whereas respectively below and above those lines the efficiency may fall down to 40%. Thus this first multi-tower field layout presented here as example is clearly to be improved by varying the separation distance between the towers.

7.3 Multi-Tower Conversion Cycle

The heat-to-power conversion cycles of the multi-tower plant are assumed to be independent from each other: each tower features its own PCU at its base. For the sake of consistency, the conversion technology is kept the same as that at the Gemasolar plant, based on a molten salt storage and a steam turbine. The solar multiple is also kept at the same high level of 2.8, allowing night operation.

When simulating the cycle operation on a perfect spring equinox (March 20_{th}), the east tower turns out to start slightly earlier than the two others (see Figure 7.5), due to the steeper increase in receiver power instantaneously caused by additional heliostats of the neighbouring field. Then the east receiver peak power of 54 [MW_{th}] is achieved at ST 11:00, one hour before the middle receiver reaches its own peak at the lower value of 50 [MW_{th}]. In the afternoon, the east receiver power decreases linearly as more and more heliostats are defocusing to aim at the two other receivers. At the same time, the west receiver operates the other way around, increasing linearly in the morning, and achieving the same peak as the east receiver two hours later.

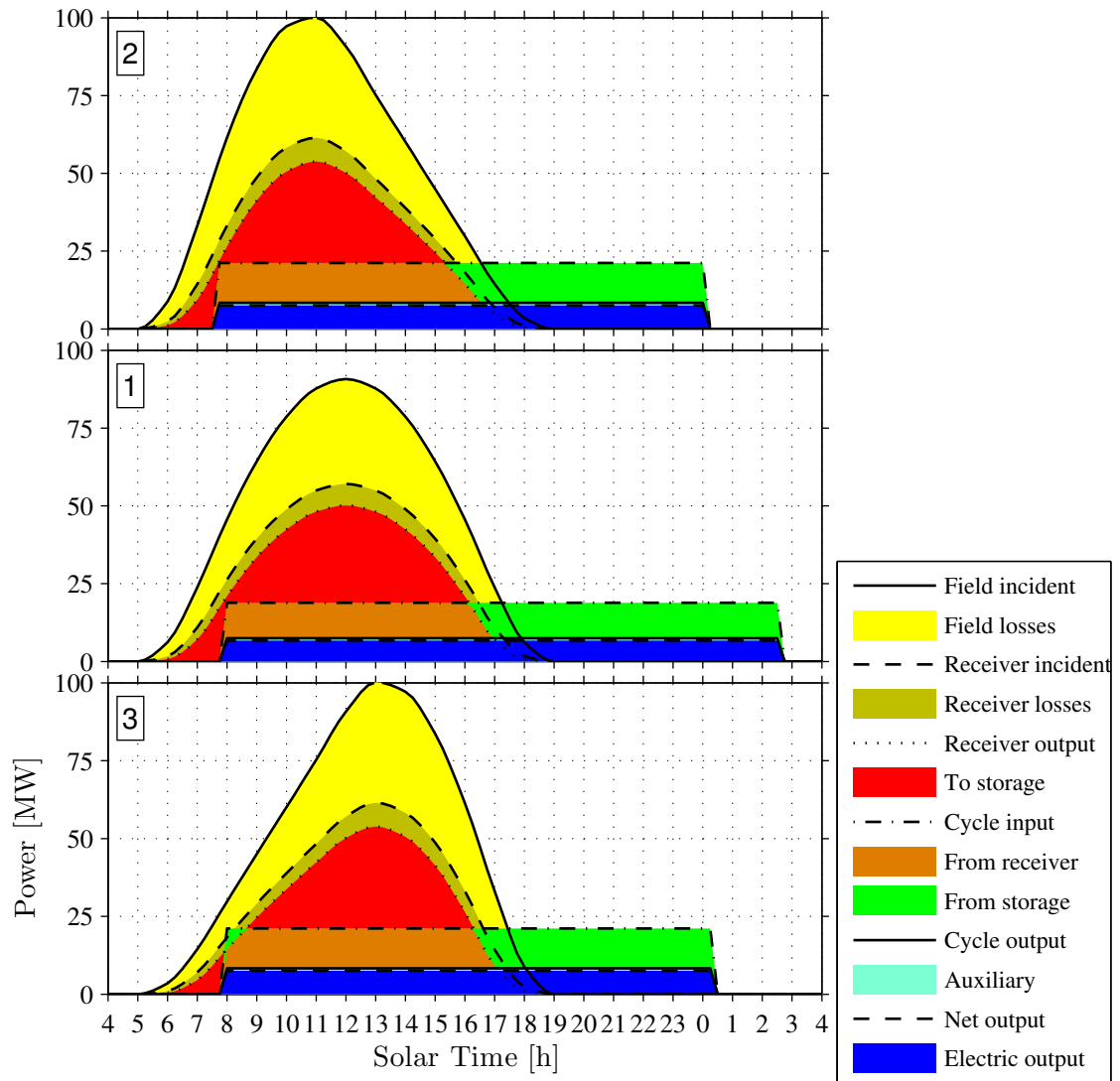


Figure 7.5 – Conversion cycle of each PCU in a three-tower plant on a perfect spring equinox (March 20th), based on the same technology as Gemasolar (molten salt storage and steam turbine).

Now the exact same way as for the perfect equinox, the conversion cycle of every tower plant is simulated over the entire year based on the local DNI database. This results in the assessment of the respective annual electricity outputs, summing up to 114.6 [GWh_{el}] in the current case, compared to the 87.5 [GWh_{el}] of the simulated Gemasolar plant (pure solar).

7.4 Single- vs. Multi-Tower Comparison Case

In order to measure the improvement brought by the heliostats ability to aim at additional receivers, a case of comparison between a single-tower and a multi-tower field layout is

presented. The Gemasolar configuration is taken as the reference for the single-tower layout, while the three-tower field shown in Figure 7.1b is kept as the multi-tower base case, with the same heliostat dimensions, number of heliostats, tower height, and receiver dimensions as Gemasolar. Moreover, the three-tower field is assessed in three successive situations by applying one, two or three of the aim selection criteria proposed previously.

First, the annual energy performance of each case is calculated, which provides among others the annual field efficiency and the maximal receiver incident thermal power as comparison tools (see Table 7.1). In the case where the cosine, the attenuation and the spillage criteria are applied, the efficiency improvement exceeds 14 points from 45.3% for Gemasolar up to 59.8% for the three-tower layout. In parallel, the receiver incident power rises by more than 40 [MW_{th}] from 138.2 [MW_{th}] up to 179.2 [MW_{th}].

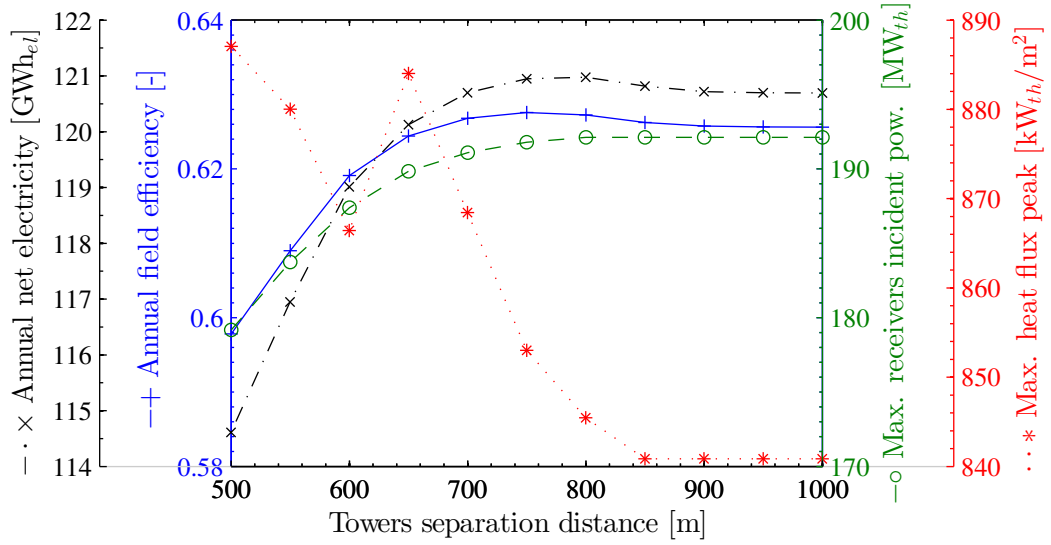
Second, the economic performance is estimated by calculating the respective equipment costs, as well as the plant funding over the entire lifetime. Two indicators are given in Table 7.1 for the comparison: the total investment cost in [M\$] and the levelised electricity cost in [¢/kWh_{el}]. Thus mainly because of the additional receivers, the total cost increases by 70% from 150.5 [M\$] up to 256.6 [M\$]. At the same time, the LEC goes up by 23% from 24.1 [¢/kWh_{el}] to 29.7 [¢/kWh_{el}]. Thus if the project economic viability is assumed to be ensured when the LEC remains below the local feed-in tariff, the three-tower base case presented here is more likely to be ruled out according to these results. Therefore the multi-tower fields in general are to be investigated through a multi-objective optimisation, in such a way that the critical parameters are found where a multi-tower layout becomes better, both at the energy and economic levels.

Table 7.1 – Comparison of the performance of a three-tower layout with that of the Gemasolar layout.

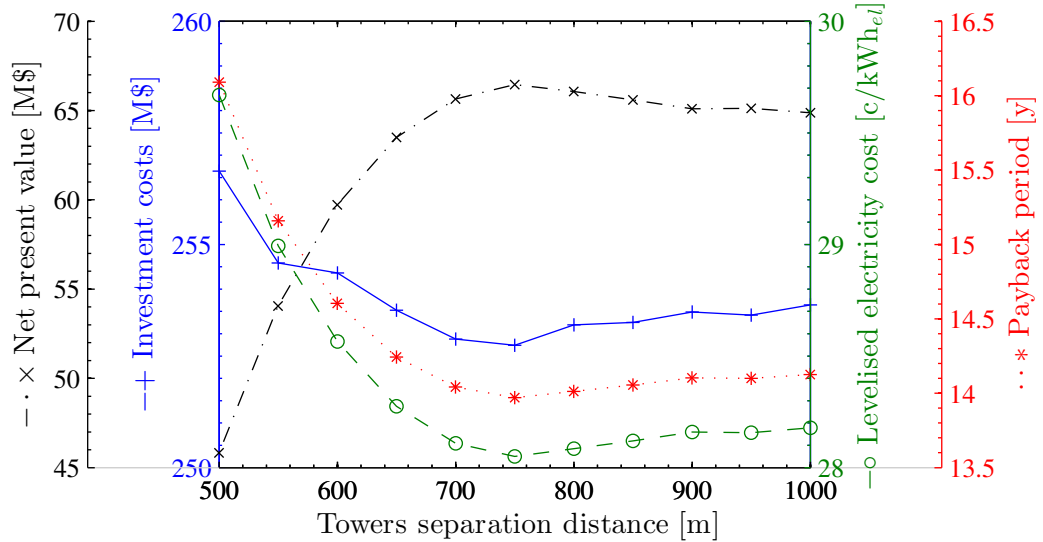
| <i>Set-up</i> | | | | | |
|------------------------------|-------|-------|----------------|--------------------------|------------------------|
| Number of heliostats | 2650 | 2650 | 2650 | 2650 | [u] |
| Number of receivers | 1 | 3 | 3 | 3 | [u] |
| Criterion of aim selection | | cos. | cos. atten. | cos. atten. spill. | |
| <i>Energy performance</i> | | | | | |
| Annual field efficiency | 45.3 | 48.5 | 52.9 | 59.8 | [%] |
| Max. receiver incident power | 138.2 | 174.9 | 175.1 | 179.2 | [MW _{th}] |
| <i>Economic performance</i> | | | | | |
| Investment cost | 150.5 | 244.7 | 246.1 | 256.6 | [M\$] |
| Levelised electricity cost | 24.1 | 35.2 | 32.5 | 29.7 | [¢/kWh _{el}] |

7.5 Sensitivity Analysis

In the following, a sensitivity analysis is led on the key parameters of a multi-tower set-up, so that their influence on the plant thermo-economic performance is identified. The analysis is performed on the same three-tower base case proposed previously, and is expected to highlight the potential improvements. First of all, the impact of the towers separation distance is investigated, secondly the number of towers. Every time both the energy and the economic



(a) Sensitivity of the energy performance.



(b) Sensitivity of the economic performance.

Figure 7.6 – Sensitivity of the energy and economic performance to the towers separation distance for a three-tower field with the same number of heliostats as Gemasolar (2650 [u]).

performance indicators are plotted against the given multi-tower variable.

Towers Separation Distance

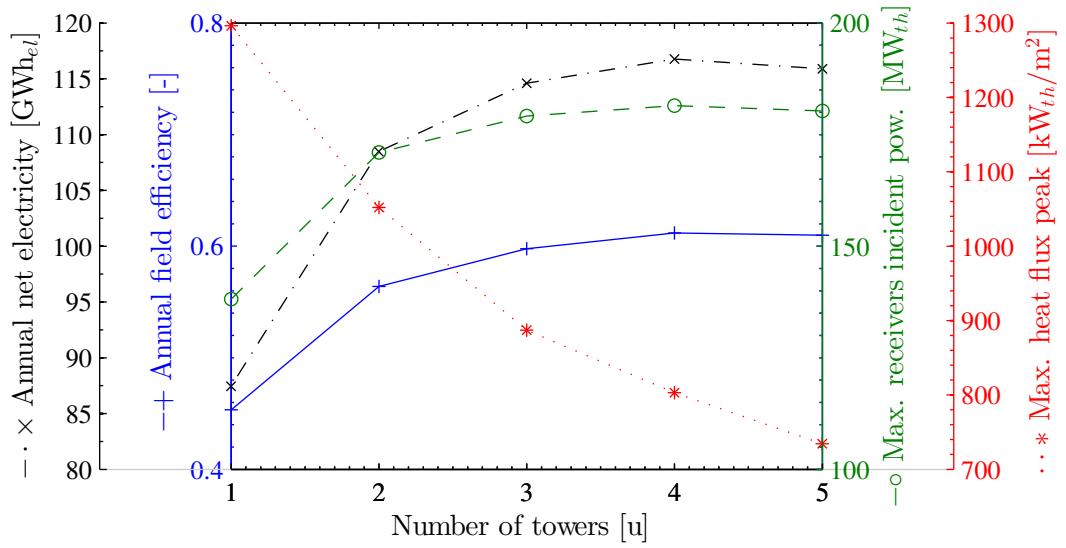
The separation between neighbouring towers is hence first varied from 500 [m] to 1000 [m] with 50 [m] steps, every other parameters being fixed. As a result, the field annual efficiency rises from below 60% up to a peak of 62.8% at 750 [m] and then stabilises slightly below that maximum value (see Figure 7.6a). Similarly, the receiver thermal power and the annual net electricity increase and stabilise above 750 [m], whereas the receiver flux peak goes down to 840 [kW_{th}/m²] since it gets progressively evenly spread between the three receivers. As a matter of fact, the critical value of 750 [m] corresponds to the appearance of three distinct circular layouts, but still differing from a set of single-tower layouts by the heliostats ability to select their aim.

Regarding the incidence on the economic performance (see Figure 7.6b), the total investment cost decreases slightly down to a minimum of 253 [M\$], mainly due to the decrease in storage costs. In parallel, the LEC also reaches a minimum of 28 [¢/kWh_{el}] at 750 [m], as well as the payback period at 14 [y], while the NPV peaks at 66.5 [M\$] and stagnates afterwards. That way, the variation of the separation distance shows here a match between the best energy and economic performances, both occurring around 750 [m]. As this is not necessarily the case for every decision variable, the influence of the number of towers is investigated in the following.

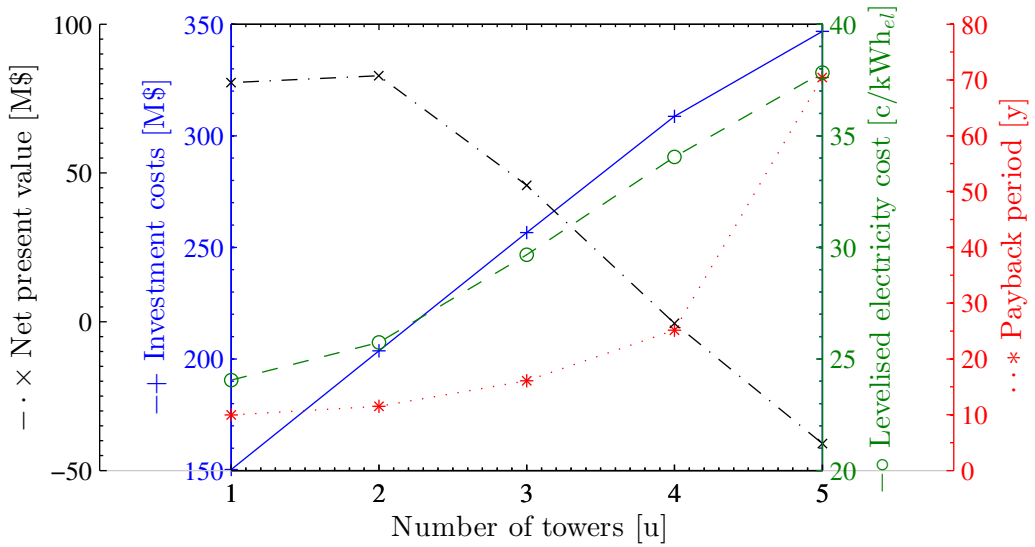
Number of Towers

Still keeping the number of heliostats constant at 2650 [u], the number of towers ranges now from one to five, all featuring the same receiver. As expected, the field efficiency goes up significantly from 45.3% with 1 tower to a maximum of 61.2% with four towers, the same way as the receiver incident power and the electricity output, as shown in Figure 7.7a. At the same time, the receiver flux peak falls down from 1296 [kW_{th}/m²] to 735 [kW_{th}/m²], as it gets divided into the different targets.

Looking at the total investment, the number of towers has a large impact due to the costs of the additional receivers. Thus the investment grows almost linearly from 151 [M\$] up to 347 [M\$] for five towers. In a similar way, the LEC increases from 24.1 [¢/kWh_{el}] to 37.8 [¢/kWh_{el}], as well as the payback period from 10 [y] to the prohibitive value of 70 [y], while the NPV drops below 0 [M\$] beyond 4 towers. Therefore the number of towers turns out to be a variable that leads to contradictory energy and economic performances: there must be a trade-off between them.



(a) Sensitivity of the energy performance.



(b) Sensitivity of the economic performance.

Figure 7.7 – Sensitivity of the energy and economic performance to the number of towers for a field layout with the same number of heliostats as Gemasolar (2650 [u]).

Receiver Area

Given the impact of the receiver cost on the total investment, the receiver area may also be varied to identify potential efficiency improvements and cost reductions. Here the sensitivity of the three-tower layout is investigated for a receiver area that ranges from 1/4 to 3/2 of the Gemasolar case (251 [m²]) with steps of 1/4. As a result, the annual field efficiency goes down to 35.8% at 62.8 [m²], and reaches a ceiling around 63.6% at 377 [m²] (see Figure G.1). However, with this configuration the LEC shows no improvement, below as well as above 251

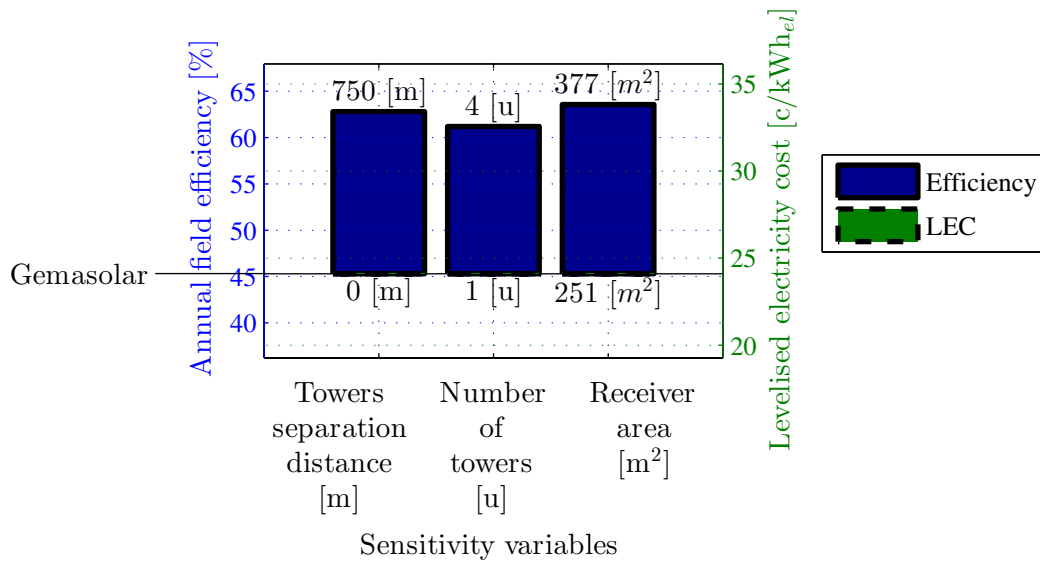


Figure 7.8 – Potential improvements of the annual field efficiency and the LEC relative to Gemasolar with a multi-tower field, brought by each sensitivity variable individually.

[m²], which seems to be already an optimum for the current three-tower field.

Figure 7.8 provides the overview of the individual impacts of each multi-tower variable on the annual efficiency and the LEC. Only the best improvements relative to the Gemasolar plant are pictured as a first identification of the multi-tower potential, keeping in mind that the combination of several parameter variations may lead to even better performances. All three sensitivity variables turn out to potentially increase the annual field efficiency by more than 15 points, with individually either a separation distance of 750 [m], a number of towers of 4 [u], or a receiver area of 3/2 of Gemasolar. On the other hand, unfortunately those sensitivity analyses do not allow to identify any LEC potential decrease under the current configuration. The following thermo-economic optimisation is expected to show that beyond a certain field size, some multi-tower set-ups are economically better solutions.

7.6 Thermo-Economic Optimisation of Multi-Tower Plants

The same way as for the thermo-economic optimisation of single-tower plants in Chapter 6, the use of a multi-objective optimiser is proposed to find the multi-tower plant configurations that reach the best thermo-economic performances.

Multi-tower Decision Variables

In the current case of multi-tower layouts, the decision variables include the same main single-tower parameters, and the two extra sensitivity variables presented previously: the heliostat width and height, the coefficient of spacing between successive rows, the south-to-north ratio

(0: north field, 1: tower-centred), the number of heliostats, the towers height, the receivers diameter and height, as well as the towers separation distance and the number of towers. The boundaries of each decision variable is shown in Table 7.2: some extreme values such as the 1000 [m] tower height or the receiver dimensions of 100 [m] may seem unrealistic, but are required to allow the optimiser to create extremely large fields. Indeed, the interesting transition from single- to multi-tower is expected to appear for sizes about 10 to 20 times the size of the Gemasolar reference.

Contradictory Performance Objectives & Constraints

Then similarly to the single-tower optimisation, the chosen objectives have to be contradictory to prevent the optimiser from degenerating into a trivial solution (e.g. minimum cost versus minimum energy, leading to 0-0 without constraints). According to the previous sensitivity analysis, the energy and economic performances of a multi-tower plant turn out to be contradictory, such as the electricity output and the investment cost when the number of towers is growing (Figure 7.7). This way, these two latter indicators are taken here as the two contradictory objectives, both of them being a primitive indicator and each of them describing one aspect of the plant thermo-economic performance. The annual electricity output is clearly the objective to maximise, while the total investment cost is to be minimised as specified in Table 7.2. Unlike the optimisation of single-tower plants in Chapter 6, the two derived indicators given by the LEC and the annual field efficiency are not selected here as objectives: in practice,

Table 7.2 – Decision variables, contradictory objectives and constraints in the thermo-economic optimisation of a multi-tower plant.

| <i>Decision variables</i> | Range | Unit |
|---------------------------------|-------------|-------------------------------------|
| Heliostat width | 1-30 | [m] |
| Heliostat height | 1-30 | [m] |
| Radial spacing coefficient | 0-1 | [-] |
| South-to-north ratio | 0-1 | [-] |
| Number of heliostats | 100-100'000 | [u] |
| Towers height | 1-1'000 | [m] |
| Receivers diameter | 1-100 | [m] |
| Receivers height | 1-100 | [m] |
| Towers separation distance | 50-5'000 | [m] |
| Number of towers | 1-10 | [u] |
| <i>Contradictory objectives</i> | | |
| Total investment cost | min. | [\$] |
| Annual electricity output | max. | [Wh _{el}] |
| <i>Constraints</i> | | |
| Receiver heat flux peak | < 1500 | [kW _{th} /m ²] |

their use for the multi-tower optimisation turns out to generate only limited field sizes, far below the expected single- to multi-tower transition.

Besides, a constraint is also added here to exclude in advance some periods of operation expected to be hazardous for the receiver integrity. The receiver incident heat flux peak over the entire is kept below the maximum of $1500 \text{ [kW}_{\text{th}}/\text{m}^2]$.

Pareto Front of Optimal Trade-Off Multi-Tower Set-Ups

By running the same MOO optimiser as for the single-tower optimisation, the initial population of multi-tower set-ups is created and appears as a scatter of points in a graph with the investment costs on the x-axis and the annual electricity output on the y-axis (see Figure7.9). Later, the front curve of trade-off solutions starts appearing and gets more precise throughout the successive iterations, thanks to the selection of the best individuals and their combinations. Then the generation of better solutions slows down and the curve hits the limit of feasibility, where the process can be stopped and assumed to have reached the optimal trade-off. Finally, once again the domain below the trade-off front is described as naive and the domain above as infeasible: all the multi-tower set-ups in the naive domain are worse than those on the curve, whereas no performance in the infeasible domain can be achieved. In the current case, the optimal front turns out to be close to a straight line, except at its end corresponding to large fields where additional investments brings proportionally less improvement in electricity output.

7.6. Thermo-Economic Optimisation of Multi-Tower Plants

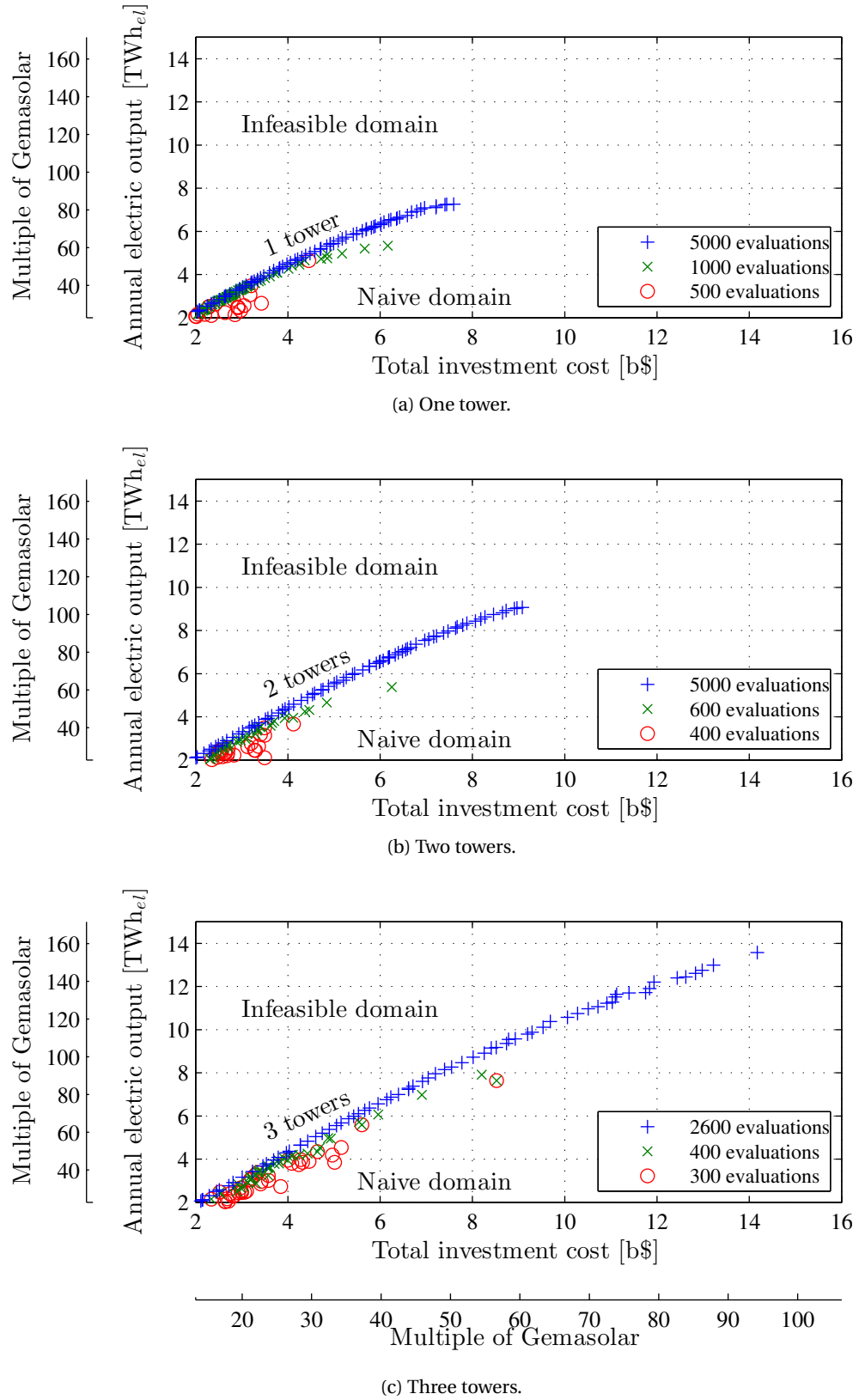


Figure 7.9 – Pareto front of optimal trade-off one-tower, two-tower and three-tower set-ups.

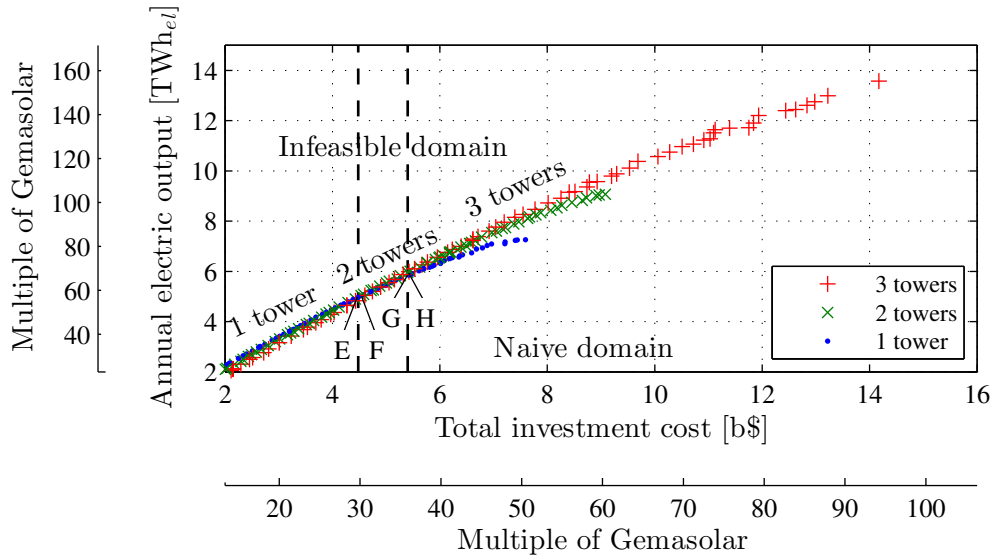


Figure 7.10 – Transition Pareto front of optimal trade-off from one- to two-tower, and two- to three-tower set-ups.

Optimum Single- to Multi-Tower Transition Size

When the three Pareto fronts of respectively one-, two- and three-tower set-ups are superimposed (see Figure 7.10), two intersection points appear and are indicated each by a vertical dashed line. The first intersection provides the transition from one- to two-tower set-ups at about 4.5 [b\$] of total investment and an annual electric output of 5 [TWh_{el}], while the second gives the transition from two- to three tower set-ups at 5.4 [b\$] and 6 [TWh_{el}]. For the sake of comparison, the first transition corresponds to 30 times the investment of Gemasolar and 57 times its electric output both estimated with the same model, and the second transition to 36 times and 68 times respectively. In terms of reflective area, the size of transition reaches 18 million square meter from one- to two-tower set-ups, and 20 million from two- to three-tower set-ups (Gemasolar has 318'000 [m²]). For each transition the reflective area shows a significant drop when adding a tower, down to 16 and 18.6 million square meter respectively.

Table 7.3 shows the design parameters of the four transitions set-ups, as well as their energy and economic performances. Looking at the heliostat dimensions first, all of them feature a greater height than the width, with a ratio of roughly 1.5. Moreover, their values almost remain the same in all four cases, at around 13 [m] by 20 [m] which leads to a much larger area per unit than the nowadays most installed heliostats (e.g. 120 [m²] at Gemasolar). Then the number of heliostats ranges from 60'000 up to nearly 80'000 units along the two successive transitions, while the towers separation distance gets closer to the limit of 5'000 [m] previously specified to the optimiser (see Table 7.2). In parallel, the dimensions of the tower and the receiver achieve very large values, above 600 [m] for the tower height and 60 [m] for the receiver diameter, which obviously is far beyond what is known from present-day existing plants, and thus is to be taken cautiously.

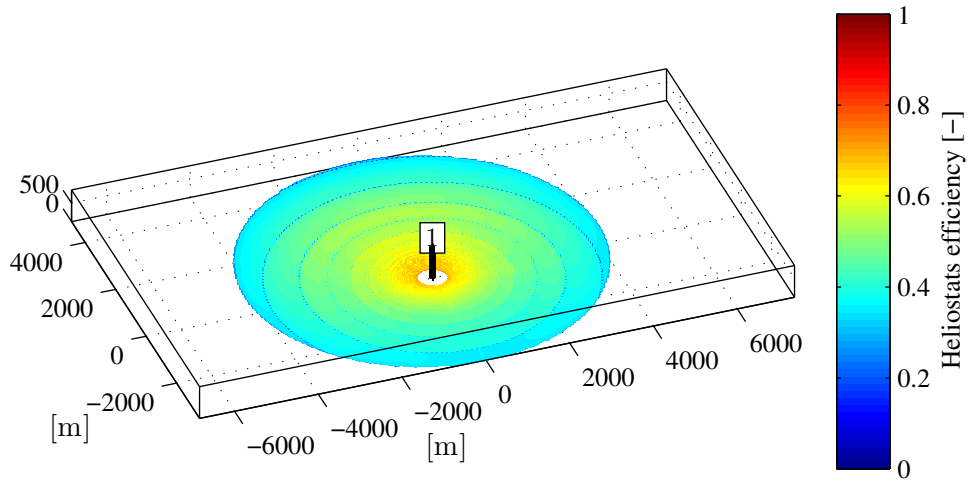
7.6. Thermo-Economic Optimisation of Multi-Tower Plants

Table 7.3 – Design variables, energy and economic performances of the optimal transition multi-tower set-ups from the Pareto fronts.

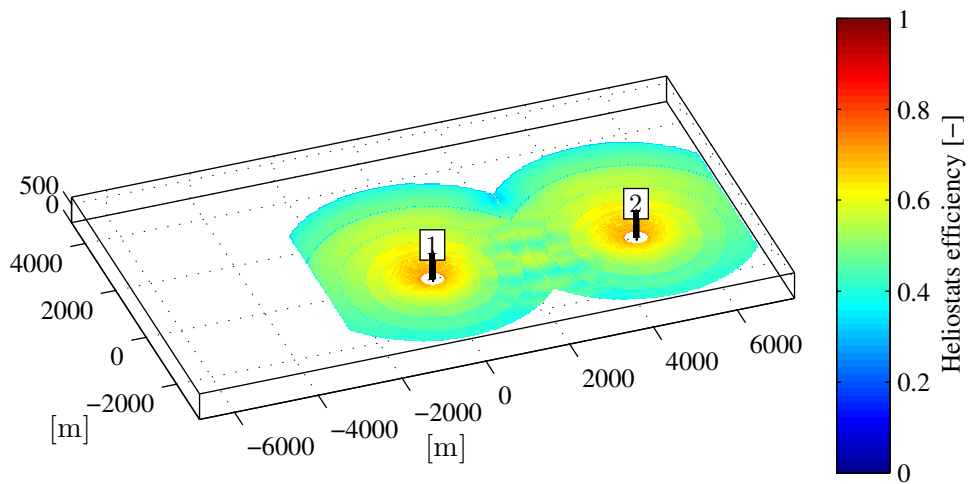
| <i>Design variables</i> | E | F | G | H | <i>Unit</i> |
|------------------------------|-------|-------|-------|-------|-------------------------------------|
| Number of towers | 1 | 2 | 2 | 3 | [u] |
| Heliostat width | 12.49 | 13.26 | 13.33 | 13.23 | [m] |
| Heliostat height | 20.10 | 19.99 | 20.06 | 18.11 | [m] |
| Radial spacing coefficient | 0.26 | 0.37 | 0.38 | 0.38 | [-] |
| South-to-north ratio | 0.72 | 0.64 | 0.68 | 0.70 | [-] |
| Number of heliostats | 71328 | 60948 | 73122 | 77448 | [u] |
| Tower(s) height | 855 | 688 | 851 | 650 | [m] |
| Receiver(s) diameter | 93 | 76 | 78 | 68 | [m] |
| Receiver height | 96 | 71 | 81 | 63 | [m] |
| Towers separation distance | - | 4863 | 4922 | 4565 | [m] |
| <i>Energy performance</i> | | | | | |
| Annual field efficiency | 0.46 | 0.52 | 0.51 | 0.53 | [-] |
| Max. receiver incident power | 8.14 | 8.24 | 9.81 | 9.74 | [GW _{th}] |
| Max. heat flux peak | 952 | 840 | 863 | 778 | [kW _{th} /m ²] |
| Annual field output | 16.43 | 16.66 | 19.75 | 19.77 | [TWh _{th}] |
| Nominal electric power | 0.92 | 0.95 | 1.14 | 1.11 | [GW _{el}] |
| Annual electric output | 4.98 | 5.03 | 5.96 | 5.98 | [TWh _{el}] |
| <i>Economic performance</i> | | | | | |
| Total investment costs | 4.48 | 4.53 | 5.40 | 5.43 | [b\$] |
| Levelised electricity cost | 15.16 | 15.17 | 15.23 | 15.24 | [¢/kWh _{el}] |
| Payback period | 4.16 | 4.17 | 4.20 | 4.20 | [y] |
| Net present value | 8.65 | 8.75 | 10.34 | 10.37 | [b\$] |

As a result of the additional receiver(s), the annual field efficiency rises from 0.46 with one tower to 0.52 with two towers in the first transition, and from 0.51 with two towers up to 0.53 with three towers in the second transition. Besides, the respective heat flux peaks remain as expected below the constraint of 1500 [kW_{th}/m²]. Regarding the economic performance, all four cases show a similar levelised electricity cost slightly above 15 [¢/kWh_{el}], with a four-year payback period and a net present value between 8 [b\$] and 11 [b\$].

Figures 7.11 and 7.12 provides the four transition field layouts and the heliostats efficiency on a color scale from 0 to 1. At the first transition, the one-tower field shows heliostats whose efficiency exceeds 0.7 close to the tower, then remains greater than 0.5 until a 2'000 [m] distance thanks to the large receiver dimensions, but falls below 0.3 near the edge of the field. On the other hand, the two-tower field features two smaller sub-fields, whose edge heliostats are slightly better due to their shorter distance from the aim. Furthermore, the ability to select between the two receivers at any time results in better efficiencies at the middle field joint, up to 0.6 instead of 0.4. Subsequently at the second transition, while the two-tower layout looks



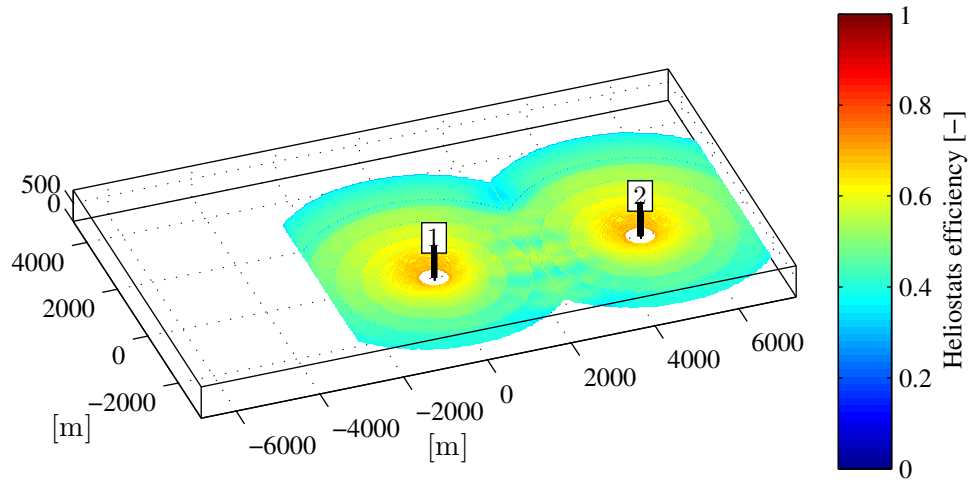
(a) One tower (point E).



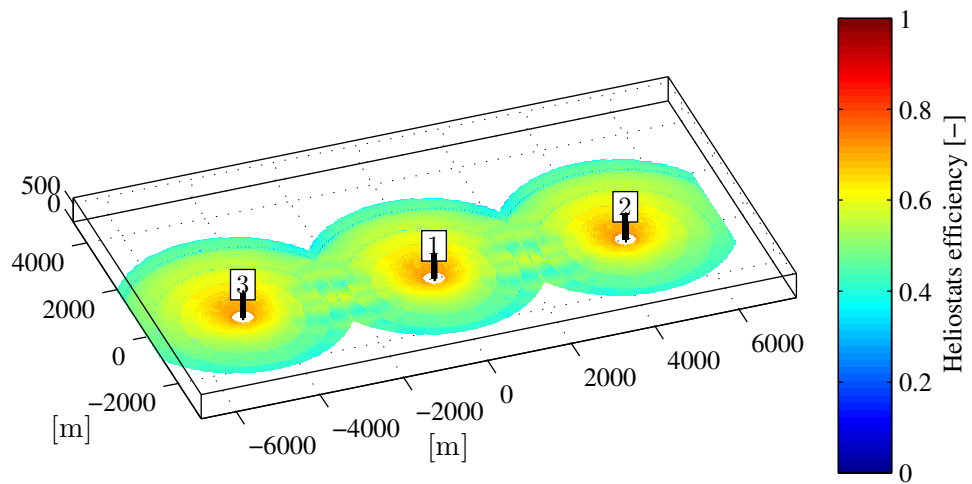
(b) Two towers (point F).

Figure 7.11 – Heliostat field layout and efficiency of the optimal one- to two-tower transition set-ups from the trade-off Pareto fronts (see zoom in Figures H.1 and H.2).

similar to the latter one (except its slightly larger diameter), the three-tower layout has smaller individual diameters and also shows improved efficiencies at the two field joints. Along with the heliostats efficiency remaining now above 0.3 at the edge unlike the one-tower layout, this obviously leads to a higher overall field efficiency as presented in Table 3.



(a) Two towers (point G).



(b) Three towers (point H).

Figure 7.12 – Heliostat field layout and efficiency of the optimal two- to three-tower transition set-ups from the trade-off Pareto fronts.

7.7 Summary

By envisaging very large heliostat fields for solar tower plants, the interest of creating multi-tower layouts is identified, as the heliostat losses increase with the distance to the central receiver. Based on the combination of several one-tower fields, a simple layout generation is presented with the example of two-, three- and four- tower layouts featuring the same amount of heliostats as the Gemasolar plant. Then, in order to decide at any time which receiver

each heliostat is individually aiming at, a selection criterion is proposed according to the instantaneous minimisation of the cosine, attenuation and spillage losses. In the base case of the Gemasolar-equivalent three-tower field, the application of the criterion allows a 32% increase in total field efficiency. Now regarding the power conversion cycle from the receiver to the electric generator, the assumption of a molten salt loop with a large storage system coupled to a steam turbine is made, and the multi-plant operation is pictured throughout the day, showing slight power shifts between the three towers. After that, the one-tower reference plant is compared with its three-tower equivalent both at the energy and economic levels. Indeed, the energy performance of the multi-tower plant turns out to clearly exceed that of the one-tower plant, but at a much higher cost, which raises the need for an optimisation of the design parameters.

This way, first a sensitivity analysis is performed on the key multi-tower parameters, so that their influence on the plant thermo-economic performance of the plant can be highlighted, as well as the potential existence of optimum values. Second, the thermo-economic optimisation results in a Pareto front of optimal trade-off set-ups for one-, two- and three-tower plants, eliminating naive solutions and converging towards the limit of feasibility. The optimal transition appears at a reflective area of 18 million square meter from one- to two-tower set-ups, and at 20 million square meter for two- to three-tower set-ups, which is respectively 57 and 63 times the size of Gemasolar. On the long-term perspective, this transition size might be reduced by significant improvements among the cost drivers such as the heliostats, the receiver, and the storage system.

8 Trough-Tower Combination

As the specific cost of a parabolic trough plant is currently lower than that of a tower plant, but a tower plant has a higher temperature potential, the combination of the two systems and its thermo-economic performance are investigated in this chapter. First, the working principle of a parabolic trough plant is reminded, modelled and simulated with the existing case of Andasol-1 in Aldeire, Spain. Second, a trough/tower combined plant is presented, a suitable steam turbine cycle is integrated, and a 100 [MW_{el}] set-up is designed and assessed from both the energy and economic points of view.

8.1 Parabolic Trough Plant

A parabolic trough collector (PTC) concentrates the direct solar radiation thanks to a cylindro-parabolic mirror assembly onto an evacuated receiver featuring a coated stainless steel tube inside a glass envelope. Nowadays, the most deployed cylindro-parabolic mirrors have an aperture width of up to 6 [m] and may be assembled in modules of up to 150 [m] in length [Dudley et al., 1994, Geyer and Lüpfer, 2002], and the evacuated receivers have a 70 [mm] outer diameter, a 4 [m] length and are assembled end-to-end [SCHOTTSolar, 2011, Siemens, 2010]. Within the receiver steel tube, a synthetic oil is circulated (mostly Therminol VP-1, an eutectic mixture of 73.5% diphenyl oxide and 26.5% biphenyl [Solutia, 2008]) and heated up typically from 295 [°C] to 395 [°C], far above its crystallisation temperature (12 [°C]) and just below its boiling point (400 [°C]). Some alternative facilities use water as HTF to perform a direct steam generation (DSG) [Pitz-Paal et al., 2005], or molten salt to feed storage tanks directly [Kamp et al., 2012].

Then the hot oil is pumped through a steam generator that runs a conventional steam turbine cycle to convert heat into electric power (see Figure I.4). In order to increase the overall first-law efficiency, the steam cycle may feature enhancements such as turbine extractions to preheat the feedwater, or additional oil/steam heat exchangers to reheat the steam after the high pressure expansion stage. In parallel, a share of the hot oil mass flow may be sent to a separate heat exchanger where molten salt (60% sodium nitrate, 40% potassium nitrate) is heated up

from a 290 [°C] cold storage tank to a 390 [°C] hot storage tank, which is able to operate the reverse way to heat up oil for cloudy periods and night operation.

Thermo-Economic Performance

First, the energy performance of a parabolic trough power plant is assessed by modelling a trough collector (see Annex §I). The temperature distribution along the collector and its thermal output for a given DNI are obtained from the system of equations based on the energy balance around every key component: the glass envelope outer and inner surfaces, the receiver tube outer and inner surfaces, and the heat transfer fluid (HTF). Each energy balance is established by applying the fundamental principles of heat transfer by radiation, conduction and convection. Some transfer coefficients are estimated by using known correlations, such as that due to Zukauskas for the forced external flow (wind) around the glass envelope, or Gnielinski for the internal flow of HTF inside the receiver tube [Bergman et al., 2011]. Moreover, the HTF properties are estimated thanks to available tables from suppliers [Solutia, 2008, DOW, 2001], such as the fluid specific enthalpy as a function of the temperature. To validate the model, the calculated increase of the fluid temperature and the global first-law efficiency are compared to those of test results [Moss and Brosseau, 2005], and show an error mean root square of respectively 3.01% and 3.63% (see Figures I.2 and I.3). Subsequently, the storage system and the PCU are modelled the same way as in §3.3, as well as the annual performance of the plant similarly to §3.5.

Second, the economic performance of a parabolic trough power plant is estimated by applying the same approach as in Chapter 5. The investment costs break down into the land, the trough collector field, the storage system, and the PCU costs. Looking at the trough field cost in detail, it breaks down mainly into foundation, structure, drives, mirrors, receivers and piping. Table I.1 shows the complete list of trough sub-costs with their reference level, the estimated progress ratio for the effect of the production volume, and the corresponding production price index from the reference year up to now. Then the specific costs and parameters of the storage system and the PCU are kept the same as in §5.1.3. The approach to estimate the financial performance remains the same as well, and the indicators are calculated as in §5.2.

Third, the case of Andasol-1 in Aldeire, Spain [SolarMillenium, 2008] is implemented and simulated: the trough field has an aperture area of 510'120 [m²] with 156 modules of 2×283 [m] length and 5.77 [m] width, and the PCU provides a nominal net electric power output of 50 [MW_{el}]. The design parameters and the simulated thermo-economic performance of Andasol-1 are given in Table I.2, where the trough field shows a 53.7% annual efficiency in comparison with approximately 50% in the reference. In particular, the greatest collector losses are due to the incidence angle (IAM, 14.3%), to the concentrated rays not intercepted by the receiver (11.5%), and the mirror reflectivity and cleanliness (10.5%), as presented in Figure I.5. Regarding the investment costs, the structure (27%), the mirrors (12.3%) and the receivers (13%) are the largest shares of the collector field, while the total trough field cost accounts for

58.5% of the plant cost (see Figures I.6 and I.7). In the end, the estimated LEC reaches 17.5 [$\text{€}/\text{kWh}_{\text{el}}$], which is lower than the estimated 24 [$\text{€}/\text{kWh}_{\text{el}}$] for Gemasolar but higher than the lower boundary of the range 14-36 [$\text{€}/\text{kWh}_{\text{el}}$] presented by [IRENA, 2012] or [Pitz-Paal et al., 2005].

8.2 Trough/Tower Combination

The combination of a trough field and a heliostat field in the same thermal power plant obviously aims at an efficiency increase and a cost reduction [López Moreno and Augsburg, 2011]. On the one hand, the heliostat field allows higher temperature levels than with the trough field alone, and thus opens the road to better steam turbine cycles with higher steam pressure and temperature, as well as enhancements through reheat or multiple evaporation pressures. On the other hand, the trough field allows to achieve lower specific costs than with the heliostat field alone, since parabolic trough costs so far remain lower than heliostat costs. Therefore the combination presented attempts to take advantage of both systems strengths, by providing low to medium level heat with the trough field and high level heat with the heliostat field, and such that the trough field is larger than the heliostat field and allows decreasing the overall specific costs.

Figure 8.1 pictures the plant diagram of the proposed trough/tower combination. The plant features a heliostat field with its tower and receiver, a field of parabolic trough collectors, a molten salt storage system, and a conventional or enhanced steam turbine cycle. As the trough

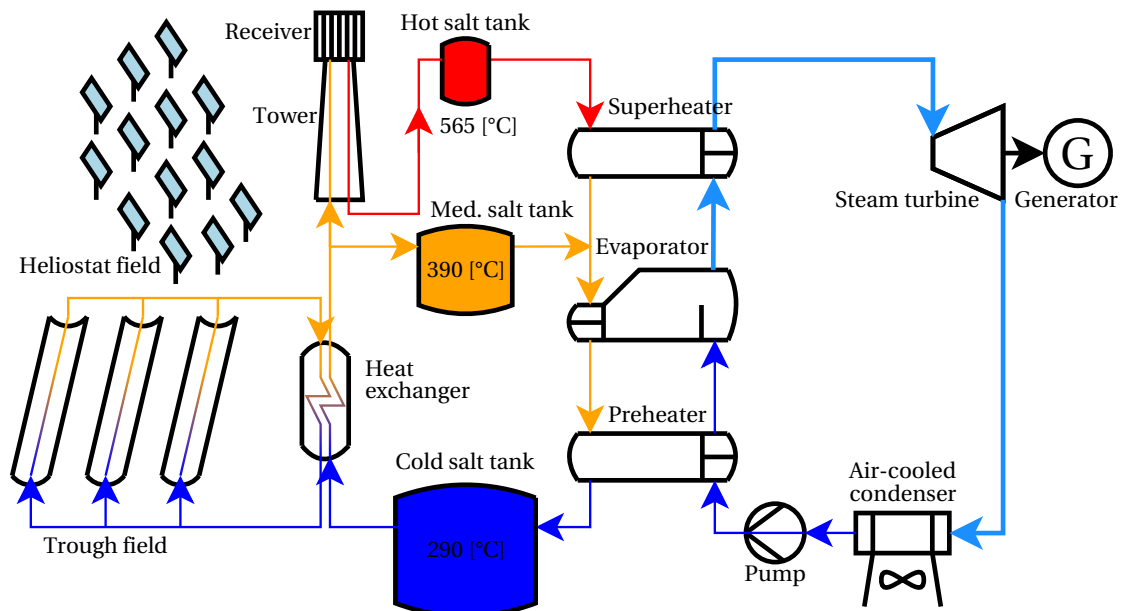


Figure 8.1 – Diagram of the combination between a parabolic trough field and a central tower system, based on molten salt loops.

field here provides limited heat at 395 [°C], it is attributed to the first stage of molten salt heating from a 290 [°C] cold tank to a 390 [°C] intermediate tank, which feeds the evaporator and the preheater of the steam cycle. In the evaporator, the molten salt is circulated in the tubes of the heat exchanger, while the preheated water is circulated in the shell and goes out as saturated steam [Pacheco, 2002]. Then in the preheater, the molten salt is circulated in the shell of the heat exchanger and the feedwater in the tubes. In parallel, a share of the salt mass flow heated by the trough field is sent to the external cylindrical receiver atop the tower, is heated up to 565 [°C], and stored in a hot tank. This way, the high temperature molten salt is circulated in the shell of the superheater, while the steam is heated in the tubes and sent to the turbine inlet. After running the turbine coupled to the electric generator, the steam is condensed in an air-cooled condenser and pumped back to the preheater.

8.2.1 Steam Cycle Integration

For the following case study, an existing steam turbine is chosen among the ones suitable for CSP, biomass and waste-to-energy applications: the MT Mid-Sized steam turbine [Alstom, 2010]. Its nominal electric power output may range from 60 [MW_{el}] up to 100 [MW_{el}], with steam parameters up to 140 [bar] and 565 [°C] with reheat or 540 [°C] without reheat. The turbine may feature two extractions for preheating the feedwater: up to 50 [bar] for the high pressure preheater, and 9 [bar] for the low pressure preheater. The temperature-entropy (T-s) diagram for a standard set-up of the MT steam turbine is calculated and presented in Figure 8.2, with a high condensation level of 50 [°C] constrained by the local temperature conditions and the air-cooled condensation because of water unavailability.

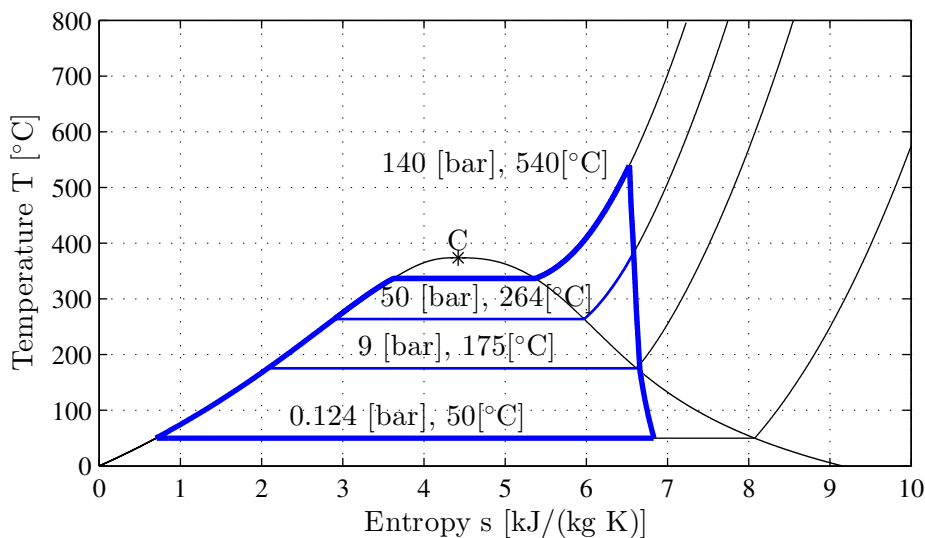


Figure 8.2 – Temperature-entropy (T-s) diagram of the steam cycle based on the Alstom Mid-Sized Steam Turbine (MT) [Alstom, 2010]. Assumptions: no pressure drop, 0.93 turbine isentropic efficiency.

However, the current steam cycle cannot be applied as such to the trough/tower combination, because of the relatively low temperature curve of the molten salt heated by the trough field from 290 [°C] to 390 [°C]. The cycle configuration has to comply with the constraint of the temperature pinch point occurring most likely at the evaporator outlet, and at the same time provide the highest global first-law efficiency. Therefore iterations and variations are

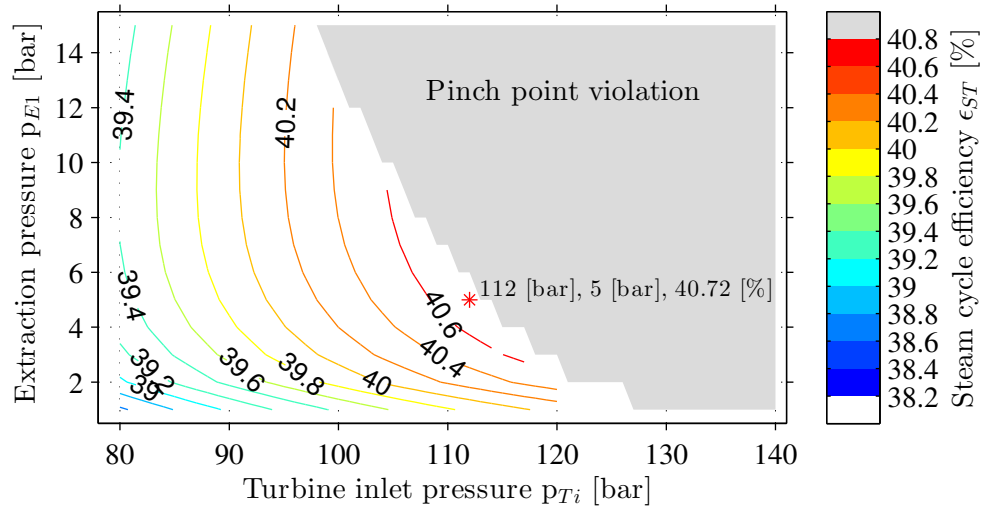


Figure 8.3 – Steam cycle optimisation of the turbine inlet pressure and the extraction pressure based on the Alstom Mid-Sized Steam Turbine (MT) [Alstom, 2010], with hot molten salt streams from both the tower and trough systems.

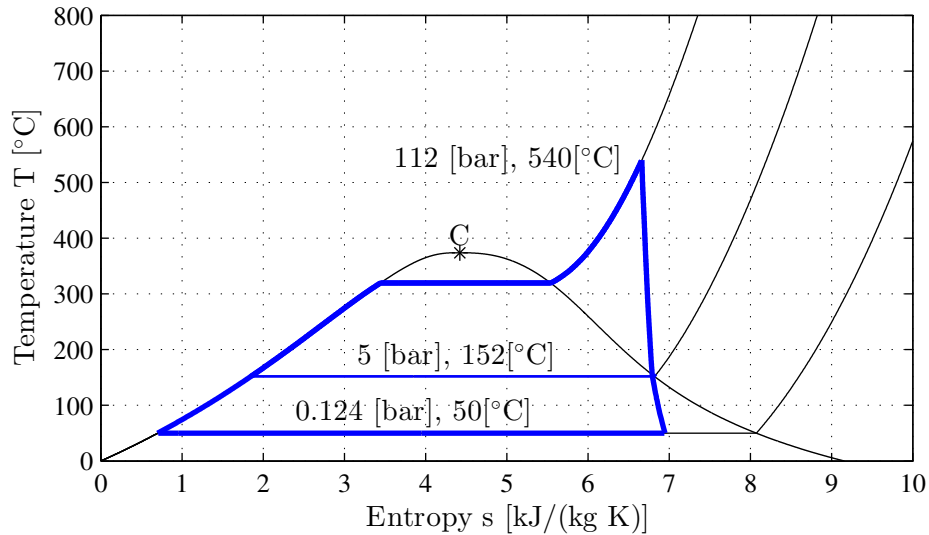


Figure 8.4 – Temperature-entropy (T-s) diagram of the steam cycle with optimised inlet and extraction pressure based on the Alstom Mid-Sized Steam Turbine (MT) [Alstom, 2010]. Assumptions: no pressure drop, 0.93 turbine isentropic efficiency.

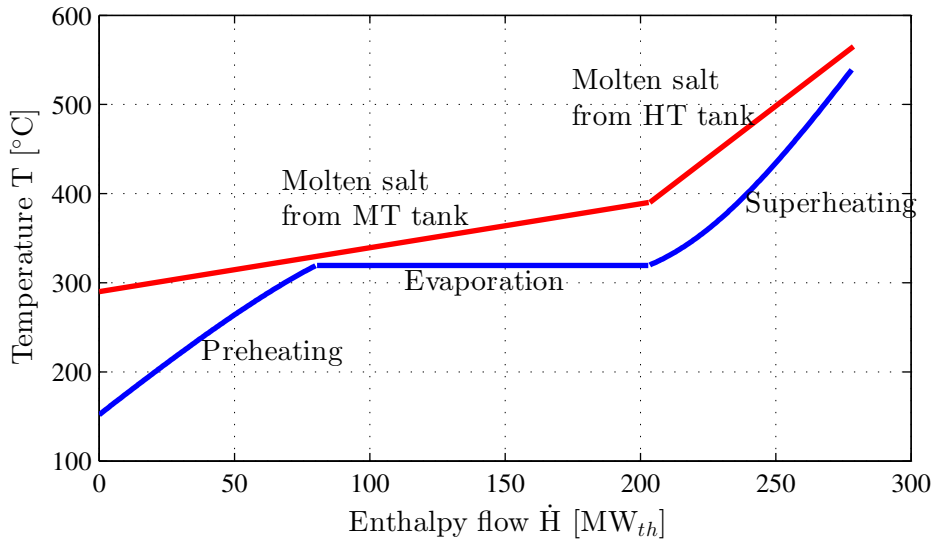


Figure 8.5 – Temperature-enthalpy flow (T - \dot{H}) diagram of the preheating, evaporation and superheating in the steam cycle with optimised inlet and extraction pressure, based on the Alstom Mid-Sized Steam Turbine (MT) [Alstom, 2010], with hot molten salt streams from both the tower and trough systems, for the 100 [MW_{el}] case study.

performed on the turbine inlet and extraction parameters and are mapped in Figure 8.3. The best efficiencies turn out to be achieved with one extraction only, and the set-up that features the maximum efficiency of 40.7% without violating the pinch point is obtained with a 112 [bar] turbine inlet pressure and a 5 [bar] low pressure extraction for feedwater preheating. Figure 8.4 gives the T - s diagram for this cycle set-up, and Figure 8.5 shows the composite curves of the molten salt streams and water/steam streams in a temperature-enthalpy flow (T - \dot{H}) diagram for the following 100 [MW_{el}] case study (\dot{H} is equivalent to the transformation power \dot{Y}).

8.2.2 100 [MW_{el}] Case Study

A trough/tower combination set-up is proposed here for a 100 [MW_{el}] nominal net electric power. First, the steam cycle is scaled up to achieve these 100 [MW_{el}] considering a 99% mechanical efficiency, a 99% electric efficiency, and 10% of overall auxiliary consumption for oil and molten salt pumps, storage electric heaters, condenser fans, etc. This results in a 278.4 [MW_{th}] nominal thermal power requirement for the entire conversion of preheated feedwater into superheated heat (see Figure 8.4), while the 5 [bar] extraction provides a 35.2 [MW_{th}] preheat power. In detail, the steam generation thus breaks down into 80.2 [MW_{th}] of preheat (excluding the 35.2 [MW_{th}] extraction preheat), 122.9 [MW_{th}] of evaporation, and 75.3 [MW_{th}] of superheat. Both the preheat and the evaporation needs have to be met by the trough system, and the superheat by the tower system, which means that 203.1 [MW_{th}] of molten salt transformation power is required from the trough system between 290 [°C] and 390 [°C], and 75.3 [MW_{th}] from the tower system between 290 [°C] and 565 [°C].

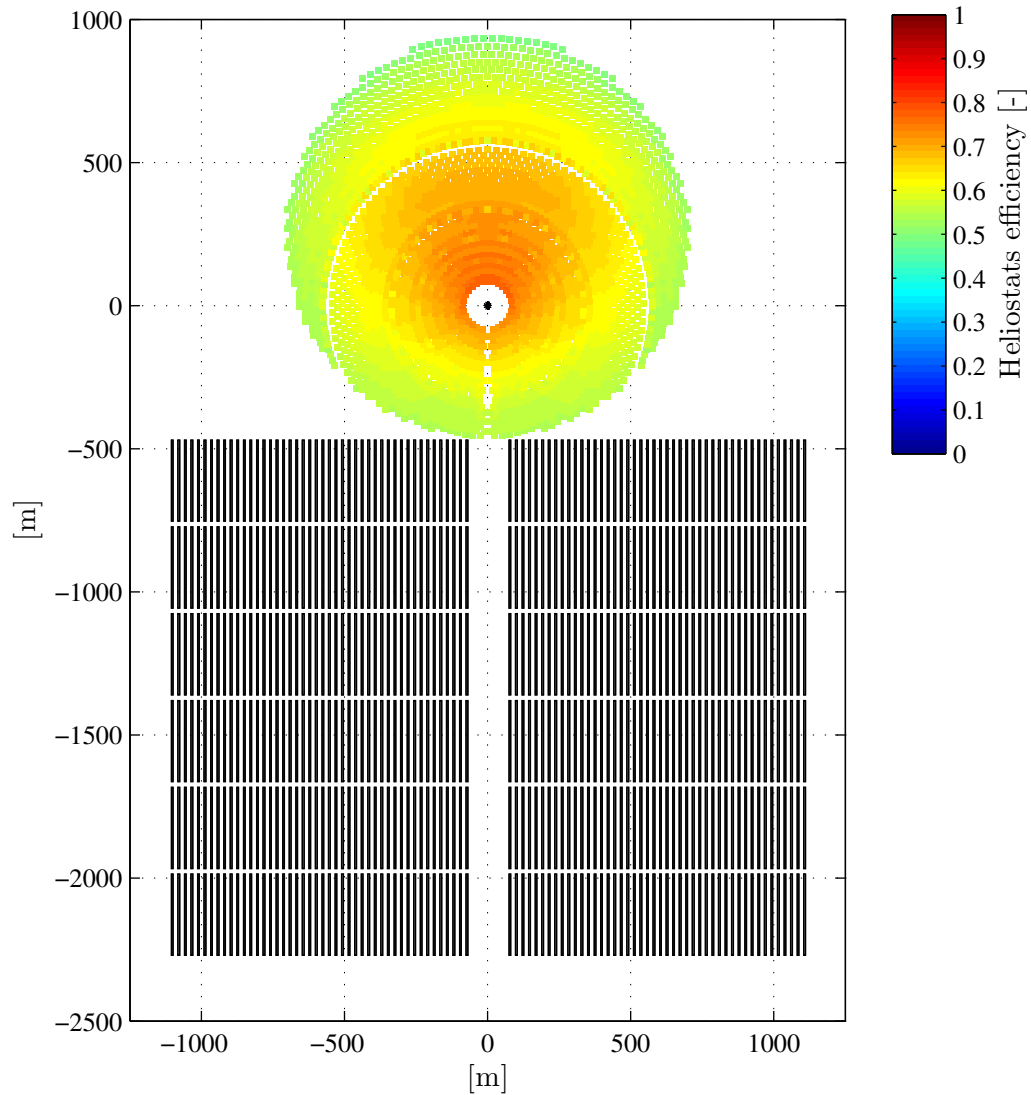


Figure 8.6 – Heliostat/trough field for 100 [MW_{el}] with Gemasolar solar multiple of 2.8 and the best steam cycle featuring one extraction (see Figures 8.4 and 8.5, heliostat field from point N in Annex F).

Second, the trough field and the tower field are designed in order to meet those identified heat requirements. The suitable trough field is obtained by scaling up the Andasol-1 plant presented in §8.1 from 156 to 266 modules to achieve 203.1 [MW_{th}] of nominal thermal power with a solar multiple of 2.8. All the other design parameters are kept the same and reminded in Table 8.1. Then the heliostat field is picked from the optimal trade-off Pareto curve presented in Annex F with a constrained receiver size (below 16 [m] width and 20 [m] height) and tower

Chapter 8. Trough-Tower Combination

Table 8.1 – Parameters of the trough/tower field for the 100 [MW_{el}] case study with Gemasolar solar multiple of 2.8 and the best steam cycle featuring one extraction (see Figures 8.4 and 8.5, heliostat field from point N in Annex F).

| <i>Trough set-up</i> | | <i>Unit</i> | <i>Tower set-up</i> | | <i>Unit</i> |
|--------------------------|-------|-------------|----------------------|-------|-------------|
| Trough module width | 5.77 | [m] | Heliostat width | 9.64 | [m] |
| Trough module length | 566.7 | [m] | Heliostat height | 12.61 | [m] |
| Number of trough modules | 266 | [u] | Rad. spacing coeff. | 0.68 | [-] |
| Glass outer diameter | 0.125 | [m] | South-to-north ratio | 0.56 | [-] |
| Glass thickness | 0.005 | [m] | Number of heliostats | 3208 | [u] |
| Tube outer diameter | 0.07 | [m] | Tower height | 196.6 | [m] |
| Tube thickness | 0.002 | [m] | Receiver diameter | 15.7 | [m] |
| | | | Receiver height | 19.5 | [m] |

height (below 200 [m]). The optimal trade-off set-up that achieves at least 75.3 [MW_{th}] of nominal thermal power with a solar multiple of 2.8 is represented by the point N, whose design parameters are also reported in Table 8.1. With more than 3'200 heliostats of about 9.6 [m] by 12.6 [m] and a tower height close to 200 [m], this heliostat field has a significantly larger reflective area than Gemasolar. Subsequently, a simple layout of the two collector fields side by side is shown in Figure 8.6: since the heliostat field has a shorter southern radius, it is located to the north of the trough field to limit the distance from the trough plant to the tower and this way anticipate piping and heat losses in the high temperature molten salt loop.

Third, the thermo-economic performance of the 100 [MW_{el}] tower/trough combination is simulated the exact same way as previously. The performances of both the trough and the tower fields are gathered together in Table 8.2 and lead to the overall energy and economic indicators for the combined set-up. From the energy point of view, the parabolic mirrors show a higher peak efficiency than the heliostat field (74.2% vs. 68.9%), but the latter shows a slightly greater annual efficiency (62.7% vs. 61.3 %). Then the trough receivers turn out to perform better than the central receiver both at the peak (91.8% vs. 89.2 %) and over the entire year (87.8% vs. 85.2 %). From the economic point of view, the specific cost of nominal thermal power reaches 1'254 [\$/kW_{th,nom}] for the trough field against 1'777 [\$/kW_{th,nom}] for the tower field, which highlights the potential cost decrease in comparison with a tower system alone. With this configuration, the heliostat field accounts for 19% of the total plant investment costs and the trough field for a large share of 36.1% (see Figure 8.7). The storage system accounts for a large share as well (35.2%), due to the high solar multiple here of 2.8 to operate over night in the summer. Concerning the PCU investment, the size of the steam turbine leads to a lower specific cost than for Gemasolar or Andasol-1 through a strong scaling effect: the turbine and generator together account for only 6.9% of the total investment.

8.2. Trough/Tower Combination

Table 8.2 – Performance of the trough/tower field for the 100 [MW_{el}] case study with Gemasolar solar multiple of 2.8 and the best steam cycle featuring one extraction (see Figures 8.4 and 8.5, heliostat field from point N in Annex F).

| <i>Energy performance</i> | Trough | Tower | |
|-----------------------------|---------------|---------------|------------------------------------------------|
| Solar incident | 2'196 (902.4) | 779.7 (348.1) | [GWh _{th}] ([MW _{th,max}]) |
| Field efficiency | 0.613 (0.742) | 0.627 (0.689) | [-] ([- _{max}]) |
| Receiver incident | 1'345 (623.8) | 488.8 (238.8) | [GWh _{th}] ([MW _{th,max}]) |
| Receiver efficiency | 0.878 (0.918) | 0.852 (0.892) | [-] ([- _{max}]) |
| Receiver output | 1'180 (572.1) | 416.4 (212.9) | [GWh _{th}] ([MW _{th,max}]) |
| Cycle thermal input | 1'173 (203.8) | 413.9 (75.8) | [GWh _{th}] ([MW _{th,nom}]) |
| Tot. cycle thermal input | 279.6 | | [MW _{th}] |
| Net electric power | 102.5 | | [MW _{el}] |
| Annual electric output | 585.1 | | [GWh _{el}] |
| <i>Economic performance</i> | | | |
| Investment costs | 255.6 | 134.7 | [M\$] |
| Storage costs | 241.8 | | [M\$] |
| PCU costs | 75.9 | | [M\$] |
| Total investment costs | 707.9 | | [M\$] |
| Levelised electricity cost | 16.1 | | [¢/kWh _{el}] |
| Payback period | 5.43 | | [y] |
| Net present value | 966.8 | | [M\$] |

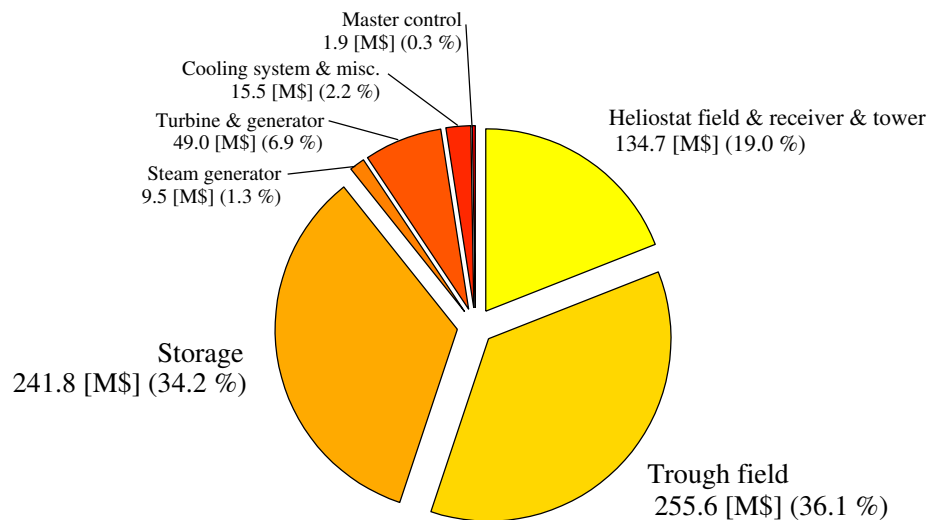


Figure 8.7 – Estimate of the plant cost breakdown of the trough/tower field for the 100 [MW_{el}] case study with Gemasolar solar multiple of 2.8 and the best steam cycle featuring one extraction (see Figures 8.4 and 8.5, heliostat field from point N in Annex F).

8.3 Summary

The combination of a field of parabolic trough collectors with a heliostat field and its central receiver is investigated to identify the potential efficiency increase and cost decrease. First, the trough plant is modelled and the thermo-economic performance of the existing Andasol-1 case [SolarMillenium, 2008] is estimated (see Annex I). Then a trough/tower plant set-up based on two molten salt levels is proposed. A conventional steam turbine cycle is selected and its inlet and extraction pressure levels are optimised to be integrated within the plant set-up considering the two temperature levels of molten salt storage.

Subsequently, a 100 [MW_{el}] combination set-up is studied by scaling up the Andasol-1 trough field and picking a heliostat field from the constrained thermo-economic optimisation in Annex F. As a result, the LEC of the trough/tower combined plant goes down to 16.1 [¢/kWh_{el}] and its payback period to 5.4 years thanks to both systems contributions: the tower system allows a higher steam temperature at the turbine inlet, a higher cycle efficiency and lower PCU specific costs, while the trough system allows lower collector field specific costs. For the sake of comparison, the equivalent 100 [MW_{el}] tower plant set-up obtained from the optimal trade-off curve in §6.3 (point B, see Figure 6.5) reaches 18.2 [¢/kWh_{el}] and 5.7 years, and the scaling of Andasol-1 up to 100 [MW_{el}] with a solar multiple of 2.8 leads to 22.2 [¢/kWh_{el}] and 9.2 years. Furthermore, as the specific environmental impacts per [MWh_{el}] of a tower plant turn out to be lower than those of a trough plant (see Annex J), the trough/tower combination is expected to decrease the specific impacts in comparison with the trough plant alone.

In further analyses of the trough/tower combination and its potentials, a complete integration of the steam cycle is recommended, including multiple preheaters, reheaters and evaporation pressure levels in order to better match the molten salt streams and increase efficiency. Then a combined thermo-economic optimisation of the trough field, the tower field and the conversion cycle at the same time is required to investigate the best trough/tower trade-off set-ups.

9 Conclusions and Outlook

With about 2 [GW_{el}] of worldwide installed capacity in 2012, the concentrating solar power industry is at an early stage of its development in comparison with other renewable technologies like photovoltaic panels or wind turbines. Despite changing regulatory frameworks and slow financing schemes such as currently in Spain and the USA, more than 2.5 [GW_{el}] are under construction, and around 13 [GW_{el}] under planning. Unlike common photovoltaic facilities, CSP plants have the potential on the long run to provide baseload capacity to the grid, and thus work in complementarity with PV plants that provide peak load. Among CSP technologies, the solar tower thermal power plants achieve the highest temperature level, which is expected to lead to better efficiencies of the heat-to-electricity conversion cycle according to Carnot, e.g. with steam cycles close to 45% or combined cycles above that. Furthermore, the cost of central tower systems on the long run is also expected to decrease and reach targets close to the grid-parity such as 6 [¢/kWh_{el}].

In this context, the heliostat field obviously is a key element both for the energy performance and the economic performance of the plant, as it accounts for the largest losses along the solar-to-electricity conversion and for the most important cost share among the plant equipments. About 30 heliostat fields have been built since the early eighties, first experimental and pilot facilities, and then medium- to large-scale commercial facilities (10'000 [m²] to 1'000'000 [m²]) from the late 2000s. The thermo-economic modelling, simulation, sensitivity analysis and optimisation presented here with an emphasis on the heliostat field allow the assessment of existing plants, the identification of potential improvements, and the selection of the best energy/cost trade-off set-ups for the next generation of very large plants to be designed.

9.1 Thermo-Economic Simulation of Solar Tower Power Plants

The thermo-economic simulation of a solar tower power plant starts with the identification of the relevant local environmental conditions: obviously the direct normal irradiance and the sun's position over time, then if needed the ambient temperature and the wind direction and velocity. For instance, high wind velocities above 10 [m/s] turn out to have a significant

impact on the first-law efficiency of a molten salt external receiver (e.g. 0.9 without wind, 0.83 at 40 [m/s]), but remain extremely rare for example in the case of Gemasolar according to local wind time maps, and lead to the shut-down of the heliostats anyway. However, the wind conditions show a strong impact on the receiver flux transients caused by clouds, even for low wind velocities: for the most frequent conditions near Sevilla (from 220° at 6.6 [m/s]), a maximum receiver power transient of 1.7 [MW_{th}/s] may be achieved due to a cloud covering the heliostat field.

Then the generation of the heliostat field layout is performed by combining a no-blocking algorithm with the definition of an azimuthal and a radial spacing coefficient. These two spacing coefficients represent a cursor between the no-touching and the no-blocking conditions applied to neighbouring heliostats, and this way they are key design variables that lead to a trade-off between field efficiency and field density. Subsequently, the numerical simulation of the heliostat field's behaviour over time shows that shading and blocking losses only account for a relatively small share of the total plant losses: e.g. respectively 1.7% and 1.6% for a Gemasolar-like layout. Furthermore, in the same example the spillage losses on the receiver turn out to be the second largest losses (after cosine losses which are nearly unavoidable), which highlights the Gemasolar field's weaknesses: the heliostats are well arranged to avoid blocking, but as a result they are in general too far away from the receiver, causing a strong spillage and in the end a rather low efficiency of 45.3%. Therefore the trade-off approach presented here is recommended for large fields and preferred to pure no-blocking approaches.

After a simulation over three specific days (the two solstices and the spring equinox), the field efficiency is interpolated over the entire year as a function of the sun's azimuth and elevation angles. In comparison with the direct annual calculation, the interpolation shows a relative error below 1% and about 100 times less computation time. Hence the obtained annual receiver power profile is implemented as the input for the storage system and the heat-to-electricity conversion cycle. The operating strategy presented allows the design of the storage capacity, the estimate of the number of full-load hours, as well as the minimisation of start-ups and shut-downs per day (e.g. 306/y in the Gemasolar simulation). Besides, a time map diagram of the electric output power highlights the periods when the plant is able to operate overnight.

In parallel, the receiver incident flux distribution is calculated in order to identify concentration peaks and gradients, as well as transients especially with cloud passages on the heliostat field. In this latter case, the proposed procedure to lower the risk of receiver failure allows to keep the transients below a given level: e.g. for a cloud covering Gemasolar, the progressive shut-down in advance of 18 heliostats per second keeps the transient below 10 [kW/m²/s]. Moreover, two strategies of multi-aiming on the receiver surface are presented and show a flux peak decrease of up to 25% with only a 2% drop in total receiver incident power. In the frame of the plant optimisation, the knowledge of the receiver flux peak is then used as a constraint to select only set-ups with less than 1500 [kW_{th}/m²].

Once the energy performance of the solar tower plant is assessed, its economic performance is estimated thanks to a detailed cost analysis of the equipment that takes the scaling, the volume and the price index effects into account. The heliostat field accounts for the largest cost share with more than 40% in the Gemasolar simulation, followed by the storage system with 20% and the receiver with 14%, the other elements remaining below 10%. Looking at the heliostats in particular, the main costs appear to be the drives with around 30%, the structure with more than 20%, and the mirrors with 18%. On the one hand, a sensitivity on the heliostat size shows only a small improvement potential of the specific cost, with a minimum reached around 200 [m²]. On the other hand, a sensitivity on the production volume clearly shows a potential cost decrease down to 150 [\$/m²] and below. Subsequently, some financial performance indicators are estimated thanks to the simulated annual plant electric output, which provides an assessment of the economic viability over the plant lifetime. For example, the levelised electricity cost achieves 24 [¢/kWh_{el}] in the Gemasolar simulation, which is below the Spanish feed-in tariff of 34 [¢/kWh_{el}]. This way the viability criterion of a positive net present value is respected and the payback period is completed long before the end of life.

9.2 Optimal Thermo-Economic Trade-Off Set-Ups

The thermo-economic optimisation of a solar tower plant results in a set of optimal trade-off configurations. First and prior to the application of an evolutionary multi-objective algorithm, a sensitivity analysis is performed on the Gemasolar case in order to determine the key design variables of the plant. The analysis highlights the contradiction between energy and economic objectives such as the field efficiency and the levelised electricity cost. At the same time, it identifies already potential improvements: for instance a 15 points increase of the annual field efficiency appears with a 4.5 times greater receiver area, while a 2 [¢/kWh_{el}] maximum decrease in LEC appears with a 3 times greater receiver area. Then the large range optimisation itself shows a potential 24 points increase in efficiency with the same LEC as Gemasolar, and a 9 [¢/kWh_{el}] drop in LEC with large plants up to 5'000'000 [m²] of reflective area. Furthermore, in the case of a constrained optimisation with the same receiver and tower dimensions as Gemasolar, the same net electric power is achieved with a 6 points higher efficiency, a 1 [¢/kWh_{el}] lower LEC, and 40% less land area.

In a second step, the generation of multi-tower layouts is expected to open the road to very large plants beyond 5'000'000 [m²]. In the example of a three-tower layout equivalent to the single-tower of Gemasolar, an aim selection criterion is implemented based on the minimisation of cosine, attenuation and spillage losses, which leads to a 15 points more efficient heliostat field but with a 5 [¢/kWh_{el}] higher LEC. Therefore, the optimal transition from single- to multi-tower set-ups is investigated: at about 55 times the reflective area of Gemasolar, the two-tower set-ups start showing a greater electric output than the single-tower set-ups. And then at around 60 times, the three-tower layouts start performing better than the two-tower set-ups. Hence these transition sizes are far beyond the nowadays largest known facilities like Ivanpah, whose reflective area is expected to be only four times larger than the Gemasolar

field. Moreover, the LEC turns out to undergo a stagnation even for multi-tower set-ups at around 15 [¢/kWh_{el}].

In a third step, the combination of a parabolic trough collector field and a central tower system with the same power conversion unit is an alternative to bring costs down in the short-term. As the trough collectors currently remain less costly than heliostats for an equivalent aperture area, the specific cost of a combined trough/tower field is lower than that of a heliostat field alone. In comparison with a trough plant alone, the tower system added to the trough system allows to raise the temperature level of the heat-to-electricity conversion cycle, and thus increase its first-law efficiency. The case study of a 100 [MW_{el}] trough/tower set-up shows a 16.1 [¢/kWh_{el}] LEC against 18.2 [¢/kWh_{el}] for an equivalent 100 [MW_{el}] tower plant taken from the optimal trade-off set-ups previously.

9.3 Future Work

Both the simulation and the optimisation of solar tower plants obviously still have potential work areas. Regarding the heliostat field layout, the topology needs to be taken into account by mapping the local bumps and hollows and adapting the heliostats positions. Forbidden areas may also have to be implemented, such as protected zones for flora or fauna in cases like Ivanpah. Such an approach minimises the impact on the land area by limiting ground levelling and the number of roads, but is a challenge for the mirror cleaning.

Then the calculation of the heliostat field losses based on a convolution-based method is less time-consuming and more flexible for the programming of add-on functions and graphics, however ray-tracing methods are more accurate and allow a greater flexibility on the heliostats and receiver shapes. A ray-tracing method is especially suitable for the receiver incident flux distribution, on the condition that its calculation can still be performed in real-time as in the case of cloud passages. Besides, in this latter situation, an appropriate strategy is required for the regulation of the receiver mass flow, whatever the heat transfer fluid is. For molten salt receiver in particular, a detailed thermo-mechanical modelling and control is needed to avoid freezing and material failure. In parallel, beyond molten salt cycles, other cycle configurations have to be taken into consideration, especially air combined cycles (hybrid or not) which are expected to reach significantly better cycle efficiencies by taking advantage of higher temperature levels at the receiver.

Looking at the assessment of the economic performance, the approach here is rather conservative: beyond the effect of scaling and production volume, some technological innovations are expected to bring the costs down and may be taken into account on the long run. For instance, the structure of the heliostats is undergoing significant improvements with lighter components and less complex assemblies. Furthermore, the growing worldwide deployment of solar tower plants also has an impact on the specific cost of single equipments like the receiver or the power block, and should further lower the final LEC.

Concerning the thermo-economic optimal set-ups, the multi-objective optimisation may be extended with the minimisation of the environmental impact as a third objective provided by a detailed life cycle analysis (including impacts on human health, ecosystem, climate change and resources). Subsequently, the optimum transition from single- to multi-tower set-ups might occur at much smaller field sizes thanks to significantly lower costs. Above all, the option of a common power conversion unit for all the towers has to be investigated by modelling for example the piping of molten salt from each tower to a central storage tank. This way the central PCU becomes much larger than for a single tower system, with potentially several hundreds of $[MW_{el}]$ and thus a strong scaling effect on the PCU costs. Finally, the trough/tower combination requires a complete integration of the conversion cycle with possibly multiple pressure levels and reheats, as well as a combined thermo-economic optimisation by adding some heat exchangers and varying the share of each technology.

A List of Heliostat Fields

Appendix A. List of Heliostat Fields

Table A.1 – List of heliostat fields sorted by ascending total reflective area (1a).

| <i>Description</i> | <i>Location</i> | <i>Country</i> | <i>Lat.</i> [°] | <i>Long.</i> [°] | <i>Alt.</i> [m] | <i>DNI</i> [kWh/ m ² /y] | <i>Start</i> | <i>Instit./Org.</i> |
|--------------------|----------------------|----------------|--------------------|---------------------|--------------------|-------------------------------------------|--------------|---------------------|
| AORA Samar | Kibbutz Samar | Israel | 29.83 | 35.02 | 100 | 1948 | 2009 | AORA Solar Ltd. |
| Solastor Cooma | Cooma, NSW | Australia | -36.23 | 149.15 | 824 | - | 2009 | Solastor |
| AORA Almeria | Almeria | Spain | 37.10 | -2.36 | 502 | 2472 | 2012 | AORA Solar Ltd. |
| Hohai | Nanjing | China | 31.92 | 118.79 | 7 | - | 2005 | Hohai University |
| NSEC 1 | Newcastle, NSW | Australia | -32.88 | 151.73 | 14 | - | 2005 | NSEC-CSIRO |
| NSEC 2 | Newcastle, NSW | Australia | -32.88 | 151.73 | 14 | - | 2011 | NSEC-CSIRO |
| Odeillo | Odeillo | France | 42.49 | 2.03 | 1537 | 2217 | 1970 | PROMES |
| UzAS | Parkent | Uzbekistan | 41.31 | 69.74 | 1048 | - | 1976 | UzAS |
| WIS | Rehovot | Israel | 31.91 | 34.82 | 56 | 1936 | 1992 | WIS |
| SSPS-CRS | Almería | Spain | 37.09 | -2.36 | 502 | 2471 | 1981 | PSA |
| Lake Cargelligo | Lake Cargelligo, NSW | Australia | -33.31 | 146.41 | 160 | - | 2011 | Solastor |
| CRTF | Albuquerque, NM | USA | 34.96 | -106.51 | 1704 | 2464 | 1978 | SNL |
| EURELIOS | Adrano | Italy | 37.65 | 14.80 | 216 | 1685 | 1981 | EEC |
| Thémis | Targassonne | France | 42.50 | 1.97 | 1660 | 2154 | 1982 | PROMES |

Table A.2 – List of heliostat fields sorted by ascending total reflective area (1b).

| <i>Description</i> | <i>Land</i> | | <i>Heliostats</i> | | | | | | | | |
|--------------------|-------------------------------|---------------------|-------------------|---------------------|-------------------------------|-----------------|-----------------|------------------------------------|-----------------|------------------------------------|----------------------------------|
| | <i>A</i> [m ²] | <i>Slope</i> [°] | <i>N</i> [u] | <i>Mirr.</i> [u] | <i>A</i> [m ²] | <i>W</i> [m] | <i>H</i> [m] | <i>Tot. A</i> [m ²] | <i>ρ</i> [%] | <i>σ_{Track}</i> [mrad] | <i>σ_{Tot}</i> [mrad] |
| AORA Samar | 2000 | - | 30 | 9 | 9.00 | - | - | 270 | - | - | - |
| Solastor Cooma | 2300 | - | 100 | 1 | 4.30 | - | - | 430 | - | - | - |
| AORA Almeria | - | - | 52 | 16 | 9.00 | - | - | 468 | - | - | - |
| Hohai | - | - | 32 | 9 | 20.00 | - | - | 640 | 85 | ≤2 | - |
| NSEC 1 | - | - | 170 | 1 | 4.30 | - | - | 731 | - | - | - |
| NSEC 2 | - | - | 450 | 1 | 4.00 | - | - | 1800 | - | - | - |
| Odeillo | - | - | 63 | 180 | 45.00 | - | - | 2835 | - | - | - |
| UzAS | - | - | 62 | 195 | 48.80 | 7.50 | 6.50 | 3026 | - | - | - |
| WIS | - | - | 64 | 20 | 54.25 | - | - | 3472 | - | - | - |
| SSPS-CRS | - | - | 91 | 12 | 39.30 | - | - | 3576 | 87 | 1.70 | 3.00 |
| Lake Cargelligo | - | - | 620 | 1 | 9.81 | - | - | 6080 | - | - | - |
| CRTF | - | - | 222 | 25 | 30.50 | - | - | 6771 | - | - | - |
| EURELIOS | - | 4.5 | 85 147 | - | 51.80 23.00 | 8.50 5.00 | 7.30 5.50 | 7784 | 80 85 | - | - |
| Thémis | 11800 | 6-18 | 201 | 48 | 53.70 | - | - | 10794 | - | - | - |

Appendix A. List of Heliostat Fields

Table A.3 – List of heliostat fields sorted by ascending total reflective area (1c).

| <i>Description</i> | <i>Tower</i> | | <i>Receiver</i> | <i>D</i> | <i>H</i> | <i>A</i> | <i>T</i> | Eff. | <i>Power</i> |
|--------------------|--------------|----------|-----------------------------------------------------|----------|----------|-------------------|----------|-------|---------------------|
| | <i>N</i> | <i>H</i> | <i>Type</i> | [m] | [m] | [m ²] | [°C] | [%] | [kW _{th}] |
| AORA Samar | 1 | 30.0 | WIS-like | - | - | - | - | - | - |
| Solastor Cooma | 1 | 24.0 | Cavity: graphite hollow | - | - | - | 800 | - | - |
| AORA Almeria | 1 | 30.0 | WIS-like | - | - | - | - | - | - |
| Hohai | 1 | 33.0 | WIS-like | - | - | - | - | - | - |
| NSEC 1 | 1 | 20.0 | Reactor | - | - | - | 1000 | - | 500 |
| NSEC 2 | 1 | 30.0 | - | - | - | - | 1000 | - | 1000 |
| Odeillo | 1 | - | - | 0.8 | - | - | - | - | 1000 |
| UzAS | 1 | - | - | - | - | - | 3000 | - | 1000 |
| WIS | 1 | 27.0 | Cavity: sec. conc. (CPC) + window + vol. abs. | 0.4 | - | - | - | 70-80 | 30-50 |
| SSPS-CRS | 1 | 43.0 | Multiple | - | - | - | - | - | - |
| Lake Cargelligo | 8 | 24.0 | Cavity: graphite hollow | - | - | - | 800 | - | - |
| CRTF | 1 | 61.0 | Multiple | - | - | - | - | - | 5000 |
| EURELIOS | 1 | 50.0 | - | 4.5 | - | 20.2 | - | - | - |
| Thémis | 1 | 100.0 | Multiple | - | - | - | 6.5 | 5.0 | 400-4600 |

Table A.4 – List of heliostat fields sorted by ascending total reflective area (1d).

| <i>Description</i> | <i>HTF Medium</i> | <i>T</i> [°C] | <i>P</i> [bar] | <i>Storage Medium</i> | <i>Capacity</i> [kWh _{th}] | <i>Length</i> [h] |
|--------------------|---------------------------|----------------------|-------------------|---------------------------|-----------------------------------------|----------------------|
| AORA Samar | air | 1000 | - | - | - | - |
| Solastor Cooma | steam | - | - | Graphite | 3000 | - |
| AORA Almeria | air | 1000 | - | - | - | - |
| Hohai | air | 900 | 4 | - | - | - |
| NSEC 1 | - | - | - | - | - | - |
| NSEC 2 | - | - | - | - | - | - |
| Odeillo | - | 3000 | - | - | - | - |
| UzAS | - | - | - | - | - | - |
| WIS | air | 900 | 10-30 | - | - | - |
| SSPS-CRS | sodium | 530 | - | - | - | 2.0 |
| Lake Cargelligo | steam | 200-500 | 20-50 | Graphite | 3000 | - |
| CRTF | air/steam /salt/sodium | 1065/518 /565/593 | 10.3/138 /-/- | - | - | - |
| EURELIOS | steam/salt | - | - | steam/salt | - | 0.5 |
| Thémis | air/salt | 1000/450 | 10/- | - | - | 5.0 |

Appendix A. List of Heliostat Fields

Table A.5 – List of heliostat fields sorted by ascending total reflective area (1e).

| <i>Description</i> | <i>PCU Type</i> | <i>Cooling</i> | <i>Nom. el. pow. [kW_e]</i> | <i>Reference</i> |
|--------------------|--------------------------|----------------|-------------------------------------------|------------------------|
| AORA Samar | hybrid micro gas turbine | - | 100 | [AORA, 2009] |
| Solastor Cooma | steam turbine | - | 83 | [Solarstor, 2009] |
| AORA Almeria | hybrid micro gas turbine | - | 100 | [AORA, 2009] |
| Hohai | micro gas turbine | - | 70 | [Jun et al., 2009] |
| NSEC 1 | - | - | - | [CSIRO, 2011] |
| NSEC 2 | hybrid gas turbine | - | - | [CSIRO, 2011] |
| Odeillo | - | - | - | [PROMES, 2011a] |
| UzAS | - | - | - | [UzAS, 2008] |
| WIS | - | - | - | [WIS, 2010] |
| SSPS-CRS | - | - | 500 | [PSA, 2012a] |
| Lake Cargelligo | steam turbine | - | 3'000 | [Lloyd, 2011] |
| CRTF | - | - | - | [SNL, 2012] |
| EURELIOS | - | - | 1'000 | [Hartung et al., 1980] |
| Thémis | hybrid gas turbine | - | 2'000-2'500 | [PROMES, 2011b] |

Appendix A. List of Heliostat Fields

Table A.6 – List of heliostat fields sorted by ascending total reflective area (2a).

| <i>Description</i> | <i>Location</i> | <i>Country</i> | <i>Lat.</i> [°] | <i>Long.</i> [°] | <i>Alt.</i> [m] | <i>DNI</i> [kWh/ m ² /y] | <i>Start</i> | <i>Instit./Org.</i> |
|--------------------|-------------------------|----------------|--------------------|---------------------|--------------------|-------------------------------------------|--------------|--------------------------------------|
| CESA-1 | Almería | Spain | 37.09 | -2.36 | 503 | 2473 | 1983 | PSA |
| Sunshine | Nio | Japan | 34.20 | 133.65 | - | - | 1981 | Agency of Industr. Sc. & Tech. |
| Jülich | Jülich | Germany | 50.91 | 6.39 | 88 | 923 | 2008 | DLR |
| SEDC | Rotem, Negev desert | Israel | 31.02 | 35.09 | 439 | 2117 | 2008 | BrightSource Energy |
| Sierra SunTower | Lancaster, CA | USA | 34.73 | -118.14 | 707 | 2646 | 2009 | eSolar, Inc. |
| SPP-5 | Shchelkino, Crimea | Ukraine | 45.40 | 35.86 | 3 | 1777 | 1986 | - |
| Coalinga | Coalinga, CA | USA | 36.17 | -120.39 | 232 | 2281 | 2011 | BrightSource Energy |
| Solar One | Barstow, CA | USA | 34.87 | -116.83 | 594 | 2829 | 1982 | DOE |
| PS10 | Sanlúcar la Mayor | Spain | 37.44 | -6.25 | 64 | 2162 | 2007 | Abengoa Solar, S.A. |
| Solar Two | Barstow, CA | USA | 34.87 | -116.83 | 594 | 2829 | 1996 | DOE |
| PS20 | Sanlúcar la Mayor | Spain | 37.44 | -6.26 | 71 | 2162 | 2009 | Abengoa Solar, S.A. |
| Gemasolar | Fuentes de Andalucía | Spain | 37.56 | -5.33 | 168 | 2097 | 2011 | Torresol Energy Invest., S.A. |
| Crescent Dunes | Tonopah, NV | USA | 38.24 | -117.36 | 1498 | 2685 | 2013 | SolarReserve, LLC |
| Ivanpah | Ivanpah Dry Lake, CA | USA | 35.54 | -115.45 | 879 | 2646 | 2013 | BrightSource Energy |

Table A.7 – List of heliostat fields sorted by ascending total reflective area (2b).

| <i>Description</i> | <i>Land</i> | | <i>Heliostats</i> | | | | | | | | |
|--------------------|-------------------------------|---------------------|-------------------|---------------------|-------------------------------|-----------------|-----------------|------------------------------------|---------------|----------------------------|--------------------------|
| | <i>A</i> [m ²] | <i>Slope</i> [°] | <i>N</i> [u] | <i>Mirr.</i> [u] | <i>A</i> [m ²] | <i>W</i> [m] | <i>H</i> [m] | <i>Tot. A</i> [m ²] | ρ [%] | σ_{Track} [mrad] | σ_{Tot} [mrad] |
| CESA-1 | 82500 | - | 300 | 12 | 39.60 | - | - | 11880 | 90 | 1.70 | 3.00 |
| Sunshine | - | - | 807 | - | 16.00 | - | - | 12912 | - | - | - |
| Jülich | 160000 | - | 2153 | 1 | 8.36 | - | - | 17999 | - | - | - |
| SEDC | - | - | 1600 | 1 | 14.40 | - | - | 23040 | - | - | - |
| Sierra SunTower | 80937 | - | 24000 | 1 | 1.14 | - | - | 27264 | - | - | - |
| SPP-5 | - | - | 1600 | - | 25.00 | - | - | 40000 | - | - | - |
| Coalinga | 404686 | - | 3822 | 2 | 15.61 | 4.27 | 3.66 | 59653 | - | - | - |
| Solar One | - | - | 1818 | 12 | 39.13 | 6.60 | 6.24 | 71138 | 90.3 | 2.10 | 3.34 |
| PS10 | 598935 | - | 624 | 28 | 120.00 | 12.94 | 10.12 | 74880 | 0.94 | 1.30 | 2.91 |
| Solar Two | - | - | 1818 108 | 12 16 | 39.13 95.00 | 6.60 9.48 | 6.24 10.02 | 81400 | 90.3 93.5 | 2.1 2.1 | 3.34 2.97 |
| PS20 | - | - | 1255 | - | 120.00 | 12.94 | 10.12 | 150600 | - | - | - |
| Gemasolar | 1850000 | - | 2650 | 35 | 120.00 | 10.96 | 10.95 | 318000 | - | - | - |
| Crescent Dunes | 5309292 | - | 17300 | - | 62.50 | - | - | 1081250 | - | - | - |
| Ivanpah | 14164000 | - | 300000 | 2 | 14.08 | - | - | 4224000 | - | - | - |

Appendix A. List of Heliostat Fields

Table A.8 – List of heliostat fields sorted by ascending total reflective area (2c).

| <i>Description</i> | <i>Tower</i> | | <i>Receiver</i> | <i>D</i> | <i>H</i> | <i>A</i> | <i>T</i> | <i>Eff.</i> | <i>Power</i> |
|--------------------|--------------|----------|-----------------------------------------|----------|----------|-------------------|----------|-------------|---------------------|
| | <i>N</i> | <i>H</i> | <i>Type</i> | [m] | [m] | [m ²] | [°C] | [%] | [kW _{th}] |
| CESA-1 | 1 | 80.0 | Multiple | - | - | - | - | - | - |
| Sunshine | - | 69.0 | - | - | - | - | - | 74.8 | - |
| Jülich | 1 | 60.0 | atm. vol. absorber | - | - | 22.0 | - | - | 2500 |
| SEDC | 1 | 60.0 | External: flat, tubular | - | - | - | - | - | 6000 |
| Sierra SunTower | 2 | 55.0 | Cavity: tubular | - | - | - | - | - | - |
| SPP-5 | 1 | - | - | - | - | - | - | - | - |
| Coalinga | 1 | 100.0 | External: flat, tubular | - | - | - | - | - | 29000 |
| Solar One | 1 | 84.0 | External: cylindrical, tubular | 7.0 | 13.7 | 301.3 | - | 78.0 | - |
| PS10 | 1 | 115.0 | Cavity: half-cylindrical, tubular | 14.8 | 12.0 | 257.3 | - | 92.0 | 47700 |
| Solar Two | 1 | 76.2 | External: cylindrical, tubular | 5.1 | 6.2 | 99.3 | - | 88.0 | 42200 |
| PS20 | 1 | 165.0 | Cavity: half-cylindrical, tubular | - | - | - | - | - | - |
| Gemasolar | 1 | 140.0 | External: cylindrical, tubular | - | - | - | - | - | 120000 |
| Crescent Dunes | 1 | 200.0 | External: cylindrical, tubular | - | - | - | - | - | 565000 |
| Ivanpah | 3 | 140.0 | External: cylindrical, tubular | - | - | - | - | - | - |

Table A.9 – List of heliostat fields sorted by ascending total reflective area (2d).

| <i>Description</i> | <i>HTF Medium</i> | <i>T [°C]</i> | <i>P [bar]</i> | <i>Storage Medium</i> | <i>Capacity [kWh_{th}]</i> | <i>Length [h]</i> |
|---------------------------|------------------------------|--------------------------|---------------------------|----------------------------------|-----------------------------------------------|------------------------------|
| CESA-1 | air | - | - | - | - | 3.5 |
| Sunshine | steam | 250 | 40 | water | - | 3.0 |
| Jülich | air | 700 | 1 | - | - | - |
| SEDC | steam | 540 | - | - | - | - |
| Sierra SunTower | steam | 440 | 60 | - | - | - |
| SPP-5 | steam | 250 | - | water/steam | - | - |
| Coalinga | steam | - | - | - | - | - |
| Solar One | steam | 516 | - | oil/rock | - | - |
| PS10 | steam | 250 | 40 | steam | 15000 | 0.5 |
| Solar Two | salt | 565 | - | salt | 107000 | 3.0 |
| PS20 | steam | 250-300 | 45 | steam | - | 1.0 |
| Gemasolar | salt | 565 | - | salt | - | 15.0 |
| Crescent Dunes | salt | 565 | - | salt | - | 10.0 |
| Ivanpah | steam | 565 | - | - | - | - |

Appendix A. List of Heliostat Fields

Table A.10 – List of heliostat fields sorted by ascending total reflective area (2e).

| <i>Description</i> | <i>PCU Type</i> | <i>Cooling</i> | <i>Nom. el. pow. [kW_e]</i> | <i>Reference</i> |
|--------------------|---------------------|----------------|-------------------------------------------|----------------------|
| CESA-1 | steam turbine | - | 1'200 | [PSA, 2012b] |
| Sunshine | steam turbine | - | 1'000 | - |
| Jülich | steam turbine | - | 1'500 | [DLR, 2008] |
| SEDC | - | - | - | [BrightSource, 2008] |
| Sierra SunTower | steam turbine | wet | 50'00 | [ESolar, 2009] |
| SPP-5 | - | - | 5'000 | - |
| Coalinga | - | - | eq. 13'000 | [BrightSource, 2011] |
| Solar One | - | - | 10'000 | [Kolb et al., 1991] |
| PS10 | steam turbine | wet | 11'000 | [Abengoa, 2007] |
| Solar Two | steam turbine | - | 11'136 | [Pacheco, 2002] |
| PS20 | steam turbine | wet | 20'000 | [Abengoa, 2009] |
| Gemasolar | steam turbine | - | 19'900 | [Torresol, 2011] |
| Crescent Dunes | steam turbine | hybrid | 110'000 | [Gould, 2011] |
| Ivanpah | steam turbine | dry | 126'000 | [BrightSource, 2012] |



Figure A.1 – Samar heliostat field (AORA, see on the left), Kibbutz Samar, Israel, 2009 [Google, 2012, AORA, 2009].



Figure A.2 – Hohai university heliostat field (see on the left), Nanjing, China, 2005 [Google, 2012, Jun et al., 2009].



Figure A.3 – NSEC heliostat field (see on the left), Newcastle, New South Wales, Australia, 2005 [Google, 2012, CSIRO, 2011].



Figure A.4 – Odeillo heliostat field, PROMES, Odeillo, France, 1970 [Google, 2012, PROMES, 2011a].



Figure A.5 – UzAS heliostat field, Parkent, Uzbekistan, 1976 [Google, 2012, UzAS, 2008].

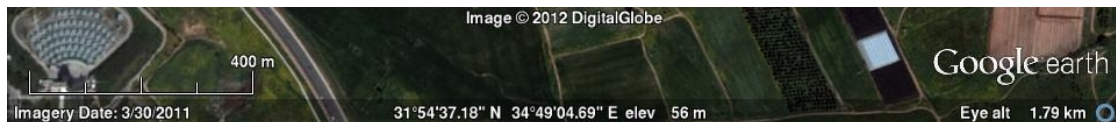


Figure A.6 – WIS heliostat field, Rehovot, Israel, 1992 [Google, 2012, WIS, 2010].



Figure A.7 – SSPS-CRS heliostat field, PSA, Almería, Spain, 1981 [Google, 2012, PSA, 2012a].

Appendix A. List of Heliostat Fields



Figure A.8 – CRTF heliostat field, SNL, Albuquerque, New Mexico, USA, 1978 [Google, 2012, SNL, 2012].



Figure A.9 – EURELIOS heliostat field, Adrano, Italy, 1981 [Google, 2012, Hartung et al., 1980].



Figure A.10 – Themis heliostat field, PROMES, Targassonne, France, 1982 [Google, 2012, PROMES, 2011b].



Figure A.11 – CESA-1 heliostat field, PSA, Almería, Spain, 1983 [Google, 2012, PSA, 2012b].



Figure A.12 – Jülich heliostat field, DLR, Jülich, Germany, 2008 [Google, 2012, DLR, 2008].



Figure A.13 – SEDC heliostat field (BrightSource Energy), Rotem Industrial Park, Negev desert, Israel, 2008 [Google, 2012, BrightSource, 2008].



Figure A.14 – Sierra SunTower heliostat field (eSolar), Lancaster, California, USA, 2009 [Google, 2012, ESolar, 2009].



Figure A.15 – SPP-5 heliostat field, Shchelkino, Crimea, Ukraine, 1986.



Figure A.16 – Coalinga heliostat field (Chevron/BrightSource), Coalinga, California, USA, 2011 [Google, 2012, BrightSource, 2011].

Appendix A. List of Heliostat Fields



Figure A.17 – PS10 heliostat field (Abengoa), Sanlúcar la Mayor, Spain, 2007 [Google, 2012, Abengoa, 2007].



Figure A.18 – Solar One/Two heliostat field, Barstow, California, USA, 1982 [Google, 2012, Pacheco, 2002].

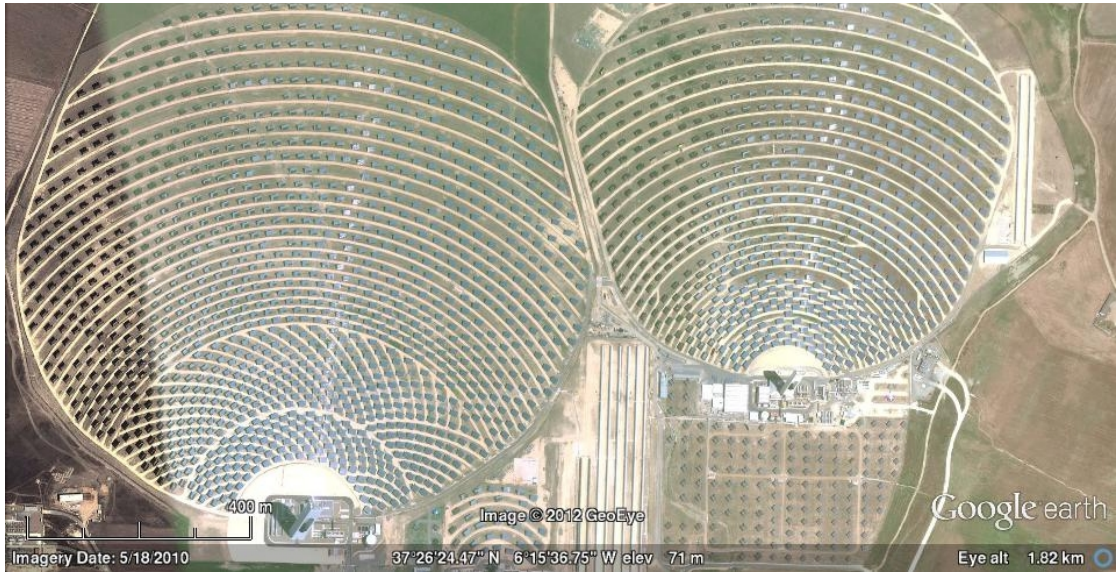


Figure A.19 – PS20 heliostat field (Abengoa), Sanlúcar la Mayor, Spain, 2009 [Google, 2012, Abengoa, 2009].

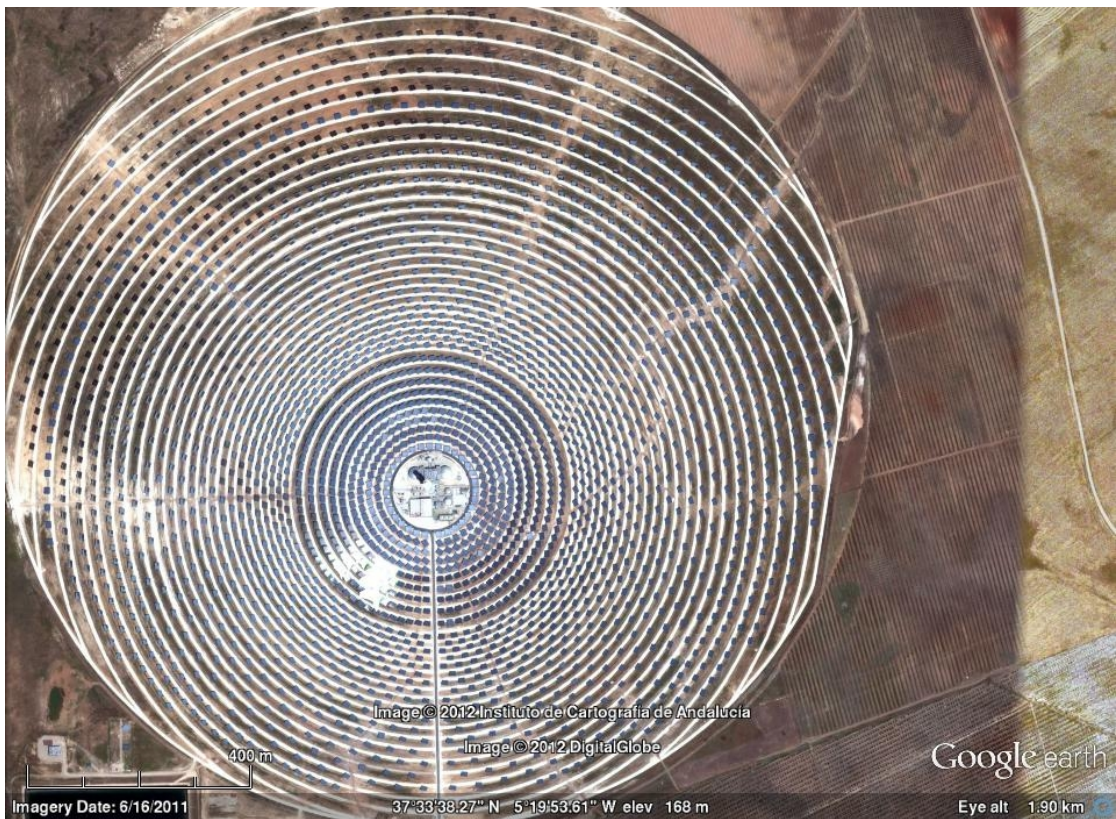


Figure A.20 – Gemasolar heliostat field (Torresol), Fuentes de Andalucía, Spain, 2011 [Google, 2012, Torresol, 2011].

Appendix A. List of Heliostat Fields

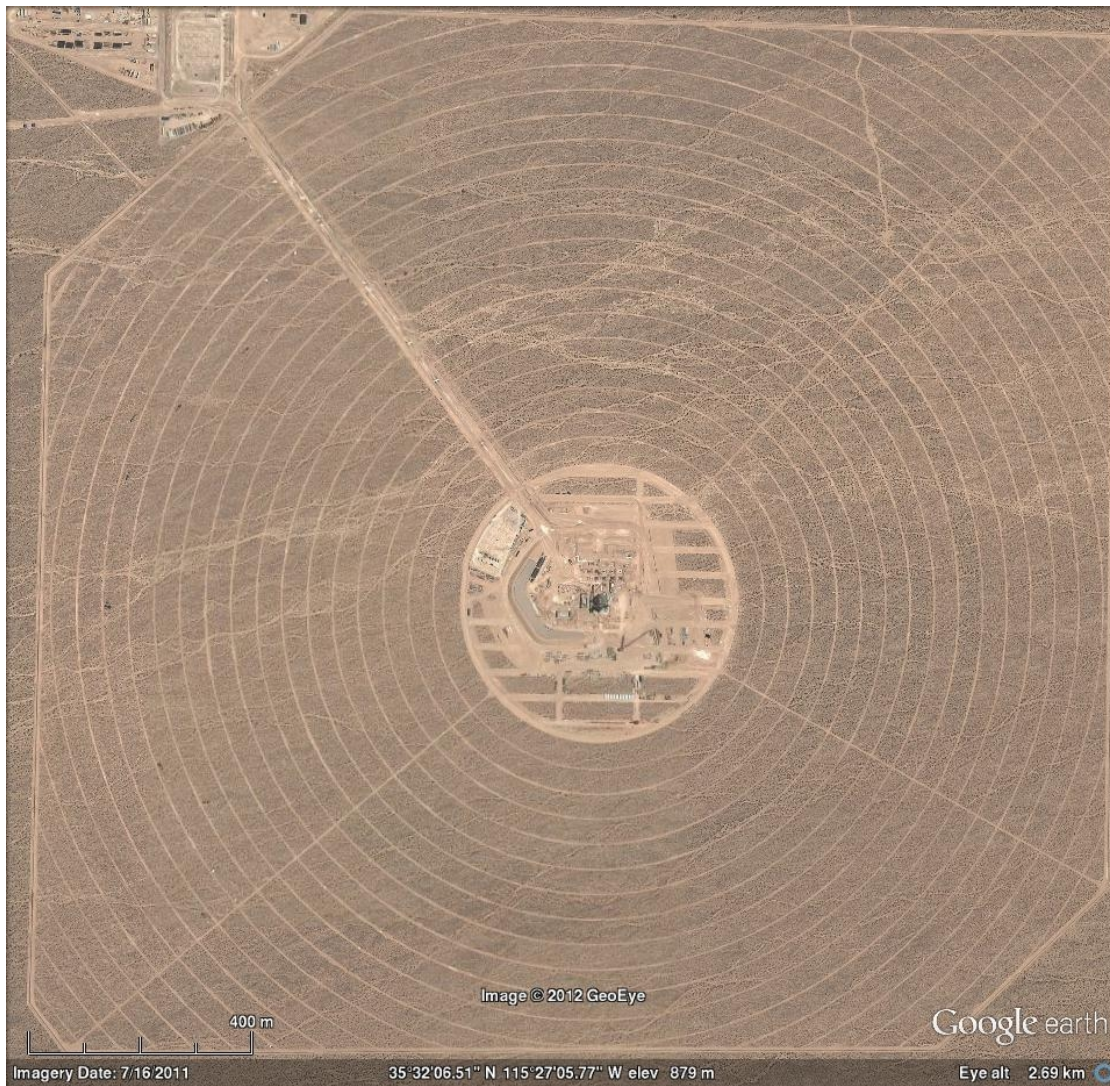


Figure A.21 – Ivanpah heliostat field (BrightSource), Ivanpah Dry Lake, California, USA, 2012 [Google, 2012, BrightSource, 2012].

B DNI comparison at Gemasolar

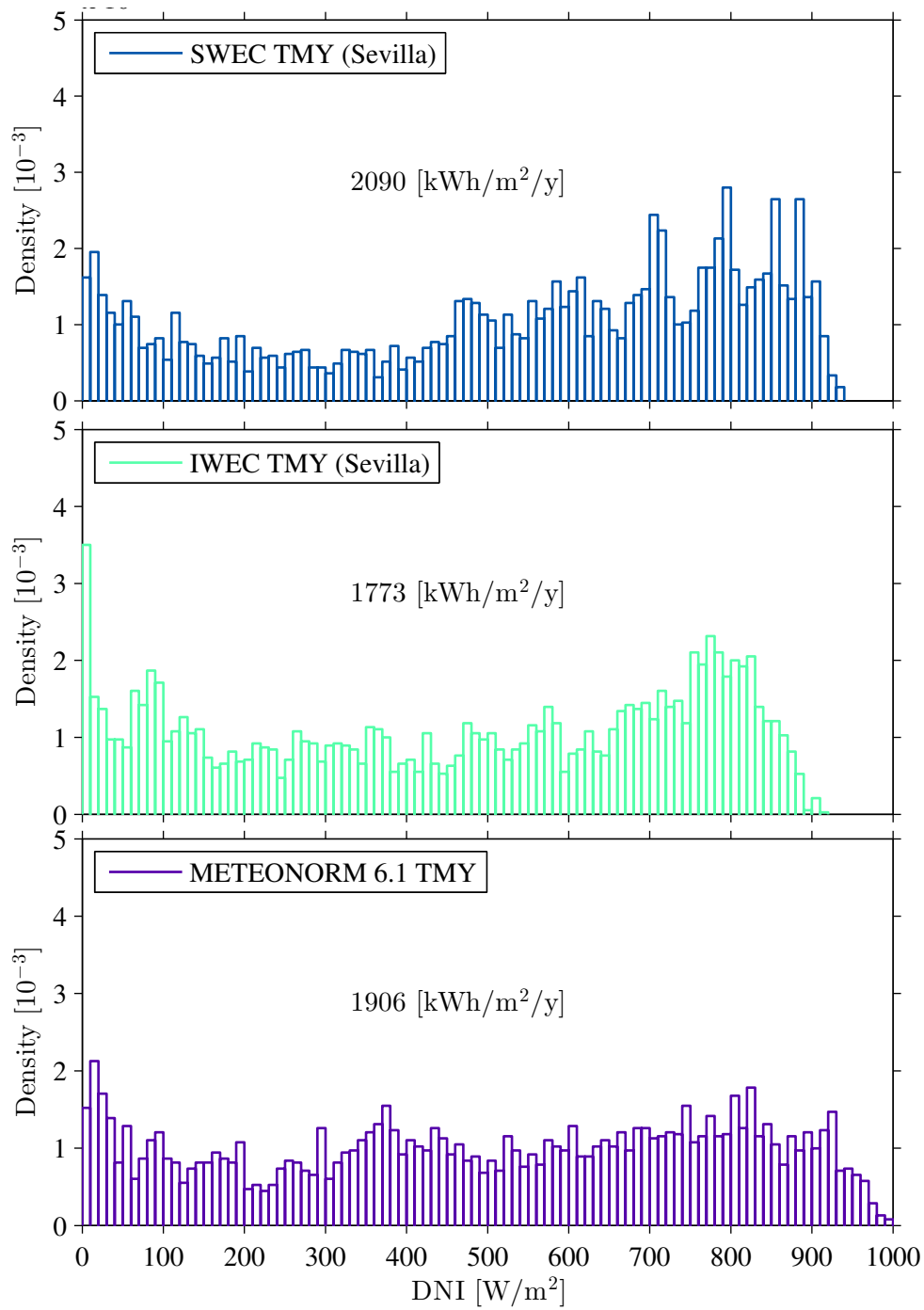


Figure B.1 – Comparison of DNI databases for the Gemasolar site, TMY data from [SWEC, 2012, ASHRAE, 2001, Meteonorm, 2012].

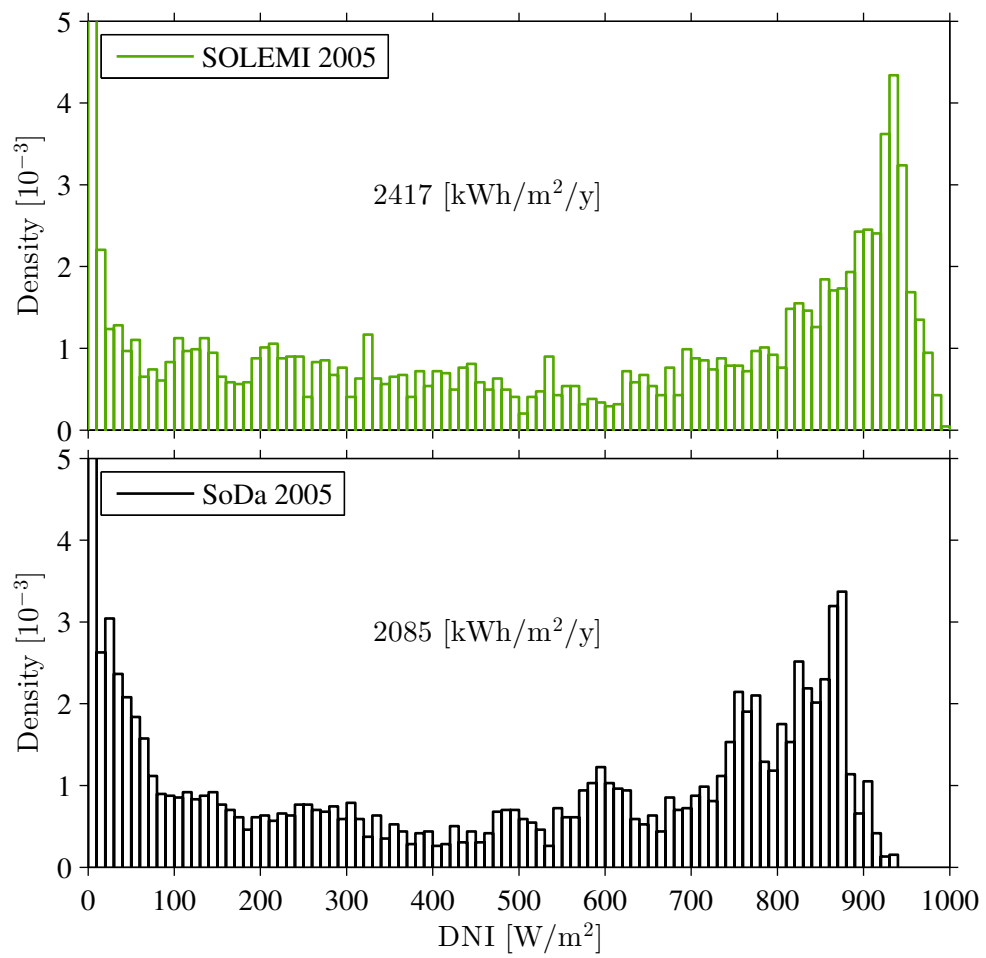


Figure B.2 – Comparison of DNI databases for the Gemasolar site, data from [SOLEMI, 2005, SoDa, 2004].

C Comparison with HFLCAL

(see internal technical report [Reiner Buck, 2008])

C.1 Assumptions for Heliostat Field Simulations

Site

- site latitude: 37.4°north (corresponding to Seville, Spain)
- site altitude: 23 m (= 75.46 ft)

Solar Radiation Data

See Table C.1 and C.2.

Other Assumptions

Shading from the tower and the receiver is neglected.

Shading and Blocking of the heliostats is taken into account.

Heliostat Specification

See Table C.3.

Heliostat Positions

The heliostat field consists of 4001 heliostats, with the heliostat positions as defined in Figure C.1.

C.1. Assumptions for Heliostat Field Simulations

Table C.1 – DNI (1) for the comparison with HFLCAL [Schwarzbözl et al., 2009].

| Day | ST [h] | DNI [W/m ²] |
|-----|-----------|----------------------------|
| 30 | 7.73 | 530 |
| 30 | 8.73 | 768 |
| 30 | 9.73 | 878 |
| 30 | 10.73 | 927 |
| 30 | 11.73 | 949 |
| 30 | 12.73 | 927 |
| 30 | 13.73 | 912 |
| 30 | 14.73 | 832 |
| 30 | 15.73 | 668 |
| 81 | 7.65 | 469 |
| 81 | 8.65 | 607 |
| 81 | 9.65 | 686 |
| 81 | 10.65 | 866 |
| 81 | 11.65 | 951 |
| 81 | 12.65 | 957 |
| 81 | 13.65 | 918 |
| 81 | 14.65 | 824 |
| 81 | 15.65 | 706 |
| 81 | 16.65 | 487 |
| 118 | 6.15 | 489 |
| 118 | 7.15 | 730 |
| 118 | 8.15 | 844 |
| 118 | 9.15 | 903 |
| 118 | 10.15 | 937 |
| 118 | 11.15 | 941 |
| 118 | 12.15 | 929 |
| 118 | 13.15 | 907 |
| 118 | 14.15 | 892 |
| 118 | 15.15 | 815 |
| 118 | 16.15 | 728 |
| 118 | 17.15 | 579 |
| 118 | 18.15 | 301 |

Appendix C. Comparison with HFLCAL

Table C.2 – DNI (2) for the comparison with HFLCAL [Schwarzbözl et al., 2009].

| Day | ST [h] | DNI [W/m ²] |
|-----|-----------|----------------------------|
| 172 | 6.67 | 351 |
| 172 | 8.67 | 254 |
| 172 | 9.67 | 888 |
| 172 | 10.67 | 888 |
| 172 | 11.67 | 897 |
| 172 | 12.67 | 864 |
| 172 | 13.67 | 848 |
| 172 | 14.67 | 816 |
| 172 | 15.67 | 764 |
| 172 | 16.67 | 686 |
| 172 | 17.67 | 592 |
| 172 | 18.67 | 317 |
| 350 | 7.85 | 396 |
| 350 | 8.85 | 672 |
| 350 | 9.85 | 770 |
| 350 | 10.85 | 856 |
| 350 | 11.85 | 859 |
| 350 | 12.85 | 867 |
| 350 | 13.85 | 835 |
| 350 | 14.85 | 721 |
| 350 | 15.85 | 489 |

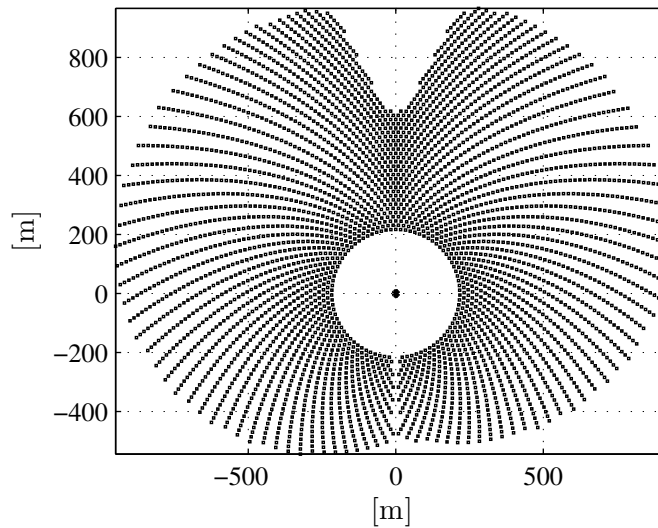


Figure C.1 – 4000 heliostats layout for a 300 [MW_{th}] receiver obtained with [Zhang et al., 2007].

C.1. Assumptions for Heliostat Field Simulations

Table C.3 – Heliostat for the comparison with HFLCAL [Schwarzbözl et al., 2009].

| Type | azimuth-elevation tracking |
|----------------------------|-------------------------------------|
| Geometry Parameters | |
| Heliostat width | 10.01 m |
| Heliostat height | 11.88 m |
| Pedestal height | 6.94 m (1 m + 1/2 heliostat height) |
| Facet size | 2.5025 m x 1.697 m |
| Facet area | 4.2471 m ² |
| no. of facet rows | 7 |
| no. of facet columns | 4 |
| gaps between facets | no |
| total reflective area | 118.92 m ² |
| Optical parameters | |
| Facet focussing | focal point = aim point |
| Canting | on-axis, canting point = aim point |
| mirror slope error | 2.6 mrad |
| tracking error (each axis) | 0.919 mrad (= 1.3 mrad total) |
| mirror reflectivity | 88 % |

Heliostat Aim Points

The heliostat aim points are located at a height of 157.37 m on the receiver surface. The circumferential position is defined by the intersection of the circular receiver outline and the vector from the heliostat center to the receiver center axis, in x,y-plane.

Receiver Dimensions

The receiver is defined as follows:

- full cylindrical receiver

The last position data set was ignored (position $x=0.0\text{m}, y=0.0\text{m}$)

- vertical orientation

- receiver height: 22 m

- receiver diameter: 12 m

- receiver center position: $x = 0 \text{ m}, y = 0 \text{ m}, z = 157.37 \text{ m}$

- flux map grid: 100 bins in circumferential direction, 30 bins along z-direction

C.2 Power Calculations with HFLCAL

Each power run was carried out with 109 rays. The results are summarized in Table C.4 and C.5. For each case, the intercepted power is given, as well as details on the different loss mechanisms (all relative to the maximum available power):

- cosine loss (only the projected heliostat area is active)
- shading loss (part of a heliostat is shadowed by another heliostat)
- reflection loss (absorption in the reflector surface)
- blocking loss (reflected radiation hits backside of another heliostat)
- atmospheric loss (attenuation of reflected radiation along the radiation path)
- intercept loss (reflected radiation does not hit the defined receiver)

The maximum available power is defined as the actual DNI multiplied by the total heliostat area.

Annual simulation runs were carried out using the "energy run" option. Each energy run was carried out with 109 rays. The annual results are summarized in Table 3.

C.2. Power Calculations with HFLCAL

Table C.4 – HFLCAL results (1).

| Case | intercept. power | cos. loss | shad. loss | refl. loss | block. loss | atm. loss | intercept. loss | field eff. |
|---------|---------------------|--------------|---------------|---------------|----------------|--------------|--------------------|---------------|
| CASE 01 | 77.97 MW | 27.26% | 27.88% | 5.38% | 1.62% | 2.65% | 4.29% | 30.92% |
| CASE 02 | 162.06 MW | 23.73% | 12.08% | 7.70% | 2.94% | 3.68% | 5.51% | 44.35% |
| CASE 03 | 210.33 MW | 21.03% | 6.24% | 8.73% | 3.59% | 4.13% | 5.93% | 50.35% |
| CASE 04 | 235.57 MW | 19.34% | 2.36% | 9.40% | 5.10% | 4.34% | 6.05% | 53.41% |
| CASE 05 | 246.25 MW | 18.62% | 0.69% | 9.68% | 6.03% | 4.41% | 6.03% | 54.54% |
| CASE 06 | 238.93 MW | 18.97% | 1.14% | 9.59% | 5.75% | 4.38% | 6.00% | 54.17% |
| CASE 07 | 226.42 MW | 20.36% | 3.62% | 9.12% | 4.54% | 4.24% | 5.93% | 52.18% |
| CASE 08 | 189.12 MW | 22.78% | 8.58% | 8.24% | 3.06% | 3.92% | 5.65% | 47.77% |
| CASE 09 | 126.27 MW | 26.06% | 16.22% | 6.93% | 2.74% | 3.31% | 5.03% | 39.73% |
| CASE 10 | 96.50 MW | 26.84% | 10.11% | 7.57% | 3.88% | 3.48% | 4.87% | 43.24% |
| CASE 11 | 143.44 MW | 23.06% | 4.41% | 8.70% | 5.00% | 3.96% | 5.20% | 49.67% |
| CASE 12 | 176.02 MW | 20.16% | 1.17% | 9.44% | 5.67% | 4.28% | 5.36% | 53.93% |
| CASE 13 | 231.20 MW | 18.33% | 0.08% | 9.79% | 5.92% | 4.43% | 5.34% | 56.11% |
| CASE 14 | 258.10 MW | 17.46% | 0.01% | 9.90% | 5.82% | 4.49% | 5.27% | 57.04% |
| CASE 15 | 258.90 MW | 17.70% | 0.01% | 9.88% | 5.84% | 4.48% | 5.24% | 56.86% |
| CASE 16 | 242.65 MW | 19.03% | 0.15% | 9.70% | 5.93% | 4.38% | 5.25% | 55.55% |
| CASE 17 | 206.50 MW | 21.42% | 1.86% | 9.21% | 5.49% | 4.16% | 5.19% | 52.67% |
| CASE 18 | 160.81 MW | 24.76% | 5.36% | 8.38% | 4.86% | 3.80% | 4.96% | 47.87% |
| CASE 19 | 93.07 MW | 28.89% | 12.93% | 6.98% | 3.25% | 3.24% | 4.55% | 40.16% |
| CASE 20 | 73.74 MW | 33.34% | 21.03% | 5.48% | 1.96% | 2.61% | 3.89% | 31.69% |
| CASE 21 | 151.41 MW | 28.75% | 8.07% | 7.58% | 3.97% | 3.46% | 4.58% | 43.59% |
| CASE 22 | 198.53 MW | 24.71% | 3.11% | 8.66% | 5.44% | 3.88% | 4.77% | 49.44% |
| CASE 23 | 230.59 MW | 21.44% | 0.22% | 9.40% | 6.24% | 4.20% | 4.84% | 53.67% |
| CASE 24 | 249.64 MW | 19.19% | 0.00% | 9.70% | 6.00% | 4.36% | 4.75% | 56.00% |
| CASE 25 | 257.37 MW | 17.82% | 0.00% | 9.86% | 5.74% | 4.45% | 4.64% | 57.48% |
| CASE 26 | 255.97 MW | 17.50% | 0.00% | 9.90% | 5.64% | 4.47% | 4.58% | 57.91% |
| CASE 27 | 246.53 MW | 18.26% | 0.00% | 9.81% | 5.79% | 4.42% | 4.60% | 57.13% |
| CASE 28 | 234.66 MW | 20.07% | 0.00% | 9.59% | 6.11% | 4.29% | 4.65% | 55.29% |
| CASE 29 | 203.40 MW | 22.85% | 0.55% | 9.19% | 6.18% | 4.08% | 4.69% | 52.45% |
| CASE 30 | 165.18 MW | 26.49% | 4.09% | 8.33% | 5.12% | 3.72% | 4.56% | 47.69% |
| CASE 31 | 113.37 MW | 30.79% | 9.85% | 7.12% | 3.45% | 3.27% | 4.37% | 41.15% |
| CASE 32 | 37.38 MW | 35.51% | 27.14% | 4.48% | 1.30% | 2.17% | 3.30% | 26.10% |
| CASE 33 | 71.23 MW | 30.77% | 8.10% | 7.34% | 3.42% | 3.36% | 4.36% | 42.65% |
| CASE 34 | 63.48 MW | 23.17% | 0.27% | 9.19% | 6.27% | 4.07% | 4.50% | 52.53% |
| CASE 35 | 232.56 MW | 20.50% | 0.00% | 9.54% | 6.30% | 4.25% | 4.37% | 55.04% |
| CASE 36 | 240.04 MW | 18.74% | 0.00% | 9.75% | 6.11% | 4.36% | 4.23% | 56.81% |
| CASE 37 | 244.96 MW | 18.03% | 0.00% | 9.84% | 6.24% | 4.38% | 4.11% | 57.40% |
| CASE 38 | 235.05 MW | 18.34% | 0.00% | 9.80% | 6.21% | 4.37% | 4.11% | 57.18% |
| CASE 39 | 226.21 MW | 19.67% | 0.00% | 9.64% | 6.13% | 4.30% | 4.19% | 56.07% |

Appendix C. Comparison with HFLCAL

Table C.5 – HFLCAL results (2).

| Case | intercept. power | cos. loss | shad. loss | refl. loss | block. loss | atm. loss | intercept. loss | field eff. |
|---------|---------------------|--------------|---------------|---------------|----------------|--------------|--------------------|---------------|
| CASE 40 | 209.05 MW | 21.94% | 0.01% | 9.37% | 6.42% | 4.14% | 4.28% | 53.85% |
| CASE 41 | 184.81 MW | 25.07% | 0.96% | 8.88% | 5.96% | 3.93% | 4.37% | 50.84% |
| CASE 42 | 150.21 MW | 28.92% | 4.67% | 7.97% | 4.56% | 3.57% | 4.29% | 46.02% |
| CASE 43 | 110.63 MW | 33.28% | 10.89% | 6.70% | 2.63% | 3.10% | 4.12% | 39.28% |
| CASE 44 | 36.06 MW | 37.86% | 28.08% | 4.09% | 1.04% | 1.99% | 3.04% | 23.91% |
| CASE 45 | 46.67 MW | 27.16% | 37.00% | 4.30% | 0.93% | 2.18% | 3.66% | 24.77% |
| CASE 46 | 132.22 MW | 23.86% | 16.26% | 7.19% | 2.35% | 3.50% | 5.48% | 41.35% |
| CASE 47 | 178.38 MW | 21.36% | 8.05% | 8.47% | 3.31% | 4.05% | 6.07% | 48.69% |
| CASE 48 | 212.01 MW | 19.87% | 3.24% | 9.23% | 5.09% | 4.29% | 6.23% | 52.06% |
| CASE 49 | 217.43 MW | 19.29% | 1.25% | 9.53% | 6.14% | 4.36% | 6.23% | 53.20% |
| CASE 50 | 217.04 MW | 19.72% | 2.13% | 9.38% | 5.65% | 4.31% | 6.19% | 52.61% |
| CASE 51 | 198.69 MW | 21.19% | 5.83% | 8.76% | 4.02% | 4.13% | 6.06% | 50.01% |
| CASE 52 | 150.60 MW | 23.60% | 13.42% | 7.56% | 2.25% | 3.67% | 5.60% | 43.90% |
| CASE 53 | 75.19 MW | 26.84% | 26.33% | 5.62% | 1.58% | 2.79% | 4.53% | 32.32% |
| Annual | 612.30 GWh | 22.42% | 5.26% | 8.68% | 4.91% | 3.96% | 4.89% | 49.88% |

C.3 Comparison

The results of HFLCAL are compared to the results of [Monterreal, 1998] combined with [Collado et al., 1986] as used in this thesis (see Figure C.2 and C.3).

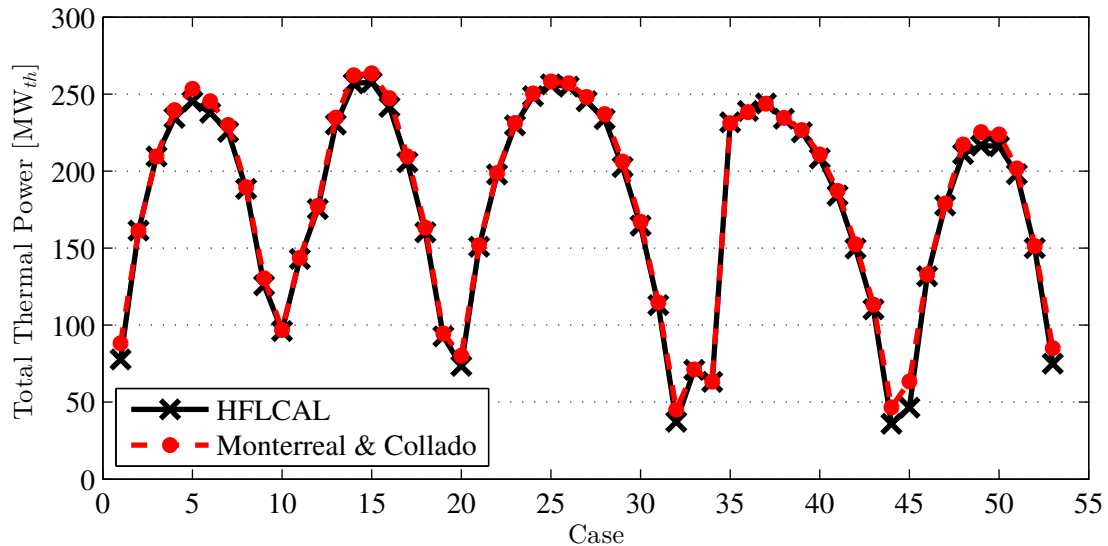


Figure C.2 – Comparison (1) of HFLCAL against [Monterreal, 1998] combined with [Collado et al., 1986].

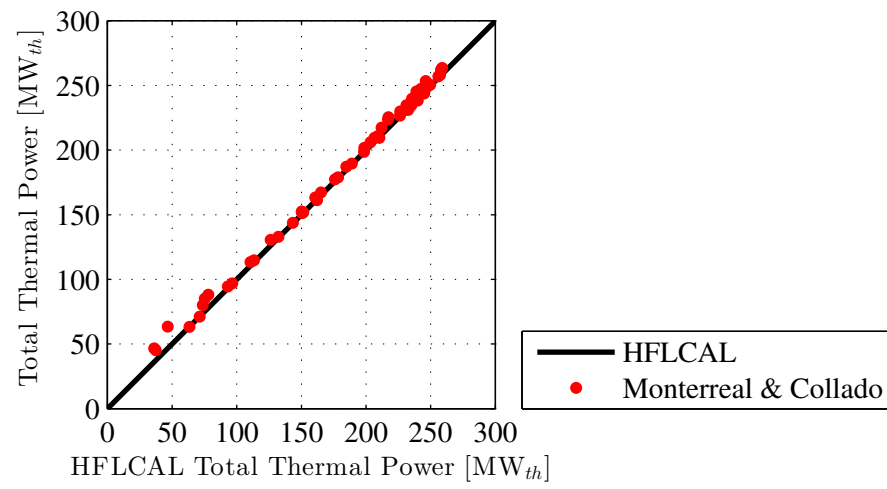
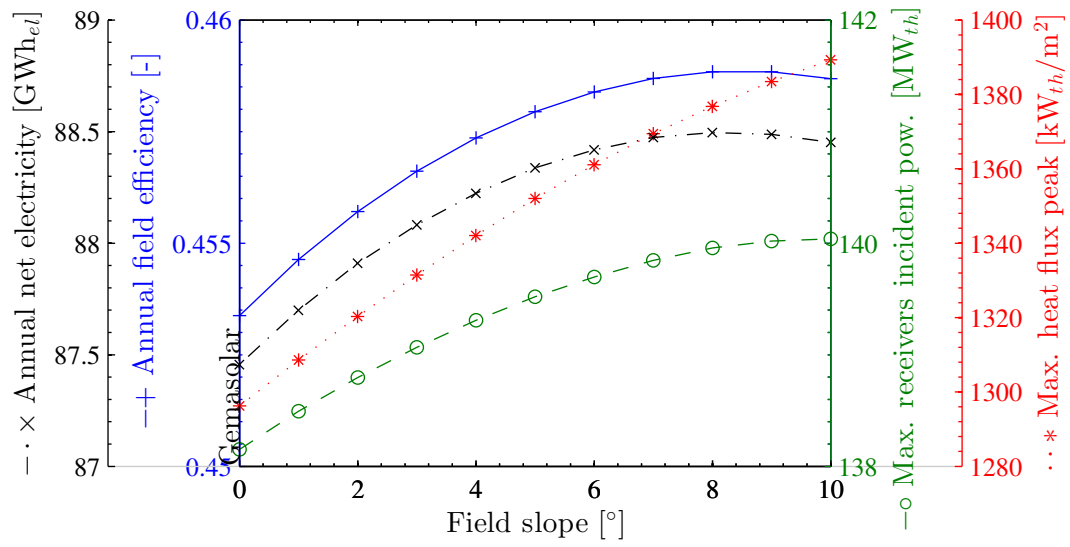


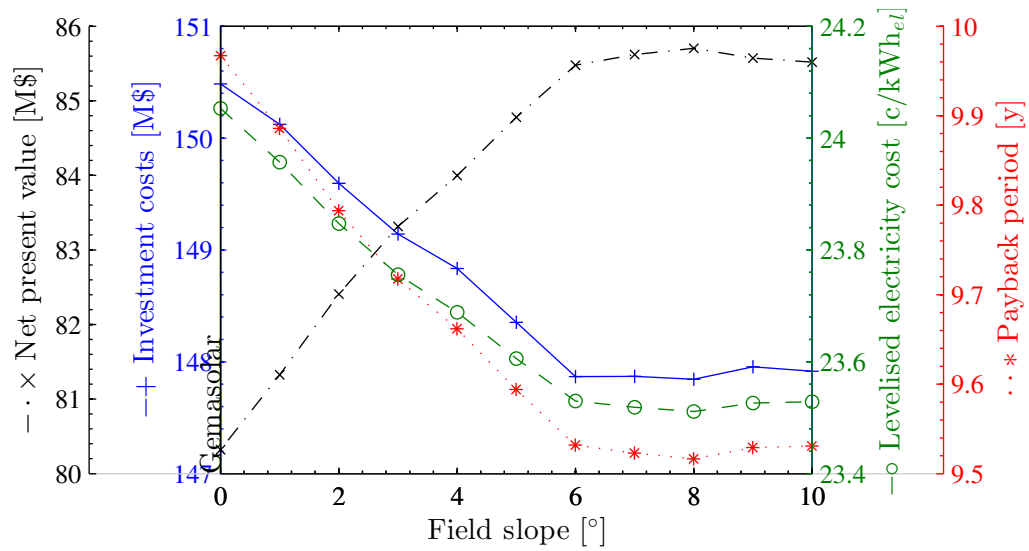
Figure C.3 – Comparison (2) of HFLCAL against [Monterreal, 1998] combined with [Collado et al., 1986].

D Sensitivity Analysis on Gemasolar

Appendix D. Sensitivity Analysis on Gemasolar

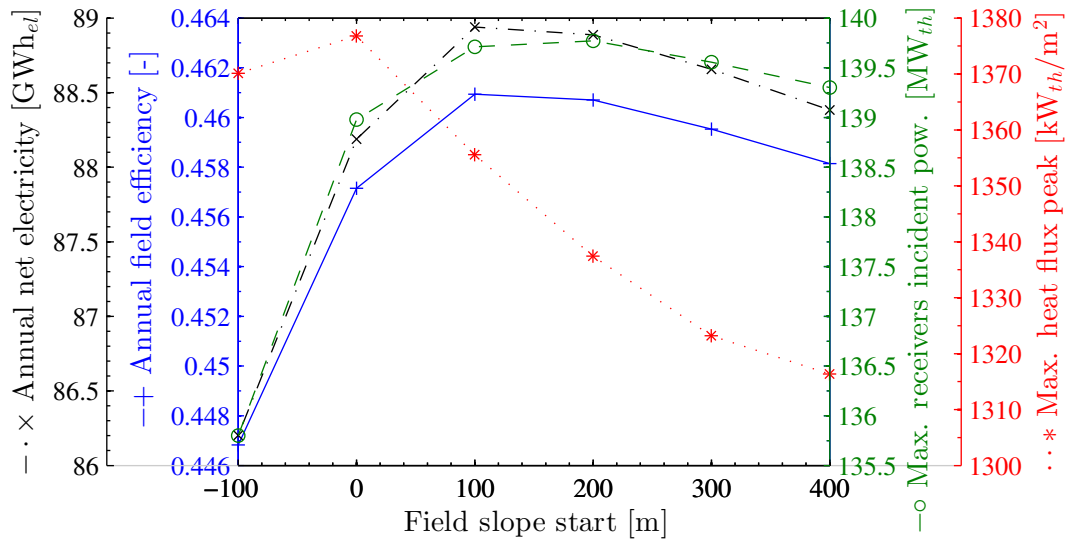


(a) Sensitivity of the energy performance.

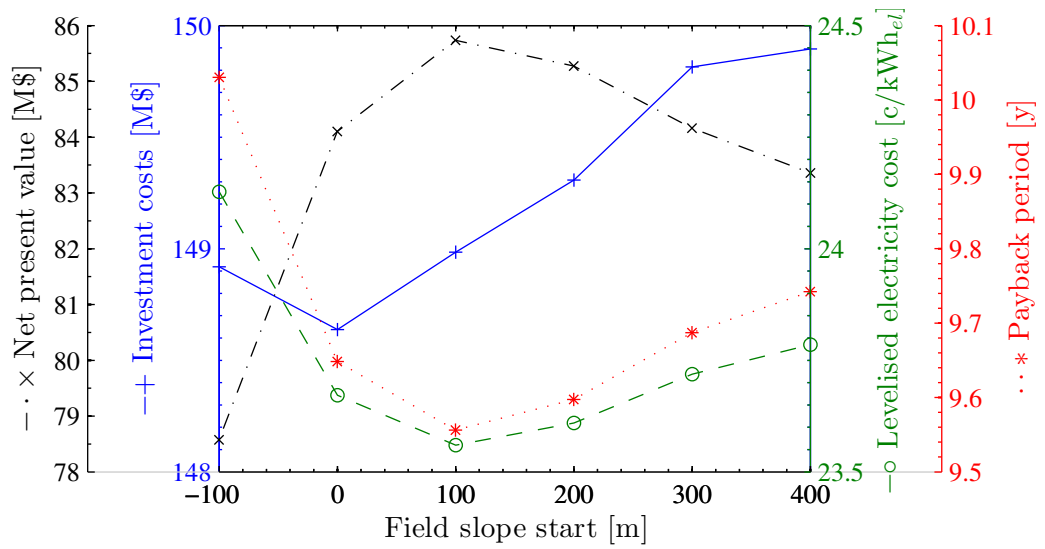


(b) Sensitivity of the economic performance.

Figure D.1 – Sensitivity of the energy and economic performance to the field slope for the Gemasolar plant set-up.

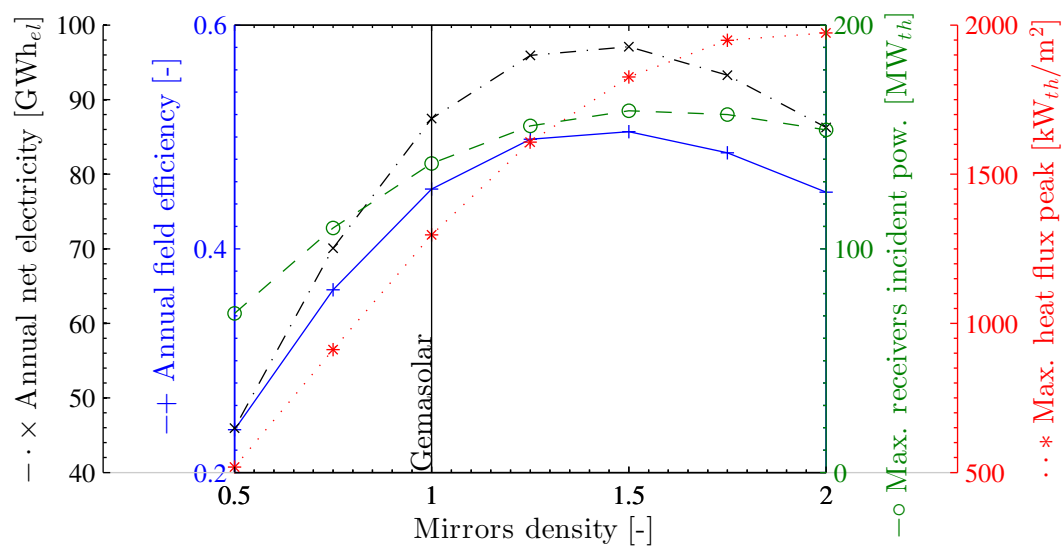


(a) Sensitivity of the energy performance.

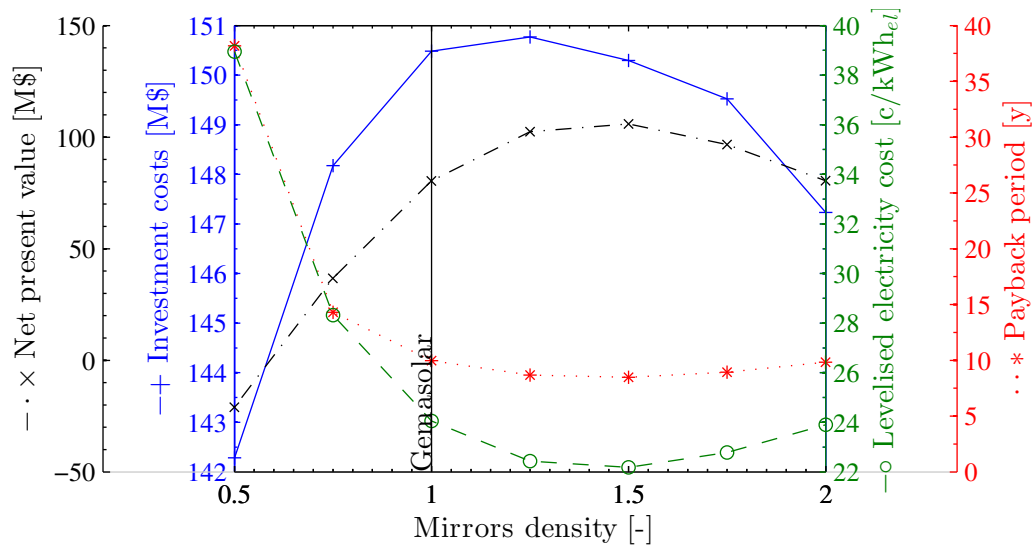


(b) Sensitivity of the economic performance.

Figure D.2 – Sensitivity of the energy and economic performance to the field slope start for the Gemasolar plant set-up.



(a) Sensitivity of the energy performance.



(b) Sensitivity of the economic performance.

Figure D.3 – Sensitivity of the energy and economic performance to the mirrors density for the Gemasolar plant set-up.

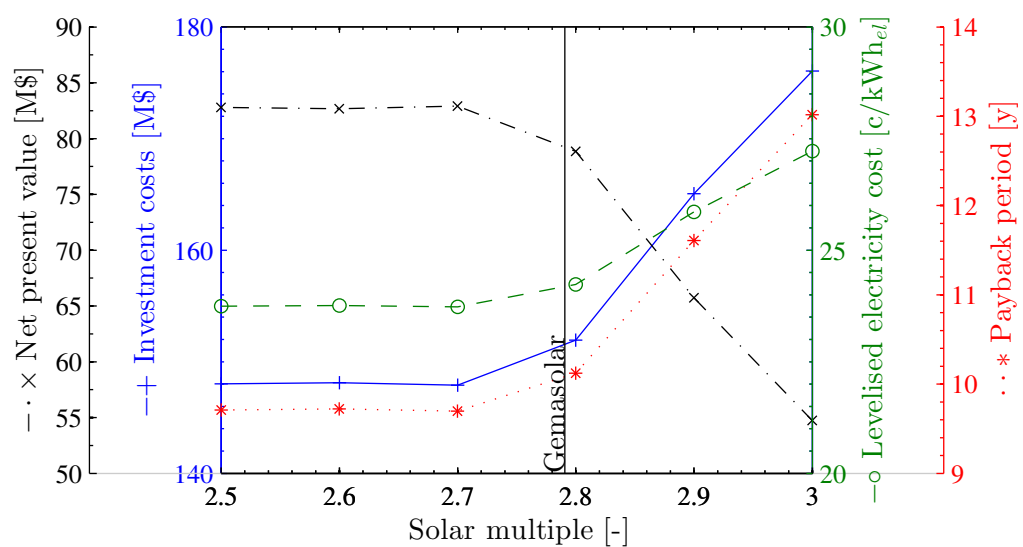


Figure D.4 – Sensitivity of the economic performance to the solar multiple for the Gemasolar plant set-up.

E Heliostat Fields from the Single-Tower Thermo-Economic Optimisation

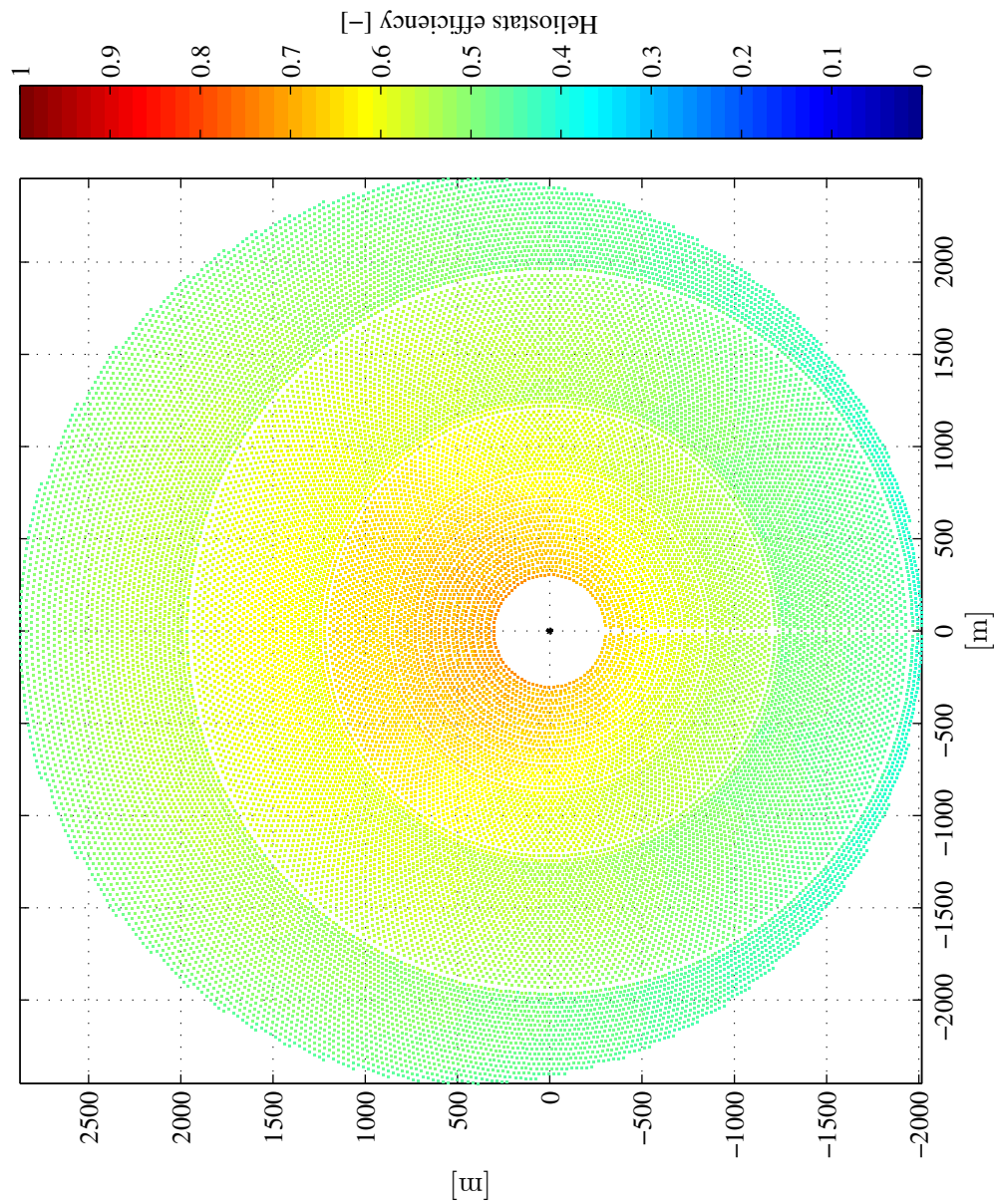


Figure E.1 – Heliostat field layout and efficiency of the single-tower set-up at point A on the trade-off Pareto fronts (see Figure 6.5).

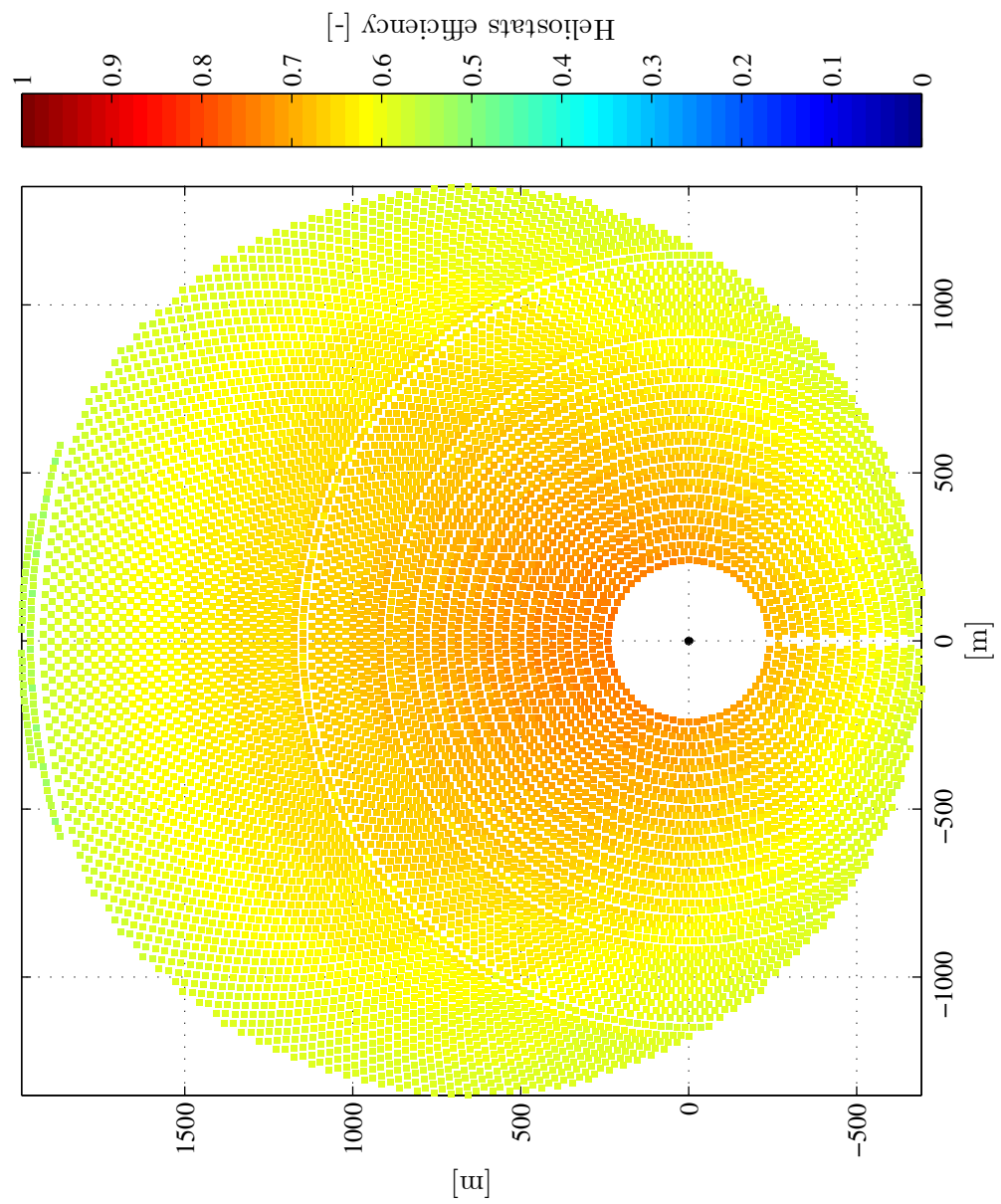


Figure E.2 – Heliostat field layout and efficiency of the single-tower set-up at point B on the trade-off Pareto fronts (see Figure 6.5).

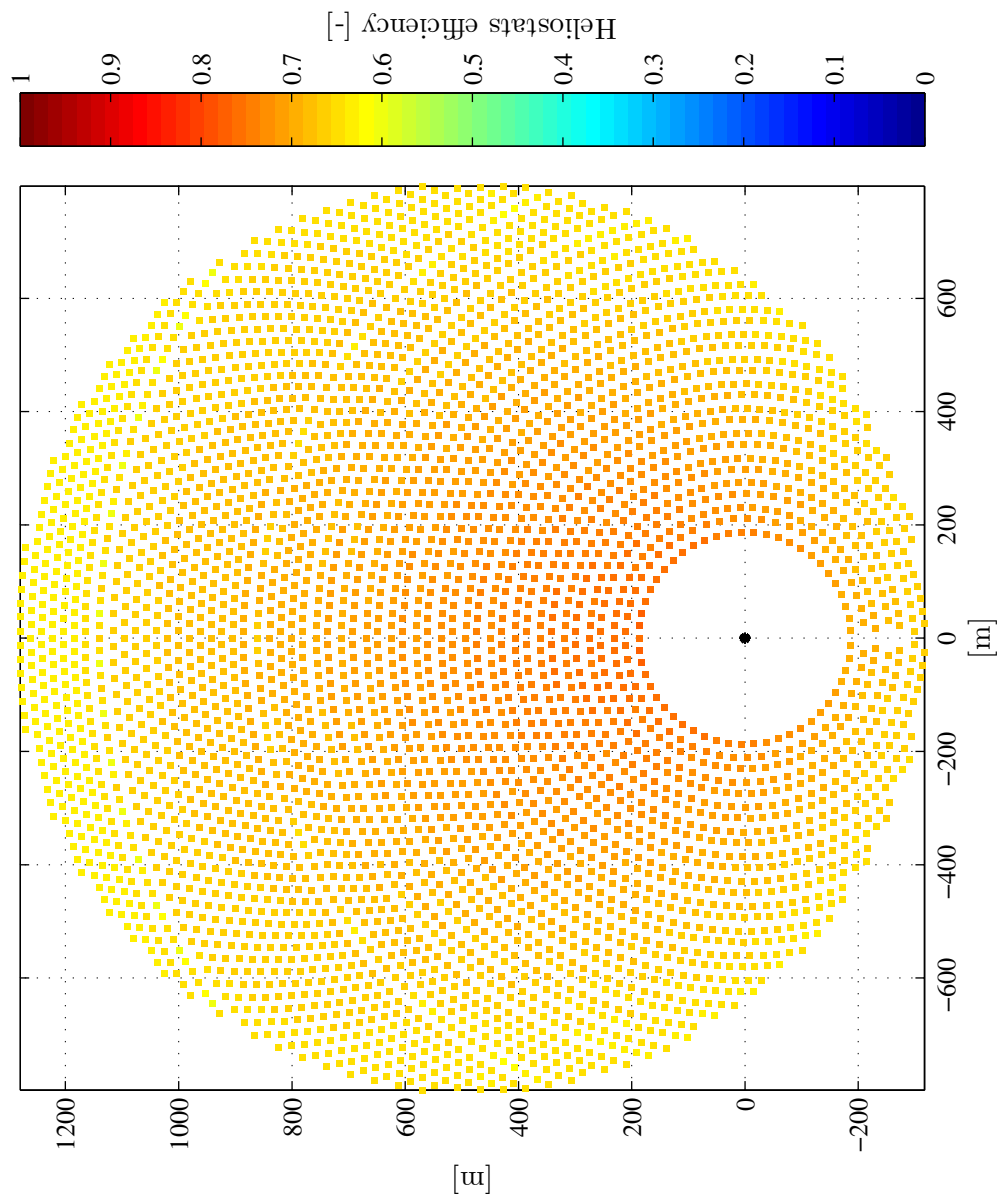


Figure E.3 – Heliostat field layout and efficiency of the single-tower set-up at point C on the trade-off Pareto fronts (see Figure 6.5).

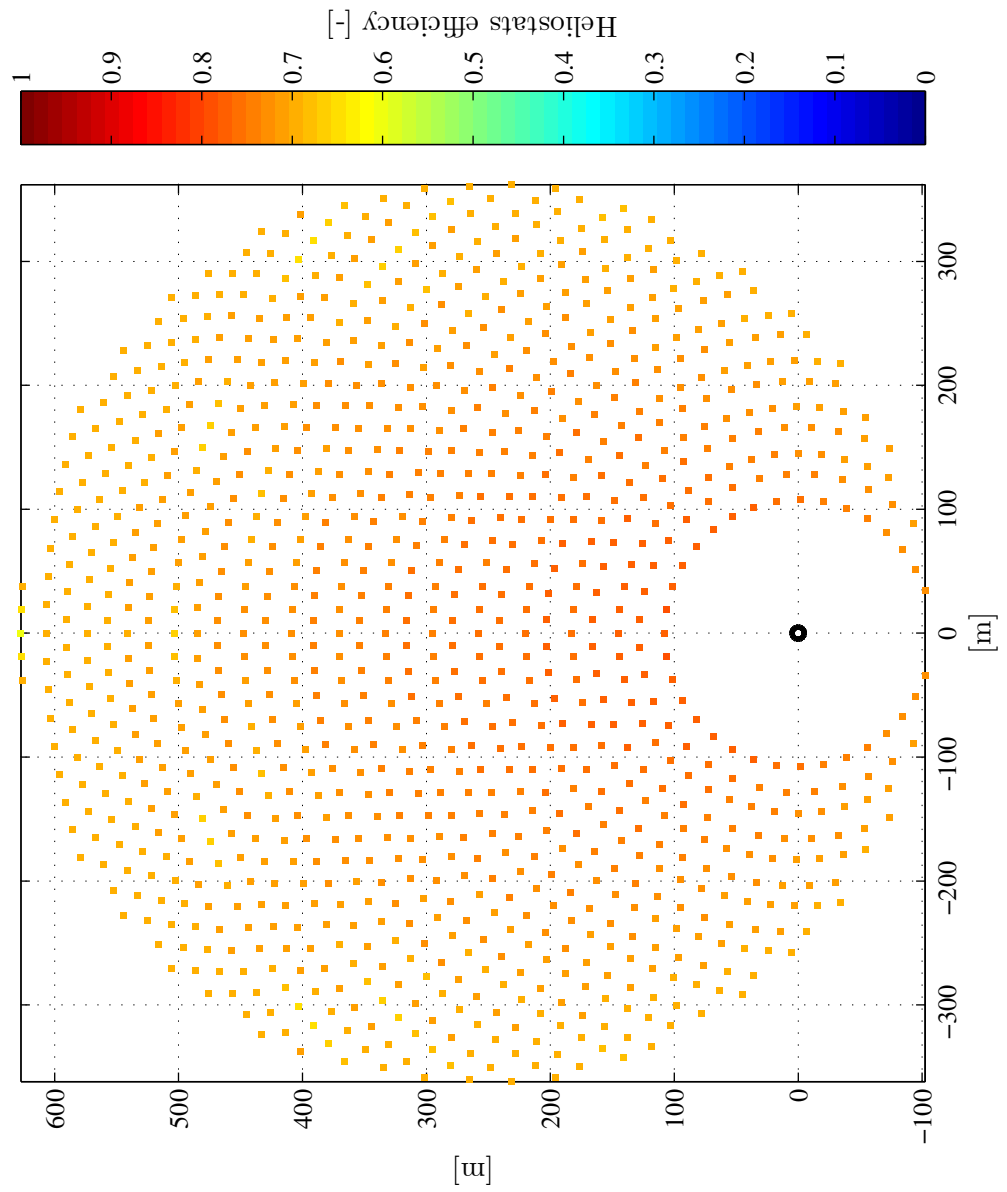


Figure E.4 – Heliostat field layout and efficiency of the single-tower set-up at point D on the trade-off Pareto fronts (see Figure 6.5).

F Thermo-Economic Optimisation with Constrained Tower and Receiver Size

F.1 Pareto Front of Optimal Trade-Off Set-Ups with Constrained Tower and Receiver Size

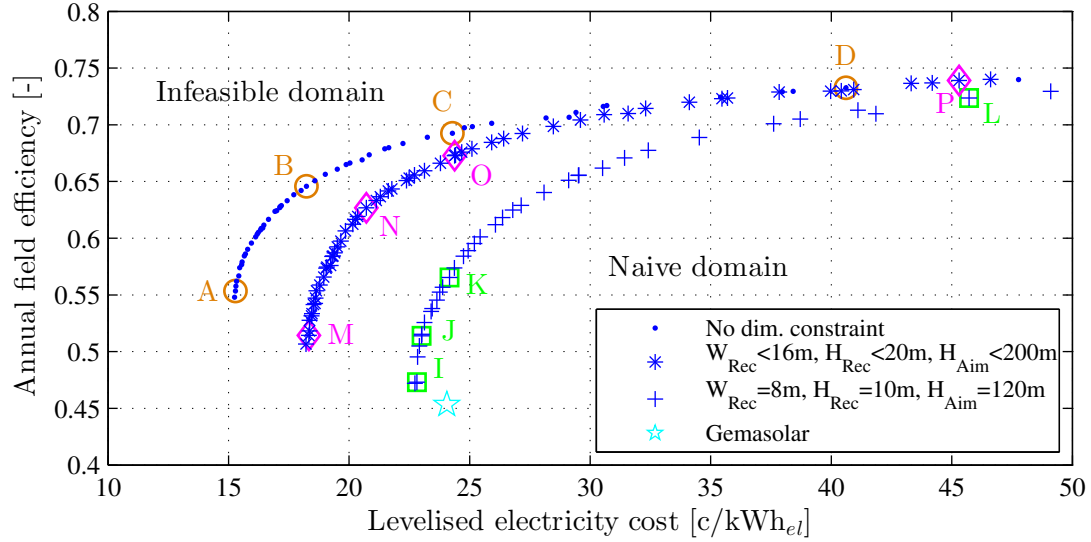


Figure F.1 – Pareto front of single-tower set-ups with constrained tower and receiver size, as an optimal trade-off between the field efficiency and the LEC.

F.2. Selected Points on the Pareto Front with $W_{Rec} = 8$ [m], $H_{Rec} = 10$ [m], $H_{Aim} = 120$ [m]

F.2 Selected Points on the Pareto Front with $W_{Rec} = 8$ [m], $H_{Rec} = 10$ [m], $H_{Aim} = 120$ [m]

Table F1 – Design variables, energy and economic performances of four single-tower set-ups from the Pareto front with fixed tower and receiver size (Gemasolar, $W_{Rec} = 8$ [m], $H_{Rec} = 10$ [m], $H_{Aim} = 120$ [m]).

| <i>Design variables</i> | I | J | K | L | <i>Unit</i> |
|------------------------------|-------|-------|-------|-------|-------------------------------------|
| Heliostat width | 9.20 | 8.39 | 8.16 | 7.37 | [m] |
| Heliostat height | 14.00 | 13.23 | 11.72 | 7.98 | [m] |
| Radial spacing coefficient | 0.36 | 0.43 | 0.59 | 0.89 | [-] |
| South-to-north ratio | 0.83 | 0.66 | 0.68 | 0.48 | [-] |
| Number of heliostats | 2686 | 2463 | 2062 | 600 | [u] |
| Tower height | 120 | 120 | 120 | 120 | [m] |
| Receiver diameter | 8 | 8 | 8 | 8 | [m] |
| Receiver height | 10 | 10 | 10 | 10 | [m] |
| <i>Energy performance</i> | | | | | |
| Annual field efficiency | 0.47 | 0.51 | 0.57 | 0.72 | [-] |
| Max. receiver incident power | 160 | 138 | 109 | 25 | [MW _{th}] |
| Max. heat flux peak | 1471 | 1481 | 1236 | 578 | [kW _{th} /m ²] |
| Annual field output | 327 | 281 | 223 | 51 | [GWh _{th}] |
| Nominal electric power | 18.1 | 15.7 | 12.4 | 2.8 | [MW _{el}] |
| Annual electric output | 99.1 | 85.1 | 68.6 | 15.5 | [GWh _{el}] |
| <i>Economic performance</i> | | | | | |
| Total investment costs | 159 | 138 | 117 | 57 | [M\$] |
| Levelised electricity cost | 22.81 | 23.00 | 24.16 | 45.71 | [¢/kWh _{el}] |
| Payback period | 8.96 | 9.11 | 10.06 | 16.26 | [y] |
| Net present value | 102 | 86 | 61 | -17 | [M\$] |

Heliostat Fields from the Pareto Front with $W_{Rec} = 8$ [m], $H_{Rec} = 10$ [m], $H_{Aim} = 120$ [m]

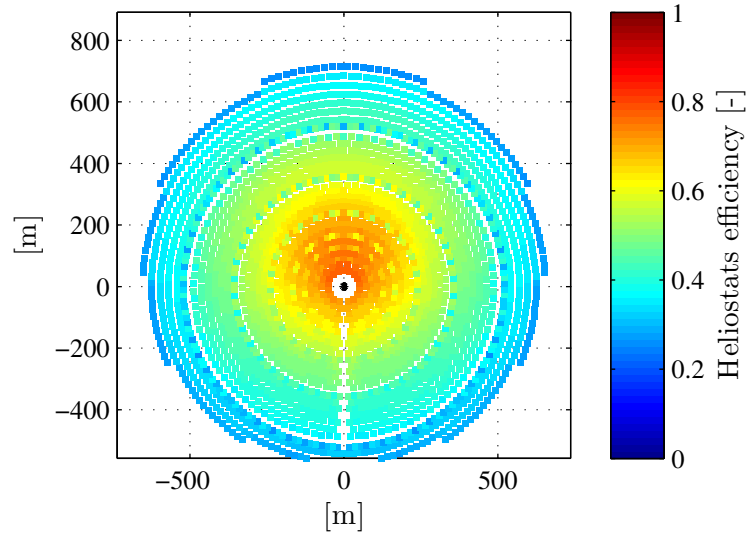


Figure F.2 – Heliostat field layout and efficiency of the single-tower set-up at point I on the trade-off Pareto front with fixed tower and receiver size (Gemastar, $W_{Rec} = 8$ [m], $H_{Rec} = 10$ [m], $H_{Aim} = 120$ [m]).

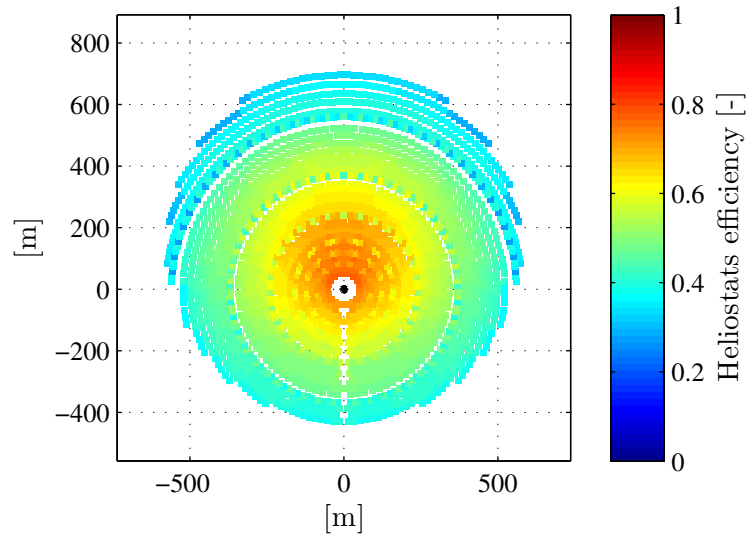


Figure F.3 – Heliostat field layout and efficiency of the single-tower set-up at point J on the trade-off Pareto front with fixed tower and receiver size (Gemastar, $W_{Rec} = 8$ [m], $H_{Rec} = 10$ [m], $H_{Aim} = 120$ [m]).

F.2. Selected Points on the Pareto Front with $W_{Rec} = 8$ [m], $H_{Rec} = 10$ [m], $H_{Aim} = 120$ [m]

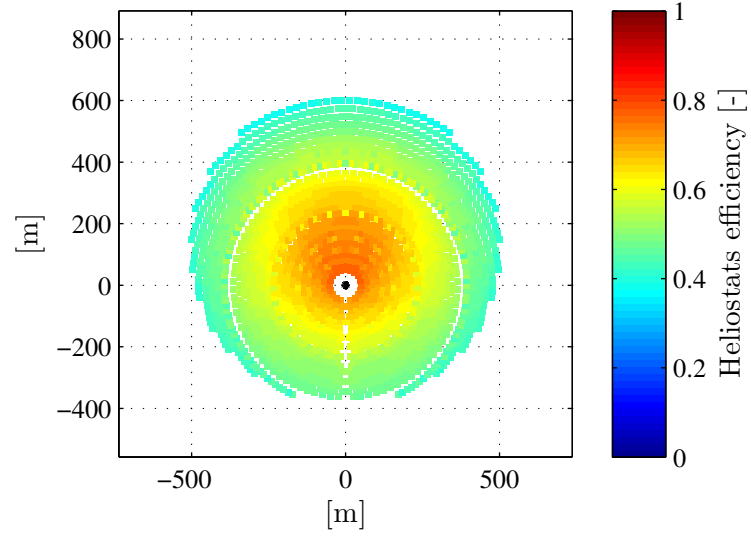


Figure E.4 – Heliostat field layout and efficiency of the single-tower set-up at point K on the trade-off Pareto front with fixed tower and receiver size (Gemasolar, $W_{Rec} = 8$ [m], $H_{Rec} = 10$ [m], $H_{Aim} = 120$ [m]).

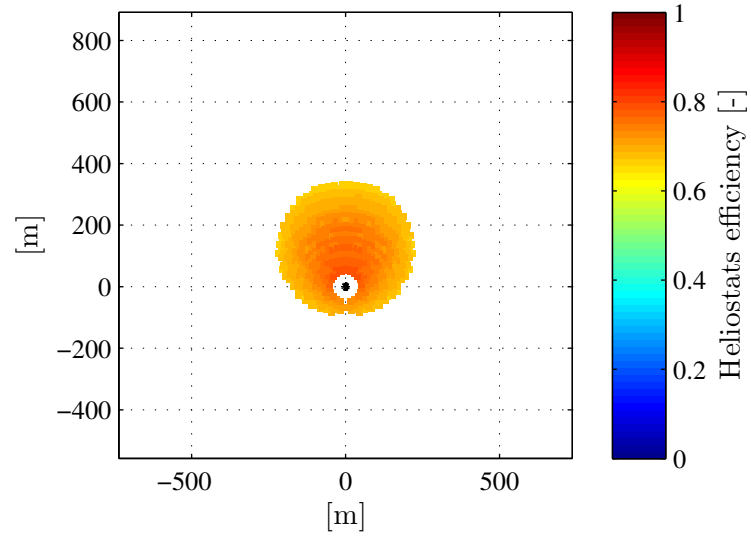


Figure E.5 – Heliostat field layout and efficiency of the single-tower set-up at point L on the trade-off Pareto front with fixed tower and receiver size (Gemasolar, $W_{Rec} = 8$ [m], $H_{Rec} = 10$ [m], $H_{Aim} = 120$ [m]).

F.3. Selected Points on the Pareto Front with $W_{Rec} < 16$ [m], $H_{Rec} < 20$ [m], $H_{Aim} < 200$ [m]

F.3 Selected Points on the Pareto Front with $W_{Rec} < 16$ [m], $H_{Rec} < 20$ [m], $H_{Aim} < 200$ [m]

Table F2 – Design variables, energy and economic performances of four single-tower set-ups from the Pareto front with constrained tower and receiver size ($W_{Rec} < 16$ [m], $H_{Rec} < 20$ [m], $H_{Aim} < 200$ [m]).

| <i>Design variables</i> | M | N | O | P | <i>Unit</i> |
|------------------------------|-------|-------|-------|-------|-------------------------------------|
| Heliostat width | 10.53 | 9.64 | 10.35 | 8.48 | [m] |
| Heliostat height | 17.52 | 12.61 | 11.93 | 8.61 | [m] |
| Radial spacing coefficient | 0.36 | 0.68 | 0.79 | 0.90 | [-] |
| South-to-north ratio | 0.65 | 0.56 | 0.42 | 0.32 | [-] |
| Number of heliostats | 5157 | 3208 | 1768 | 803 | [u] |
| Tower height | 197.6 | 196.6 | 195.6 | 195.5 | [m] |
| Receiver diameter | 15.9 | 15.7 | 15.6 | 15.3 | [m] |
| Receiver height | 19.3 | 19.5 | 19.3 | 19.3 | [m] |
| <i>Energy performance</i> | | | | | |
| Annual field efficiency | 0.51 | 0.63 | 0.67 | 0.74 | [-] |
| Max. receiver incident power | 482 | 239 | 144 | 43 | [MW _{th}] |
| Max. heat flux peak | 1442 | 948 | 773 | 410 | [kW _{th} /m ²] |
| Annual field output | 978 | 489 | 293 | 87 | [GWh _{th}] |
| Nominal electric power | 54.5 | 27.0 | 16.3 | 4.8 | [MW _{el}] |
| Annual electric output | 296 | 148 | 89 | 26 | [GWh _{el}] |
| <i>Economic performance</i> | | | | | |
| Total investment costs | 353 | 209 | 156 | 97 | [M\$] |
| Levelised electricity cost | 18.33 | 20.71 | 24.38 | 45.30 | [¢/kWh _{el}] |
| Payback period | 5.92 | 7.43 | 10.25 | 16.87 | [y] |
| Net present value | 428 | 182 | 79 | -27 | [M\$] |

Heliostat Fields from the Pareto Front with $W_{Rec} < 16$ [m], $H_{Rec} < 20$ [m], $H_{Aim} < 200$ [m]

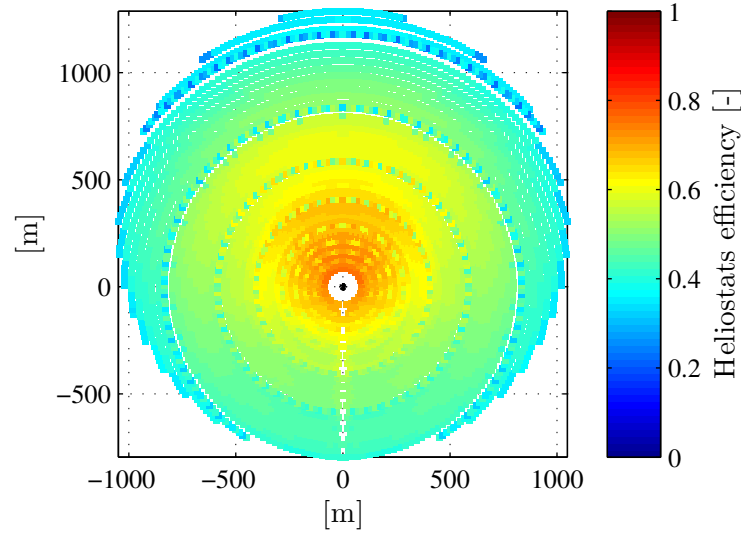


Figure E.6 – Heliostat field layout and efficiency of the single-tower set-up at point M on the trade-off Pareto front with constrained tower and receiver size ($W_{Rec} < 16$ [m], $H_{Rec} < 20$ [m], $H_{Aim} < 200$ [m]).

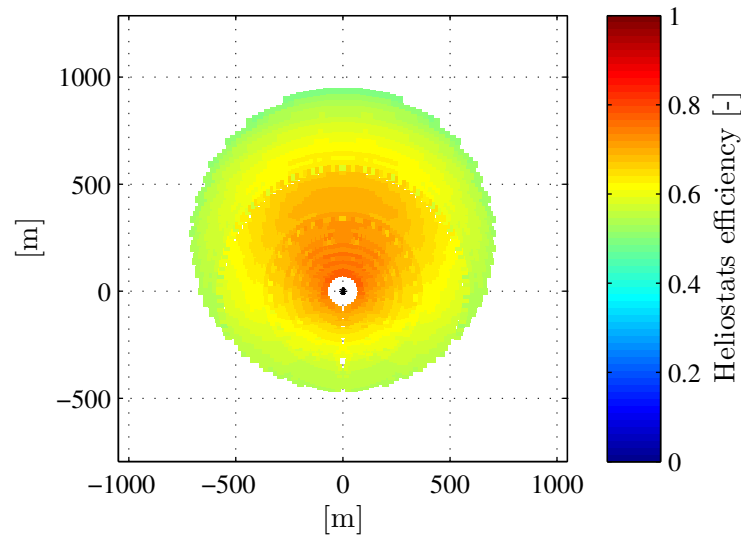


Figure E.7 – Heliostat field layout and efficiency of the single-tower set-up at point N on the trade-off Pareto front with constrained tower and receiver size ($W_{Rec} < 16$ [m], $H_{Rec} < 20$ [m], $H_{Aim} < 200$ [m]).

F.3. Selected Points on the Pareto Front with $W_{Rec} < 16$ [m], $H_{Rec} < 20$ [m], $H_{Aim} < 200$ [m]

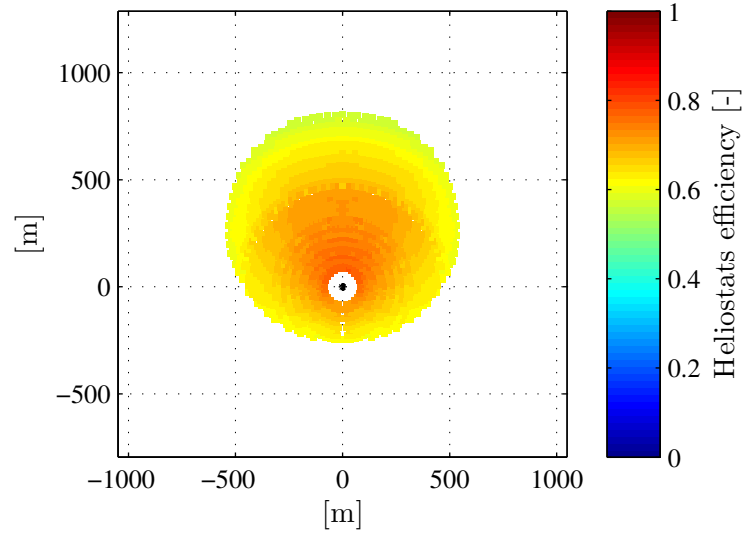


Figure E.8 – Heliostat field layout and efficiency of the single-tower set-up at point O on the trade-off Pareto front with constrained tower and receiver size ($W_{Rec} < 16$ [m], $H_{Rec} < 20$ [m], $H_{Aim} < 200$ [m]).

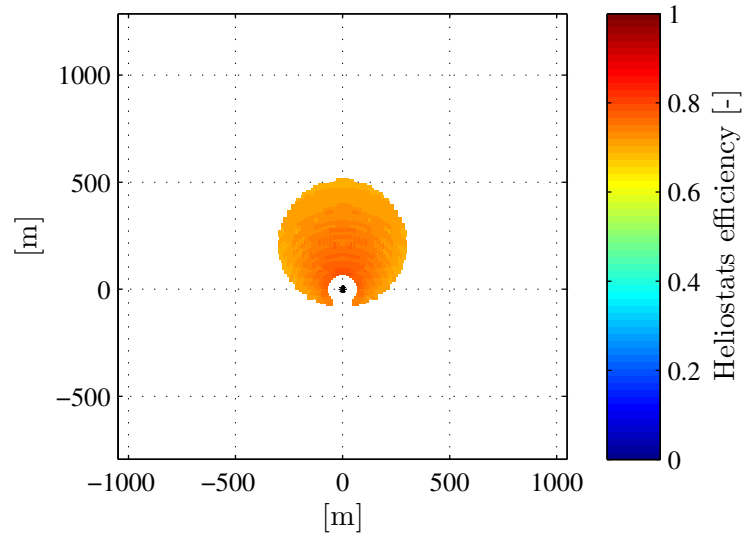
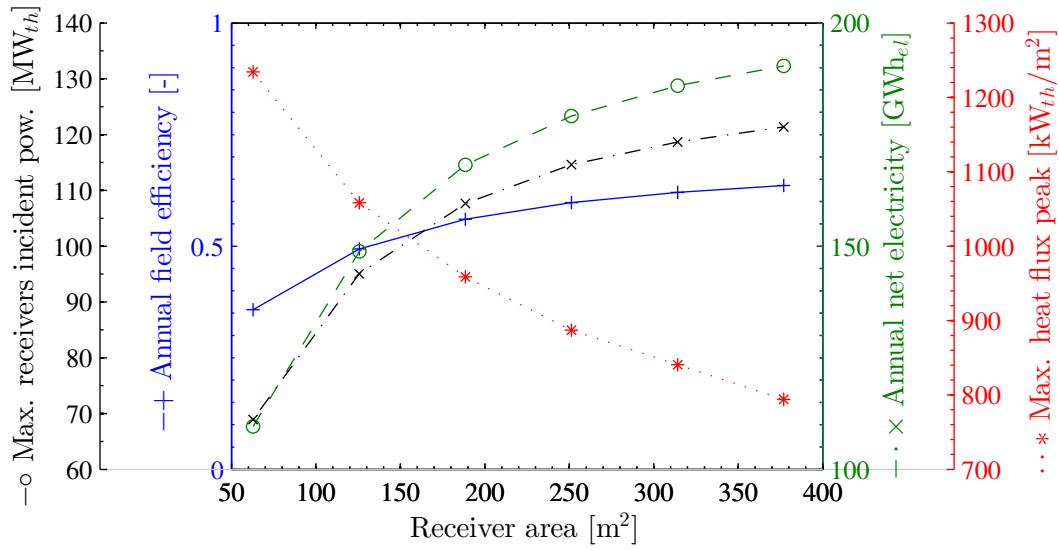


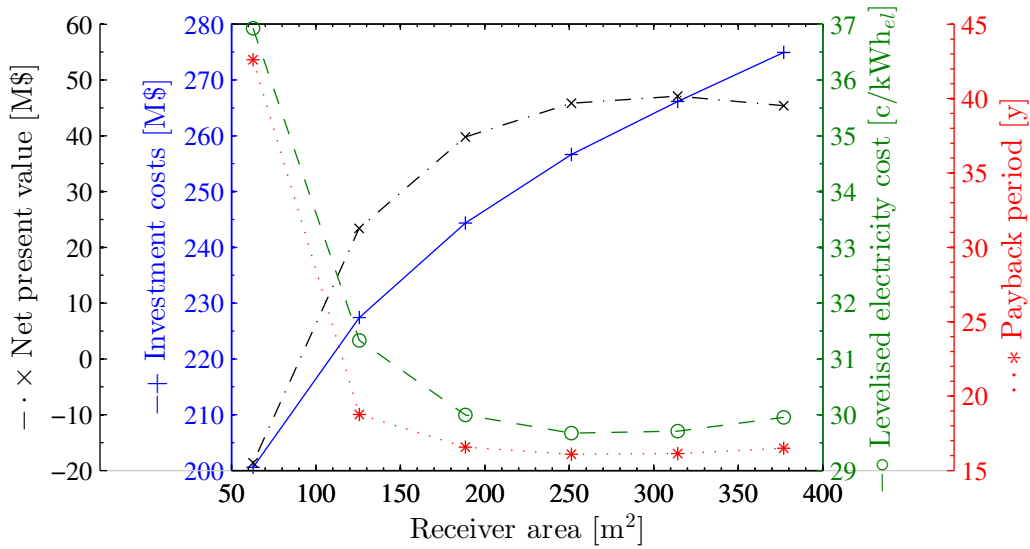
Figure E.9 – Heliostat field layout and efficiency of the single-tower set-up at point P on the trade-off Pareto front with constrained tower and receiver size ($W_{Rec} < 16$ [m], $H_{Rec} < 20$ [m], $H_{Aim} < 200$ [m]).

G Sensitivity Analysis on a Multi-Tower Set-Up

Appendix G. Sensitivity Analysis on a Multi-Tower Set-Up



(a) Sensitivity of the energy performance.



(b) Sensitivity of the economic performance.

Figure G.1 – Sensitivity of the energy and economic performance to the receiver area for a field layout with the same number of heliostats as Gemasolar (2650 [u]).

H Heliostat Fields from the Multi-Tower Thermo-Economic Optimisation

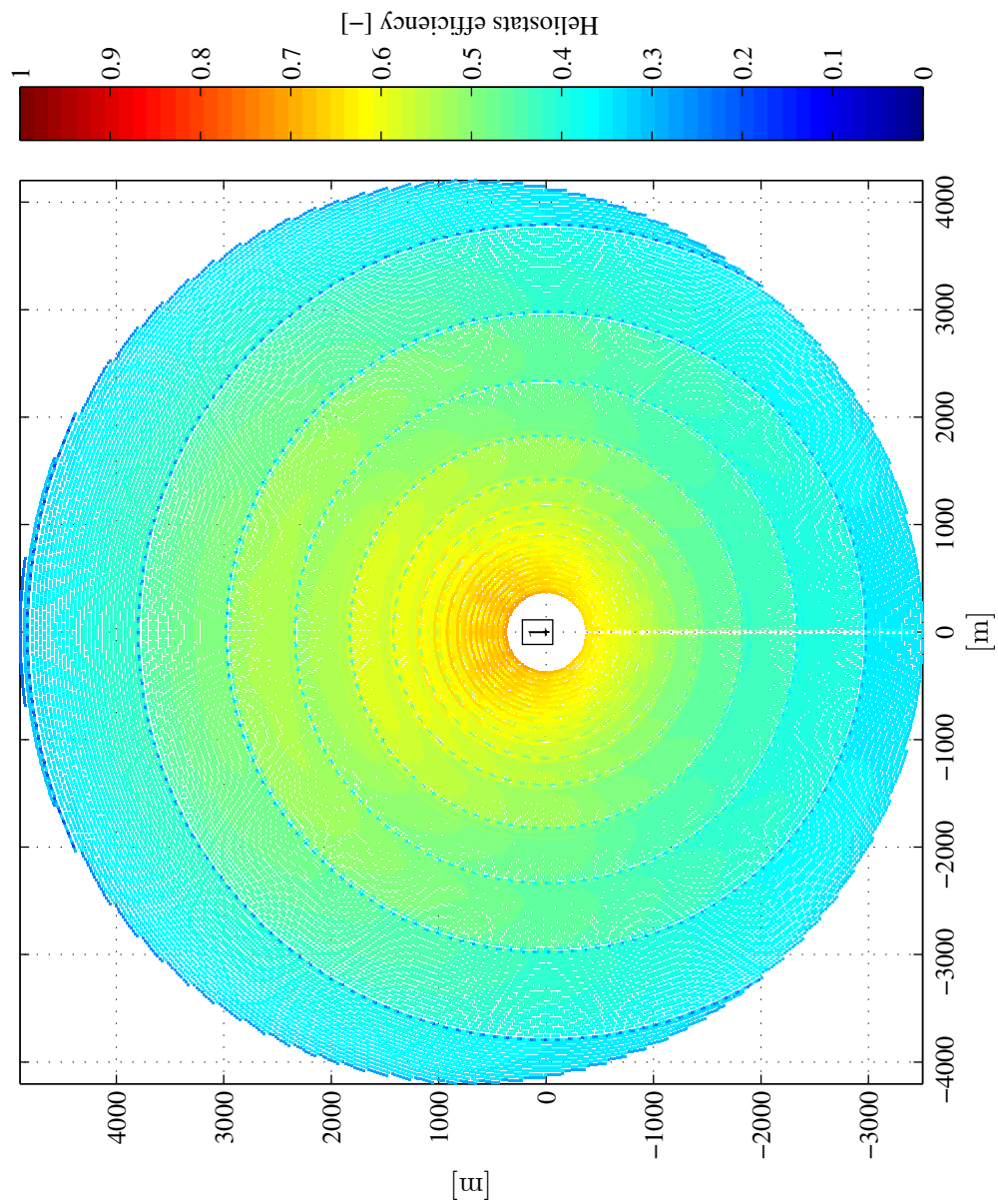


Figure H.1 – Heliostat field layout and efficiency of the optimal one- to two-tower transition set-up from the trade-off Pareto fronts (point E).

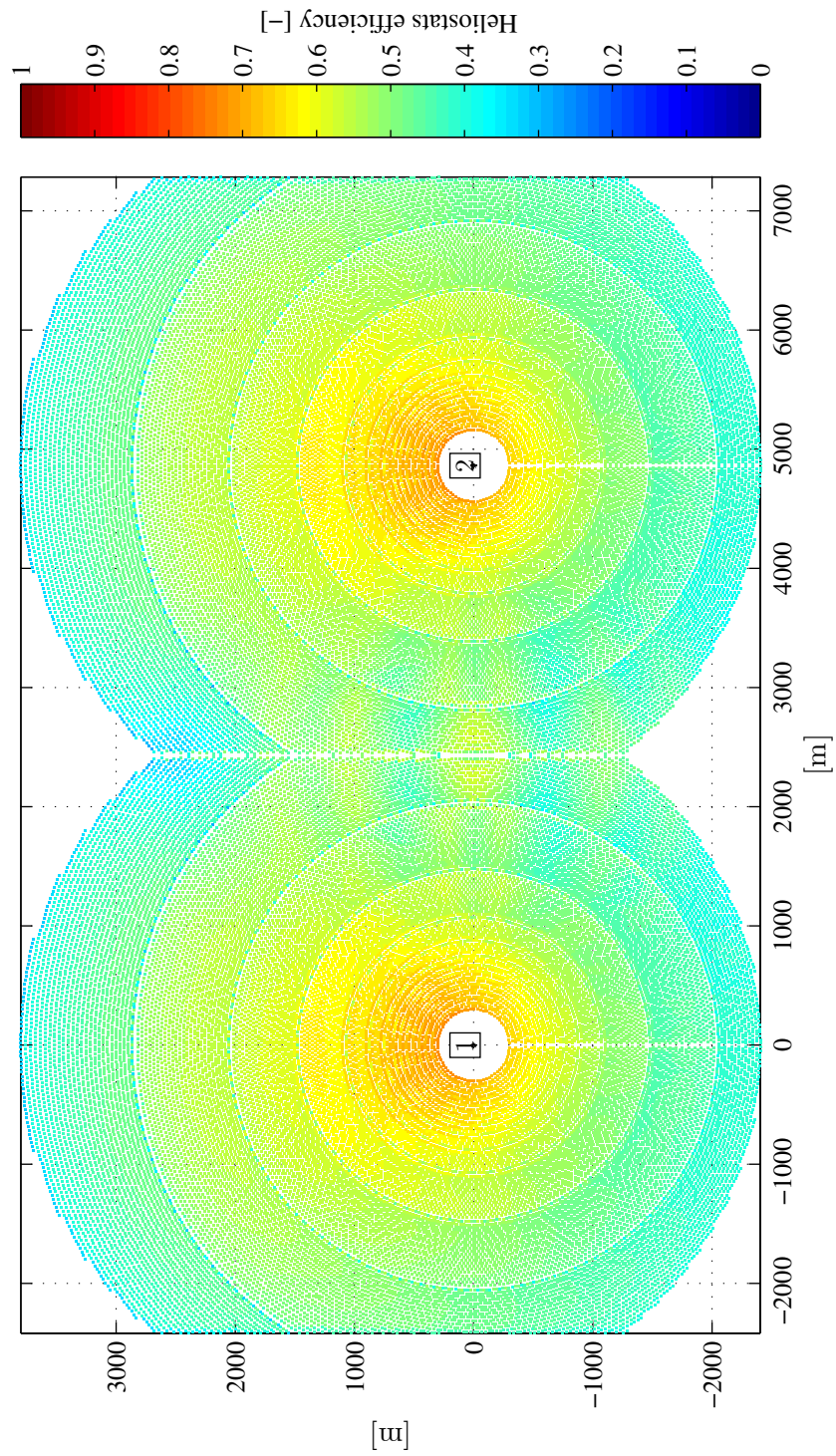


Figure H.2 – Heliostat field layout and efficiency of the optimal one- to two-tower transition set-up from the trade-off Pareto fronts (point F).

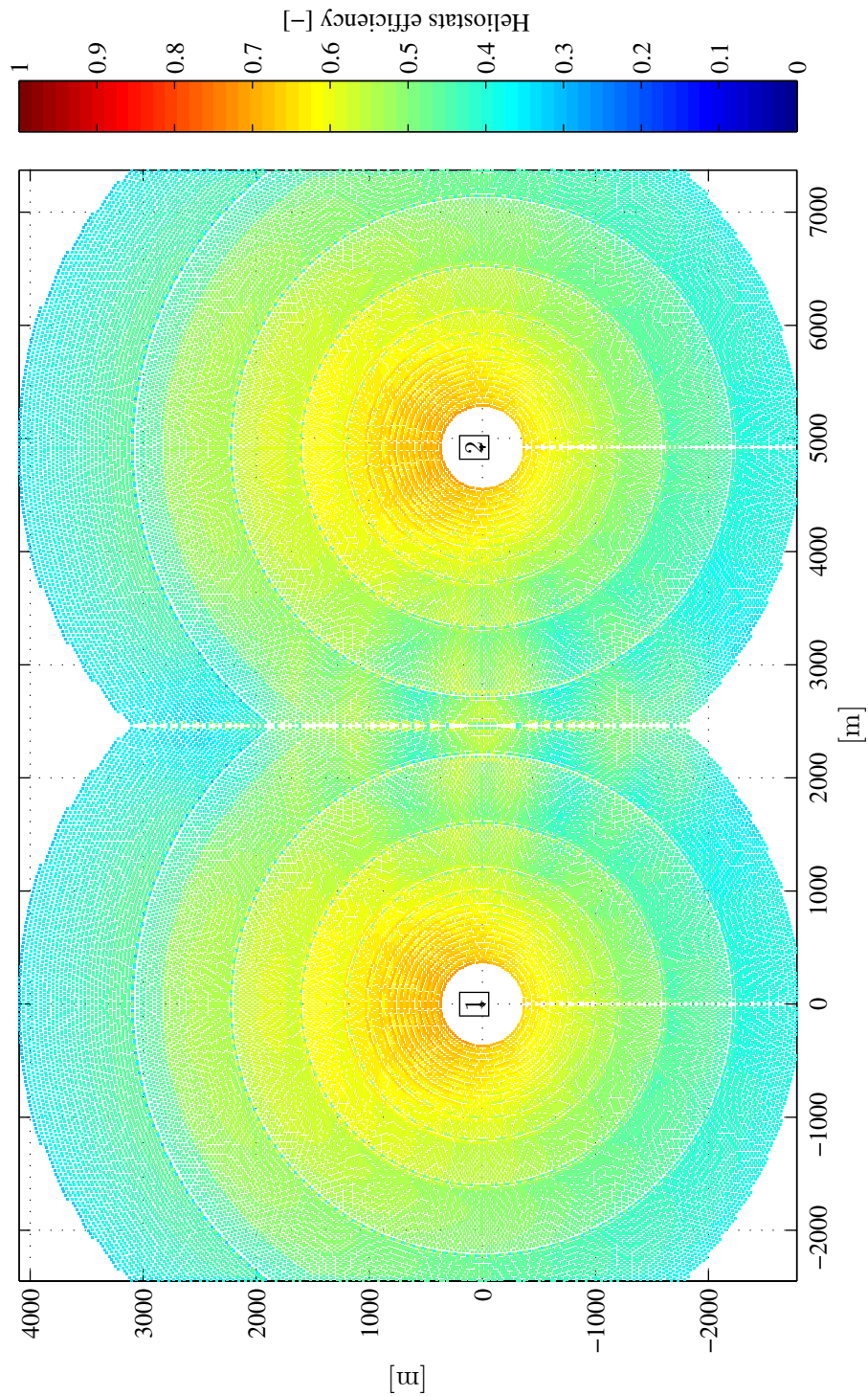


Figure H.3 – Heliostat field layout and efficiency of the optimal two- to three-tower transition set-up from the trade-off Pareto fronts (point G).

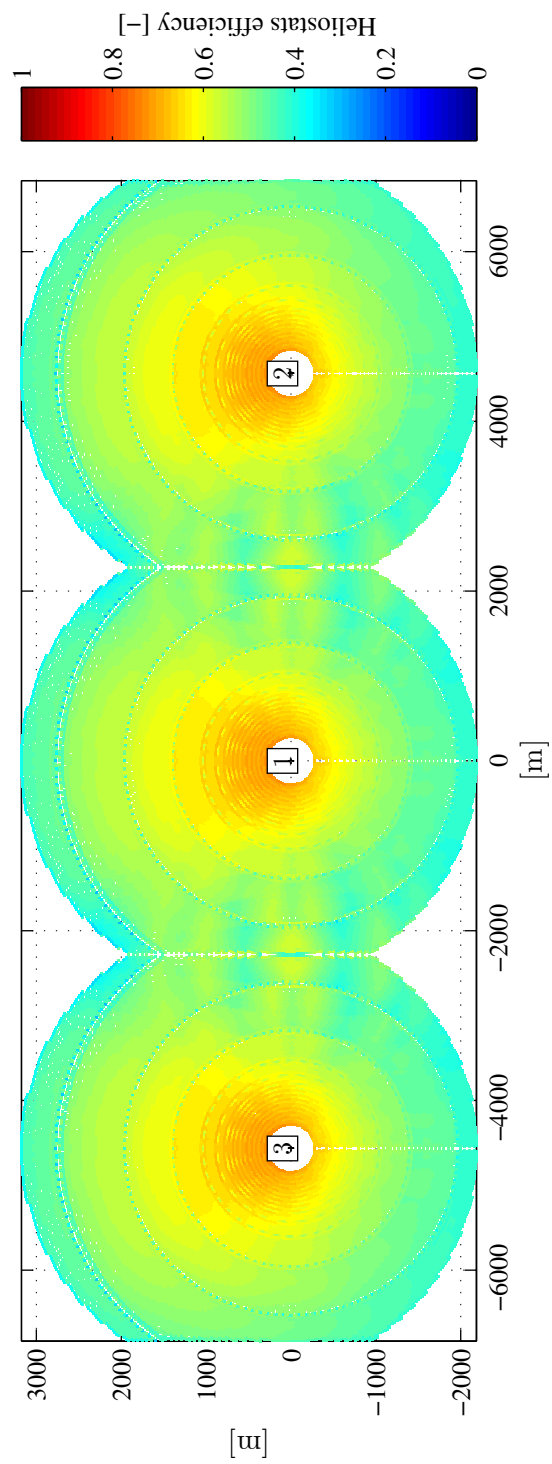


Figure H.4 – Heliosat field layout and efficiency of the optimal two- to three-tower transition set-up from the trade-off Pareto fronts (point H).

I Trough Field Model

I.1 Energy Performance

I.1.1 Trough Field

Assumptions

- The inter-reflections between the parabolic mirror, the glass envelope and the receiver tube are neglected.
- The glass envelope is considered as opaque to infrared radiation coming from the atmosphere and the receiver receiver.
- The convection heat transfer between the receiver tube and the glass envelope within the vacuum is neglected.
- The conduction heat transfer at the sealing between the glass envelope and the receiver tube is neglected.
- The convection heat transfer between the glass-receiver sealing and the atmosphere is neglected.

System of Equations

1st equation: balance around the glass envelope outer surface (Go)

$$\dot{Q}_{Rad,S\&M-Go} + \dot{Q}_{Cond,Gi-Go} - \dot{Q}_{Rad,Go-Sky} - \dot{Q}_{Cond,Go-a} = 0 \quad (I.1)$$

Radiation from sun and mirror ($S\&M$) onto the glass envelope outer surface (Go):

$$\dot{Q}_{Rad,S\&M-Go} = (1 - \rho_{Glass} - \tau_{Glass}) \cdot (\rho_{Mirr} IAM \gamma A_{Mirr,eff} + L_{Glass} d_{Go}) \cdot DNI \quad (I.2)$$

Appendix I. Trough Field Model

where the Incidence Angle Modifier (IAM) is estimated from [Geyer and Lüpfer, 2002]

$$IAM = \cos \omega + C_{IAM1} \omega + C_{IAM2} \omega^2 + C_{IAM3} \omega^3 \quad (I.3)$$

$$C_{IAM1} = -0.0005569$$

$$C_{IAM2} = -2.563 \cdot 10^{-5}$$

$$C_{IAM3} = -2.866 \cdot 10^{-8}$$

with the incidence angle ω obtained from

$$\omega = \begin{cases} \arccos\left(\sqrt{1 - \cos^2 az \cos^2 el}\right) & \text{if N-S orientation} \\ \arccos\left(\sqrt{1 - \sin^2 az \cos^2 el}\right) & \text{if E-W orientation} \end{cases} \quad (I.4)$$

and the interception factor γ by [INABENSA, 2002]

$$\gamma = 0.8554 \quad (I.5)$$

Conduction from glass envelope inner surface (Gi) to outer surface (Go):

$$\dot{Q}_{Cond, Gi-Go} = 2\pi L_{Glass} k_{Glass} \frac{T_{Gi} - T_{Go}}{\log\left(\frac{d_{Go}}{d_{Gi}}\right)} \quad (I.6)$$

Radiation from glass envelope outer surface (Gi) to the sky:

$$\dot{Q}_{Rad, Go-Sky} = A_{Go} \varepsilon_{Glass} \sigma \left(T_{Go}^4 - T_{Sky}^4 \right) \quad (I.7)$$

Convection from glass envelope outer surface (Gi) to the atmosphere (a):

$$\dot{Q}_{Conv, Go-a} = A_{Go} U_{Conv, Go-a} (T_{Go} - T_a) \quad (I.8)$$

where the convection heat transfer coefficient $U_{Conv, Go-a}$ is given by

$$U_{Conv, Go-a} = \frac{Nu_{Go-a} k_a}{d_{Go}} \quad (I.9)$$

with the Nusselt number Nu_{Go-a} obtained from the correlation due to Zukauskas [Bergman et al., 2011]

$$Nu_{Go-a} = C_{Z1} Re^{C_{Z2}} Pr^{C_{Z3}} \left(\frac{Pr}{Pr_{Go}} \right)^{1/4} \quad (I.10)$$

2nd equation: balance around the glass envelope inner surface (Gi)

$$\dot{Q}_{Rad,Ro-Gi} + \dot{Q}_{RefI,Ro-Gi} - \dot{Q}_{Cond,Gi-Go} = 0 \quad (I.11)$$

Radiation from receiver tube outer surface (Ro) onto the glass envelope inner surface (Gi) considering glass opaque to infrared radiation:

$$\dot{Q}_{Rad,Ro-Gi} = \frac{A_{Ro}\sigma(T_{Ro}^4 - T_{Gi}^4)}{\frac{1}{\epsilon_{Rec}} + \frac{A_{Ro}}{A_{Gi}}\left(\frac{1}{\epsilon_{Rec}} - 1\right)} \quad (I.12)$$

Infrared reflection from receiver tube outer surface (Ro) onto the glass envelope inner surface (Gi) considering glass opaque to infrared radiation:

$$\dot{Q}_{RefI,Ro-Gi} = (1 - \alpha_{Rec})\tau_{Glass} \cdot (\rho_{Mirr}IAM\gamma A_{Mirr,eff} + L_{Rec}d_{Ro}) \cdot DNI \quad (I.13)$$

Conduction from glass envelope inner surface (Gi) to outer surface (Go):

$$\dot{Q}_{Cond,Gi-Go} = 2\pi L_{Glass}k_{Glass} \frac{T_{Gi} - T_{Go}}{\log\left(\frac{d_{Go}}{d_{Gi}}\right)} \quad (I.14)$$

3rd equation: balance around the receiver tube outer surface (Ro)

$$\dot{Q}_{Rad,S\&M-Ro} - \dot{Q}_{Rad,Ro-Gi} - \dot{Q}_{Cond,Ro-Ri} = 0 \quad (I.15)$$

Radiation from sun and mirror ($S\&M$) onto the receiver tube outer surface (Ro):

$$\dot{Q}_{Rad,S\&M-Ro} = \alpha_{Rec}\tau_{Glass} \cdot (\rho_{Mirr}IAM\gamma A_{Mirr,eff} + L_{Glass}d_{Go}) \cdot DNI \quad (I.16)$$

Radiation from receiver tube outer surface (Ro) onto the glass envelope inner surface (Gi) considering glass opaque to infrared radiation:

$$\dot{Q}_{Rad,Ro-Gi} = \frac{A_{Ro}\sigma(T_{Ro}^4 - T_{Gi}^4)}{\frac{1}{\epsilon_{Rec}} + \frac{A_{Ro}}{A_{Gi}}\left(\frac{1}{\epsilon_{Rec}} - 1\right)} \quad (I.17)$$

Conduction from receiver tube outer surface (Ro) to inner surface (Ri):

$$\dot{Q}_{Cond,Ro-Ri} = 2\pi L_{Rec}k_{Rec} \frac{T_{Ro} - T_{Ri}}{\log\left(\frac{d_{Ro}}{d_{Ri}}\right)} \quad (I.18)$$

Appendix I. Trough Field Model

4th equation: balance around the receiver tube inner surface (Ri)

$$\dot{Q}_{Cond,Ro-Ri} - \dot{Q}_{Conv,Ri-HTF} = 0 \quad (I.19)$$

Conduction from receiver tube outer surface (Ro) to inner surface (Ri):

$$\dot{Q}_{Cond,Ro-Ri} = 2\pi L_{Rec} k_{Rec} \frac{T_{Ro} - T_{Ri}}{\log\left(\frac{d_{Ro}}{d_{Ri}}\right)} \quad (I.20)$$

Convection from receiver tube inner surface (Ri) to heat transfer fluid (HTF):

$$\dot{Q}_{Conv,Ri-HTF} = A_{Ri} U_{Conv,Ri-HTF} (T_{Ri} - T_{HTF}) \quad (I.21)$$

where the convection heat transfer coefficient $U_{Conv,Ri-HTF}$ is given by

$$U_{Conv,Ri-HTF} = \frac{Nu_{Ri-HTF} k_{HTF}}{d_{Ri}} \quad (I.22)$$

with the Nusselt number Nu_{Ri-HTF} obtained from the correlation due to Gnielinski [Bergman et al., 2011]

$$Nu_{Ri-HTF} = \frac{(f/8)(Re - 1000)Pr}{1 + 12.7(f/8)^{1/2}(Pr^{2/3} - 1)} \quad (I.23)$$

5th equation: balance around the heat transfer fluid (HTF)

$$\dot{Q}_{Conv,Ri-HTF} - \dot{Y}_{HTF} = 0 \quad (I.24)$$

Convection from receiver tube inner surface (Ri) to heat transfer fluid (HTF):

$$\dot{Q}_{Conv,Ri-HTF} = A_{Ri} U_{Conv,Ri-HTF} (T_{Ri} - T_{HTF}) \quad (I.25)$$

Transformation power rate of the heat transfer fluid (HTF):

$$\dot{Y}_{HTF} = \dot{M}_{HTF} (h_{HTF,out} - h_{HTF,in}) \quad (I.26)$$

where the specific enthalpy h_{HTF} is estimated according to the fluid used:

Therminol VP-1 [Solutia, 2008]

$$h_{HTF} = C_{HTF1} (T_{HTF})^{C_{HTF2}} + C_{HTF3} \quad (I.27)$$

$$C_{HTF1} = 25.2$$

$$C_{HTF2} = 1.635$$

$$C_{HTF3} = -2.593 \cdot 10^5$$

or Syltherm 800 [DOW, 2001]

$$h_{HTF} = \frac{C_{HTF1}}{2} (T_{HTF})^2 + C_{HTF2} T_{HTF} + C_{HTF3} \quad (I.28)$$

$$C_{HTF1} = 1.707$$

$$C_{HTF2} = 1108$$

$$C_{HTF3} = -3.047 \cdot 10^5$$

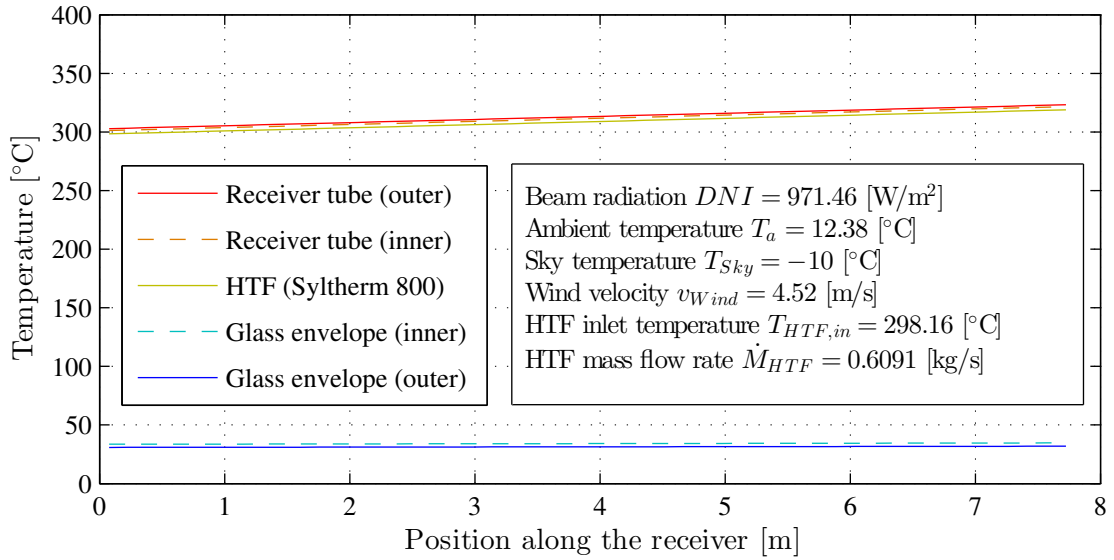


Figure I.1 – Parabolic trough calculated temperature profile under the same conditions as tests [Moss and Brosseau, 2005] for the Schott PTR70 receiver [SCHOTTSolar, 2011] on a LS-2 collector with HTF Syltherm 800 [DOW, 2001].

Comparison with Measurements

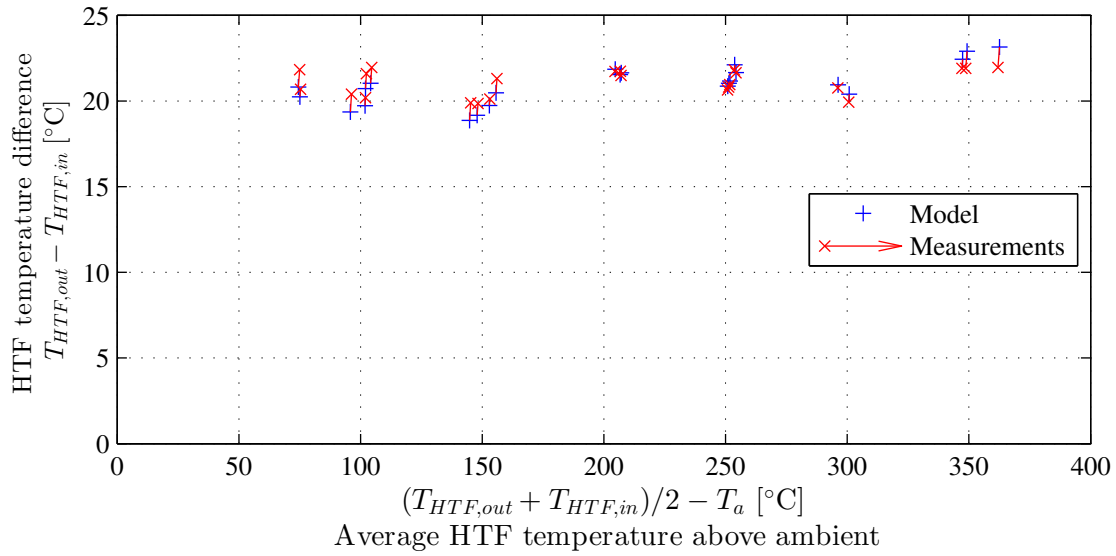


Figure I.2 – Parabolic trough model comparison of ΔT_{HTF} against the test results [Moss and Brosseau, 2005] for the Schott PTR70 receiver [SCHOTTSolar, 2011] on a LS-2 collector with HTF Syltherm 800 [DOW, 2001]. Error root mean square = 0.0309.

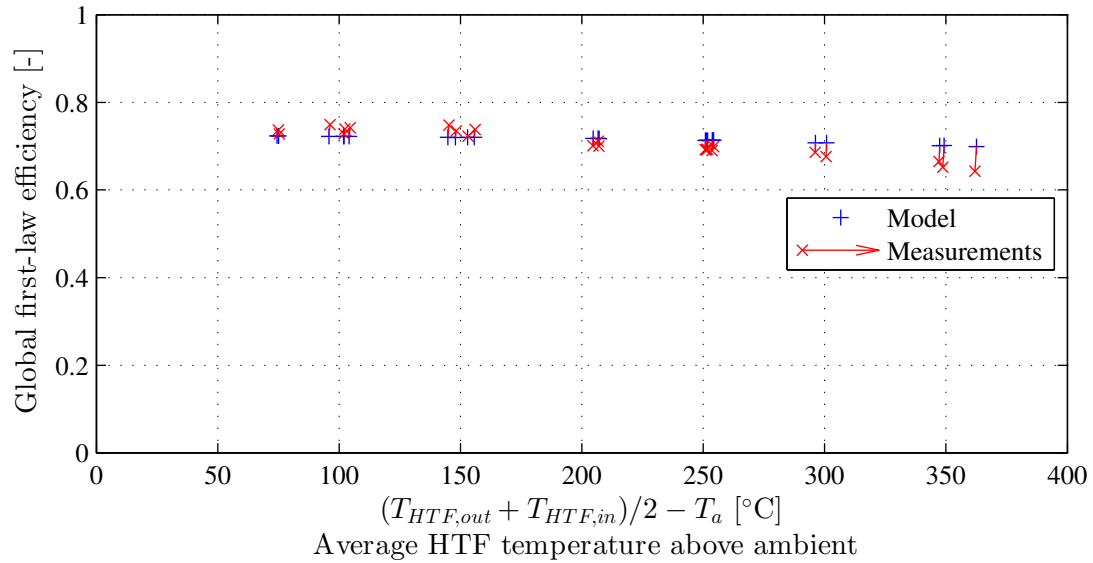


Figure I.3 – Parabolic trough model comparison of the global first-law efficiency against the test results [Moss and Brosseau, 2005] for the Schott PTR70 receiver [SCHOTTSolar, 2011] on a LS-2 collector with HTF Syltherm 800 [DOW, 2001]. Error root mean square = 0.0363.

I.1.2 Power Conversion Unit

See §3.3.

I.2 Economic Performance
I.2.1 Investment Costs
Trough Field

Land See §5.1.1.

Trough modules See §5.1.1 with parameters from Table I.1.

Table I.1 – Estimated direct cost parameters of a trough field [Sargent & Lundy, 2003, BLS, 2011].

| <i>Trough direct cost i</i> | c^0 [\$/m ²] | pr [-] | pi [-] |
|------------------------------------------|----------------------------|----------|----------|
| Foundation | 21 | 0.8993 | 1.0958 |
| Concentrator structure | 50 | 0.9408 | 1.6869 |
| Drives | 14 | 0.8059 | 1.3280 |
| Mirrors | 40 | 0.8839 | 1.0505 |
| Receivers | 43 | 0.8753 | 1.0505 |
| Electronics & control | 16 | 0.7196 | 1.1894 |
| Interconnection piping | 11 | 0.7319 | 1.2677 |
| Header piping | 8 | 0.8318 | 1.2677 |
| Installation | 17 | 0.8933 | 1.0000 |
| Other | 17 | 0.8665 | 1.0000 |
| Total reference direct costs | 237 | | |

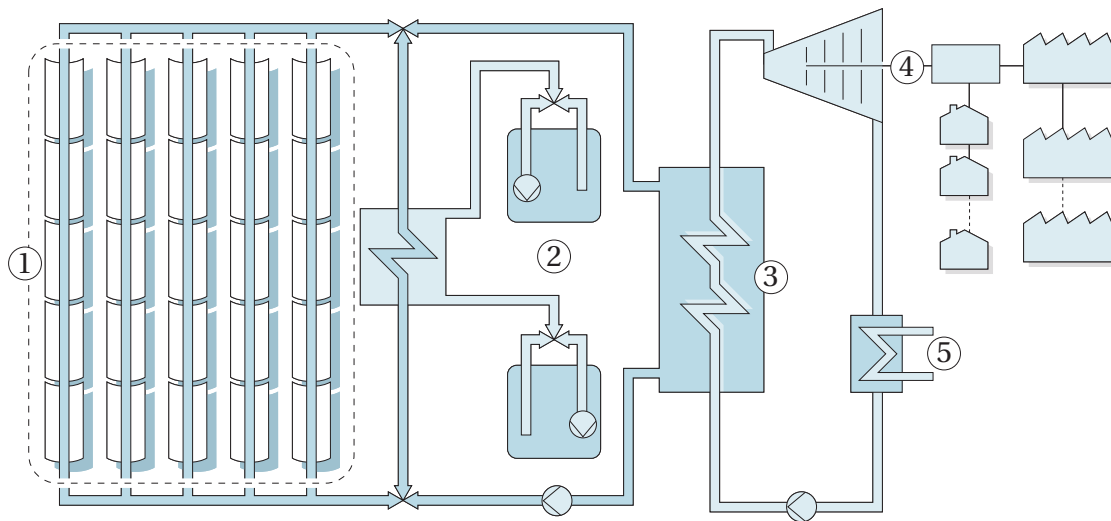
Power Conversion Unit

See §5.1.3.

I.2.2 Financial Performance

See §5.2.

I.3 Andasol-1 Case Study



1. Solar field, 2. Storage, 3. Heat exchanger, 4. Steam turbine and generator, 5. Condenser

Figure I.4 – Trough plant diagram of Andasol-1 [SolarMillenium, 2008].

Table I.2 – Parameters and performance of the trough field for Andasol-1 [SolarMillenium, 2008].

| <i>Design variables</i> | | <i>Unit</i> |
|-----------------------------|--------|------------------------|
| Trough module width | 5.77 | [m] |
| Trough module length | 566.73 | [m] |
| Number of trough modules | 156 | [u] |
| Glass outer diameter | 0.125 | [m] |
| Glass thickness | 0.005 | [m] |
| Tube outer diameter | 0.07 | [m] |
| Tube thickness | 0.002 | [m] |
| <i>Energy performance</i> | | |
| Annual field efficiency | 0.5374 | [-] |
| Max. thermal power | 335.5 | [MW _{th}] |
| Annual field output | 692 | [GWh _{th}] |
| Nominal thermal power | 185.2 | [MW _{th}] |
| Net electric power | 50 | [MW _{el}] |
| Annual electric output | 186.8 | [GWh _{el}] |
| <i>Economic performance</i> | | |
| Total investment costs | 248.6 | [M\$] |
| Levelised electricity cost | 17.51 | [¢/kWh _{el}] |
| Payback period | 6.14 | [y] |
| Net present value | 286.2 | [M\$] |

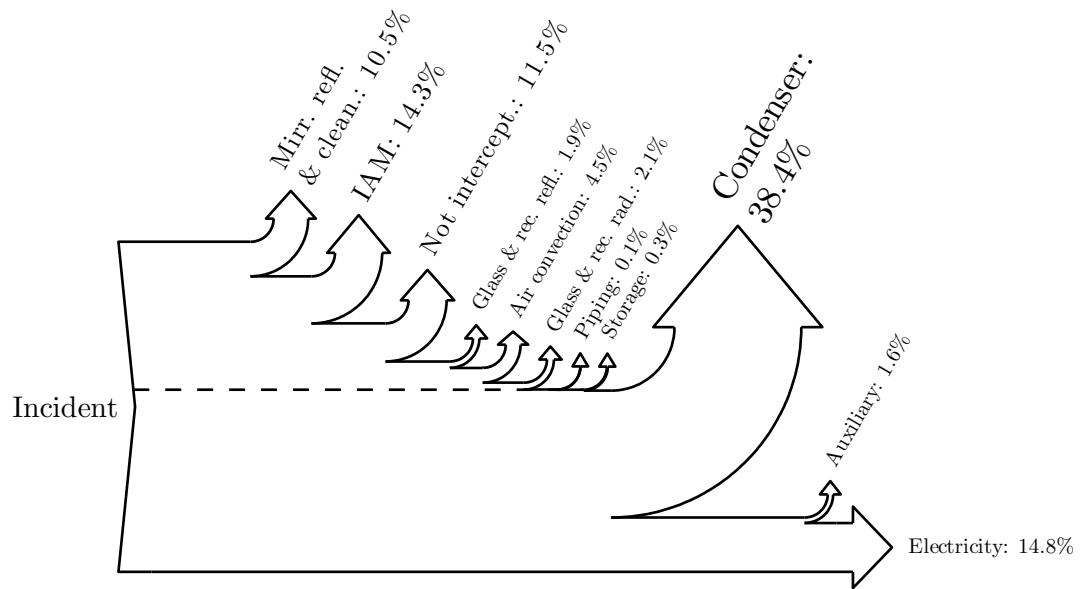


Figure I.5 – Trough plant Sankey diagram of losses for the Andasol-1 set-up over the three specific days (graphic tool from [Spelling et al., 2011]).

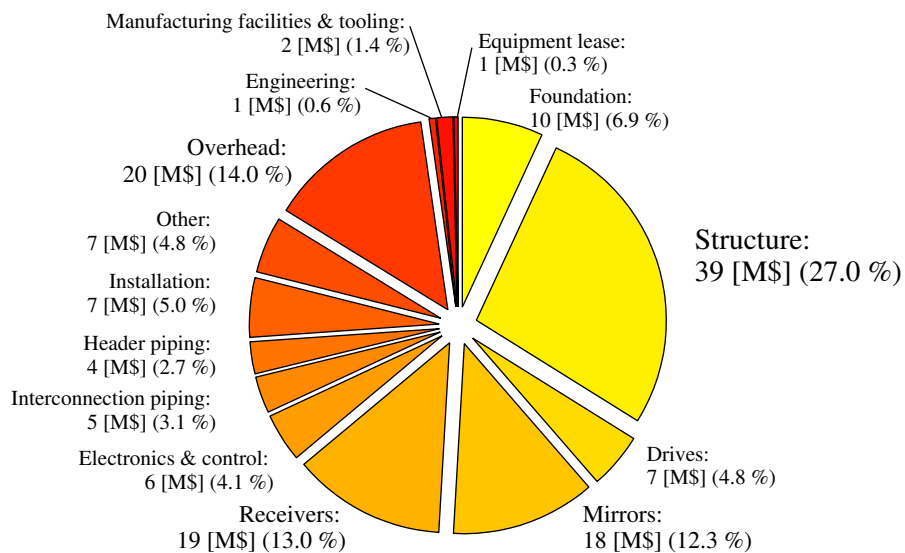


Figure I.6 – Estimate of the trough cost breakdown in the Andasol-1 case.

Appendix I. Trough Field Model

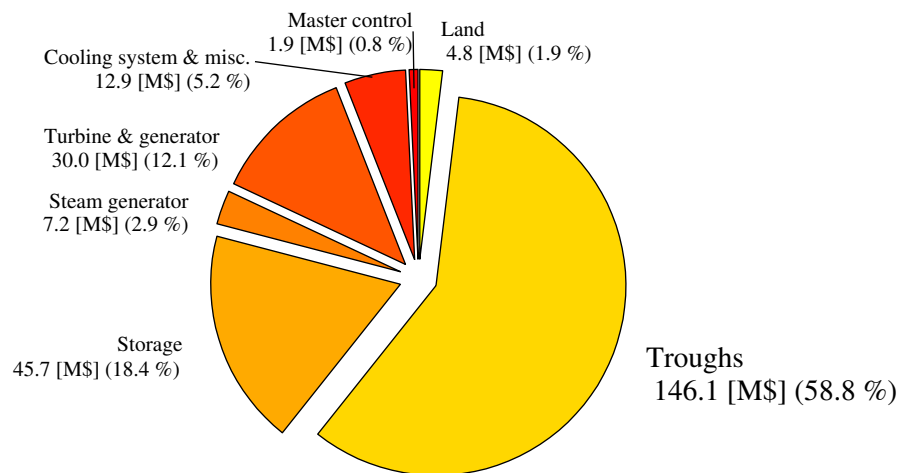


Figure I.7 – Estimate of the plant cost breakdown in the Andasol-1 case.

J Life Cycle Analysis of CSP

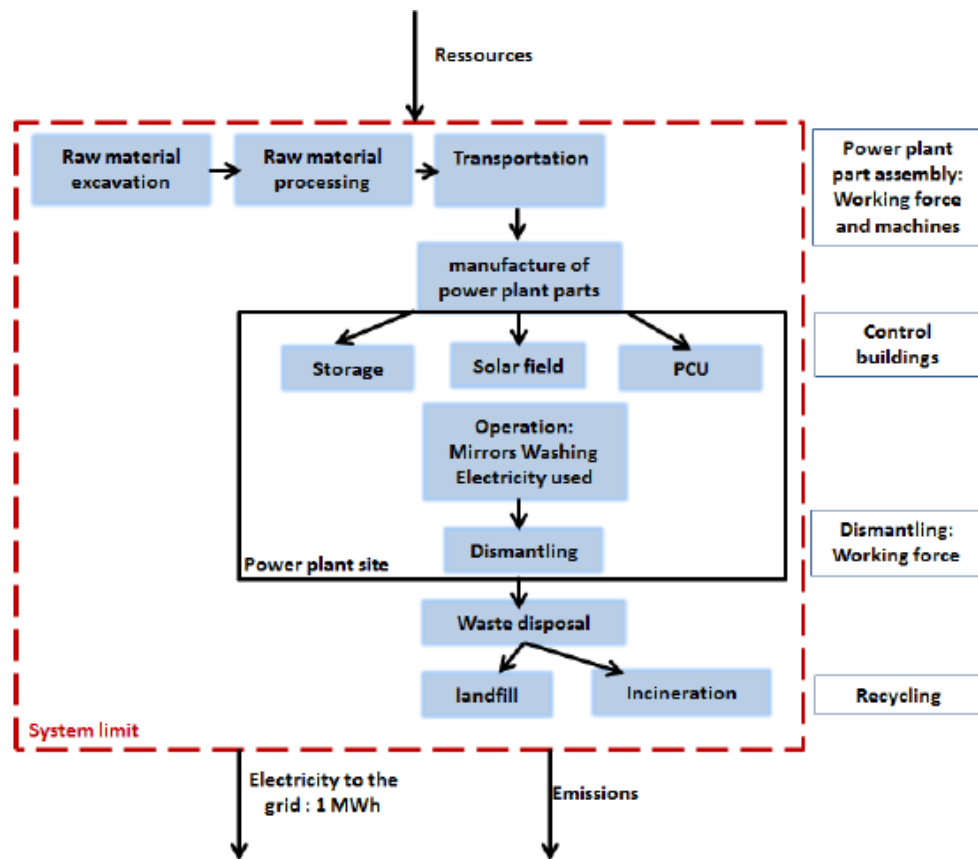


Figure J.1 – Limits of the CSP system for the life cycle analysis [Kuenlin et al., 2011].

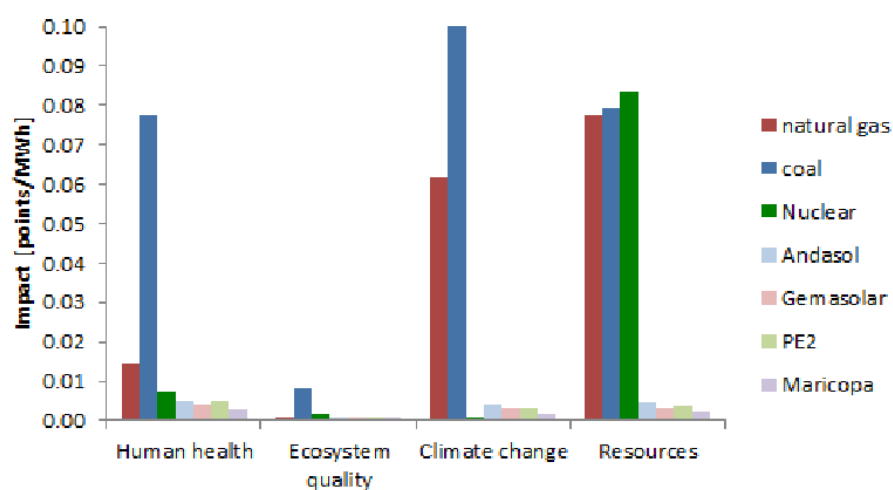


Figure J.2 – Impact comparison between CSP plants and fossil plants [Kuenlin et al., 2011].

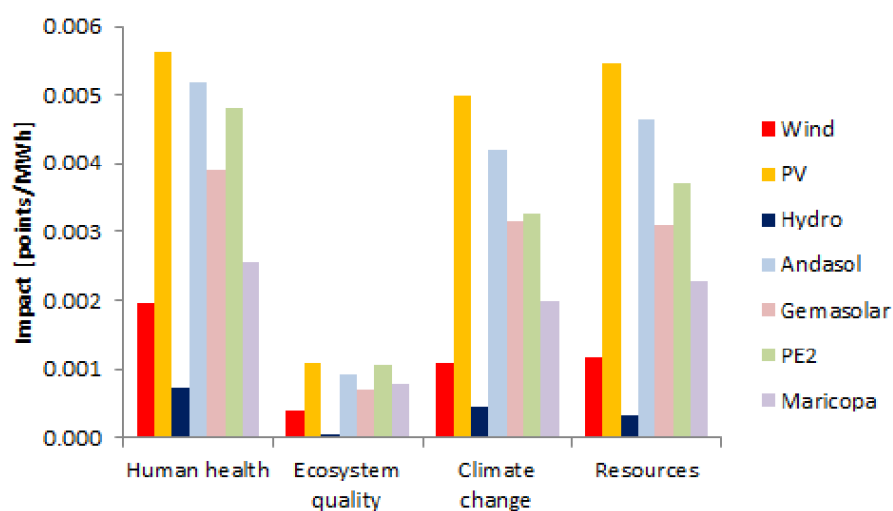


Figure J.3 – Impact comparison between CSP plants and other renewable plants [Kuenlin et al., 2011].

Bibliography

- [Abengoa, 2007] Abengoa (2007). PS10, the first solar power tower worldwide. Technical report, Abengoa Solar, S.A., C/ de la Energía Solar, Palmas Altas, 41014 - Sevilla.
- [Abengoa, 2009] Abengoa (2009). PS20, the largest solar power tower worldwide. Technical report, Abengoa Solar, S.A., C/ de la Energía Solar, Palmas Altas, 41014 - Sevilla.
- [Abengoa, 2011] Abengoa (2011). Heliostato Sanlúcar 120. Technical report, Abengoa Solar, S.A., C/ de la Energía Solar, Palmas Altas, 41014 - Sevilla.
- [Aerospace, 1978] Aerospace (1978). Preliminary definition of Barstow standard cloud model. Technical report, The Aerospace Corporation, El Segundo, California 90245.
- [Allani et al., 1997] Allani, Y., Favrat, D., and von Spakovsky, M. (1997). CO₂ mitigation through the use of hybrid solar-combined cycles. *Energy Conversion and Management*, 38:S661–S667.
- [Alstom, 2010] Alstom (2010). MT Steam Turbine - Mid-Sized Turbine. Technical report, Alstom (Switzerland) Ltd, Brown Boveri Strasse 7, CH-5401 Baden.
- [Alstom, 2012] Alstom (2012). Steam Turbines. Technical report, Alstom (Switzerland) Ltd, Brown-Boveri Strasse 7, CH-5401 Baden, Switzerland.
- [Andrade da Costa and Lemos, 2009] Andrade da Costa, B. and Lemos, J. (2009). An adaptive temperature control law for a solar furnace. *Control Engineering Practice*, 17(10):1157–1173.
- [AORA, 2009] AORA (2009). Tulip™ DST Unit - Features Summary. Technical report, AORA Solar Ltd., 12A Hamada Street, Rabin Park, Rehovot 76703, ISRAEL.
- [ASHRAE, 2001] ASHRAE (2001). *International Weather for Energy Calculations (IWECC Weather Files) Users Manual and CD-ROM*. Atlanta.
- [ASHRAE, 2011] ASHRAE (2011). *2011 ASHRAE Handbook—HVAC Applications*. 1791 Tullie Circle, Atlanta, GA 30329.
- [ASTM, 2006] ASTM (2006). Standard - Solar Constant and Zero Air Mass Solar Spectral Irradiance. In *Annual Book of ASTM Standards*, volume i, pages 1–16. ASTM International, 100 Barr Harbor Drive, PO Box C700, West Conshohocken, PA 19428-2959, United States.
- [Augsburger and Favrat, 2010] Augsburger, G. and Favrat, D. (2010). Thermo-economic Optimisation of the Heliostat Field of Solar Tower Thermal Power Plants. In *ecos 2010 - 23rd International Conference on Efficiency, Cost, Optimization, Simulation and Environmental Impact of Energy Systems*, pages 1–8, Lausanne, Switzerland. EPFL-LENI.

Bibliography

- [Augsburger and Favrat, 2012] Augsburger, G. and Favrat, D. (2012). From Single- to Multi-Tower Solar Thermal Power Plants: Investigation of the Thermo-Economic Optimum Transition Size. In *Proceedings of the SolarPACES 2012 Conference on Concentrating Solar Power and Chemical Energy Systems*, Marrakesh, Morocco.
- [Augsburger and Favrat, 2013] Augsburger, G. and Favrat, D. (2013). Modelling of the receiver transient flux distribution due to cloud passages on a solar tower thermal power plant. *Solar Energy*, 87:42–52.
- [Augsburger et al., 2012] Augsburger, G., Zhang, H., Jüchli, I., and Pelet, X. (2012). Lenisolar: a Code for the Thermo-economic Optimisation of Solar Tower Power Plants. Technical report, Industrial Energy Systems Laboratory, École Polytechnique Fédérale de Lausanne, Bât. ME A2, Station 9, CH - 1015 Lausanne, Vaud, Switzerland.
- [Aviador, 2011] Aviador (2011). Wind Profile Stats (Beta).
- [Avila-Marín, 2011] Avila-Marín, A. L. (2011). Volumetric receivers in Solar Thermal Power Plants with Central Receiver System technology: A review. *Solar Energy*, 85(5):891–910.
- [Ballestrín and Marzo, 2012] Ballestrín, J. and Marzo, A. (2012). Solar radiation attenuation in solar tower plants. *Solar Energy*, 86(1):388–392.
- [Battleson, 1981] Battleson, K. W. (1981). Solar power tower design guide: solar thermal central receiver power systems, a source of electricity and/or process heat. *Annals of Nuclear Energy*.
- [Bergman et al., 2011] Bergman, T. L., Lavine, A. S., Incropera, F. P., and Dewitt, D. P. (2011). *Fundamentals of Heat and Mass Transfer*. John Wiley & Sons, Hoboken, N.J., 7th edition.
- [Biggs and Vittitoe, 1979] Biggs, F. and Vittitoe, C. N. (1979). The Helios model for the optical behavior of reflecting solar concentrators. Technical report, Sandia Laboratories, Albuquerque, NM 87185 (USA).
- [BLS, 2011] BLS (2011). Producer Price Index Industry Data.
- [Boletín Oficial del Estado, 2007] Boletín Oficial del Estado (2007). REAL DECRETO 661/2007, de 25 de mayo, por el que se regula la actividad de producción de energía eléctrica en régimen especial. Technical report.
- [Boletín Oficial del Estado, 2012] Boletín Oficial del Estado (2012). Real Decreto-ley 1/2012, de 27 de enero, por el que se procede a la suspensión de los procedimientos de preasignación de retribución y a la supresión de los incentivos económicos para nuevas instalaciones de producción de energía eléctrica a partir de cog. Technical report.
- [Bolle et al., 1985] Bolle, G., Ciccarella, G., and Marietti, P. (1985). Automatic aiming and tracking of the solar disc using photosensitive charge coupled devices (CCD). *Applied Energy*, 19(3):197–208.
- [BrightSource, 2008] BrightSource (2008). Solar Energy Development Center. Technical report, BrightSource Energy, 11 Kiryat Mada St., Amot bldg #6, P.O. Box 45220, Har Hotzvim, Jerusalem, 91450 Israel.

- [BrightSource, 2011] BrightSource (2011). Coalinga Chevron/BrightSource Solar-to-Steam Demonstration Facility. Technical report, BrightSource Energy, 1999 Harrison Street, Suite 2150, Oakland, CA 94612.
- [BrightSource, 2012] BrightSource (2012). Ivanpah Solar Electric Generating System. Technical report, BrightSource Energy, 1999 Harrison Street, Suite 2150, Oakland, CA 94612.
- [Buck et al., 2002] Buck, R., Bräuning, T., Denk, T., Pfänder, M., Schwarzbözl, P., and Tellez, F. (2002). Solar-Hybrid Gas Turbine-based Power Tower Systems (REFOS). *Journal of Solar Energy Engineering*, 124(1):2.
- [Burgaleta et al., 2011] Burgaleta, J. I., Arias, S., and Ramirez, D. (2011). GEMASOLAR, the First Tower Thermosolar Commercial Plant With Molten Salt Storage. In *Proceedings of the SolarPACES 2011 Conference on Concentrating Solar Power and Chemical Energy Systems*, Granada, Spain.
- [Caldwell, 2009] Caldwell, D. W. (2009). Multi-receiver heliostat system architecture.
- [CHE, 2011] CHE (2011). Plant Cost Index.
- [Chen et al., 2006] Chen, Y., Lim, B., and Lim, C. (2006). Off-axis aberration correction surface in solar energy application. *Solar Energy*, 80(3):268–271.
- [Collado, 2008] Collado, F. (2008). Quick evaluation of the annual heliostat field efficiency. *Solar Energy*, 82(4):379–384.
- [Collado et al., 1986] Collado, F. J., Gómez, A., and Turégano, J. A. (1986). An analytic function for the flux density due to sunlight reflected from a heliostat. *Solar Energy*, 37(3):215–234.
- [Crespo et al., 2012] Crespo, L., Latorre, M. P., Fernández, M., Leung, J., Dufour, E., and Garcia Iglesias, E. (2012). The First 5 Years of ESTELA. Technical report, European Solar Thermal Electricity Association, Rue d’Arlon, 63-67 B - 1040 - Brussels.
- [CSIRO, 2011] CSIRO (2011). National Solar Energy Centre. Technical report, Commonwealth Scientific and Industrial Research Organisation, Steel River Estate 10 Murray Dwyer Circuit, Mayfield West NSW 2304, Australia.
- [Czisch and Trieb, 2002] Czisch, G. and Trieb, F. (2002). Optionen einer Europäisch-, Transeuropäischen Stromversorgung aus erneuerbaren Energien. Technical Report 1734.
- [DLR, 2005] DLR (2005). Concentrating Solar Power for the Mediterranean Region. Technical report, Systems Analysis and Technology Assessment, Institute of Technical Thermodynamics, Deutsches Zentrum für Luft- und Raumfahrt e.V. (DLR), Pfaffenwaldring 38-40, D-70569 Stuttgart, Germany.
- [DLR, 2008] DLR (2008). Der Solarturm Jülich. Technical report, Deutsches Zentrum für Luft- und Raumfahrt, Institut für Solarforschung, Linder Höhe, 51147 Köln.
- [DOW, 2001] DOW (2001). SYLTHERM 800 - Silicone Heat Transfer Fluid. Technical report, The Dow Chemical Company.
- [Dudley et al., 1994] Dudley, V., Kolb, G., Mahoney, A., Mancini, T., Matthews, C., Sloan, M., and Kearney, D. (1994). Test results: SEGS LS-2 solar collector. Technical report, Sandia National Laboratories, Albuquerque, New Mexico.

Bibliography

- [ESolar, 2009] ESolar (2009). Sierra SunTower. Technical report, eSolar, Inc., 3355 W. Empire Avenue, Suite 200, Burbank, CA 91504.
- [Eugene Moeller et al., 1980] Eugene Moeller, C., Brumleve, T. D., Grosskreutz, C., Seamons, L., Moellert, C. E., and I, L. O. S. (1980). Central receiver test facility Albuquerque, New Mexico. *Solar Energy*, 25(4):291–302.
- [Fernandez, 2006] Fernandez, V. (2006). PS10 : a 11-MWe Solar Tower Power Plant with Saturated Steam Receiver.
- [Fricker, 2004] Fricker, H. (2004). Regenerative thermal storage in atmospheric air system solar power plants. *Energy*, 29(5-6):871–881.
- [Garcia et al., 2008] Garcia, P., Ferriere, A., and Bezian, J.-J. (2008). Codes for solar flux calculation dedicated to central receiver system applications: A comparative review. *Solar Energy*, 82(3):189–197.
- [Garmendia et al., 2012] Garmendia, A. E., Gilaberte, R. N., Jiménez, J. B., and Méndez Marcos, J. M. (2012). Description of Abengoa Solar Tower Solution with Superheated Steam Technology. In *Submission to the Proceedings of the SolarPACES 2012 Conference on Concentrating Solar Power and Chemical Energy Systems*, Marrakesh, Morocco.
- [GE, 2005] GE (2005). Steam Turbine Products. Technical report, GE Energy, 4200 Wildwood Parkway, Atlanta, GA 30339.
- [Geyer and Lüpfer, 2002] Geyer, M. and Lüpfer, E. (2002). EUROTROUGH - Parabolic Trough Collector Developed for Cost Efficient Solar Power Generation. In *Proceedings of the 11th Int. Symposium on Concentrating Solar Power and Chemical Energy Technologies*, pages 1–7, Zurich, Switzerland.
- [Google, 2012] Google (2012). Google Earth.
- [Gould, 2011] Gould, W. R. (2011). SolarReserve’s 565 MWt Molten Salt Power Towers. In *Proceedings of the SolarPACES 2011 Conference on Concentrating Solar Power and Chemical Energy Systems*, Granada, Spain.
- [Grena, 2008] Grena, R. (2008). An algorithm for the computation of the solar position. *Solar Energy*, 82(5):462–470.
- [Grena, 2012] Grena, R. (2012). Five new algorithms for the computation of sun position from 2010 to 2110. *Solar Energy*.
- [Hartung et al., 1980] Hartung, V., Hofmann, J., and Kindermann, C. (1980). The heliostat field layout of the EEC experimental solar power plant. *Electric Power Systems Research*, 3(1-2):77–89.
- [Hoffschmidt et al., 2003] Hoffschmidt, B., Téllez, F. M., Valverde, A., Fernandez, J., and Fernandez, V. (2003). Performance Evaluation of the 200-kW[sub th] HiTRec-II Open Volumetric Air Receiver. *Journal of Solar Energy Engineering*, 125(1):87.
- [Honeywell, 1977] Honeywell (1977). Solar Pilot Plant, Phase I. Preliminary design report. Volume II, Book 3. Dynamic simulation model and computer program descriptions. CDRL item 2. [SPP dynamics simulation program]. Technical report, Honeywell, Inc., Energy Resources Center, Minneapolis, MN (USA).

- [INABENSA, 2002] INABENSA (2002). EUROTROUGH II - Extension, Test and Qualification of EUROTROUGH from 4 to 6 Segments at Plataforma Solar de Almería. Technical Report April 2003, INABENSA, SOLUCAR, IBERDROLA, FLABEG Solar International, Schlaich Bergemann und Partner, CIEMAT, DLR, SOLEL,.
- [IRENA, 2012] IRENA (2012). Renewable Technologies: Cost Analysis Series - Concentrating Solar Power. Technical Report 2, International Renewable Energy Agency, C67 Office Building, Khalidiyah (32nd) Street, P.O. Box 236, Abu Dhabi, United Arab Emirates.
- [Jun et al., 2009] Jun, W., Yaoming, Z., Deyou, L., and Su, G. (2009). Introduction of the First Solar Power Tower System in China. In Goswami, D. Y. and Zhao, Y., editors, *Proceedings of ISES World Congress 2007 (Vol. I – Vol. V)*, pages 1738–1742. Springer Berlin Heidelberg.
- [Kalogirou, 2009] Kalogirou, S. (2009). *Solar Energy Engineering - Processes and Systems*. Academic Press.
- [Kamp et al., 2012] Kamp, H., Schmidt, M., Sauerborn, A., and Kuckelkorn, T. (2012). SCHOTT Parabolic Trough Receivers for Operation with Molten Salt. In *Proceedings of the SolarPACES 2012 Conference on Concentrating Solar Power and Chemical Energy Systems*, volume 49, Marrakesh, Morocco.
- [Kane and Favrat, 2002] Kane, M. and Favrat, D. (2002). Multicriteria Optimisation of Small Hybrid Solar Power System. In *Proceedings of EuroSun 2002, The fourth ISES-Europe Solar Congress, Bologna, Italy, 23.-26. June, 2002*, Bologna, Italy.
- [Kane et al., 2000] Kane, M., Favrat, D., Ziegler, K., and Allani, Y. (2000). Thermoeconomic Analysis of Advanced Solar-Fossil Combined Power Plants. *International Journal of Thermodynamics*, 3(4):191–198.
- [Karg et al., 1982] Karg, E., Mueller, H., and Quenzel, H. (1982). Determination of the cumulus cloud size distribution on the basis of Landsat imagery. *Annalen der Meteorologie*, 18:142–144.
- [Kiehl and Trenberth, 1997] Kiehl, J. T. and Trenberth, K. E. (1997). Earth's Annual Global Mean Energy Budget. *Bulletin of the American Meteorological Society*, 78(2):197–208.
- [Kistler, 1986] Kistler, B. (1986). A user's manual for DELSOL3: A computer code for calculating the optical performance and optimal system design for solar thermal central receiver plants. Technical report, Sandia National Laboratories, Livermore, CA (USA).
- [Kolb et al., 1991] Kolb, G., Alpert, D., and Lopez, C. (1991). Insights from the operation of Solar One and their implications for future central receiver plants. *Solar Energy*, 47(1):39–47.
- [Kolb et al., 2011] Kolb, G. J., Ho, C. K., Mancini, T. R., and Gary, J. A. (2011). Power Tower Technology Roadmap and cost reduction plan. Technical report, Sandia National Laboratories, Albuquerque, New Mexico 87185 and Livermore, California 94550.
- [Kolb et al., 2007] Kolb, G. J., Jones, S. A., Donnelly, M. W., Gorman, D., Thomas, R., Davenport, R., and Lumia, R. (2007). Heliostat Cost Reduction Study. Technical Report June, Sandia National Laboratories, Albuquerque, New Mexico 87185 and Livermore, California 94550.

Bibliography

- [Kroyzer, 2011] Kroyzer, G. (2011). Method and apparatus for operating a solar energy system to account for cloud shading. Technical report, BrightSource Industries (Israel), Ltd, Jerusalem, IL.
- [Kuenlin et al., 2011] Kuenlin, A., Maréchal, F., Gerber, L., and Augsburger, G. (2011). Life Cycle Analysis and Thermo-Environomic Optimization of Concentrated Solar Thermal Power Plants. Technical report, Industrial Energy Systems Laboratory, Swiss Federal Institute of Technology Lausanne, Lausanne, Switzerland.
- [Lloyd, 2011] Lloyd (2011). Lake Cargelligo Solar Thermal Project. Technical Report August, Lloyd Energy Systems Pty Ltd.
- [López-Martínez et al., 2002] López-Martínez, M., Vargas, M., and Rubio, F. (2002). Advances in Artificial Intelligence — IBERAMIA 2002. In Garijo, F. J., Riquelme, J. C., and Toro, M., editors, *Lecture Notes in Computer Science, 2002, Volume 2527/2002*, volume 2527 of *Lecture Notes in Computer Science*, pages 943–952. Springer Berlin Heidelberg, Berlin, Heidelberg.
- [López Moreno and Augsburger, 2011] López Moreno, J. and Augsburger, G. (2011). Thermo-Economic Optimization of a Tower-Trough Combination Thermal Solar Power Plant. In *Proceedings of the 4th World Engineers' Convention, September 4-9*, Geneva, Switzerland.
- [Lowrie, 1979] Lowrie, A. (1979). SRE receiver subsystem experiment: solar test procedure. Technical report, Martin Marietta Corp, Denver, CO (USA).
- [Maffezzoni and Parigi, 1982] Maffezzoni, C. and Parigi, F. (1982). Dynamic analysis and control of a solar power plant - I Dynamic analysis and operation criteria. *Solar Energy*, 28(2):105–116.
- [Mancini, 2000] Mancini, T. R. (2000). Catalog of Solar Heliostats. Technical Report Iii, SolarPACES, Deutsches Zentrum für Luft- und Raumfahrt e.V., Solare Energietechnik (DLR, EN-SE), D-51170 Köln.
- [Martínez-Chico et al., 2011] Martínez-Chico, M., Batlles, F., and Bosch, J. (2011). Cloud classification in a mediterranean location using radiation data and sky images. *Energy*, 36(7):4055–4062.
- [MathWorks, 2011] MathWorks (2011). MATLAB - The Language of Technical Computing.
- [McDonnell, 1978] McDonnell (1978). 10-MWe pilot-plant-receiver-panel test-requirements document: Solar Thermal Test Facility. Technical report, McDonnell Douglas Astronautics Co., Huntington Beach, CA (USA).
- [Meteonorm, 2012] Meteonorm (2012). Meteonorm - Global meteorological database.
- [Météosuisse, 2012] Météosuisse (2012). MétéoSuisse - Portail de données.
- [Molyneaux et al., 2010] Molyneaux, A., Leyland, G., and Favrat, D. (2010). Environomic multi-objective optimisation of a district heating network considering centralized and decentralized heat pumps. *Energy*, 35(2):751–758.
- [Monterreal, 1998] Monterreal, R. (1998). New computer code for solar concentrating optics simulation. In *Proceedings of the 1998 9th SolarPaces International Symposium on Solar Thermal Concentrating Technologies, STCT 9; Font-Romeu; 22 June 1998 through*

- 26 June 1998, Proceedings of the 1998 9th SolarPaces International Symposium on Solar Thermal Concentrating Technologies, STCT 9, Plataforma Solar de Almeria, Aptdo. 22, 04200 Tabernas, Spain.
- [Moss and Brosseau, 2005] Moss, T. A. and Brosseau, D. A. (2005). Final Test Results for the Schott HCE on a LS-2 Collector. Technical Report July, Sandia National Laboratories, Albuquerque, New Mexico 87185 and Livermore, California 94550.
- [Nasa, 2011] Nasa (2011). Surface meteorology and Solar Energy.
- [NREL, 2012] NREL (2012). SunShot Vision Study. Technical Report February, National Renewable Energy Laboratory, U.S. Department of Energy, Office of Energy Efficiency and Renewable Energy.
- [Ortega et al., 2008] Ortega, J. I., Burgaleta, J. I., and Tellez, F. M. (2008). Central Receiver System Solar Power Plant Using Molten Salt as Heat Transfer Fluid. *Journal of Solar Energy Engineering*, 130(2):024501.
- [Osuna et al., 2007] Osuna, R., Geyer, M., Burgaleta, J. I., Zarza, E., Schiel, W., Pitz-Paal, R., Tamme, R., Laing, D., Heller, P., Möller, S., Sugarmen, C., Olalde, G., Flamant, G., and Konstandopoulos, A. (2007). Concentrating Solar Power: from Research to Implementation. Technical report, European Commission, Directorate - General for Energy and Transport Directorate, Directorate - General for Research, Luxembourg.
- [Pacheco, 2002] Pacheco, J. E. (2002). Final Test and Evaluation Results from the Solar Two Project. Technical report, Sandia National Laboratories, Albuquerque, New Mexico 87185 and Livermore, California 94550.
- [Pelet et al., 2006] Pelet, X., Favrat, D., Sanchez, M., and Romero, M. (2006). Design of Heliostat Fields Using a Multi-Objective Evolutionary Algorithm. In *Proceedings of the 13th International Symposium on Concentrated Solar Power and Chemical Energy Technologies, Seville, Spain, 20-23 June 2006*, Sevilla, Spain.
- [Peterka et al., 1987] Peterka, J., Bienkiewicz, B., Hosoya, N., and Cermak, J. (1987). Heliostat mean wind load reduction. *Energy*, 12(3-4):261–267.
- [Pitz-Paal et al., 2005] Pitz-Paal, R., Dersch, J., and Milow, B. (2005). ECOSTAR - European Concentrated Solar Thermal Road-Mapping. Technical report, Deutsches Zentrum für Luft- und Raumfahrt e.V.
- [Pritzkow, 1991] Pritzkow, W. E. (1991). Pressure loaded volumetric ceramic receiver. *Solar Energy Materials*, 24(1-4):498–507.
- [PROMES, 2011a] PROMES (2011a). Odeillo High-Flux Solar Furnace. Technical report, Laboratoire de Procédés, Matériaux et Énergie Solaire, PROMES - CNRS, 7, rue du Four Solaire, 66120 Font Romeu Odeillo, FRANCE.
- [PROMES, 2011b] PROMES (2011b). Themis solar tower. Technical report, Laboratoire de Procédés, Matériaux et Énergie Solaire, PROMES - CNRS, 7, rue du Four Solaire, 66120 Font Romeu Odeillo, FRANCE.
- [PSA, 2012a] PSA (2012a). 2.7 MWt SSPS-CRS Facility. Technical report, Plataforma Solar de Almería, Ctra. de Senés km. 4,5 Tabernas (04200) Almería.

Bibliography

- [PSA, 2012b] PSA (2012b). 7 MWt CESA-I Facility. Technical report, Plataforma Solar de Almería, Ctra. de Senés km. 4,5 Tabernas (04200) Almería.
- [PVGIS, 2007] PVGIS (2007). Photovoltaic Geographical Information System - Interactive Maps.
- [Raade et al., 2012] Raade, J. W., Elkin, B., and Vaughn, J. (2012). Novel 700 °C Molten Salt for Solar Thermal Power Generation with Supercritical Steam Turbines. In *Submission to the Proceedings of the SolarPACES 2012 Conference on Concentrating Solar Power and Chemical Energy Systems*, volume 001, Marrakesh, Morocco.
- [Reiner Buck, 2008] Reiner Buck (2008). Evaluation of Optical Characteristics of Two Heliostat Configurations - Report prepared for ALSTOM - Contract Number 3 001 129. Technical Report 3, DLR - Deutsches Zentrum für Luft- und Raumfahrt e.V., Germany.
- [Ren et al., 2012] Ren, N., Wu, Y.-t., and Ma, C.-f. (2012). Experimental Study on Thermal Properties of New Kinds of Mixed Nitrate Salts. In *Submission to the Proceedings of the SolarPACES 2012 Conference on Concentrating Solar Power and Chemical Energy Systems*, number 100, Marrakesh, Morocco.
- [Sargent & Lundy, 2003] Sargent & Lundy (2003). Assessment of Parabolic Trough and Power Tower Solar Technology Cost and Performance Forecasts. Technical report, Sargent & Lundy LLC Consulting Group; National Renewable Energy Laboratory, Chicago, Illinois; Golden, Colorado (US).
- [Satel-Light, 2005] Satel-Light (2005). Satel-Light - The European Database of Daylight and Solar Radiation.
- [SCHOTTSolar, 2011] SCHOTTSolar (2011). SCHOTT PTR ® 70 Receiver - Setting the benchmark. Technical report, SCHOTT Solar CSP GmbH, Hattenbergstraße 10, 55122 Mainz, Germany.
- [Schramek, 2003] Schramek, P. (2003). Multi-tower solar array. *Solar Energy*, 75(3):249–260.
- [Schwarzbözl et al., 2009] Schwarzbözl, P., Schmitz, M., and Pitz-paal, R. (2009). Visual HFLCAL - A Software Tool for Layout and Optimisation of Heliostat Fields. In *Proceedings of the SolarPACES 2009 Conference on Concentrating Solar Power and Chemical Energy Systems*, Berlin, Germany.
- [SENER, 2010] SENER (2010). Case Study: GEMASOLAR Central Tower Plant Tower.
- [Siala and Elayeb, 2001] Siala, F. and Elayeb, M. (2001). Mathematical formulation of a graphical method for a no-blocking heliostat field layout. *Renewable Energy*, 23(1):77–92.
- [Siemens, 2010] Siemens (2010). The unrivaled benchmark in solar receiver efficiency Precise engineering ensures peak performance - Siemens UVAC 2010. Technical report, Siemens AG, Energy Sector, Renewable Energy Division, Solar Power, Hugo-Junker-Strasse 15, 90411 Nürnberg, Germany.
- [Siemens, 2012] Siemens (2012). Industrial Steam Turbines. Technical report, Siemens AG, Energy Sector, Freyeslebenstrasse 1, 91058 Erlangen, Germany.
- [Singh et al., 2010] Singh, H., Saini, R., and Saini, J. (2010). A review on packed bed solar energy storage systems. *Renewable and Sustainable Energy Reviews*, 14(3):1059–1069.

- [SNL, 2012] SNL (2012). Central Receiver Test Facility. Technical report, National Solar Thermal Test Facility, Sandia National Laboratories, MS 1127 Albuquerque, NM 87185.
- [Sobin et al., 1976] Sobin, A., Wagner, W., and Easton, C. (1976). Central collector solar energy receivers. *Solar Energy*, 18(1):21–30.
- [SoDa, 2004] SoDa (2004). Time Series of Solar Radiation Data.
- [SolarMillenium, 2008] SolarMillenium (2008). The parabolic trough power plants Andasol 1 to 3. Technical report, Solar Millennium AG, Nögelsbachstraße 40, D-91052 Erlangen, Germany.
- [SolarPACES, 2009] SolarPACES (2009). Concentrating Solar Power - Global Outlook 09 - Why Renewable Energy is Hot. Technical report.
- [Solarstor, 2009] Solarstor (2009). Cooma Product Development, Manufacturing and Demonstration site. Technical report, Solastor, 73 Polo Flat Road, Cooma, NSW, Australia, 2630.
- [SOLEMI, 2005] SOLEMI (2005). SOLEMI - Solar Energy Mining.
- [Solúcar, 2005] Solúcar (2005). 10 MW Solar Thermal Power Plant for Southern Spain. Technical Report November 2006.
- [Solugas, 2012] Solugas (2012). Solugas - Solar Up-scale Gas Turbine System.
- [Solutia, 2008] Solutia (2008). Therminol VP-1, Heat Transfer Fluid by Solutia. Technical report, Solutia Inc., St. Louis, MO.
- [Spelling et al., 2011] Spelling, J., Favrat, D., Martin, A., and Augsburg, G. (2011). Thermoeconomic optimization of a combined-cycle solar tower power plant. *Energy*, 41(1):120–113.
- [Stoddard, 1986] Stoddard, M. (1986). Convective loss measurements at the 10 MWe Solar Thermal Central Receiver Pilot Plant. Technical report, Sandia National Laboratories, Livermore, CA (USA).
- [Strand et al., 2012] Strand, T., Spelling, J., Nilsson, L. R. K., and Hansson, H.-e. (2012). An Innovative Hybrid Solar Gas-Turbine Power Plant Based on the Topcycle Concept. In *Submission to the Proceedings of the SolarPACES 2012 Conference on Concentrating Solar Power and Chemical Energy Systems*, Marrakesh, Morocco.
- [SWEC, 2012] SWEC (2012). SWEC - Spanish Weather for Energy Calculations.
- [Torresol, 2011] Torresol (2011). Gemasolar, the world's first solar thermal plant consisting of central tower technology and salts receiver. Technical report, Torresol Energy Investments, S.A., A4 p.k. 475, 41420 Fuentes de Andalucía, Seville - Spain.
- [UzAS, 2008] UzAS (2008). 1000kW Parkent Solar Furnace. Technical report, Uzbek Academy of Sciences, Acad. Gulyamova Yahya, 70, 100047, Tashkent, Uzbekistan.
- [Šúri et al., 2009] Šúri, M., Remund, J., Cebecauer, T., Hoyer-klick, C., Dumortier, D., Huld, T., Stackhouse, P. W., and Ineichen, P. (2009). Comparison of Direct Normal Irradiation Maps for Europe. In *Proceedings of the SolarPACES 2009 Conference on Concentrating Solar Power and Chemical Energy Systems*, number i, pages 1–8, Berlin, Germany.
- [Winter, 1991] Winter, C.-J. (1991). *Solar power plants*. Springer.

Bibliography

- [WIS, 2010] WIS (2010). Solar Research Facilities. Technical report, Weizmann Institute of Science, P.O.Box 26, Rehovot 76100, Israel.
- [WMO, 2012] WMO (2012). World Weather Information Service - Official Observations. Official Forecasts.
- [Zhang et al., 2007] Zhang, H., Juchli, I., Favrat, D., and Pelet, X. (2007). Multi-objective thermoeconomic optimisation of the design of heliostat field of solar tower power plants. In *Engineering for Sustainable Energy in Developing Countries, Rio de Janeiro, Brasil, 15 to 18 August 2007.*, Rio de Janeiro, Brasil.

Germain Augsburgger

M.Sc. in Mechanical Engineering, Ph.D. Cand. in Doctoral Program in Energy at Ecole Polytechnique Fédérale de Lausanne

germain.augsburger@epfl.ch

Experience

M.Sc., Ph.D. Cand. at EPFL

September 2008 - Present (4 years 5 months)

Thermo-economic modelling, simulation and optimisation of solar tower thermal plants
in collaboration with ALSTOM (Switzerland) AG

Education

Ecole polytechnique fédérale de Lausanne

Master, Mechanical Engineering, 2007 - 2008

Ecole polytechnique fédérale de Lausanne

Minor, Management of Technology, 2007 - 2007

RWTH Aachen

Exchange, Mechanical Engineering, 2006 - 2007

Ecole polytechnique fédérale de Lausanne

Bachelor, Mechanical Engineering, 2003 - 2005

Publications

Modelling of the Receiver Transient Flux Distribution Due to Cloud Passages on a Solar Tower Thermal Power Plant

Solar Energy, 87, 42–52 2013

Authors: Germain Augsburgger, Daniel Favrat

From Single- to Multi-Tower Solar Thermal Power Plants: Investigation of the Thermo-Economic Optimum Transition Size

In Proceedings of the SolarPACES 2012 Conference on Concentrating Solar Power and Chemical Energy Systems, Marrakesh, Morocco 2012

Authors: Germain Augsburgger, Daniel Favrat

Thermo-economic Optimisation of the Heliostat Field of Solar Tower Thermal Power Plants

In Proceedings of ecos 2010 - 23rd International Conference on Efficiency, Cost, Optimization, Simulation and Environmental Impact of Energy Systems, Lausanne, Vaud, Switzerland 2010

Authors: Germain Augsburgger, Daniel Favrat

Thermoeconomic optimization of a combined-cycle solar tower power plant

Energy, 41(1), 120–113 2011

Authors: James Spelling, Daniel Favrat, Andrew Martin, Germain Augsburg

Thermo-Economic Optimization of a Tower-Trough Combination Thermal Solar Power Plant

Proceedings of the 4th World Engineers' Convention, September 4-9. Geneva, Switzerland 2011

Authors: Jorge López Moreno, Germain Augsburg

Evaluation of a Combined-Cycle Setup for Solar Tower Power Plants

Proceedings of the SolarPACES 2009 Conference on Concentrating Solar Power and Chemical Energy Systems. Berlin, Germany 2009

Authors: James Spelling, Germain Augsburg, Daniel Favrat

Languages

French

(Native or bilingual proficiency)

English

(Professional working proficiency)

German

(Professional working proficiency)

Skills & Expertise

Concentrated Solar Power

Solar Thermal

Solar Energy

Energy Systems

Energy Conversion

Renewable Energy

Energetics

Heat Transfer

Thermodynamics

Thermal Engineering

Turbomachinery

Evolutionary Algorithms

Energy Modelling

Numerical Simulation

Matlab

Linux

Ubuntu

LaTeX

Radiance

Interests

Solar Thermal Power Plants, Concentrated Solar Power, Thermo-economics, Multi-Objective Optimisation, Evolutionary Algorithms, Environomics, Life Cycle Analysis, Exergy, Energy Integration, Heat and Mass Transfer, Turbomachinery, Renewable Energy, Project Management, Academic Teaching, Scouting, Abseiling, Mountain Bike, Running, Hiking
